

UCLA

UCLA Electronic Theses and Dissertations

Title

Statistical mechanics and dynamics of semiflexible filaments, and the role of curvature in elastic low dimensional soft matter

Permalink

<https://escholarship.org/uc/item/5cb2s328>

Author

Kernes, Jonathan Matthew

Publication Date

2020

Peer reviewed|Thesis/dissertation

UNIVERSITY OF CALIFORNIA

Los Angeles

Statistical mechanics and dynamics of semiflexible filaments, and the role of
curvature in elastic low dimensional soft matter

A dissertation submitted in partial satisfaction
of the requirements for the degree
Doctor of Philosophy in Physics

by

Jonathan Matthew Kernes

2020

© Copyright by
Jonathan Matthew Kernes
2020

ABSTRACT OF THE DISSERTATION

Statistical mechanics and dynamics of semiflexible filaments, and the role of curvature in elastic low dimensional soft matter

by

Jonathan Matthew Kernes

Doctor of Philosophy in Physics

University of California, Los Angeles, 2020

Professor Alex J. Levine, Chair

In Part I, we examine both the statistical mechanics and dynamics of semiflexible filaments that are coupled to an external system. Chapters 2 and 3 look at semiflexible filaments in network, where the external system is the elastic response of the filamentous network itself. The linear elastic compliance of the network is modeled by attaching a Hookean spring at the boundary of the filament, which in turn, introduces a nonlinearity into the Hamiltonian. Chapter 2 uses this model to propose a method for noninvasive microrheology measurements of semiflexible filament networks based on thermal fluctuations of transverse undulations. The external force is seen to counteract bending strain, broadening fluctuations at the boundaries. Chapter 3 considers the dynamics of this model, using the Martin-Siggia-Rose-Janssen-De-Dominicis formalism to compute the time-dependent correlation functions of transverse undulations and of the filament's end-to-end distance. The spring serves to renormalize the filament's tension, altering the cross-over frequency between tension- and bending-dominated modes of the system.

In Chapter 4, we look at the dynamics of bundles of semiflexible filaments, bound together by transient crosslinkers. We explore bundle dynamics across a broad range of unbinding times τ_{off} , finding the behavior is determined by whether crosslinkers prefer to relax via diffusion or unbinding. In both cases, the linker stiffness is effectively reduced. Linker unbinding introduces a frequency scale τ_{off}^{-1} , set by the unbinding rate, at which the bundle dynamics are affected by cross-linkers

In Part II, we explore the properties of lower dimensional elastic structures whose stress-free state is curved. The mechanics of these structures depends strongly on geometry. Chapter 5 studies the coupling of in-plane to out-of-plane elastic modes, focusing on the simplest nontrivial structure – a curved elastic rod. We find undulatory waves becomes gapped in the presence of finite curvature. Bending modes are absent below a frequency proportional to the curvature of the rod. Undulatory waves with frequencies in the gap associated with the curved region, may tunnel through that curved region via conversion into compression waves.

Finally, motivated by the results of Chapter 5, Chapter 6 explores the fate of undulatory waves across a nearly flat, thin membrane, roughened by a Gaussian quenched disordered height field with power-law correlations. We adopt the Donnell-Mushtari-Vlasov theory of membrane elasticity in which the membrane responds instantaneously to relieve in-plane stress. The amplitude of undulatory waves is related to its energy density, a conserved quantity, and shown to obey a diffusion equation at long length/time scales. Time-reversed interference corrections, the so-called coherent backscattering effect, are shown to reduce the diffusion coefficient logarithmically with respect to system size, in agreement with general results for 2D localization.

The dissertation of Jonathan Matthew Kernes is approved.

Robijn Bruinsma

Dolores Bozovic

Shenshen Wang

Alex J. Levine, Committee Chair

University of California, Los Angeles

2020

To my family

TABLE OF CONTENTS

List of Figures	xi
Preface	xxvi
Curriculum Vitae	xxix
1 Introduction	1
1.0.1 Functional methods in classical field theory	15
1.0.2 Free energy of lower dimensional elastic solids	21
I Semiflexible networks	29
2 Equilibrium fluctuations of a semiflexible filament cross linked into a network	30
2.1 Introduction	30
2.2 Semiflexible filament model	32
2.3 Two-point function of filament attached to springs	38
2.3.1 Transverse boundary spring	39
2.3.2 Longitudinal spring	43
2.4 Transverse and longitudinal springs	51
2.5 Conclusion	54

3	Dynamics of undulatory fluctuations of semiflexible filaments in a network	58
3.1	Introduction	58
3.2	Filament dynamics	63
3.2.1	The Model	63
3.2.2	Spring-free results	66
3.3	The longitudinal spring: perturbative expansion	67
3.4	Projected length auxiliary field theory	81
3.4.1	Mean field theory	84
3.4.2	Fluctuations/Random phase approximation	94
3.5	Conclusion	100
4	Dynamics of transiently cross-linked bundles	106
4.1	Introduction	106
4.2	Overview	111
4.3	Kinetic railway track model	119
4.4	Memory model	128
4.5	Diffusive cross-linkers	137
4.6	Conclusion	145
II	Membranes and rods	147

5	Effects of curvature on the propagation of undulatory waves in lower dimensional elastic materials	148
5.1	Introduction	148
5.2	Model	150
5.3	Eigenmodes and frequencies	155
5.3.1	Zero curvature	156
5.3.2	Uniform curvature	159
5.4	Scattering	165
5.4.1	Transmission/reflection through constant curvature	168
5.5	Conclusion	174
6	Geometrical diffusion of undulatory waves on a warped membrane	177
6.1	Introduction	177
6.2	Generalized Donnel-Mushtari-Vlasov (DMV) linearized shallow shell theory	179
6.3	Signatures of localization	185
6.4	Hydrodynamics	189
6.5	Diffusion and weak/strong localization	195
6.6	Results	204
6.7	Conclusion	216
A	Appendices for equilibrium fluctuations of a semiflexible filament cross linked into a network	221

A.1	Real space MFT Green's functions	221
B	Appendices for dynamics of undulatory fluctuations of semiflexible filaments in a network	224
B.1	Diagrammatic perturbation theory to $\mathcal{O}(k^2)$	224
B.2	Mean-field theory solution in time-domain	226
B.3	Polarization function calculation	230
B.4	Transverse spring only	232
C	Appendices for dynamics of transiently cross-linked bundles	235
C.1	Perturbative ϵ expansion of kinetic railway track model	235
C.2	One dimensional nearest-neighbor free energy	240
C.3	Master equation for linker hopping	244
D	Appendices for geometrical diffusion of undulatory waves on a warped membrane	250
D.1	Self-energy calculation	250
D.1.1	perturbation series	253
D.1.2	self-consistent screening approximation	255
D.2	δ_c calculation	267
D.3	Ward identity	271
D.4	Derivation of Diffuson and Cooperon	274
D.5	Full analytic expressions	277

D.5.1	$d_H = 0$	277
D.5.2	$d_H = 1$	278
D.5.3	$d_H = 2$	278
Bibliography		281

LIST OF FIGURES

2.1	(color online) A schematic diagram of a particular filament (blue) cross linked into a network of similar filaments (red). The cross links are represented by rings.	31
2.2	(color online) Above: Schematic diagram of a single semiflexible filament with the left endpoint pinned. Both endpoints are subject to torque-free boundary conditions. The right endpoint is attached to a combination of a longitudinal spring of rest length x_0 with spring constant k_{\parallel} , and a transverse spring of zero rest length with spring constant k_{\perp} . These represent the elastic compliance of the network. Below: A schematic diagram showing the connection of the longitudinal spring and the various lengths defined in the text. The spring's anchor point x_0 is positive when that spring applies tension to the perfectly stretched filament, $\ell = \ell_{\infty}$. The change in projected length $\Delta\ell$ is defined oppositely, becoming positive as the filament contracts.	34
2.3	The free propagator and nonlocal vertex. Slashes denote multiplication by momentum squared. The four field interaction depends on two independent momenta.	41
2.4	The first three diagrams in the perturbative expansion of Green's function. No loops are possible in the connected diagrams, allowing the series to be resummed.	45

- 2.5 Parameter space spanned by the ratios of the tension length and the longitudinal spring length to the filament's length. The three regions are defined by the type of boundary term that dominates the fluctuation profile: tension, network compliance (spring), or filament bending. The three regions coincide at the point $((2/z)^{1/3}\pi^{-4/3}, \pi)$. The persistence length is set to be $\ell_p = \ell$ so that $z = 1$ 47
- 2.6 (color online) Log-log plot of the two-point function $G(p)$ with respect to wavenumber for parameters $\ell = 1\mu m$, $\kappa = 0.0413(pN\mu m)$, $\tau = 4.133(pN)$, and $k_{\parallel} = 5(pN/\mu m)$. There are two scaling regimes. The dashed lines illustrate their slopes in the two regimes. At low wavenumber, the fluctuations are dominated by a combination of tension and network compliance, while at high wavenumber, they are controlled by the filament's bending stiffness. Network compliance shifts the transition $p_* \approx (\ell_k^3\ell)^{-1/4}$ to the higher wavenumbers, provided we are in the spring-dominated regime $\ell_t \gtrsim (\ell_k^3\ell)^{1/4}$. 49
- 2.7 Plots of the exact root mean square height-height fluctuations for parameters $\ell = 1\mu m$, $\ell_p = 4/3\ell$, $\ell_t = 0.1\ell$. The average tensions of 0.1, 1, and $10(pN/\mu)$ correspond to lengths $\ell_k = 0.1123$, .0498, and .01937(μm) respectively. The mean tension $\langle\tau\rangle$ is calculated using Eq. 2.37. 50
- 2.8 (color online) The MFT root-mean square fluctuations for various values of the transverse spring constant k_{\perp} . The inset provides a log plot of the root-mean square fluctuations at the spring (right hand side), as a function of k_{\perp} . For large large k_{\perp} , the endpoint fluctuation scales as $\sqrt{u^2(\ell)} \sim k_{\perp}^{-1}$, as expected for an ideal spring. Parameter values are $\kappa = 0.0413(pN\mu m)$, $\tau = 4.133(pN)$, and $k_{\parallel} = 5(pN/\mu m)$ 53

3.1	(color online) Top: visualization of a particular filament (red) cross linked into a network of similar filaments (blue). The cross links are represented by black and gray rings. Bottom: schematic diagram of a single semi-flexible filament. The left endpoint is pinned, and the right attached to a longitudinal spring with spring constant k and a transverse spring with spring constant k_{\perp} . These represent the elastic compliance of the network. We focus on the effect of the longitudinal spring. Both endpoints are subject to torque-free boundary conditions.	61
3.2	Diagrams contributing to the perturbation theory of the (u, \bar{u}) fields. The propagator (left) is a function of a single p and the time difference: $\langle u_p(t)u_{p'}(t') \rangle = \delta_{pp'}G_p^0(t - t')$. The noise vertex (middle) produces two outgoing lines, and has a coefficient D . The interaction vertex (right) is equivalent to $\frac{-Dk\ell^2}{8}p^2q^2\delta_{pp'}\delta_{qq'}$. It carries two Kronecker deltas, and depends on two wavenumbers p, q . This is a consequence of the spatial nonlocality of the nonlinear interaction. Dashed lines connect two points at equal times. In the interaction vertex (right), we associated a factor of $p^2\delta_{pp'}$ ($q^2\delta_{qq'}$) with each vertex of the dashed and solid lines, and a factor of $\frac{-Dk\ell^2}{8}$ with the dashed line itself.	70
3.3	All diagrams contributing to the self-energy (see definition preceding Eq. 3.25) through $\mathcal{O}(k^2)$. There are two $\mathcal{O}(k)$ contributions marked by an asterisk. For detailed calculations, see Appendix B.1. Diagrams A1 and B1 are later used to renormalize tension (Eq. 3.34) and self-consistently compute the self-energy (Eq. 3.28).	73

3.4	(color online) NCA dynamical correlation function normalized by its first mode at both low (black) and high (blue) tension in the presence (solid) or absence (dashed) of the longitudinal spring. $\bar{\omega} = 100$. The solid black curve overlaps with the solid blue curve at low mode numbers, indicating that the spring generates tension in the absence of any pre-existing tension, given in a nondimensionalized form as ϕ . In the presence applied tension $\phi > 0$, the spring increases the effective tension, pushing the transition from tension- to bending-governed fluctuations to higher mode numbers (blue curves).	77
3.5	(color online) Lowest mode of the dynamic correlation function vs. (top) spring constant and (bottom) applied tension. The top panel is evaluated at low tension, $\phi = 10^{-2}$, and the bottom at $\bar{\omega} = 1$. At large \bar{k} , the effective tension grows sublinearly as $\sim \bar{k}^{2/3}$, leading to the $\bar{k}^{-4/3}$ dependence of C_1 . In the bottom panel, the lowest mode dynamic correlation function decays as ϕ^{-2} , which is identical to the spring-free $k = 0$ case. The transition to the ϕ^{-2} decay occurs at tensions higher than $\phi \approx \bar{k}\langle\Delta\ell\rangle$.	80
3.6	$\lambda\bar{u}u$ and $\bar{\lambda}uu$ interactions. The Hubbard-Stratonovich transformation cuts the four-point vertex into two three-point vertices. Dashed lines are now directed, with λ incoming and $\bar{\lambda}$ outgoing.	82
3.7	(color online) Growth of additive tension renormalization $\Delta\phi$ as a function of the dimensionless spring constant \bar{k} . $\phi = 100$. At $k = \tau/\Delta\ell_0$, we can no longer approximate $\Delta\ell$ as being k -independent. It decays like $k^{-1/3}$, leading to the shift to $\bar{k}^{2/3}$ growth in $\Delta\phi$.	89

3.8	(color online) MFT longitudinal linear response normalized by the plateau value $\chi_{\Delta\ell}^0 = \chi_{\Delta\ell}(\bar{t} = \infty, \bar{k} = 0)$ of the spring-free filament. $\bar{t} = t\ell^4\xi_{\perp}/\kappa\pi^4$. At early times, there is $\bar{t}^{3/4}$ growth, but the function does not exhibit power-law behavior. The longitudinal spring decreases the relaxation time, roughly proportional to $\bar{k}^{4/3}$	93
3.9	(color online) Ratio of the longitudinal correlator to its spring-free value. $\phi = 1$. At high frequency, individual modes have not relaxed to a new equilibrium that accounts for the longitudinal spring, so the ratio flattens to one. As frequency decreases, we approach the static result of Eq. 3.46, whereby we find a reduced amplitude, with zero slope. The inset shows that, for a fixed frequency ($\bar{\omega} = 10$) and zero tension $\phi = 0$, the ratio decays as \bar{k}^{-2} after passing a frequency-dependent cross-over spring constant k^*	98
3.10	Random phase approximation for computing renormalized interaction vertex. When used in a diagram, the directed dashed lines must join to external solid lines according to Fig. 3.6. M_{ij} refers to the matrix elements of \mathbf{M} . $M_{21} = \langle\lambda\bar{\lambda}\rangle$ is directed from a vertex with two incoming lines, to one with an incoming and outgoing.	100

3.11 (color online) Real (solid lines) and imaginary (dashed lines) parts of the shear modulus $\tilde{G}(\omega)$ and network compliance $J(\omega)$ for $\bar{k} = 0$ (black) and for $\bar{k} = 10^4$ (blue). $\phi = 10^2$. \tilde{G} and J are normalized by their spring-free plateau values. The transition of $\tilde{G}(\omega)$ from $\omega^{1/2}$ to $\omega^{3/4}$ scaling signals the shift from tension- to bending-dominated behavior [138, 45]. The longitudinal spring does not alter the power-law dependence, but shifts the cross-over between them to higher frequencies.	101
4.1 (color online) Filament bending introduces cross-linker shearing. Filaments are constrained to distance a apart, with hard rod widths σ set by the spacing of adsorption sites. Transverse displacements are labeled by $u(x)$, with x representing the distance along the mean orientation. Arc-length mismatch incurs a shear energy cost for cross-linkers attached at locations where the filament is not directed along the mean orientation. .	108
4.2 (color online) Walking cycle to traverse one lattice spacing. Reverse processes are ignored for clarity. Red bubbles indicates a bound linker, clear bubbles an unbound site. Linkers unbind according to rates $k_{\text{on/off}}$. For $k_{\text{on}} \gg k_{\text{off}}$, and for ϵ small, the linker is more likely to re-attach to an adjacent site (bottom right) than to completely unbind (center), and for small enough distances, the linkers prefer to equilibrate via walking. . . .	109

4.3	(color online) From left to right we describe a binding mediated transition to a preferred curved metastable state. The left figure is the preferred flat configuration. The center figure illustrates linker unbinding to relax stress in response to bundle induced shear. The right figure shows the linkers re-binding into a zero shear configuration, despite the bundle having curvature. The far right figure will incur a shear penalty if it tries to flatten out, and is thus a meta-stable energy minimum, compared to the global minimum on the leftmost figure.	113
4.4	(color online) Trajectories of relaxation rates as function of dimensionless filament length. Top: $\frac{k_{\times} a^2 n_0 \pi^2}{\zeta K_{\text{walk}} \sigma^2} = 5 > 1$. Bottom: $\frac{k_{\times} a^2 n_0 \pi^2}{\zeta K_{\text{walk}} \sigma^2} > 1 = 0.2 < 1$. The shortest time scale determines the dominant mechanism describing dynamics, and hence the appropriate model to choose. On the right we give an alternative viewpoint, where length is fixed and the detachment rate free to change. For long enough filaments (or short τ_{off}) linker unbinding is always fastest, leading to the memory model. Conversely, at short lengths (or long unbinding time) the bundle relaxes as if linkers are permanent, while linkers respond to deformations diffusively. In the intermediate regions, precession/hopping must be considered in concert with bundle fluctuations.	115
4.5	(color online) Railway track model at fixed $u(x, t)$. Bundle deformation causes bound cross-linkers to shear, regardless of when they first attached, driving them to cluster along regions locally aligned with the mean bundle orientation. Linker concentration (indicated by blue shading) near these wells is Gaussian distributed, with boundary layer length $\xi = \sqrt{T/k_{\times} a^2} R ^{-1}$, for R the local radius of curvature.	121

4.6	Renormalization of linker density with respect to linker stiffness. $L = \pi$, $n_0 = 20$, $z = 10$. Solid line represents self-consistent solution, while the dashed line the bare solution, whereby the right side of Eq. 4.23 uses $n_R = n_0$. At high ϕ the bundle undergoes a discontinuous unbinding transition at $\phi^* \approx 2\sqrt{2}(N + 1)^2/\pi^2$	126
4.7	(color online) $C_n(\bar{\omega})$ as function of the n^{th} mode, normalized by the first mode: $\bar{\omega} = 1$, $\epsilon = 1$, $\phi = 100$, $N = 20$, $z = 10$. Below $n^* \approx 52$, $C_n(\bar{\omega})$ exhibits the usual transition from tension to bending like behavior. Above n^* , linker dynamics become important, causing $C_n(\bar{\omega})$ decay more slowly as $\sim n^{-6}$	128
4.8	Transverse load response function of $n = 1$ mode in high K_{off} limit, normalized by the plateau response $\chi(\omega = 0)$. $\epsilon = 10$. The solid curve corresponds to the WLC result. There are two transition frequencies, when $\bar{\omega} = \epsilon, \phi$	132
4.9	(color online) Mode dependence of power spectrum, normalized by first mode: $\epsilon = 10^4$, $\phi = 50$, $\bar{\omega} = 10$. Solid line is the memory model, and the dashed line the permanently-linked railway track model for comparison. The memory model behaves like the WLC with $C_n \sim n^{-8}$ up until a transition wavenumber n^* denoted by the gridline, whereby it only decreases as n^{-6}	135
4.10	(color online) Dynamic shear modulus normalized by $G^0 = G(\bar{\omega} = 0)$: $\epsilon = 10$, $\phi = 10^3$. Gridlines at $\bar{\omega} = \epsilon, \phi$ show where the power-law self averaging behavior of the bundle is destroyed by linker unbinding, similar to that observed in Ref. [111].	136

4.11 (color online) Structure function for unhinged ($d_{\perp}\alpha = 2$) and hinged ($d_{\perp}\alpha = 4$) cross-linkers at a packing fraction of $n_0\sigma = 0.7$. HS denotes the hard rod solution without Casimir interactions. Wavenumber is in units of lattice spacing.	140
4.12 (color online) Mode-dependent ϕ renormalization to first order in the diffusion dominated $\eta = \infty$ regime($\phi = 0.1$). At increased packing fraction, linker induced corrections increase, localizing around peaks in the structure function. The inset shows ϕ dependence of the mode $n = 46$, corresponding to the first peak. More generally, for all modes $\Delta\phi_n$ decreases with respect to ϕ	143
4.13 Renormalization of measured density n_l with respect to stiffness force. $L = 1$ and σ is adjusted to keep the packing fraction at 0.25 for each curve. At high ϕ , the density vanishes, indicating a unbinding transition.	146
5.1 (color online) Schematic representation of an undulatory wave on a curved rod. The (black) solid line is the space curve of the undeformed rod with radius of curvature R supporting a sinusoidal wave (not to scale) shown as the (red) dashed line. Deformations about the undeformed state are decomposed locally into a displacement u (wide blue arrow) along the local tangent, and a displacement f (wide red arrow) along the local normal. The weak curvature approximation assumes that the radius of curvature R of the stress-free state (solid black line) is much larger than wavelength λ of characteristic deformations (dashed red line).	151

- 5.2 (color online) Dispersion relation of a uniformly curved rod. $M = 0.05$. The degeneracy between the $M = 0$ dispersion curves (dashed black lines) is lifted due to curvature. Level splitting between the upper branch (red) and lower branch (black) is $\mathcal{O}(M)$ near wavenumbers $k = \pm 1$ and $k = 0$. 158
- 5.3 (color online) The dispersion relation of a rod with uniform curvature, color-coded according to the normalized amplitude of its corresponding $|f\rangle$ eigenstate. $M = 0.15$ and $\ell = 1$. Mode mixing is strongest near the degeneracy points of the $M = 0$ case. In the inset, we show the behavior for larger curvature $M > 1$. At small k , the upper branch is essentially flat, while the lower branch develops an $\omega_- \approx |k|^3/M$ power law, in contrast to its quadratic dispersion relation at small curvature. . 160
- 5.4 (color online) The frequency spectrum of a clamped rod of length $\ell = 20$ as a function of curvature M . Top: the M -dependence of the frequency spectrum, color coded by the relative amplitude of its f to u mode, where lighter colors represent more bending f -amplitude. Due to parametric M -dependence, each curve represents one eigenmode. We find three distinct regimes: high ω where the curves look like their infinite-rod counterparts, intermediate ω , where they spectrum is approximated by free dispersion curves with level splitting, and low ω where curvature strongly distorts the spectrum. Bottom: a close up view of the frequency spectrum (black solid lines) overlaid with the infinite rod dispersion curves for several modes labeled by n in the figure (dashed lines). Level splitting occurs between even and odd numbered modes, as explained in the text. 164

5.5	(color online) Schematic representation of an elastic rod (solid gray line) formed by adjoining two semi-infinite straight rods at the (black) dashed lines to the left ($s = -\ell/2$) and right ($s = \ell/2$) of the curved rod segment (arc of a circle with radius R), such that the rod and its tangent are everywhere continuous. We consider the scattering of an incoming bending f wave from the left, through the region of constant curvature M . Curvy arrows correspond to propagating asymptotic states, and decaying arrows to evanescent states. The darker (lighter) colors refer to u (f) modes. There are six unknown transmission/reflection amplitudes. In the curved region, there are either two or four propagating channels, determined by the value of M	169
5.6	(color online) Transmission and reflection coefficients for a bending wave of unit amplitude incident on a region of length $\ell = 10$, with uniform curvature $M = 3$. Top: the transmission coefficients for bending (orange) and compression (black) waves. Bottom: the total transmission and reflection coefficients. Due to conservation of energy, the coefficients obey $T_f + T_u + R_f + R_u = 1$. Curvature mixes eigenmodes, converting the incident pure bending wave into a linear combination of bending and compression waves.	172
5.7	(color online) Transmission and reflection coefficients for a compression wave of unit amplitude incident on a region of length $\ell = 10$, with uniform curvature $M = 3$. Top: the transmission coefficients for bending (orange) and compression (black) waves. Bottom: the total transmission and reflection coefficients. In contrast to an incident bending wave, see Fig. 5.6, the transmission coefficients vanish as $\omega \rightarrow 0$	175

6.1	(color online) parametrization of a physical membrane middle surface \mathbf{X}_0 in the Monge representation, with small deformations f , u_1 , and u_2 given in normal coordinates. Displacements u_1, u_2 (in blue) are along the local surface tangent of the curved background surface, while displacements f (in red) are in the direction of the local surface normal. Misalignment of the local surface normal with the global \hat{z} direction is responsible for additional curvature terms in the strain (see Eq. 6.8).	180
6.2	(color online) diagrammatic construction of the maximally crossed irreducible vertex. White boxes represent the bare irreducible vertex \hat{U}^0 ; the shaded box represents the diffusive four-point function in Eq. 6.55. <i>Crossing</i> refers to overlap of \hat{U}^0 vertices. The summation over maximally crossed diagrams can alternatively be viewed as summation over uncrossed diagrams with all lines on the lower rung reversed. Time-reversal symmetry allows us to flip arrow orientation bringing it to standard form.	201
6.3	(color online) diffusion coefficient as a function of both disorder α (top) and frequency ω (bottom). D decays $\sim \alpha^2$ at small α , and grows like ω^2 at large α . At low ω there is a localization transition where D vanishes. At smaller system size L , the localization transition is pushed to smaller/larger frequencies/disorder.	211

6.4	(color online) diffusion coefficient in $d_H = 1$ versus both disorder amplitude (top) and frequency (bottom). As for $d_H = 2$, $D \sim \alpha^{-2}$ at low alpha, and reaches a localization transition at large α . The transition decrease logarithmically in frequency. If the system localizes, it occurs first at high frequency. In the lower panel, the weak frequency dependence of D is shown to hold ten orders of magnitude, and even up to the upper limit $\omega \approx \Lambda^2$	212
6.5	(color online) top: localization length and mean free path as a function of disorder in $d_H = 2$. Solid (dashed) lines refer to ξ (ℓ). Black is for $\omega = 10^{-3}$, red is for $\omega = 0.1$. Bottom: ξ and ℓ as a function of frequency at fixed $\alpha = 10^{-3}$ (black) and $\alpha = 0.1$ (red). Localization occurs at both high disorder and low frequency.	214
6.6	(color online) localization length ξ and mean free path ℓ in $d_H = 1$ as a function of both disorder amplitude (top) and frequency (bottom). In the top panel, black (red) lines correspond to $\omega = 1$ ($\omega = 10^{-4}$). Solid (dashed) lines refer to ξ (ℓ). The wave localizes when ξ falls below ℓ . This occurs at weaker disorder (smaller α) with increasing frequency. In the lower panel, we show the $\omega^{-1/2}$ decay of the mean free path. The localization length is ω -independent, and not shown.	215
C.1	Top: direct correlation function of cross-linker fluid. $\sigma = 1$, $\beta P = 1$ and 3000 modes were summed over in the Fourier series. The inset shows a close up of the transition at $x = \sigma$. Bottom: radial distribution function for the physically relevant case $d_{\perp} \alpha = 2$ compared to hard rods. Packing fraction is 0.5 and we summed over 1000 Fourier modes.	245

D.1	Straight (wavy) lines represent propagators for the undulation (disorder) fields. The effective disorder vertex corresponding to Eq. 6.14, is on the third line. The vertex carries factors of wavenumber that can be accounted for by the following rule: each line (both wavy and solid) carries one factor wavenumber for each intersection that it terminates at. Only diagrams that remain connected when disorder lines are cut contribute to disorder averages.	251
D.2	A: The first order correction to the self-energy and Green's function. The absence of an internal propagator makes this contribution purely real. B: Second order correction of higher order $\mathcal{O}(1/d_c^2)$. C: Second order term in SCSA and first order term for the imaginary component of self energy. D: An example of forbidden diagrams, in which a horizontal cut across disorder lines leaves the graph disconnected. Double solid lines indicate fully dressed Green's function. E: Third order term in SCSA, but left out by the NCA. F: An example of a crossed diagram, whose phase space is restricted, leading to a result of higher order in $1/(p_F\ell)$. These diagrams are small in both the SCSA and NCA approximations.	252
D.3	The full disorder averaged propagator is represented by a double solid line, and the full vertex by a shaded bubble with two wavy lines and two solid lines attached. Top: The SCSA for the fully dressed Green's function. Bottom: The SCSA for the renormalized vertex function	255

D.4	Data points represent the numerical integration result for $\text{Re}\bar{\Sigma}_q$ and Π_q , using the numerical integrations defined in Eqs. D.15a D.15b. Curves represent the analytic result. We consider the cases $d_H = 1, 2$, where the solutions for $\bar{\Sigma}_q, \Pi_q$ are nontrivial functions. Beyond weak scattering we find our analytic approximations to be inaccurate, however, the shape of the curves is still accurate, which we need for deriving the diffusion coefficient.	268
D.5	The bare irreducible vertex. This is the simplest four-point vertex that can be constructed that remains fully connected after cutting all wavy lines.	269
D.6	Angles between unit vectors at fixed orientation in the calculation of M_0 . Only \hat{q} is not integrated over. We first fix \hat{k} , then perform the integrations over $d\hat{p} = d\theta$ and $d\hat{p}' = d\theta'$. This yields a function $J_{d_H}(k; \phi)$ that is then integrated over ϕ	270
D.7	Dominant contributions to the four-point vertex in the diffusive limit. Upper/lower lines carry retarded/advanced propagators, each with frequency $\omega + (-)\Omega/2$. The frequency is a passive index and is not integrated over since the disorder field is quenched. Top: diagrammatic representation of the Bethe-Salpeter equation defining the diffuson contribution to the four point vertex $\hat{\Gamma}$. Bottom: diagrammatic derivation of the cooperon. The new wavenumbers are $\tilde{p} = \frac{1}{2}(p - p' + q)$, $\tilde{p}' = \frac{1}{2}(p' - p + q)$, and $Q = p + p'$, in agreement with Fig. 6.2.	275

PREFACE

It has been a long, long journey. I first want to thank Stephanie Krilov. Without you, I don't think I would have made it through the degree. From switching teaching assignments, to general advice, you were an invaluable part of helping me accomplish this.

From the early days, I want to thank my office companions Lu Shen, Alexander Serov, and Louis Foucard. Lu, thank you for teaching me bad Chinese and inspiring me to apply for conferences near ski resorts. Alexander, thank you for opening me up to the world of biology, and helping me reaffirm that I am indeed, a physicist and not a biologist. Louis, you were my very first experience walking into the lab. I'll never forget our first interaction; I was sitting in my cubicle in the old GEO 4607 office, and I asked if you could help out on a problem from Kardar's *Statistical physics of fields*. Your response, "Oh ... no... I'm not a physicist," still sticks with me. I learned right away that I needed to think broader about my target audience, not just those who shared the same training as I.

I also want to thank my long-standing officemate Valentin Slepukhin. Believe it or not, I knew you before you knew me. I'll never forget walking to the comp exam and thinking, "Who's this strange Russian guy and why is he walking the complete opposite direction of the exam? Should I tell him?" Thankfully, you (and I) both passed though! Thank you for being a fellow student to go through all of this with, from our days of trying to work on networks up until our days of trying to work with the Germans. It was always nice to have someone else to discuss interesting problems with, or reminisce with about the good old days working in high energy

theory.

To those that came before me, Devin Kachan and Christian Vaca, I want to thank both of you for your advice and wisdom. Christian, during the hardest parts of the degree, your advice helped me push through to the finish line. Also, thanks for leaving a trove of hard cover textbooks in the office for two plus years. I still miss the days of reading actual books and actual paper.

To my advisor Alex, thank you for spending the time and energy to work with me. It's been a long haul, and you were always patient and understanding, especially during tough circumstances in my personal life. I apologize for the long papers, this last one is it, I promise.

Finally, I thank my family and friends.

Chapter 2 is a version of Jonathan Kernes and Alex J. Levine “Equilibrium fluctuations of a semiflexible filament cross linked into a network,” *Phys. Rev.* **E101**, 012408 (2020).

Chapter 3 is a version of Jonathan Kernes and Alex J. Levine, “Dynamics of undulatory fluctuations of filament segments cross linked into a network,” *Phys. Rev. E* (2020). preprint: arxiv:2006.10251, which has been submitted to *Physical Review E*.

Chapter 4 is a version of Jonathan Kernes and Alex J. Levine “Dynamics of transiently cross-linked bundles,” *Phys. Rev. E* (2020), currently in preparation.

Chapter 5 is a version of Jonathan Kernes and Alex J. Levine “Effects of curvature on the elasticity of lower dimensional structures,” *Phys. Rev. E* (2020). preprint: arxiv:2006.13383, which has been submitted to *Physical Review E*.

Chapter 6 is a version of Jonathan Kernes and Alex J. Levine “Geometrically

induced diffusion of flexural waves on thin warped elastic membranes,” Phys. Rev. E (2020), which has been submitted to Physical Review E.

The dissertation author is the primary author on all publications/works.

CURRICULUM VITAE

2010 – 2014	B.S. in Physics/Mathematics/Integrated Science, Northwestern University, Evanston, Illinois.
2013	Outstanding Junior in Physics, Undergraduate Division, Northwestern University, Evanston, Illinois.
2014	Best Senior Thesis in Physics, Undergraduate Division, Northwestern University, Evanston, Illinois.
2014 – Present	Ph.D. student in Physics, University of California, Los Angeles (UCLA).
2014 – 2015	M Sc. in Physics, University of California, Los Angeles (UCLA).
2014	Leo P. Delsasso Fellow, Graduate Division, University of California, Los Angeles (UCLA).
2014-2018	UCLA Alumni Association Fellow, Graduate Division, University of California, Los Angeles (UCLA).

PUBLICATIONS

Jonathan Kernes and Alex J. Levine “Dynamics of transiently cross-linked bundles,” Phys. Rev. E (2020). In preparation

Jonathan Kernes and Alex J. Levine “Geometrically induced diffusion of flexural waves on thin warped elastic membranes,” Phys. Rev. E (2020), submitted. preprint: arxiv:2011.07152

Maximillian J. Grill, Jonathan Kernes, Alex J. Levine, Valentin M. Slepukhin, and Wolfgang A. Wall, “Tension trajectories in semiflexible filament networks,” *Soft Matter* (2020), submitted. preprint: arxiv:2006.15192.

Jonathan Kernes and Alex J. Levine “Effects of curvature on the elasticity of lower dimensional structures,” *Phys. Rev. E* (2020), submitted. preprint: arxiv:2006.13383.

Jonathan Kernes and Alex J. Levine, “Dynamics of undulatory fluctuations of filament segments cross linked into a network,” *Phys. Rev. E* (2020), submitted. preprint: arxiv:2006.10251.

Jonathan Kernes and Alex J. Levine “Equilibrium fluctuations of a semiflexible filament cross linked into a network,” *Phys. Rev.* **E101**, 012408 (2020).

CHAPTER 1

Introduction

Soft condensed matter is concerned with the physics of bodies that behave classically, which includes both classical and statistical mechanics. Recently, physicists have increasingly drawn inspiration from the realm of biology, where a diverse array of complex structures gives rise to nontrivial mechanics. Understanding these structures has applications not just for biology, but more broadly in understanding and classifying interesting soft materials.

To examine soft matter structures, we typically appeal to elasticity theory, which provides an extension of the classical mechanics of point-like objects to the classical mechanics of deformable bodies. Objects deform in response to an applied force, whether it is applied in the bulk of the material or at the boundary. Elastic objects are defined by the property that upon removing the forces responsible for deformation, known as *stresses*, they relax back to a unique undeformed state. Of course, this does not describe all materials, as anyone who has bent a paper clip, or “worn in” a baseball glove knows (such examples would be plastic deformations, which do not return to their undeformed state). However, for sufficiently small forces, all deformable materials approach an elastic regime. This is a simple consequence of the known result in classical mechanics, that at small enough distances near a potential minimum, everything looks like a spring. Thus, elastic theory provides a rather good

approximation for the behavior of many soft materials.

Though the theories of elasticity, classical mechanics, and statistical physics have been established for centuries [83], their application to biologically inspired structures is still an active area of research. The principal reason for this has to do with geometry. The starting point in elasticity theory is understanding the deformations of a solid block of some material, assumed to be homogeneous in the sense that if the theory is defined by some set of elastic constants, then these constants are the same throughout the block. Typically, we think of this elastic block as representing some physical material, and therefore imagine that it has some volume in three dimensional space, and can deform in any of those three dimensions. This problem can be understood without too much difficulty. In biology however, we rarely encounter such slabs of material, and indeed if we did, they wouldn't be terribly useful to perform functions in the body.

As engineers have known since antiquity, elastic objects can be much more useful if we form them into some shape. Indeed, biology agrees, and there exist a number of elastic architectures [61, 156]. By shaping our hypothetical block of material, we do two things: first, we are endowing it with some sort of geometry. For example, like carving a statue we could chip away at the edges to form say a sphere instead of a block. The sphere certainly has different elastic behavior, but that's an entirely due to the boundary. If we are concerned with elasticity in the bulk, not much has changed. A second and more interesting thing we can do is to reduce some of the dimensions of the elastic block. For example, we could fashion it into a rod or a thin membrane. These represent *lower dimensional elastic structures*. As it turns out, the mechanics of such structure is driven largely by geometry. This dependence on geometry allows for the same elastic block to exhibit wildly different mechanics

simply based on how it's shaped.

In this thesis, we study the geometrical mechanics of lower dimensional elastic structures. We do this both on a broad theoretical level (such as in Chapter 5), and also in the context of particular biological structures. One structure that is common throughout biology, is the semiflexible network, which is composed of semiflexible biopolymers. Biopolymers represent a rod-like lower dimensional elastic structure, consisting of a material whose two lateral dimensions are much smaller than its length. Examples of semiflexible networks include the extra-cellular matrix (ECM), cytoskeleton, and filamentous-actin (F-actin) [15]. Another structure that appears frequently is a membrane. A membrane is an elastic structure in which one dimension (the membrane thickness) is much smaller than the others. Examples include red blood cells, cell membranes, and viral capsids [156, 121, 73, 81].

In Part I of this thesis, we focus on understanding the physics of semiflexible networks. The physics of a single constituent, the semiflexible filament, can be understood phenomenologically rather easily. It's easiest to first think of a thermalized filament. In general, such a filament will want to contract. This is a consequence of entropy. As the filament straightens out, there are fewer configurations available in its phase space. A semiflexible filament, can then be thought of as a filament whose bending stiffness is just strong enough such to compete with the entropically driven contraction, keeping the filament nearly straight.

There are two effects: there is an energetic cost to extension/contraction of the filament length, and an energetic cost due to bending. The former is often much greater (and in fact infinite in the case of inextensible filaments) than the latter. To a good approximation, we can treat semiflexible filaments as inextensible leaving

only bending as the remaining effect. To model bending, we can view the filament as possessing a number of rods placed normal to its longitudinal direction, that measure its deviation from a straight configuration. For small deformations about the straight state, mismatch of the local normal directions will result in an energy penalty. Since the deformation is small, we can model the rods as feeling as a spring-like restoring force to maintain alignment of normals. Summing over all rods leads to the discrete Hamiltonian

$$H_{\text{bend}} = \sum_i \frac{\tilde{\kappa}}{2} (\hat{n}_{i+1} - \hat{n}_i)^2 \approx \sum_{\langle ij \rangle} k \hat{n}_i \cdot \hat{n}_j, \quad (1.1)$$

where we have introduced some spring constant $\tilde{\kappa}$ and normal vectors \hat{n}_i . We note, that this decomposition of the elastic structure into a lattice of normals is capable of describing a discrete membrane as well. Taking the continuum limit in which \hat{n}_j approaches \hat{n}_i , we obtain a Hamiltonian

$$H_{\text{bend}} = \int_0^\ell \frac{\kappa}{2} \left| \frac{d\mathbf{t}}{ds} \right|^2 ds, \quad (1.2)$$

where we identify the bending rigidity κ , the filament length ℓ , the arclength s , and the local tangent vector \mathbf{t} . In terms of the arclength parametrization, inextensibility is trivial. Since the filament is assumed to be nearly straight, we can instead consider a Monge representation whereby we define a transverse undulation field $u(x)$, in terms of longitudinal displacement x . Inextensibility is then enforced via lagrange multiplier τ , which we identify as the tension along the filament. We arrive at the semiflexible filament Hamiltonian in the nearly straight limit

$$H_{\text{fil}} = \int_0^\ell dx \left\{ \tau \left(\frac{du}{dx} \right)^2 + \kappa \left(\frac{d^2u}{ds^2} \right) \right\}. \quad (1.3)$$

As expected, there are clearly two contributions: bending and tension. One of the most important features of such filaments are their force-extension curve [98].

Suppose we have a solution or gel of such semiflexible filaments separated by mesh spacing ξ . For small applied tension, the filaments will extend by some amount $k\delta\ell$, where k is determined by longitudinal linear response of the filament. If this tension is due to a macroscopic stress in the material, we can similarly consider the extension as arising from some strain θ , with the relation $\delta\ell = \theta\ell$. A given cross-section will contain on average ξ^{-2} filament segments per area, and so by eliminating $\delta\ell$ we can determine a shear modulus $G' \sim k/\xi^2$ of the network that is determined solely by the behavior of a single filament.

The ability to understand the elasticity of an entire network of filaments based on the mechanics of only a single constituent filament is a powerful tool. This is further reinforced by the ease with which single filaments can be fabricated experimentally. In the laboratory, *in-vitro* biopolymer networks can be synthetically created from filamentous actin, microtubules and intermediate filaments [15], thus providing a suitable test ground for theories of filamentous networks.

In our brief overview, we have largely ignored the details of computing the force-extension curve. Critically, we have not discussed boundary conditions at all. In fact, the mechanics of individual filaments depend strongly on the type of boundary condition. In Chapters 2 and 3 we fully consider this problem. We look at both the equilibrium and dynamical consequences of the boundary condition on the statistical mechanics of individual filaments. Such an analysis is relevant to the behavior of semiflexible networks, in which the local mechanical properties can deviate strongly from elastic behavior. We propose the detailed analysis of the fluctuations of in-network filaments as means to determine a local tension mapping of semiflexible networks, a technique known as activity microscopy.

We have so far not discussed the methods by which semiflexible networks are dynamically formed. Semiflexible networks can exhibit varying degrees of structure from solutions to rigid networks. Broadly, filaments form structures by joining together at certain intersection points with the help of proteins known as cross linkers. Cross linkers themselves can exhibit a number of properties, including a bias to bind filaments along certain angles. One important feature is that cross linkers are not necessarily permanently bound. Indeed, in response to stress, networks can relax by unbinding cross linkers. As a result, there is an inherent dynamical aspect of the mechanics of semiflexible networks, due to cross linker transience. These can be viewed most strikingly via a non-Newtonian rheology in the low-frequency regime of transiently cross-linked networks. In Chapter 4, we consider the cross-linker filament interaction more broadly, and explore the consequences of cross-linker transience on the mechanics of bundled networks. These are networks whose constituents are not individual filament segments, but instead bundles of such filaments that are cross-linked together. The network is a hierarchical structure composed from a collection of such bundles.

In Part II, we consider more theoretical aspects of the elasticity of lower dimensional elastic structures, beyond the results of a single system such as semiflexible networks. Geometry biases between different directions of deformation along the elastic structure. For example, for physically realizable membranes there is everywhere a normal direction (not necessarily unique) along the elastic structure breaks the symmetry of an isotropic material with D internal dimensions living in D dimensional space. The consequences of this can be seen by re-examining the Hamiltonian of a nearly straight semiflexible filament in Eq. 1.3.

An unusual feature is the appearance of the second spatial derivative of the field

u. Normally, when constructing a Landau-Ginzburg free energy for say a scalar field $\phi(\mathbf{x})$, one retains only the first order derivative term $\sim |\nabla\phi|^2$. With filaments and membranes, we must also retain the bending term (for fluid membranes there is an analogous surface tension term [112]), which implies a separation in scales between bending and tension effects. For membranes, broken symmetry means that deformations in the local surface normal known as *undulations*, will behave qualitatively different than in-plane deformations. Suppose we want to ask what would be the effective two-dimensional Young's modulus Y_{2D} , found by squeezing a material with usual Young's modulus $Y = Y_{3D}$ into a membrane. The result is expressed as an algebraic combination of phenomenological parameters called the Lamé coefficients. We would find that the Lamé coefficients are directly proportional to the membrane thickness h , *i.e.* $\sim \lambda \sim Y_{3D}h$, while the bending modulus is proportional to the third power of membrane thickness $\kappa \sim \kappa \sim Y_{3D}h^3$ [77]. As a result, there is a separation in energy scales between undulations and in-plane deformation for thin membranes, with undulations requiring much lower energies. We see that bending plays a crucial role in lower dimensional systems.

The aforementioned separation of energy scales between in-plane and out-of-plane deformations is due only to the thinness of the membrane. Flat, thin plates, lacking any kind of nontrivial geometry, will exhibit this separation of scales. We are more interested in the way that geometry can use this scale separation to significantly impact mechanics. To this end, we consider curved lower dimensional elastic structures. Of course, by nature any body that is deformed will obviously be curved. More specifically, we are referring to structures whose stress-free state is curved. That is, upon removal of all stresses or external forces, the relaxed state of the body is curved.

The principle effect of curvature, is that it mixes bending and stretching in an elastic material. A curved elastic structure is then a complicated interacting field theory, where one field represents bending deformations, another in-plane deformations, and finally a third the curvature, which couples these two fields. Though our study is couched in the more complicated language of field theory, the effects of curvature on elasticity can be understood through a simple thought experiment.

Consider the inflation of a balloon, modeled as a spherical shell of radius R in the stress-free state. A convenient property of the sphere is that the local radius of curvature, which is inversely proportional to the curvature, is everywhere given by $1/R$. We now deform the balloon uniformly by increasing the radius from $R \rightarrow R + \delta R$. This is a pure out-of-plane displacement, *i.e.* a bending deformation. However, such a deformation would necessarily increase the surface area by an amount $S \rightarrow S + 8\pi R\delta R + \mathcal{O}(\delta R^2)$, which we note is first order in the change of the radius of curvature δR . The increase in surface area indicates that even to lowest order in δR , bending must be accompanied by stretching. When a system has inherent curvature in the undeformed state, further bending and stretching cannot occur independently. For lower dimensional objects with internal structure (*i.e.* excluding things like fluid membranes) the softer bending modes are stiffened by in-plane deformation. The importance of considering in-plane deformations has long been known to be crucial to the “order-from-disorder” stability of tethered polymerized membranes [112]. By integrating out in-plane modes, one finds an effective action that couples Gaussian curvatures via a massless $\sim \nabla^4$ scalar. This pseudo-long range potential leads to a finite crumpling transition for physical membranes, even at the naïve lower critical dimension of $D = 2$ internal dimensions.

Understanding the elasticity of non-idealized objects, especially in biological con-

texts, can be complicated by several factors. Typical biological membranes can be highly heterogeneous, and furthermore may not be constructed from a block of elastic material. These problems can be partially remedied by working instead with a phenomenological theory. Despite the lack of well-defined elastic continua in biological contexts, the theory of thin shells and rods has nevertheless successfully been applied provided we supply the theory with a set of minimal phenomenological parameters. These usually pertain to a bending rigidity and Young’s modulus type term penalizing stretching. The problem of heterogeneity however, still persists.

When systems exhibit seemingly random behavior from sample to sample, they are a good candidate for applying probabilistic analysis. The problem of heterogeneity can be greatly simplified by considering ensembles of systems. While the physics of one particular instance of the ensemble would be difficult if not impossible to solve for analytically, averages over the ensemble tend to be tractable. In the context of ensembles, we consider deviations in heterogeneity of the system from sample to sample as specifying a specific realization of “disorder”. In this thesis, we will not be concerned with disorder in the elastic constants of materials, but instead in disorder due to geometry. This is explored fully in Chapter 6, where we analyze the mechanics of warped membranes, which are nearly flat membranes whose background height configuration is disordered. Per our previous discussion of the role of curvature in coupling bending and stretching, this allows us to further understand how this coupling is affected by a disordered geometry

Dynamically, to linear order in elasticity theory membranes support waves like any other material. One major effect of curvature on such waves is the scattering of undulations via change in Gauss curvature. This suggests that disordered geometry can place undulatory waves in an effective random media, where the media is

represented by scattering due to Gauss curvature. This analogy leads us in to the extensively studied field of localization and wave propagation in random media. This subject has a long history, stretching back to its roots in Anderson's seminal 1958 paper *Absence of Diffusion in certain random lattices* [5], regarding the localization of electrons in a lattice with impurities. Much of the early work on the localization problem was done in hard condensed matter, looking at the conductivity of dirty metals. However, concurrently many of the same conclusions were reached through parallel studies in classical contexts, such as coherent backscattering in the albedo. What these parallel tracks have in common, is a mesoscopic treatment of wave equations. This is a length scale below the transition to a geometric optics approach, yet above the length scales of a single quantum state or eigenmode. In this regime, waves undergoing multiple scattering due to the random medium can interfere constructively, leading to long-range quantities. Though it's easy to understand how random scattering can lead to diffusive transport, what is less obvious is that these coherent paths can lead to localization.

Localization is when the eigenstates of a system become spatially localized in the absence of a potential well. In other words, there are eigenstates of the system that are impervious to boundary conditions. In real space this indicates that a wavepacket whose amplitude is initially confined to a small spatial region will remain in that region for all time. This is a mesoscopic effect arising from coherence, and does not have to do with whether or not waves possess enough energy to tunnel through an energy barrier (to clarify, there are no energy barriers in localization).

To oversimplify things, one can imagine starting at the limit of freely propagating waves. These have constant velocity, and they transport energy linearly in time away from an initial disturbance. If we add in disorder that scatters these waves

into random directions while still conserving energy, we can imagine that due to bouncing around and no longer taking a straight path, the waves will spread out slower. This is the diffusive regime, where energy propagates like \sqrt{t} away from a disturbance. With increasing disorder, waves can become essentially trapped among many scatterings, staying localized around the initial disturbance.

To understand the latter point, let's consider two quantities. The average amplitude of a wave away from the origin and the average intensity. Suppose we start with a monochromatic wave $e^{i\mathbf{k}\cdot\mathbf{x}}$. We can construct a scattering experiment where we inject a plane wave $e^{i\mathbf{k}\cdot\mathbf{x}}$ into the random media, then look for outgoing plane waves $e^{i\mathbf{k}'\cdot\mathbf{x}}$. The amplitude/probability to go from the incoming plane wave \mathbf{k} to the outgoing plane wave \mathbf{k}' is given heuristically via

$$A(\mathbf{k}', \mathbf{k}) = \sum_{i,j} f(\mathbf{x}_i, \mathbf{x}_j) e^{i(\mathbf{k}\cdot\mathbf{x}_i - \mathbf{k}'\cdot\mathbf{x}_j)}, \quad (1.4)$$

where $f(\mathbf{x}_i, \mathbf{x}_j)$ denotes an amplitude/probability for a wave/particle to travel from location \mathbf{x}_i to \mathbf{x}_j . The disorder average is taken by summing over all scattering events, which can be considered as sum over scatters being put at all locations.

The sum over paths can be viewed as a series of multiple scattering events at positions x_1, x_2, \dots

$$f(x_N, x_0) = f(x_N, x_{N-1})f(x_{N-1}, x_{N-2}) \dots f(x_1, x_0), \quad (1.5)$$

hence prior use of the term multiple scattering. Each complex amplitude/probability for a single path can be broken into a number times a phase as

$$f_{\text{one path } j} = |f_j| e^{i\delta_j}. \quad (1.6)$$

The phase is additive in length, and the source of familiar interference effects like two-slit interference and thin lensing. Taking a disorder average of the amplitude, we find that it is a sum of random phases

$$\langle A(k', k) \rangle \sim \sum_j |f_j| e^{i\delta_j} \rightarrow 0, \quad (1.7)$$

which on average will vanish. The further away we get from the source at the origin (in the context of our simulation) or the further a monochromatic wave travels through a disordered medium, the more scattering it will encounter, and the more possible paths that exist to average over and destroy phase coherence. As a result, the amplitude is a *short range* object. It is as often positive as negative and will exhibit exponential decay on average with respect to distance traveled. This is the mean free path ℓ we try to calculate later

More interesting is the propagation of intensity. This can be written in terms of the amplitude/probability

$$|A(\mathbf{k}', \mathbf{k})|^2 = \sum_{i,j,m,n} f(\mathbf{x}_i, \mathbf{x}_j) f^*(\mathbf{x}_m, \mathbf{x}_n) e^{i(\mathbf{k} \cdot \mathbf{x}_i - \mathbf{k}' \cdot \mathbf{x}_j)} e^{i(\mathbf{k} \cdot \mathbf{x}_m - \mathbf{k}' \cdot \mathbf{x}_n)}. \quad (1.8)$$

The spatial intensity amplitude now contains two phases

$$f(\mathbf{x}_i, \mathbf{x}_j) f^*(\mathbf{x}_m, \mathbf{x}_n) = \sum_{ij} |f_i| |f_j| e^{i(\delta_i - \delta_j)}, \quad (1.9)$$

one for the retarded amplitude associated with $\zeta(x, t)$ and the advanced amplitude associated with $\zeta^*(x, t)$. These can be viewed as a wave moving forward in time paired with a wave moving backwards. This sum behaves fundamentally differently. If the phases cancel $\delta_i = \delta_j$, then there is no random phase cancellation due to disorder averaging, and the intensity becomes a *long range* object, capable of traveling diffusive distances. This occurs when the retarded/advanced fields follow the

same scattering trajectory, and is a coherent effect capable of withstanding multiple scattering. This is the source of diffusion.

There is an additional contribution to the sum that the system will have if it exhibits time reversal symmetry. In other words, if the probability to go from one spot to another is the same forwards moving forward or backward in time. In this event, we can run the advanced trajectory backwards in time. This is easier seen in terms of monochromatic waves. The total amplitude for identical scattering paths would be

$$|A(\mathbf{k}', \mathbf{k})|^2 = \sum_{i,j} |f(\mathbf{x}_i, \mathbf{x}_j)|^2 \left(1 + e^{i(\mathbf{k}+\mathbf{k}') \cdot (\mathbf{x}_i - \mathbf{x}_j)} \right). \quad (1.10)$$

In general, the second term vanishes due to phase cancellation. However, if we look at process that either A: return to the origin ($\mathbf{x}_i = \mathbf{x}_j$), or B: backscattering in the direction of the initial incoming wave ($\mathbf{k} = -\mathbf{k}'$), then the second term also vanishes. This is the origin of the coherent backscattering effect whereby the amplitude of a wave coming out of disordered media doubles coming back.

The outline of the thesis is as follows. We first conclude the introduction by presenting a brief summary of two relevant topics that will be used throughout. The first is a discussion functional techniques in classical field theory. This includes a definition of the self energy, which we will make extensive use of. The second is a general derivation of the equations of elasticity for lower dimensional elastic structures. We show that the principal effect of reducing dimensionality is to introduce soft bending modes. The derivation is most relevant to the mechanics of membranes, however can also be used to understand rods and filaments by shrinking an additional internal dimension of the membrane.

We then break the thesis into two parts. The first part is concerned with filaments, and more generally networks of such filaments. In Chapters 2 and 3 we discuss the equilibrium and dynamical behaviors of semiflexible filaments cross linked into a network. These calculations depend critically on the boundary conditions imposed on the filament, which we here model as a spring representing the linear compliance of the network. This introduces a nonlinearity that we treat through functional methods. Our main objective is to study the precise role of boundary conditions on height-height correlation functions of an individual filament. More broadly, we propose this as a means of noninvasive microrheology of filamentous networks. We model a network as composed of semiflexible filaments joined by crosslinkers at a collection of junctions. For any given filament in network, the local tension determines the boundary conditions. By solving for the fluctuation spectrum as a function of the boundary, we provide a precise profile specific to a given tension. By measuring the fluctuation spectrum for each filament in network, in principle one may then deduce a tension map of the whole system. In order to test and calibrate the method, precise manipulation of the boundary conditions may be done via optical tweezers, pinning one end of the filament, or sandwiching a filament between two known forces. In Chapter 4, we discuss the interaction between filaments and cross linkers, particularly looking at how cross linker transience affects the mechanics of bundles.

In Part II, we look at the elasticity of lower dimensional structures more theoretically. In Chapter 5, we first demonstrate the main effects of coupling in-plane stretching to out-of-plane bending, namely a gapping of the frequency spectrum and a suppression of undulations in regions of curvature. This is a simpler example of the well-known result that bending undulations on a membrane are suppressed in regions

of positive Gauss curvature [153]. However, due to the coupling of undulations to stretching, we find that bending waves can “tunnel” through such regions, by first converting to stretching modes. These points motivate our study in Chapter 6 of the fate of undulatory waves on randomly curved surfaces. Since we know that curvature scatters undulatory waves, we study the propagation of undulatory waves through a random media that is entirely geometrically induced. We find that undulatory waves undergo geometrically induced diffusion. This diffusion is reduced by the usual weak localization corrections studied for other waves in random media. We find that the behavior of this reduction though, is highly dependent on the nature of the disorder. For sufficiently jagged surfaces, low frequency undulatory waves can become localized.

1.0.1 Functional methods in classical field theory

For simplicity, in this section we shall work with a scalar field $\phi(x, t)$, with the understanding that x represents some d -dimensional position vector, t the time, and ϕ some field; for example, ϕ could represent the spin density on an ising lattice, or the longitudinal compression amplitude of a sound wave. The mechanics of our field are determined by its Hamiltonian $H = H([\phi(x, t)], x, t)$. We are interested in hamiltonians that do not depend explicitly on either x or t , and can be expressed in terms of polynomials of the field $\phi(x, t)$ and its gradients $\nabla\phi(x, t)$, $\nabla^2\phi(x, t)$. Suppose we have a Hamiltonian of the form

$$H = \int d^d x \left\{ \frac{1}{2}(\nabla\phi)^2 + \frac{m}{2}\phi^2 + V(\phi(x)) \right\}, \quad (1.11)$$

where we have omitted the time dependence, and grouped nonlinear terms into a general potential of the form $V([\phi(x)])$. First, the equations of equilibrium are

defined by the condition $\delta H/\delta\phi(x) = 0$. Here, we use δ to denote a functional derivative. A functional derivative can be viewed as an infinite dimensional gradient as follows. Looking at one dimension for simplicity (the result easily generalizes) we first discretize the function $\phi(x)$ into N lattice positions, such that it is described by the N -dimensional vector

$$\phi(x) \rightarrow \begin{pmatrix} \phi_1 \\ \phi_2 \\ \cdot \\ \cdot \\ \cdot \\ \phi_N \end{pmatrix}, \quad (1.12)$$

where each component is determined by evaluating the continuous function at each of the lattice sites $\phi_i = \phi(x_i)$. Given the functional $F([\phi(x)])$, F now becomes a multivariable function of the N components ϕ_i , *i.e.* $F \rightarrow F(\phi_1, \dots, \phi_N)$. We take the functional derivative acting with the N -dimensional gradient operator $\partial_{\phi_i} F$. To rederive the continuum limit, it's easiest to consider the Taylor series

$$F([\phi(x) + \delta\phi(x)]) \rightarrow F(\phi_i + \delta\phi_i) = F(\phi_i) + \sum_j \frac{\partial F}{\partial \phi_j} \delta\phi_j + \mathcal{O}(\delta\phi_j). \quad (1.13)$$

multiplying by an infinitesimal length $1 = dx/dx$, we take the continuum limit to find

$$F([\phi(x) + \delta\phi(x)]) = F([\phi(x)]) + \int dx \frac{\delta F}{\delta\phi(x)}, \quad (1.14)$$

where we have defined

$$\frac{\delta F}{\delta\phi(x)} = \lim_{dx \rightarrow 0} \frac{F(\dots, \phi_i + \delta\phi_i, \dots) - F(\dots, \phi_i, \dots)}{dx \delta\phi_i}. \quad (1.15)$$

In the continuum limit, the perturbation $\delta\phi_i$ is confined precisely to location x_i . We can enact this via a delta function, and formally define the functional derivative as

$$\frac{\delta F([\phi(x)])}{\delta\phi(y)} = \lim_{\epsilon \rightarrow 0} \frac{F([\phi(x)] + \epsilon\delta(x-y)) - F([\phi(x)])}{\epsilon}. \quad (1.16)$$

The trivial case gives $\delta\phi(x)/\delta\phi(y) = \delta(x-y)$. Using this, we can retain the chain rule from single variable calculus, and write the formal result

$$\frac{\delta F([\phi(x)])}{\delta\phi(y)} = \frac{\partial F}{\partial\phi}\delta(x-y). \quad (1.17)$$

The functional derivative will be our main tool. Often times, we are interested in computing the Green's function of a system. The Green's function is a kernel associated with linear partial differential equations that allows us to determine the solution ϕ in the presence of a δ -function forcing. From this, we can find the solution in the presence of any arbitrary source function by summing over a collection of δ -potential forces. Broadly, suppose that we are given a linear differential operator \hat{L} , and a source field $j(x)$, such that the scalar field obeys the equation of motion

$$\hat{L}\phi = j = \int d^d x' L(x, x')\phi(x') = j(x). \quad (1.18)$$

Here, x is once again d -dimensional. Now, suppose that we know another function G , such that

$$\hat{L}G = \mathbb{1} = \int d^d x'' L(x, x'')G(x'', x') = \delta(x-x'), \quad (1.19)$$

which depends on two positions x and x' . By multiplying the first equation on the left by G and the second on the left by ϕ then subtracting, we find

$$\phi = \hat{G}j + [\phi\hat{L}G - G\hat{L}\phi], \quad (1.20)$$

where we have suppressed the position labels, and in position space the operator acts explicitly as $\hat{G}\phi = \int d^d x' G(x, x')\phi(x')$. Now, since \hat{L} is a linear differential

operator, it consists of terms ∇, ∇^2, \dots . If the operator describes a well-posed partial differential equation, it is specified at the boundary and we can integrate by parts the term in brackets to produce something that depends only on the (known) boundary conditions. We are then left with a general solution to ϕ in terms of any source j .

Though the Green's function, if it can be computed, is a powerful tool for analyzing systems, it is limited to only linear partial differential equations. Thus, in the presence of the nonlinear potential $V([\phi(x)])$, the equations of motion do not possess a Green's function. Despite this, we can still define an operator \hat{G} that satisfies Eq. 1.19 for \hat{L} nonlinear. This operator is usually referred to as the two-point function, as it depends on two positions x and x' .

The Green's function can be reformulated in terms of functional integral, as the moments of some generating function. This representation has the added advantage that nonlinearities can easily be incorporated, and we can generalize to higher point functions. Furthermore, these higher point functions can be interpreted as moments of the field ϕ , distributed according to some ensemble. This allows us greater freedom to study ensembles originating from both thermal and quantum fluctuations, making the functional integral approach a robust method. To begin, we start with the generating function definition

$$Z[j] = \int \mathcal{D}[\phi(x)] e^{-\beta H([\phi(x)])} e^{\int d^d x \phi(x) j(x)}, \quad (1.21)$$

where j is a source field, β some constant ($\beta = (k_B T)^{-1}$ in statistical physics), and $\mathcal{D}[\phi(x)]$ denotes the path integral measure over all configurations of field ϕ (these configurations include any imposed boundary conditions). Expectation values are found via functional derivatives $\delta/\delta j(x)$. For example, the expectation of ϕ can be

found via

$$\frac{\delta \ln Z[j]}{\delta j(x)} = \frac{\int \mathcal{D}[\phi(x)] \phi(x) e^{-\beta H([\phi(x)])} e^{\int d^d x \phi(x) j(x)}}{\int \mathcal{D}[\phi(x)] e^{-\beta H([\phi(x)])} e^{\int d^d x \phi(x) j(x)}} = \langle \phi(x) \rangle, \quad (1.22)$$

where we have used $\langle \dots \rangle$ to denote the normalized expectation value of some quantity.

Taking two functional derivatives produces

$$\frac{\delta^2 \ln Z[j]}{\delta j(x) \delta j(y)} = \frac{Z[j] \langle \phi(x) \phi(y) \rangle}{Z[j]^2} - \frac{(Z[j] \langle \phi(x) \rangle) (Z[j] \langle \phi(y) \rangle)}{Z[j]^2} = \langle \phi(x) \phi(y) \rangle - \langle \phi(x) \rangle \langle \phi(y) \rangle, \quad (1.23)$$

which we identify as the second cumulant. Generally, we may find the n^{th} cumulant via functional differentiation

$$\langle \phi(x_1) \dots \phi(x_n) \rangle_c = \prod_{i=1}^n \frac{\delta}{\delta \phi(x_i)} \ln Z[j], \quad (1.24)$$

We define the expectation without the subscript c as the *n-point function*. Let us now consider the two-point function specifically. Given suitable boundary conditions, the total functional derivative of a functional vanishes:

$$\int \mathcal{D}[\phi(x)] \frac{\delta}{\delta \phi(x)} (\dots) = 0. \quad (1.25)$$

Applying this identity to the expectation value $\langle \phi(x) \rangle$ evaluated at $j = 0$, we find

$$\frac{1}{Z[0]} \int \mathcal{D}[\phi(y)] \frac{\delta}{\delta \phi(x)} (\phi(y) e^{-\beta H([\phi(y)])}) = \frac{1}{Z[0]} \int \mathcal{D}[\phi(x)] \times \frac{\delta}{\delta \phi(x)} \left(\delta(x-y) - \beta \frac{\delta H}{\delta \phi(y)} \phi(x) \right). \quad (1.26)$$

In terms of expectation values, exchanging $x \leftrightarrow y$ this yields the equation

$$\beta \left\langle \frac{\delta H}{\delta \phi(x)} \phi(y) \right\rangle = \delta(x-y). \quad (1.27)$$

If H is at most quadratic in ϕ , its functional derivative leads to a linear differential operator \hat{L} . In this case, we can pull \hat{L} outside of the expectation value, thus

recovering the Green's function equation of Eq. 1.19 provided we identify

$$\langle \phi(x)\phi(y) \rangle = G(x, y). \quad (1.28)$$

We have thus shown that the Green's function of an operator may be computed via the identity

$$G(x, y) = \frac{\delta}{\delta j(x)} \frac{\delta}{\delta j(y)} \ln \int \mathcal{D}[\phi(x)] e^{-\frac{1}{2} \int \phi(x) G^{-1}(x, y) \phi(y) d^d x d^d y} e^{\int j(x) \phi(x) d^d x} \Big|_{j=0}. \quad (1.29)$$

The functional integral approach lends itself well to nonlinear potentials, since we can generalize our idea of the Green's function in the presence of nonlinearity to the computation of the two point function. Furthermore, if the potential is small in some parameter about a Gaussian Hamiltonian, we can perform a perturbation expansion of the two-point function in terms of this small parameter. The series can be organized in terms of diagrams, and goes by the name of diagrammatic perturbation theory.

Continuing our analysis of the two-point function, it can be entirely specified in terms of a new object called the self-energy, denoted by the operator $\hat{\Sigma}$. The self-energy is defined provided we split the Hamiltonian into a Gaussian piece H_0 , whose Green's function \hat{G}_0 is known, plus an interaction term H_{int} containing the nonlinearities. The full two point function $G(x, y) = \langle \phi(x)\phi(y) \rangle$, can be decomposed as

$$\hat{G} = \hat{G}_0 - \hat{\Sigma}. \quad (1.30)$$

This equation defines $\hat{\Sigma}$. All terms are understood to be operators. Since G_0 is assumed known, finding $\hat{\Sigma}$ is equivalent to finding G . An important property of $\hat{\Sigma}$, that it is diagrammatically given by the set of all diagrams that remain connected upon cutting any propagator/Green's function (known as one-particle irreducible or

1PI). To see the equivalence, define \hat{O} as the 1PI vertex operator. We can then construct the full Green's function by summing all numbers of insertions of operator \hat{O} . Schematically, we have

$$\hat{G} = \hat{G}_0 + \hat{G}_0 \hat{O} \hat{G}_0 + \hat{G}_0 \hat{O} \hat{G}_0 \dots \hat{G}_0 \hat{O} \hat{G}_0 = \hat{G}_0 + \hat{G}_0 \hat{O} \hat{G} \quad (1.31)$$

In the last equality, we have used that the infinite summation can be related to the definition of \hat{G} providing a self consistent equation. Making use of the operator inverse $(\hat{A}\hat{B})^{-1} = \hat{B}^{-1}\hat{A}^{-1}$, we easily arrive at the solution $\hat{G} = (\hat{G}_0 - \hat{O})^{-1}$. Comparison with the defining equation for the self energy confirms that $\hat{\Sigma}$ is indeed the 1PI vertex.

1.0.2 Free energy of lower dimensional elastic solids

In this section, we derive the general equations of motion and free energy governing curved lower dimensional elastic structures, for which bending is the softest energy scale. We will further work in the limit of weak curvature, to be defined more precisely. This lays the groundwork for all future calculations, in which elasticity of specific structures may be derived of subsets of the general formulas. Without loss of generality, we refer to such structures as *membranes*, with specific structures like rods consisting of a membrane in which one of its later dimensions is shrunk.

We define a lower dimensional elastic structures as a surface whose internal coordinate dimension is less than the embedding dimension. In particular, we consider structures that are curved in the stress-free state. to determine the mechanics, we develop a phenomenological free energy or Hamiltonian governing the structure

Lower dimensional structures break the symmetry amongst deformations in the embedding space. In doing so, fluctuations about an equilibrium configuration are

both dependent on the internal coordinate, as well as the direction of deformation in the embedding space. These complications lead us to analyze membranes separately in terms of bending undulations out of the tangent plane, and stretching modes in the plane. On a curved background, these two types of displacement fields are coupled.

First we introduce an effect Landau-Ginzburg free energy for the elastic deformations of a curved rod, with the condition that it has a stable ground state. The parameters of the theory can be related to the three dimensional elasticity constants of an isotropic material by carefully considering the limiting process from higher to lower dimension, or analyzing the deformation under constant pressure stresses. The limiting process is given schematically as follows: given a parametrization $\mathbf{X}^{(V)}(x_1, \dots, x_d)$ of the volume of the elastic solid, we define a lower dimensional surface $\mathbf{X}^{(S)}(x_1, \dots, x_{d-d_c})$, that depends only on the $d-d_c$ internal coordinates. The volume parametrization is related to the surface parametrization by including the d_c normal vectors \hat{n}_i , to give $\mathbf{X}^{(V)} = \mathbf{X}^{(S)} + \sum_{i=d-d_c+1}^d x_i \hat{n}_i$. The new normal coordinates $x_{i>d-d_c}$ now regulate the membrane thickness, and can easily be taken small. In making this mapping, we have required that the surface vector $\mathbf{X}^{(S)}$ describes a stress-free state. The $d \rightarrow (d-d_c, d_c)$ decomposition for $d_c = 1$ arises in the initial-value formulation of relativity, from which we find that the lower dimensional surface now depends on two $(d-1)$ dimensional tensors, i.e. the metric and extrinsic curvature tensors.

A similar effect occurs here: the energy of the membrane must solely be a function of the metric tensor and extrinsic curvature tensor. This is in contrast to elastic continua, in which the energy is dependent only on the metric tensor. Our goal then, is to formulate an a reduced elastic theory that depends only on the internal coordinates x_1, \dots, x_{d-d_c} . We start by defining, for a given parametrization \mathbf{X} , the

metric tensor g_{ab} :

$$g_{ab} = \partial_a \mathbf{X} \cdot \partial_b \mathbf{X}, \quad (1.32)$$

where indices a, b run over internal dimension. The metric tensor fully specifies *intrinsic* curvature, that is, the properties of the surface in the local tangent plane. Since our embedding dimension is not equal to our internal dimension, there exists *extrinsic* curvature in the system. For a given metric tensor, multiple surface can lead to the same intrinsic curvature. The extrinsic curvature differentiates between these surfaces, and depends on the shape of the surface in the embedding dimension. Extrinsic curvature is controlled by the curvature tensor d_{ab} , also known as the second fundamental form. It can be defined in terms of covariant derivatives D_a of the parameterization field and normal vector \mathbf{n} as

$$d_{ab} = \mathbf{n} \cdot D_a D_b \mathbf{X}. \quad (1.33)$$

Though the free energy or Hamiltonian of an elastic solid must depend on some function of the metric and curvature tensors, not all arguments represent a physically realizable surface. In order to ensure that there exists a physical parametrization that reproduces a given combination of g_{ab} and d_{ab} , we must impose integrability conditions known as the Gauss-Mainardi-Codazzi equations. The compatibility equations essentially impose that the non-covariant partial derivatives in the embedding space commute, *i.e.* that we must have $D_a d_{bc} = D_b d_{ac}$. Since we will be deriving our free energy or Hamiltonian starting from a parametrization, we will no longer concern ourselves with this issue.

Bending is, essentially, an energetic cost to rotations of the normal vectors. We can generalize the concept of bending to higher dimensions by associating a bending energy with the cost of normal vector rotations in a locally orthonormal frame. As

the dimension of the internal space is reduced, more frame rotations of out-of-plane normals become available, leading to more tensors need to describe the embedding. For codimension one, we have only a single normal vector, and so the energy can be represented by only a metric and bending tensor. For codimension two, relevant to rods or filaments, there are two normal directions. There now exists the possibility that the two normal vectors can rotate, without changing the orientation of the local tangent plane. These deformations correspond to twisting, and can be associated with a torsion tensor. Since we are modeling the lower dimensional elastic structures as truly lower dimensional, we have no means twist the local frame, other than by curving it. In this case, torsion effects correspond to higher curved surfaces. Following a space curve along such a surface, the curvature, which corresponds to rotations between the local tangent vector and normal, will increase as the torsion, which corresponds to rotations in the plane spanned by the local tangent and binormal, increases. We can thus focus on bending as the primary and dominant aspect of the elasticity of lower dimensional elastic structures.

We now construct the free energy or Hamiltonian. Energy is assumed minimum for some background surface configuration given by the d -dimensional vector $\mathbf{X}_0(\sigma_a)$ and parametrized by $d-d_c$ internal coordinates σ_a . For small displacements from mechanical equilibrium, we construct a Landau-Ginzburg free energy, listing all terms allowed by symmetry. The equilibrium state is assumed curved, with fixed background metric g_{ab}^0 . Global translational and rotational invariance imply the energy can only be a function of contractions of the local tangent vector $\mathbf{t} \equiv \partial_a \mathbf{X}$. We find for some coefficients c_i :

$$\begin{aligned}
F_0 &= F_{\text{top}} + \int d^D \sigma \sqrt{g_0} \{ c_0 t_a \cdot t^a + c_1 (t_a \cdot t^a)^2 + c_2 (t_a \cdot t^b)^2 \\
&+ c_3 n \cdot \nabla_c \cdot t^c + c_4 \nabla_a t^b \cdot \nabla_b t^a + c_5 \nabla_a t^a \cdot \nabla_b t^b \}. \tag{1.34}
\end{aligned}$$

The c_3 term represents a spontaneous mean curvature and only appears in three dimensions. F_{top} indicates topological terms. Examples include the winding number $W = \frac{1}{2\pi\ell} \int d\sigma |\mathbf{t} \times \dot{\mathbf{t}}|$ for $d = 1$, $d_c = 1$, and the Euler character $4\pi\chi = \int d^2\sigma \sqrt{g} R$ for $d = 2$, $d_c = 1$. Provided our surface is in the regime of elasticity and does not undergo major changes such as puncturing, this term can safely be ignored. If we were to introduce a local field such as for hexatic membranes with topological defects though, these terms may be important.

If the background metric is approximately flat, then only the first line in Eq. 1.34 may be kept: this has a minimum for $c_0 < 0$ provided that $\mathbf{t}_i \cdot \mathbf{t}_j = -c_0 g_{ij}^0 / (2Dc_1 + 2c_2)$, which tells us that \mathbf{t} may be interpreted as a tangent field of some surface. Thus, the term $\nabla_a \mathbf{t}_b$ represents the second fundamental form \mathbf{d}_{ab} of the background surface. We can now remove the constraint of a nearly flat background with the knowledge that the \mathbf{t}_a represent tangent vectors in equilibrium. Dynamics are found by expanding to second order about the minimum. This somewhat lengthy procedure is simplified by instead varying the quantities $\delta(\mathbf{t}_a \cdot \mathbf{t}_b) \equiv 2U_{ab}$ and $\delta(\nabla_a \mathbf{t}^b) \equiv \mathbf{K}_a^b$. The justification for this is two-fold.

Although we demand only that $\delta F / \delta t_a = 0$, solution $g_{ab} \sim t_a \cdot t_b$ also implies $\delta F / \delta g_{ab} = 0$. Since δg_{ab} contains terms of order δt^2 , some nonlinear terms in the fluctuation will actually vanish.

Second, varying the extrinsic curvature supposes that the equilibrium solution for $\mathbf{t}_a(\sigma_b)$ is consistent with the background extrinsic curvature, and whatever external

pressures are needed to ensure this are implied. The two tensors are recognized from elasticity theory as the shear strain tensor and bending strain tensor.

If we were to keep the next order in derivatives, we would produce a tensor $T_{abc} \sim \delta(\nabla_a \nabla_b \vec{t}_c)$. For codimension one, this will simply be derivatives of the bending and stretching tensors. For higher codimension, it will contain new terms describing torsion, *i.e.* rotation of the normal vectors amongst themselves. We can now make more precise our earlier claim that such terms can be ignored.

Between two points infinitesimally far apart, there will be an energy cost incurred by changes in length and changes in the coordinate frame. The former corresponds to the metric, which for codimension zero will be the only tensor needed to construct the energy. In codimension one, the unit normal vector breaks local euclidean invariance, indicating a preferred set of local orthonormal coordinates. If we look at a non-coordinate basis with unit normal \hat{e}_n , then the energy due to bending of the normal is $\hat{e}_a \cdot \nabla_b \hat{e}_n \equiv \omega_{abn}$, for ω_{abc} the Ricci rotation coefficient.

For a given geodesic parametrized by coordinate s , there is a unique normal vector satisfying $\mathbf{n} D\hat{\mathbf{t}}/Ds = 1$. The generalized Serret-Frenet relations tell us that each additional normal vector to this tangent can be ordered by powers of tangential derivative, since $\partial_s^{(m)} \mathbf{t} \sim \mathbf{n}_m$. Thus, torsional effects are small compared to bending and stretching.

Lastly, the spin connection implies an addition to the Christoffel symbols accounting for the change of orthonormal frame. Indeed, the covariant derivative is modified by $\tilde{\nabla} \rightarrow \nabla - h^2 d_{ab}$ as the thickness h of the normal direction goes to zero, reaffirming our earlier statement that bending and stretching are coupled.

Finally, we arrive at our expression for the free energy of a membrane

$$F = \frac{1}{2} \int d^D \sigma \quad \sqrt{g_0} \left\{ \lambda U_a^a U_b^b + 2\mu U_a^b U_b^a \right. \\ \left. + (\kappa - \kappa_G) K_a^a K_b^b + \kappa_G K_a^b K_b^a \right\} \quad (1.35)$$

The coefficients have been renamed to reflect elastic theory. K_G has been singled out as the coefficient of a purely topological term in $D = 2$, $d = 3$.

Indices are raised and lowered with the background metric g_{ab}^0 . While it's tempting to consider U_{ab} , K_{ab} as the fundamental fields to vary, we must remember that they are subject to the Gauss-Codazzi constraints. In this instance, the constraints are further complicated by the fact that the constraint equations involve the full metric and curvature tensors, i.e. background plus perturbation. Instead, the relations will be automatically satisfied if we instead vary the fields \mathbf{t}_a describing the embedding.

In order to understand the relationship between bending and stretching, as well as describe the actual deformations of the structure, we must implement a coordinate system. Naturally, we choose the normal coordinate representation. We parametrize displacements in the along the local tangent plane and the local normals via: $\delta \vec{X} = \sum_c u_c \hat{t}_c + f \hat{n}$. To linear order in the out-of-plane displacements f_α and in-plane displacements f_a , the shear and bending strain tensors are

$$U_{ab} = \frac{1}{2} (D_a u_b + D_b u_a) - d_{ab} f \quad (1.36)$$

$$K_a^b = D_a D^b f + d_a^c d_c^b f + u^c D_a d_c^b \quad (1.37)$$

In general, the definition of K_{ab} is somewhat arbitrary, since raising and lowering indices add terms $2U^{ac} K_{cb}$ to the definition. To remedy this, we look at the regime of linearized shallow shelly theory, also known as the *Donnell-Mushtari-Vlasov* (DMV)

equations. Here, only the first term $\nabla_a \nabla_b f_\alpha$ for the bending tensor is retained. Since this is the only term unchanged with respect to definition of K_{ab} , it is a physically reasonable approximation. It pertains to the limit $h \ll \lambda \ll R$, where the wavelength of characteristic deformations λ is much greater than the small dimensions h (membrane thickness or filament radius), yet much smaller than the local radius of curvature R .

Finally, to formulate a dynamical theory, we will need a kinetic energy term. Curvature causes non-uniformity of the displacement field, implying a spatially dependent rotational inertia. We must take into account the volume elements due to the finite thickness of the membrane.

We work according to the Kirchoff hypothesis, that normals remain normals (*i.e.* the membrane is like a sandwich of width). This can be written mathematically as the condition that under a small displacement of surface $\mathbf{X} \rightarrow \mathbf{X} + \delta\mathbf{X}$ that $(\mathbf{n} + \delta\mathbf{n}) \cdot (\mathbf{t} + \delta\mathbf{t}) = 0$. This implies that $\mathbf{t} \cdot \delta\mathbf{n} = -\mathbf{n} \cdot \delta\mathbf{t}$. Since the background does not fluctuate, the kinetic term writes:

$$T_{membrane} = \frac{\sigma}{2} \int_{-h/2}^{h/2} dz (\delta\dot{\mathbf{X}})^2 \quad (1.38)$$

for μ the mass per unit volume. The variation of X , $\delta\vec{X} = \delta\vec{X}_0 + z\delta\vec{n} = (u^c + \vec{t}^c \cdot \delta\vec{n})\vec{t}_c + f\vec{n}$. Using $\delta t_a = (\partial_a f + d_{ab}u^b)\vec{n} + (\dots)\vec{t}$, the Kirchoff assumption, and the unit normalization of \hat{n} , we have the kinetic energy:

$$T_{membrane} = \frac{\sigma}{2} \int_{-z/2}^{z/2} dz \left\{ \dot{u}_a^2 + \dot{f}^2 + z^2 \left(\partial_a \dot{f} - d_{ab}\dot{u}^b \right)^2 \right\}. \quad (1.39)$$

In the limit of weak curvature, the last term may be dropped, leaving just the usual kinetic terms for non-curved structures.

Part I

Semiflexible networks

CHAPTER 2

Equilibrium fluctuations of a semiflexible filament cross linked into a network

2.1 Introduction

A variety of biological materials are composed of semiflexible filamentous networks, including F-actin, collagen, fibrin, and intermediate filaments [125, 15, 21]. Such networks have a rich linear rheology [106, 107, 109] and exhibit a characteristic set of nonlinear mechanical features such as negative normal stress [62, 67], nonaffine deformations [52, 55, 35], and strain hardening [145, 98]. Because of these nonlinearities, tension propagation in filament networks appears to strongly deviate from the predictions of continuum elasticity theory, making it difficult to predict both the interactions between molecular motors in cytoskeletal networks and between force-generating cells in the extracellular matrix. Microrheology has been a useful probe for the local mechanical properties of such systems and a number of techniques have been developed [21]. This approach uses the position fluctuations of tracer particles, measured using any one of a variety of instruments such as optical tweezers [144, 1, 85] or laser deflection tracking [41, 136], to extract the collective elastic response properties of the network. A related microrheological approach that might allow one to map tension in filament networks, is to monitor the transverse

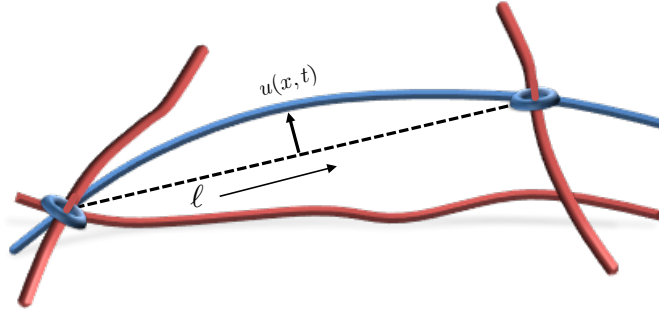


Figure 2.1: (color online) A schematic diagram of a particular filament (blue) cross linked into a network of similar filaments (red). The cross links are represented by rings.

undulations of network's filaments. Each filament's observed fluctuation profile is specified by its intrinsic bending rigidity and applied tension so these measurements produce a tension map in the network, as already explored by Lissek et al. [97]. To enable this *activity microscopy*, one must consider the predicted fluctuation spectrum of a filament cross linked into a network of similar filaments. This cross linking to the network introduces new mechanical boundary conditions on the ends of the filament so that the filament's fluctuation spectrum not only reports on its intrinsic mechanics, *e.g.*, bending modulus, but also on the collective mechanical compliance and stress state of the network to which it is coupled.

In this chapter we focus on this question of the role of the boundary conditions on filament fluctuations, showing that coupling the filament to an elastic network necessarily introduces a non-quadratic term in the filament's Hamiltonian, even in the small bending approximation. The analysis of this issue, which is necessary to enable activity microscopy in the filament networks, poses a few theoretically interesting problems explored here.

In the remainder of this chapter, we explore the role of boundary conditions of various complexities, starting from the classic problem [98] of a filament with its ends constrained to lie along one axis and subjected to a fixed tensile load. Our analysis culminates with the case in which the filament's end point is coupled to a combination of two Hookean (linear) elastic springs with differing spring constants such that one is oriented perpendicular and the other parallel to the undeformed filament's path. This is the most general possible coupling of the filament to a linear elastic solid. We do not consider the effect of applied constraint torques at the boundary, because we assume that the linker molecules are too small to provide significant torques. In addition, we allow a variation of the rest length of the longitudinal spring, enabling us to apply a fluctuating tension with a nonzero mean. This allows us to explore how the local filament fluctuations report on the stress state of the network. We summarize our result as well as discuss experimental tests and dynamical extensions in section 2.5.

2.2 Semiflexible filament model

To study the effect of various boundary conditions on filament fluctuations, we will compute the two-point correlation function of the transverse displacement $u(x)$ of an element of a filament labeled by an arclength variable x . The two-point function

$$G(x, x') = \langle u(x)u(x') \rangle, \quad (2.1)$$

is a natural extension of the particle mean-square displacement to filaments. The angular brackets $\langle \dots \rangle$ denote a thermal average. We do not consider here nonequilibrium (e.g., motor driven) situations, but such extensions are, in principle, possible.

A schematic drawing of the filament is shown in the upper panel of Fig. 2.2. The projected length ℓ , contour length ℓ_∞ , and longitudinal spring anchor point x_0 are all shown in the lower panel of that figure. We treat the filament as being inextensible with contour length ℓ_∞ less than its persistence length $\ell_p \equiv \kappa/k_B T$. In this limit we may neglect states of the filament containing loops or overhangs and describe its state of deformation by a two dimensional vector valued function $\mathbf{u}(\mathbf{x})$, giving the transverse displacement of a material element of the filament parameterized by the arclength. To quadratic order in these displacements, the Hamiltonian admits two independent polarization states of these undulatory waves; we focus on just one of these here, replacing the vector $\mathbf{u}(\mathbf{x})$ by a scalar quantity $u(x)$. In the presence of externally applied tension τ_{applied} , the elastic energy of deformation is given by [98]

$$H_0 = \frac{1}{2} \int_0^\ell dx [\kappa u''(x)^2 + \tau_{\text{applied}} u'(x)^2] + \quad (2.2)$$

$$-\tau_{\text{applied}} \ell_\infty + \frac{1}{2} \tilde{k}_\parallel (\Delta\ell + x_0)^2.$$

Here primes denote derivatives with respect to arclength x . \tilde{k}_\parallel is the spring constant of the external longitudinal spring. We introduce the transverse spring shown in Fig. 2.2 through the boundary conditions, as discussed below. To this order in u , we may neglect the distinction between that arclength and the projected length along the direction of the undeformed filament \hat{x} . We here, and throughout this chapter, take the range of integration to be over the projected length ℓ and hereafter suppress the limits of integration on such integrals. One may neglect the penultimate term in Eq. 2.2 proportional to the externally applied tension, τ_{applied} .

Inextensibility demands that the contour length ℓ_∞ remain unchanged, while filament undulations decrease the filament's projected length ℓ relative to the contour

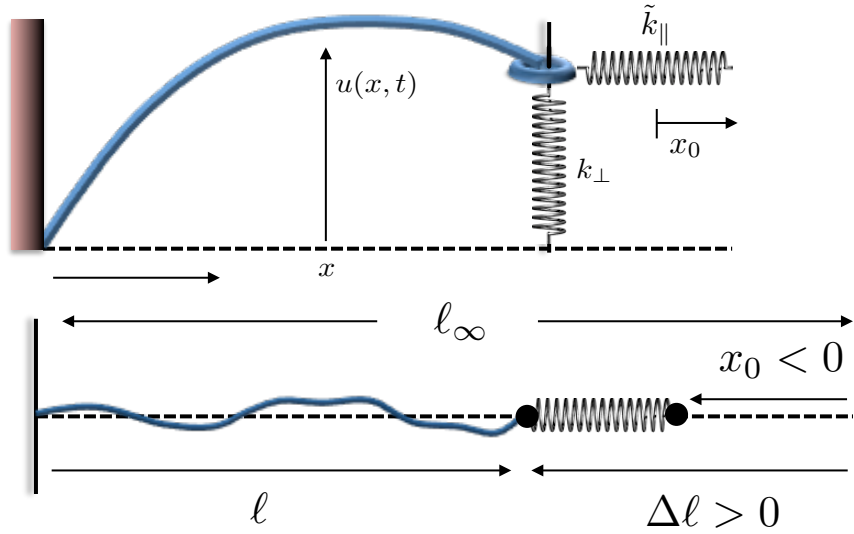


Figure 2.2: (color online) Above: Schematic diagram of a single semiflexible filament with the left endpoint pinned. Both endpoints are subject to torque-free boundary conditions. The right endpoint is attached to a combination of a longitudinal spring of rest length x_0 with spring constant k_{\parallel} , and a transverse spring of zero rest length with spring constant k_{\perp} . These represent the elastic compliance of the network. Below: A schematic diagram showing the connection of the longitudinal spring and the various lengths defined in the text. The spring's anchor point x_0 is positive when that spring applies tension to the perfectly stretched filament, $\ell = \ell_{\infty}$. The change in projected length $\Delta\ell$ is defined oppositely, becoming positive as the filament contracts.

length. Geometry relates the difference between these two lengths, defining $\Delta\ell$ as

$$\Delta\ell \equiv \ell_\infty - \ell \approx \frac{1}{2} \int u'(x)^2 dx, \quad (2.3)$$

where we have kept terms in the integral up to $\mathcal{O}(u'^2)$.

The boundary conditions obeyed by the filament are found by applying the variational principle to Eq. 2.2. Due to the appearance of fourth order derivatives in the equation of motion, there are four equations to be satisfied. Pinning the left end of the filament at zero and demanding that the second derivatives $u''(x)$ vanish at both endpoints (the torque free condition) eliminates three of these. The remaining boundary condition corresponds to controlling either the transverse force F_\perp^{ext} (conjugate to u) or the displacement of the right end point. The first choice of fixing the transverse force leads to

$$-\kappa u'''(\ell) + \tau u'(\ell) = F_\perp^{ext}, \quad (2.4)$$

while pinning the transverse displacement at the right end leads to the simpler condition

$$u(\ell) = 0. \quad (2.5)$$

Using Eq. 2.4 we may impose any number of forces on the end point that depend on that point's displacement. The most useful for our purposes is that of a Hookean spring (with zero rest length), which we implement by adding to the Hamiltonian

$$H_{k_\perp} = \frac{1}{2} k_\perp u(L)^2, \quad (2.6)$$

which leads to the boundary condition

$$F_\perp^{ext} = -k_\perp u(\ell). \quad (2.7)$$

We have assumed the rest length of the transverse spring to be zero. Any finite rest length can be eliminated by rotating the mean filament axis, and insisting that

the longitudinal spring remain longitudinal. In this chapter we consider boundary conditions in which the two springs remain orthogonal to each other so that their energies decouple to lowest order in stretching. More complex elastic boundary conditions can also be explored.

Eqs. 2.2, and 2.3 allow us to account for the forces associated with the deformation of the longitudinal spring. This generates a shift in the tension from the externally applied one τ_{applied} to one that accounts for the spring's forces τ – see below. Due to that spring, the instantaneous tension acting on the filament depends on its deformation state. This introduces a nonlinear and nonlocal term into the energy functional, because the tension depends on the difference between the projected length and arclength of the filament, which is given by an integral over the filament's configuration. We obtain

$$\begin{aligned}
 H &= \frac{1}{2} \int [\kappa u''(x)^2 + \tau u'(x)^2] dx + \\
 &+ \frac{k_{\parallel}}{2} \int u'(x)^2 u'(y)^2 dx dy,
 \end{aligned}
 \tag{2.8}$$

provided we identify

$$\tau = \tau_{\text{applied}} + \tilde{k}_{\parallel} x_0
 \tag{2.9}$$

$$k_{\parallel} = \tilde{k}_{\parallel}/4.
 \tag{2.10}$$

In this calculation we assume that the change in tension along the filament is instantaneous. This means that we treat the longitudinal speed of sound in the filament as being infinite, which is consistent with our inextensibility condition. Presumably, this condition may be violated for very high wavenumber modes on very long filaments so that these modes relax faster than the tension propagation time.

There are, indeed, other nonlinear terms associated with higher curvature configurations of the filament. Such corrections include geometrically nonlinear but local terms in the Hamiltonian of the form $(u''u'^{2n})^2$ for $n \geq 1$ [79]. There may also be local elastic nonlinearities that affect the energetics of highly bent configurations of the filament. We justify neglecting all of these terms by requiring the persistence length be sufficiently large, which suppresses highly bent (small radius of curvature) configurations. The new nonlinear and nonlocal term introduced by the longitudinal spring may not be neglected in this limit of stiff filaments. We emphasize that, while both the longitudinal and transverse springs affect the boundary conditions, only the longitudinal spring introduces nonlocal terms in the Hamiltonian.

Before studying the full problem, we first briefly review the properties of the equilibrium two-point function (Eq. 2.1) for a filament with pinned transverse undulations at its endpoints [98]. The remaining pieces of the Hamiltonian are diagonalized by Fourier sine series

$$u(x) \equiv \sum_p u_p \sin(px). \quad (2.11)$$

The zero displacement boundary condition – see Eq. 2.5 – is satisfied by expanding the transverse displacements in half-integer wavelengths $p = \frac{n\pi}{\ell}$ $n \in \mathbb{N}$. The two-point function is then

$$G_{nm}^{(0)} = \frac{2k_B T / \ell}{\kappa p_n^4 + \tau p_n^2} \delta_{nm}. \quad (2.12)$$

There is a crossover between curvature-dominated modes at high p and tension-dominated ones for modes with wavenumber smaller than $\sqrt{\tau/\kappa}$. Thus, tensed filaments admit a second length scale in addition to the thermal persistence length:

$$\ell_t = \sqrt{\kappa/\tau}, \quad (2.13)$$

which we refer to as the *tension length*. An alternative description of this result is that the filament's fluctuations are governed primarily by bending provided that the tension is small in magnitude when compared to scale of the compressive force necessary to induce Euler-buckling: $\kappa/\ell^2 = k_{\text{B}}T\ell_p/\ell^2$.

Because of the Kronecker delta linking the wavenumbers p and p' in the two-point function, it is straightforward to transform $G_{mn}^{(0)}$ back into position space to obtain $G_0(x, x')$. We find

$$G(x, x') = \frac{2k_{\text{B}}T}{\tau} \sum_{n=1}^{\infty} \frac{\sin(n\pi x/\ell) \sin(n\pi x'/\ell)}{\ell_t^2 p_n^4 + p_n^2}. \quad (2.14)$$

We observe that the amplitude of mean square undulations $\sqrt{G(x, x)}$ peaks at the midpoint $\ell/2$, and that the fluctuation amplitude is dominated by the longest wavelength modes, which are on the order of the contour length ℓ .

2.3 Two-point function of filament attached to springs

We now determine fluctuations of a filament attached to both a transverse and longitudinal spring, k_{\perp} and k_{\parallel} respectively, at its right end point. These elastic couplings may be thought of as representing the elastic compliance of the network in which the filament is embedded. A sketch of such a situation is shown in Fig. 2.1. The schematic diagram corresponding to the single filament model is shown in the upper panel of Fig. 2.2. We begin by examining the effect of each type of spring individually on the fluctuation spectrum of the filament, before considering their combined effect.

2.3.1 Transverse boundary spring

We start with only a transverse spring. This spring shifts introduces a force-controlled boundary condition given by Eqs. 2.4 and 2.7. The terms of the sine series introduced in Eq. 2.11 no longer individually satisfy this boundary condition. This and the additional energy associated with the transverse spring constitute its full effect.

We seek to compute the partition sum

$$Z = \int \mathcal{D}u e^{-\beta H}. \quad (2.15)$$

Normally, this is accomplished by expanding the conformations of the filament in terms of the eigenfunctions of the Hamiltonian. This expansion makes the sum over states straightforward. The introduction of the more complex boundary condition at the right end of the filament makes these eigenfunctions much more complicated than the simple sine series we used earlier. In this subsection, we first show that one can still use the sine series and impose the transverse force boundary condition as a constraint on the infinite sum of the amplitudes of these sine modes. We then translate those constraints into a correction to the Hamiltonian, which now may be expanded in the sine series without further consideration of the problematic boundary condition.

We begin by writing the partition sum, Eq. 2.15, in terms of a sine series, and impose the boundary conditions by a delta function as

$$Z = \int \prod_q du_q \left[\delta \left(\sum_q F[u_q] \right) \right] e^{-\beta H[u_q]}. \quad (2.16)$$

These boundary conditions introduce a constraint on the set of all the Fourier mode necessary to satisfy transverse force balance at the right hand side of the filament.

We further assume that the equation of constraint is a homogeneous function of the amplitude of the Fourier mode u_q of first degree so that it may be written as

$$F[u_n] = \psi_n u_n. \quad (2.17)$$

There is no sum over the repeated index. The form of ψ_n depends on the boundary condition employed, but this form will always result as long as that boundary condition is a linear function of the displacement field and its derivatives.

We replace the delta functions by their limit as narrow Gaussians and thereby push the equations of constraint into the exponent, writing

$$Z = \lim_{\epsilon \rightarrow 0} \frac{1}{\sqrt{4\pi\epsilon}} \int \prod_n du_n e^{-\beta \sum_{nm} \left\{ \frac{F[u_n]F[u_m]}{4\epsilon\beta} + H[u_n] \right\}}. \quad (2.18)$$

The boundary conditions now make up part of a new Hamiltonian of the filament $\tilde{H}[u_q]$ which is still quadratic in the u fields but no longer diagonal in them. The effective Hamiltonian is given by

$$\tilde{H}_{nm} = \frac{1}{2} [G_{nm}^{(0)}]^{-1} u_n^2 + \frac{1}{2} [G^{(1)}]_{nm}^{-1} u_n u_m. \quad (2.19)$$

The purely diagonal part $G_{nm}^{(0)} \propto \delta_{nm}$ is given by Eq. 2.12. The correction to this coming from enforcing the boundary conditions is

$$[G_{nm}^{(1)}]^{-1} = \frac{\psi_n}{\sqrt{2\epsilon\beta}} \frac{\psi_m}{\sqrt{2\epsilon\beta}}. \quad (2.20)$$

For the case of a transverse spring attached to the right endpoint, we find that

$$\psi_n = (-1)^n [\kappa p_n^3 + \tau p_n + k_{\perp} \cos(n\pi) \sin(n\pi)]. \quad (2.21)$$

It appears that the last term in the above expression can be safely set to zero, but this amounts to an incorrect ordering of limits that will result in not enforcing the

$$\begin{aligned}
\begin{array}{c} p \\ \longrightarrow \\ p' \end{array} &= \frac{\delta_{pp'} 2k_B T / \ell}{\kappa p^4 + \tau p^2} \\
\begin{array}{c} p \\ \text{---} \\ p' \end{array} &= \frac{k_{\parallel} \ell^2 p^2 p'^2}{8k_B T}
\end{aligned}$$

Figure 2.3: The free propagator and nonlocal vertex. Slashes denote multiplication by momentum squared. The four field interaction depends on two independent momenta.

transverse force balance term correctly at the endpoint. We return to this point below.

The Sherman-Morrison identity [141] allows one to write the inverse of a matrix plus a dyadic as

$$(G^{-1} + vw^T)^{-1} = G - \frac{Gvw^TG}{1 + w^TGv}. \quad (2.22)$$

Using this, we invert the quantity $[G^{(0)}]^{-1} + [G^{(1)}]^{-1}$ and obtain

$$\tilde{G}_{nm} = G_{nm}^{(0)} - \frac{G_{nk}^{(0)} \psi_k \psi_l G_{lm}^{(0)}}{2\epsilon + \psi_k G_{kl}^{(0)} \psi_l}. \quad (2.23)$$

This $\epsilon \rightarrow 0$ limit is now well defined. Taking that limit here, we arrive at the two-point function corrected for the transverse spring boundary conditions.

The result as written contains indeterminate parts equal to divergent sums multiplying zero. We address these now. We may write the two point function in Eq. 2.23 in form

$$\tilde{G}_{nm} = G^{(0)}(p_n) \delta_{nm} - \frac{F_n F_m}{D} \quad (2.24a)$$

$$D = \psi_k G_{kl}^{(0)} \psi_l \quad (2.24b)$$

$$F_n = G_{nm}^{(0)} \psi_m. \quad (2.24c)$$

The key term is D , which is given by

$$\begin{aligned}
D\beta &= \sum_{n=1}^{\infty} (\kappa p_n^2 + \tau) + k\ell \sum_{n=1}^{\infty} \frac{\sin 2n\pi}{n\pi} + \\
&+ k^2 \ell^2 \sum_{n=1}^{\infty} \frac{\sin^2 n\pi}{n^2 \pi^2}.
\end{aligned} \tag{2.25}$$

D is clearly divergent. This arises because we are evaluating a Fourier-series outside of its radius of convergence, requiring us to analytically continue the sums. We start by noting that the third term is convergent so we may safely set it to zero using the sine function. The first term may be quickly calculated by noting continuations of the Riemann zeta function: $\zeta(0) = 1/2$ and $\zeta(-2) = 0$. Since the sums start at $n = 1$ we find for the first line $-\tau/2$. The second term is indeterminate. However, we notice that it is the Fourier sine series of the function $k\ell \left(\frac{1}{2} - \frac{x}{2L}\right)$, evaluated at $x = 2L$. From this we observe that the sum must give $-k\ell/2$.

Turning to the calculation of F we find

$$\frac{2\beta}{\ell} F_n = (-1)^n / p_n, \tag{2.26}$$

as may be checked directly from Eq. 2.24c and the definitions of $G^{(0)}$ and ψ . Putting these pieces together we find the corrected two-point function:

$$\tilde{G}_{nm} = \frac{2k_B T / \ell}{\kappa p_n^4 + \tau p_n^2} \delta_{nm} + \frac{4k_B T / \ell}{\tau + k_{\perp} \ell} \frac{(-1)^{n+m}}{p_n p_m}. \tag{2.27}$$

The two-point function decomposes into a sum of a diagonal part identical to that of the pinned filament – see Eq. 2.12 – and an off-diagonal term, coupling modes with different wavenumbers. This off-diagonal coupling results from the transverse spring boundary condition that introduces a coupling between various modes (labeled by wavenumber) since that boundary condition enforces a constraint on the sum of those modes.

The off-diagonal term in Eq. 2.27 depends on the sum of two tensions: the externally imposed tension τ and a term proportional to the transverse spring constant $k_{\perp}\ell$. The magnitude of this term is controlled by the larger of these two tensions. When both the tension and transverse spring constant both go to zero, we have the problem of a filament with a free end. The expansion of the system in terms of sines then fails, as is signaled by the divergence of the two-point function. We note that the real-space solution for the two-point function $G(x, x')$ for the case of a transverse spring can also be obtained, as shown in Appendix A.1.

2.3.2 Longitudinal spring

We now consider a filament pinned at its right endpoint and attached to a longitudinal spring. The Hamiltonian is Eq. 2.8, with the boundary condition Eq. 2.5. This time, incorporating the boundary condition generates a nonlocal term in the Hamiltonian:

$$V = \frac{k_{\parallel}}{2} \int u'(x)^2 u'(y)^2 dx dy, \quad (2.28)$$

as seen in the second line of Eq. 2.8. Despite this complication, the two-point function remains exactly solvable. We write the two-point function in terms of a perturbation theory in the parameter k_{\parallel} . Although the second term of Eq. 2.8 is not small, we will find that we can sum up all perturbative corrections to obtain a finite answer.

The two-point function can be written as a sum over cumulants [68],

$$\langle u(x)u(x') \rangle = \sum_{n=0}^{\infty} \frac{(-\beta)^n}{n!} \langle V^n u(x)u(x') \rangle_{0,c}, \quad (2.29)$$

where $\langle \dots \rangle_{0,c}$ denotes the cumulant averaged with respect to the Hamiltonian in Eq. 2.2. The perturbation series is most easily evaluated by reciprocal space. We

may organize the perturbation theory diagrammatically – see Fig. 2.3. The interaction vertex, Eq. 2.28, is rather unusual. It is represented by a pair of disconnected propagators, with arbitrary wavenumbers p, p' respectively.

The series Eq. 2.29 is shown diagrammatically for the first few terms in Fig. 2.4. Consider the m^{th} order contribution to the two-point function. It is given by all possible contractions of m vertices and two external legs. Due to the form of the interaction term, all loops are disconnected and thus do not contribute to the cumulant. As a result, only lines contribute to the two-point function. Each diagram at m^{th} order is identical and equal to $\frac{\beta k_{\parallel} \ell^2}{8} p^4 G_0(p) G_0(p)^{2m}$, with $G_0(p)$ defined in Eq. 2.12. The final step is to determine the combinatoric factor counting the number of identical diagrams at m^{th} order. Inspecting Fig. 2.4, we find a total of $(4m)!!$ possible contractions at m^{th} order. Thus we obtain

$$\langle u_p u_{p'} \rangle = \delta_{pp'} G_0(p) \sum_{n=0}^{\infty} (-\beta k_{\parallel} \ell^2 p^4 G_0(p)^2)^n \frac{(4n)!!}{8^n n!}. \quad (2.30)$$

The sum can be simplified by two identities. First $(4n)!! 8^{-n} n!^{-1} = (2n-1)!!$. The second is $(2n-1)!! = (2\pi)^{-1/2} \int ds e^{-s^2/2} s^{2n}$. The second identity regulates the infinite sum in Eq. 2.30. Inserting these two identities and summing the resulting geometric series yields

$$G(p) = G_0(p) \sqrt{\frac{2}{\pi}} \int_0^{\infty} ds \frac{e^{-s^2/2}}{1 + \beta k_{\parallel} \ell^2 p^4 G_0^2 s^2}, \quad (2.31)$$

where we have written $G_{nm}(p) = G(p) \delta_{nm}$. Performing this integral, we complete the calculation of the two-point function. We find

$$G_{nm}(p) = \sqrt{\frac{\pi}{2\beta k_{\parallel} \ell^2}} \frac{e^{z_n^2} \text{Erfc}(z_n)}{p_n^2} \delta_{nm}, \quad (2.32)$$

where we have introduced

$$z_n = \frac{\kappa p_n^2 + \tau}{2\sqrt{2k_{\parallel}/\beta}}. \quad (2.33)$$

$$G(p) = \text{[diagram 1]} + \text{[diagram 2]} + \text{[diagram 3]} + \text{[diagram 4]} + \text{[diagram 5]} + \dots$$

Figure 2.4: The first three diagrams in the perturbative expansion of Green's function. No loops are possible in the connected diagrams, allowing the series to be resummed.

In order to gain some physical insight into this result, we rewrite Eq. 2.32 as an integral by using the definition of the complimentary error function:

$$G(p) = \frac{1}{p^2} \int_0^\infty d\lambda e^{-\frac{1}{2}\beta\ell(\kappa p^2 + \tau)\lambda - \frac{1}{2}\beta k_\parallel \ell^2 \lambda^2}. \quad (2.34)$$

The integral is dominated by its small λ behavior. Specifically, the integral is controlled by the value of λ for which the argument of the exponential

$$-2\Phi(\lambda) = \left(p^2 \ell \ell_p + \frac{\ell_p \ell}{\ell_t^2} \right) \lambda + \frac{\ell_p \ell^2}{\ell_k^3} \lambda^2 \quad (2.35)$$

equals one. Here we have defined a new length scale

$$\ell_k = (\kappa/k_\parallel)^{1/3} \quad (2.36)$$

governing the competition between bending and spring effects. Considering the thermal persistence length and the tension length, the filament coupled to a longitudinal spring admits three independent length scales. The dependence of the integral upon p and these length scales is determined by which of the three terms in Eq. 2.35

reaches unity first with increasing λ . There are clearly three possibilities generating three distinct results as shown in Fig. 2.5.

We fix the ratio of the persistence length to the total of the filament: $z = \ell_p/\ell$. Since the lowest order bending mode will dominate, we may replace the wavenumber $p\ell$ by π in the following. In the spring dominated region the λ^2 term in Φ reaches unity before the other two terms (with increasing λ). This provides two inequalities. The first, it requires that $y = \ell_t/\ell$ is greater than $x^{3/4}(z/2)^{1/4}$ where $x = \ell_k/\ell$. The second, it requires $x < x^* = (2/z)^{1/3}\pi^{-4/3}$. These provide the boundaries of the spring dominated regime (spring). Below and to the right of the spring dominated region lies the tension-dominated regime (tension) in which the tension term $(z/2)\lambda y^{-2}$ reaches unity before the other two terms. This region extends to the right of $y = x^{3/4}(z/2)^{1/4}$ and bounded above by $y = 1/\pi$. Finally, the remaining part of the parameter space diagram is dominated by the longest wavelength bending mode. This is the bending dominated regime (bending). See Fig. 2.5.

The basic principle determining these regions is that the stiffest elastic element exerts the dominant influence upon the fluctuation amplitude. This corresponds to picking the shortest of the length scales associated with tension, bending, and network compliance introduced above. The key signature of these three regimes can be understood as follows. Within the bending-dominated regime, the bending modulus dominates the amplitude of transverse undulations so that $\langle u^2 \rangle \sim \ell^3 T/\kappa$. In the tension-dominated regime, the same undulations are controlled by the tensile stress in the network so we expect $\langle u^2 \rangle \sim \ell T/\tau$. Finally, in the region of parameter space where the network's compliance controls the amplitude of filament undulations, we expect to observe $\langle u^2 \rangle \sim \ell \sqrt{T/k_{\parallel}}$, making the variance of u in this regime proportional to \sqrt{T} .

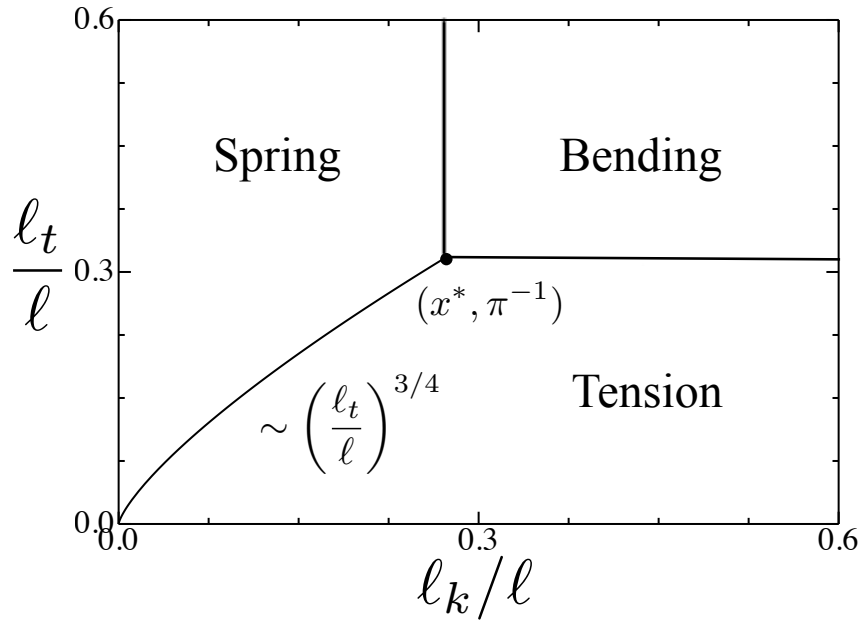


Figure 2.5: Parameter space spanned by the ratios of the tension length and the longitudinal spring length to the filament's length. The three regions are defined by the type of boundary term that dominates the fluctuation profile: tension, network compliance (spring), or filament bending. The three regions coincide at the point $((2/z)^{1/3}\pi^{-4/3}, \pi)$. The persistence length is set to be $\ell_p = \ell$ so that $z = 1$.

In order to use the observed fluctuations for a filament-based tension probe, it is desirable to be in the tension dominated regime. For most semiflexible filaments of interest $z = \ell_p/\ell \leq 1$. As a result, the boundary x^* is typically quite small, resulting in a large tension-dominated regime. Based on the boundary between the tension and network compliance (spring) dominated regions, we expect that the minimum observable tension should be $\sim \sqrt{Tk_{\parallel}}$. In fact, the region of parameter space at small tension $y < \pi^{-1}$ where there is a transition from the tension-dominated fluctuation spectrum to the transverse spring dominated fluctuation spectrum (along the curve $y = \pi^{-1}(x/x^*)^{3/4}$) is likely to be hard to access experimentally. All three regions, however, may be observable, particularly for sufficiently stiff filaments.

For a fixed set of parameters we examine the scaling behavior of the two-point function with wavenumber p . Using the result for the two-point function with a longitudinal spring in Eq. 2.32, we make a log-log plot as shown in Fig. 2.6. For large k_{\parallel} , a series expansion shows that $G(p) \sim p^{-2}$, as expected for a tension-dominated filament. As for a simply pinned filament, there is a transition with increasing wavenumber from this tension-dominated regime $G(p) \sim p^{-2}$, to a bending dominated one where $G(p) \sim p^{-4}$. The presence of the longitudinal spring changes that crossover point when that spring constant is sufficiently large.

These two scaling regimes are well-known for semiflexible polymers under a fixed tension [98]. The crossover wavenumber is there given as $p_* = \ell_t^{-1} = \sqrt{\tau/\kappa}$. When the spring constant is sufficiently small, i.e., $k_{\parallel} < k_{\parallel}^* = \min(\frac{\tau^2\ell}{\kappa}, \frac{\pi^4\kappa^2}{2\ell^4k_B T})$, the crossover wavenumber is essentially unaltered by the presence of the spring. But, when $k_{\parallel} > k_{\parallel}^*$, then $p_* \approx (\ell_k\ell)^{1/4}$, which implies that, with decreasing spring constant, p_* decreases as $p_* \sim k_{\parallel}^{1/4}$ until it reaches ℓ_t^{-1} .

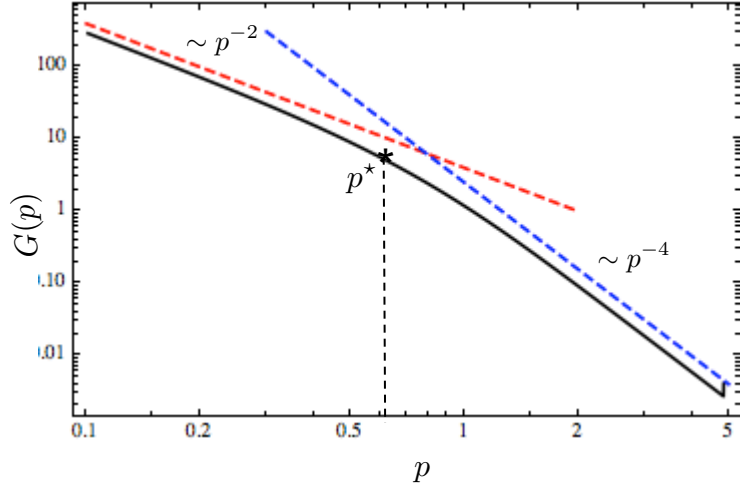


Figure 2.6: (color online) Log-log plot of the two-point function $G(p)$ with respect to wavenumber for parameters $\ell = 1\mu m$, $\kappa = 0.0413(pN\mu m)$, $\tau = 4.133(pN)$, and $k_{\parallel} = 5(pN/\mu m)$. There are two scaling regimes. The dashed lines illustrate their slopes in the two regimes. At low wavenumber, the fluctuations are dominated by a combination of tension and network compliance, while at high wavenumber, they are controlled by the filament's bending stiffness. Network compliance shifts the transition $p_* \approx (\ell_k^3 \ell)^{-1/4}$ to the higher wavenumbers, provided we are in the spring-dominated regime $\ell_t \gtrsim (\ell_k^3 \ell)^{1/4}$.

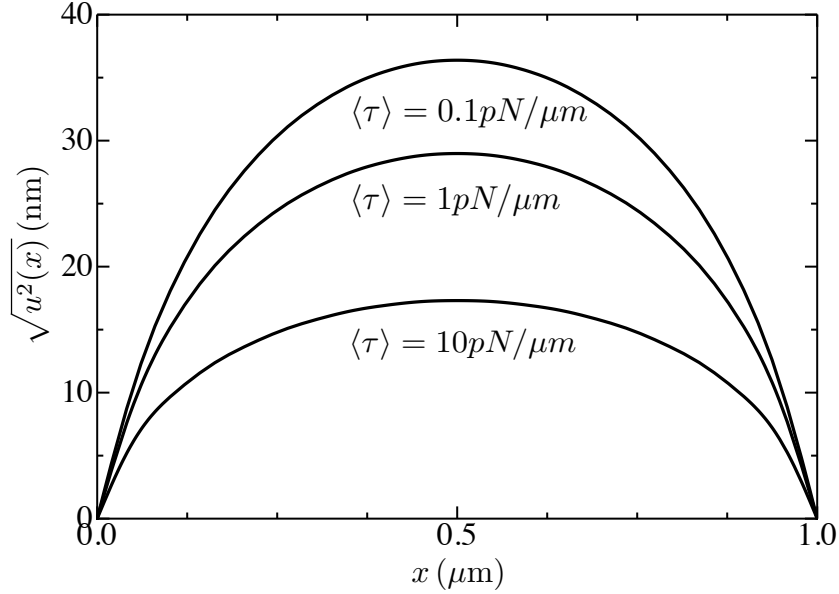


Figure 2.7: Plots of the exact root mean square height-height fluctuations for parameters $\ell = 1\mu\text{m}$, $\ell_p = 4/3\ell$, $\ell_t = 0.1\ell$. The average tensions of 0.1, 1, and 10(pN/μ) correspond to lengths $\ell_k = 0.1123$, .0498, and .01937(μm) respectively. The mean tension $\langle \tau \rangle$ is calculated using Eq. 2.37.

The transition from bending dominated to tension dominated modes should be experimentally accessible upon changing the longitudinal spring constant using a laser trap to hold one end of the filament. For filaments with lengths on the order of μm and a slightly longer persistence length, the longitudinal spring k_{\parallel} controls the crossover wavenumber p_* when the applied tension is $\mathcal{O}(1)\text{pN}$, and the longitudinal spring constant is sufficiently small: $k_{\parallel} \lesssim \mathcal{O}(1)\text{pN}/\text{nm}$. This is achievable with laser traps.

In addition to the crossover between bending and tension dominated regimes, one may look for the mean tension in the filament. This is perhaps the most important

theoretical result for the purposes of activity microscopy in networks. We can simply determine the mean filament tension from the relation

$$\langle \tau \rangle = \tau_{\text{applied}} + k_{\parallel} x_0 + k_{\parallel} \langle \Delta \ell \rangle. \quad (2.37)$$

The average reduction of projected length of the filament due to thermal undulations can be directly computed from the two-point function via: $\langle \Delta \ell \rangle = \frac{\ell}{2} \sum_p G(p) p^2$. We show in Fig. 2.7 the expected fluctuation profiles for a range of values κ and $\langle \tau \rangle$. From these one can compute the mean tension.

2.4 Transverse and longitudinal springs

Now we consider the combination of a longitudinal and a transverse spring attached to the right end point. This represents the most complex boundary condition that will be encountered in a generic filament network. For this combination of springs, we have not found an exact solution, but we provide a self-consistent (Hartree) calculation for the fluctuation spectrum in which we replace the fluctuating tension in the filament by the longitudinal spring with its mean value obtained self-consistently in the calculation.

The essential step is to replace the quartic term in the Hamiltonian Eq. 2.8 by

$$\frac{k_{\parallel}}{2} \left[\int u'(x)^2 dx \right]^2 \rightarrow \sum_p k_{\parallel} \left[\left(\frac{\ell}{2} \right) p^2 \langle \Delta \ell \rangle + \frac{1}{2} \left(\frac{\ell}{2} \right)^2 p^4 G_p \right] u_p^2. \quad (2.38)$$

The second term results from the mixed term $\langle u'(x)u'(y) \rangle$. We will show that it may be safely ignored. Upon substituting Eq. 2.38, the two-point function is immediately found to be

$$\langle u_p u_p \rangle_{\text{MFT}} = \frac{2k_B T / \ell}{\kappa p^4 + \tau p^2 + 2k_{\parallel} \langle \Delta \ell \rangle p^2 + k_{\parallel} \ell p^4 \langle u_p u_p \rangle_{\text{MFT}}}. \quad (2.39)$$

The final term in the denominator on the right hand side of Eq. 2.39 depends on the full two-point function and must be satisfied self-consistently. In short, we replace:

$$\frac{k_{\parallel}}{2} \left[\int u'(x)^2 dx \right]_{\text{MFT}}^2 \longrightarrow k_{\parallel} \langle \Delta \ell \rangle \int u'(x)^2 dx. \quad (2.40)$$

Now we impose a self-consistency condition on the heretofore unknown value of $\langle \Delta \ell \rangle$. This approximation is valid provided that the variance of $\Delta \ell$ is small, *i.e.*, $\sqrt{\langle \Delta \ell^2 \rangle_c} \ll \langle \Delta \ell \rangle$.

The MFT Hamiltonian is of the form Eq. 2.2, but with $\tau \longrightarrow \tau + k_{\parallel} \langle \Delta \ell \rangle$. The two-point function is found using our previous analysis of the transverse spring problem. We write

$$\langle u_p u_p \rangle_{\text{MFT}} = \frac{2k_B T / \ell}{\kappa p^4 + \tau p^2 + 2k_{\parallel} \langle \Delta \ell \rangle p^2}. \quad (2.41)$$

We now impose the self-consistency condition by requiring that

$$\langle \Delta \ell \rangle = \frac{k_B T}{2} \sum_p \frac{1}{\kappa p^2 + \tau + 2k_{\parallel} \langle \Delta \ell \rangle}. \quad (2.42)$$

Because of the slow convergence of the sum, it is more convenient to solve the self-consistency condition Eq. 2.42 in position space. We note that Eq. 2.41 is the Fourier-transformed Green's function associated with the equation of motion for $u(x)$, as can be obtained by the functional derivative of the self-consistent Hamiltonian. This result, however, applies to the case in which we do not allow transverse displacements at the right end. By changing this Green's function to the one appropriate for the transverse spring boundary condition while keeping the shift in tension, we can obtain the correct self-consistent condition for the case of a transverse spring (as well as a longitudinal spring). The position space Green's functions for transverse boundary conditions, and their respective self-consistency conditions are shown in

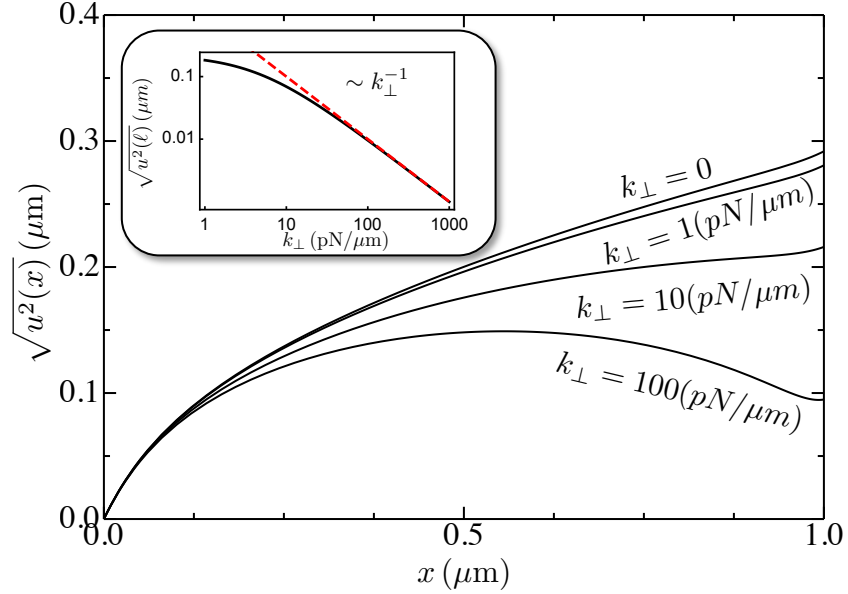


Figure 2.8: (color online) The MFT root-mean square fluctuations for various values of the transverse spring constant k_{\perp} . The inset provides a log plot of the root-mean square fluctuations at the spring (right hand side), as a function of k_{\perp} . For large large k_{\perp} , the endpoint fluctuation scales as $\sqrt{u^2(\ell)} \sim k_{\perp}^{-1}$, as expected for an ideal spring. Parameter values are $\kappa = 0.0413(\text{pN}\mu\text{m})$, $\tau = 4.133(\text{pN})$, and $k_{\parallel} = 5(\text{pN}/\mu\text{m})$.

Appendix A.1. Specifically, we make use of Eqs. A.7 and A.11 to plot fluctuation dependence on transverse spring strength, as shown in Fig. 2.8.

Fig. 2.8 plots the self-consistent two-point function $\langle u(x)^2 \rangle_{\text{MFT}}$ with a transverse and longitudinal spring. We vary the spring constant of the transverse spring k_{\perp} making several curves. Stiffer transverse springs clearly suppress endpoint fluctuations, but that suppression only decreases the variance of the endpoint logarithmically in k_{\perp} . Modest amplitude decreases require exponentially larger spring constants.

2.5 Conclusion

We have analyzed the effect of various mechanical boundary conditions on the equilibrium fluctuation spectrum of a semiflexible filament. This work expands upon the well-known case of equilibrium filament undulations for a filament constrained to have its end points fixed to lie on an axis and with a prescribed tension. Specifically, we have considered the case in which there are Hookean elements constraining both the transverse and longitudinal displacement of an end in the presence of mean tension (or compression). We have shown that one can directly account for the effect of a transverse harmonic pinning potential acting on the filament ends. More interestingly, the effect of the longitudinal harmonic potential acting on the projected length of the filament introduces a fluctuating tension, which is manifested as a nonlinear (quartic) term in the filament Hamiltonian, even in the case of filaments shorter than their own thermal persistence length, where geometric nonlinearities associated with the local filament curvature can be neglected. Understanding the implications of these boundary conditions for the fluctuations enable one to quantitatively interpret the fluctuations of a filament segment cross-linked to a network of such filaments in terms of the various model parameters, since the surrounding network acts to impose elastic constraints on the segment's end points.

Previous studies of worm-like chain dynamics have incorporated local filament extensibility by introducing a new elastic variable, the elongational strain, which is geometrically related to transverse undulations [116]. Our tensile load is treated as being uniform along the filament, but it is controlled by the transverse undulations of the filament, leading to our nonlocal term in the Hamiltonian. For extensible filaments, however, the locally varying tension would also depend on these elongational

modes.

We point out that applying the elastic element to only one end should be relevant for this application to networks, since the energy of these “network springs” depends only on the filament’s deviation from being straight and its projected length along its path in an unstressed state. Moreover, the local effect of shear deformation should be to apply a local tension or compression. Even in the case of nonaffine deformation [52, 159], where applied shear stress leads to local bending, we expect that the linearity of the response of the filament to bending (over small angles) will decouple the fluctuations from the mean bending. Thus, this analysis should allow one rather generally to use the observed transverse fluctuations as sort of a microrheological probe of tension propagation in networks using activity microscopy.

When we consider a filament subjected to a longitudinal elastic boundary condition that also imposes a finite mean tension, we note that there are three distinct regimes of fluctuations in which the scale of transverse undulations is controlled by one of: (i) the elastic boundary condition, (ii) filament bending, or (iii) mean tension. We have determined the boundaries of these parameter regimes, showing that tension dominates the longitudinal compliance down to small tensions on the order of $\sqrt{Tk_{\parallel}}$. This result sets the minimum tension that may be resolved by activity microscopy. Using this result, we expect that for biopolymer networks with a modulus on the order of kPa and mesh size on the order of one micron, we will be able to resolve tensions down to $\sim 1\text{pN}$. This should enable the detection of both prestress in networks and molecular motor activity. For small affine network deformations, we may use the self-consistent longitudinal spring constant k_{\parallel} to estimate the real part G' of the network shear modulus. For a given cross section of the network, there are ξ^{-2} segments, for ξ the average network mesh size. This leads to a modulus $G \sim k_{\parallel}/\xi$ [98].

Using as an example an F-actin network with modulus $\sim 100\text{Pa}$ and a mesh size of $0.5\ \mu\text{m}$, we estimate this network generates an effective $k_{\parallel} \approx 0.2\text{pN/nm}$. Thus, the network compliance should affect the cross over from tension to bending dominated fluctuations – see the discussion of Fig. 6.

The most direct experimental test of the theory is, however, in the analysis of the fluctuations of a single filament with one pinned end and Hookean constraints on the other. This might be achieved using a filament bound to particles that are either optically or magnetically trapped. The trapping potential of the bead provides (approximate) Hookean boundary conditions, which are both adjustable and independently measurable. As a result, the theory may be tested using a biopolymer filament of known bending modulus and measured length (e.g., F-actin) with no remaining fitting parameters.

Based on these calculations, one may imagine two directions for further study. First, one may attempt a self-consistent evaluation of the compliance of the “network springs” under the assumption that they represent a network of filaments identical to the one under consideration. Such effective medium or mean-field theories have been pursued for networks of filaments and springs [34, 23, 139].

Secondly, one may ask how the various boundary conditions affect the dynamics of filament undulations. Other studies have explored the dynamics of the longitudinal response of inextensible worm-like chains to local perturbations [117, 18, 47, 49]. It remains an open question as to how the boundary conditions studied here in equilibrium affect those dynamical results. The presence of a longitudinal compliance once again renders the basic Langevin theory (with a local drag approximation [59] or even slender body hydrodynamics [86]) nonlinear. We intend to explore this question

in future work in the limit of slow dynamics where the tension propagation time along the filament may be neglected. Of course, this is consistent with our treatment here of the filament being inextensible.

CHAPTER 3

Dynamics of undulatory fluctuations of semiflexible filaments in a network

3.1 Introduction

Semiflexible filaments networks underlie the structure of a number of biological materials, including the cytoskeleton and the extracellular matrix of tissues [125, 15, 21]. The mechanical properties of such materials depend on the mechanics of their individual filaments. These semiflexible filaments are essentially inextensible, with lengths less than their thermal persistence length, indicating a large bending rigidity κ that keeps them oriented along a mean direction.

Filamentous networks exhibit a number of interesting mechanical properties that differ from typical elastic continua, such as nonaffine deformation [56, 35] and negative normal stress [62, 67]. There is now a well-developed theory connecting the tension response of individual filaments to the linear collective shear response of their networks: $G(\omega)$. Due to the appearance of multiple time scales in the networks' dynamics, $G(\omega)$ exhibits a rich variety of behaviors [41, ?, 45, 108].

There is currently considerable interest in local microrheological probes of tension within the network at the single filament scale. Individual filaments in network are

subject to thermal fluctuations. Their fluctuation spectrum is, in part, controlled by the filament’s mechanical boundary conditions imposed by its coupling to the rest of the network. For example, the fluctuations of the (red) filament in Fig. 3.1 are modified by that filament’s mechanical coupling via cross links (black/gray circles) to the surrounding network of (blue) filaments. These boundary conditions include the tension imposed on the filament, allowing, in principle, one to extract local tensions from the observations of the stochastic undulations of individual strands within the network. The technique is called *activity microscopy* [97, 71].

In our previous paper [71], we examined how the surrounding network, including its elastic compliance and state of tension, affects the equilibrium fluctuation spectrum of the transverse undulations of a constituent filament in the network. In this chapter, we expand our analysis to dynamics, looking at the time-dependent correlation and response functions of both individual transverse modes of the filament and its end-to-end distance. These results will be important for future work on the frequency-dependent *nonequilibrium* fluctuations of network filament segments driven by endogenous molecular motors [105, 99, 104, 90].

We model the mechanical boundary conditions on the semiflexible filament by both a mean state of tension τ and a linear elastic compliance, representing the surrounding network. This elastic compliance may be thought of as attaching the filament’s end to a pair of Hookean springs, one longitudinal spring aligned with the mean extension of the filament and one perpendicular to it. These springs have spring constants k and k_{\perp} respectively. The lower panel of Fig. 3.1 shows a schematic illustration of the system, whose dynamics will be the focus of this chapter. The perpendicular spring changes the spatial structure of the eigenmodes of filament deformation – see Appendix B.4. The longitudinal spring is the most interesting, as

it introduces a nonlinearity into the filament's Hamiltonian even in the limit of small bending. The origin of this nonlinearity (explained more fully below and in Ref. [71]) is that the state of tension in the filament depends on the instantaneous projected length of the filament. Since we work in the limit that the filament is inextensible, tension propagation is instantaneous, and the longitudinal spring introduces a term that is non-diagonal in the Fourier modes of the filament's undulations, but local in time. As a result of this nonlinearity, the equilibrium fluctuation spectrum [71] of the filament and its dynamics are controlled by the set of parameters (κ, τ, k) , and are related to deformation of the network under compression and shear.

The nonlinearity introduced by the boundary compliance (due to the rest of the network) alters the power spectrum of the variations of the projected length of a filament's end-to-end distance when it is cross linked into a network. We study that here. Using our model, we also calculate the response of that distance to applied forces. The time-dependent, single-filament response can be then be used to calculate the dynamic shear modulus and compliance of the network by well-known methods [?]. The most direct experimental test of our theory, however, is to be found at the single filament level. We propose that one can directly measure the relaxational dynamics of a single filament anchored to a substrate and attached to a bead held in an optical trap [144, 1, 85]. In such a configuration, the trap provides a longitudinal spring of known (in principle) spring constant. By moving the trap's center, one can measure the changes in filament's fluctuations as a function of tension. In addition to passive measurements, one should also be able to actively measure the response function of the filament's end-to-end distance by driving it via the sinusoidal oscillations of the trap's center. We predict that the new effect associated with the elastic compliance of the trap will be most evident at small values of applied tension.

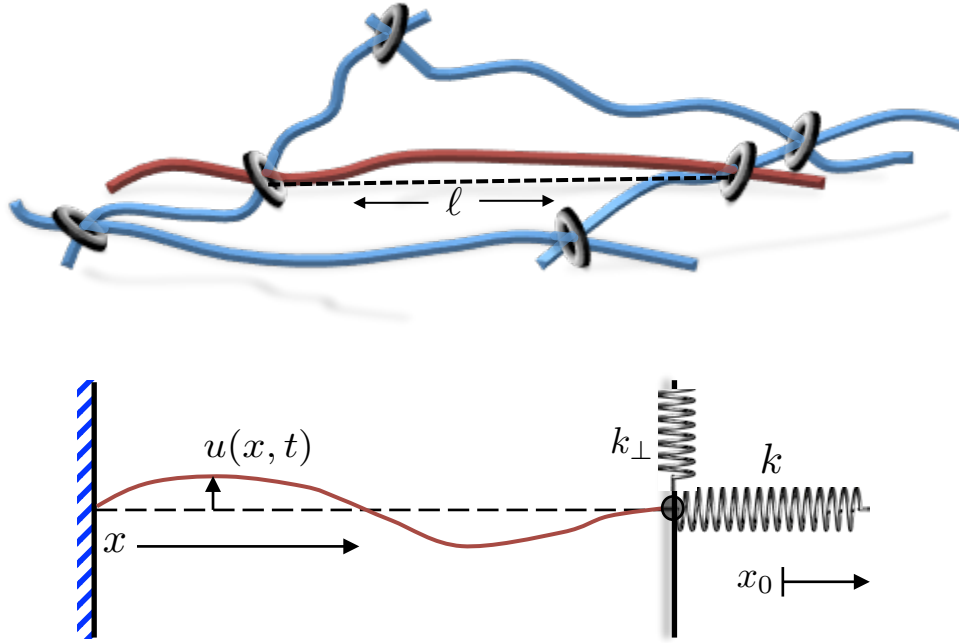


Figure 3.1: (color online) Top: visualization of a particular filament (red) cross linked into a network of similar filaments (blue). The cross links are represented by black and gray rings. Bottom: schematic diagram of a single semiflexible filament. The left endpoint is pinned, and the right attached to a longitudinal spring with spring constant k and a transverse spring with spring constant k_{\perp} . These represent the elastic compliance of the network. We focus on the effect of the longitudinal spring. Both endpoints are subject to torque-free boundary conditions.

The remainder of this chapter is organized as follows. We introduce the model, including the stochastic equation of motion (Langevin equation) of the filament using slender body dynamics, in Sec. 3.2.1. Due to the nonlinearity in the Hamiltonian, we cannot solve these dynamical equations exactly. Instead, in Sec. 3.3 we first compute the linear response to transverse applied loads in the wavenumber domain to second order in the longitudinal spring constant. From this, we determine the dynamical two-point function $\langle |u_p(\omega)|^2 \rangle$ in Fourier space. These perturbative calculations are organized using the Martin-Siggia-Rose/Janssen-De-Dominicis (MSRJD) functional integral formalism [146]. Within this diagrammatic expansion, we comment on various classes of diagrams and propose an approximation using a resummation of the dominant terms of the perturbation series.

To make these approximations precise, we develop an effective field theory (in Sec. 3.4), whose mean-field solution reproduces the resummation of the dominant terms. The mean-field solution is a type of dynamical self-consistent theory, which we analyze in Sec. 3.4.1. This self-consistent approach allows us to explore non-equilibrium dynamics and the time-dependent response of pulled filaments. Later, in Sec. 3.4.2 we expand our effective field theory about its mean-field solution, allowing us to compute fluctuations, particularly of normal modes and the filament's projected length. These corrections are found to be rooted diagrammatically in the random phase approximation borrowed from solid state physics. By considering the terms arising at higher orders in the expansion about the mean field, we identify the various classes of diagrams postulated from the second-order perturbative result, thus determining the validity of our initial approximations. We conclude with a discussion of our results in Sec. 3.5, where we discuss the expected experimental signature of the filament's mechanical boundary conditions on its dynamics. The

reader interested primarily in those predictions is encouraged to turn first to that section.

We find two principal effects of the longitudinal spring. The primary one is a renormalization of the tension by the mean force of the spring, which can be schematically viewed as $\tau \rightarrow \tau + k\langle\Delta\ell\rangle$. Even if one tunes the applied tension to a small value, the spring, responding to the fluctuations of the end-to-end filament distance, will impose a tension on its own. The spring thus adds an additional energy scale that competes with the work done by the imposed tension. We may approximate the value k^* at which the spring begins to compete with tension by using the spring-free result for projected length change $\langle\Delta\ell^{\text{free}}\rangle = k_{\text{B}}T\ell^2/12\kappa$ [98]. Using that estimate to compute the renormalized tension, we find the longitudinal spring constant becomes significant when $k \geq k^* \approx 12\kappa\tau/k_{\text{B}}T\ell^2$. Secondly, the nonlinearity generically reduces the effective longitudinal spring constant k , as a result of the nonlinearity transferring the elastic energy amongst the normal modes of filament deformation to a more energetically favorable configuration. This effect is primarily seen in the dynamical projected length fluctuations. At high frequencies, this effect goes away so that the bare spring constant once again becomes observable.

3.2 Filament dynamics

3.2.1 The Model

The filament Hamiltonian with the spring-induced nonlinearity was discussed earlier [71], but we briefly reintroduce it here. Since the filament of length ℓ is assumed to be nearly straight, we work in a Monge representation, omitting overhangs, so

we may specify the filament's configuration by its transverse coordinate $u(x)$ at a distance x along the mean orientation. Here we work in two dimensions, with the understanding that in three dimensions the dynamics simply involves two copies of the fluctuations considered here, one for each polarization state of the undulations. Where necessary, we later mention the inclusion of both transverse degrees of freedom. We treat the filament as being inextensible. Tension propagation is instantaneous. The change in the filament's projected length due to bending is given to quadratic order in the transverse displacement by

$$\Delta\ell = \frac{1}{2} \int_0^\ell (\partial_x u)^2 dx. \quad (3.1)$$

The Hamiltonian of the filament with bending rigidity κ , under tension τ , and coupled to a longitudinal spring with spring constant k is

$$H = \frac{\kappa}{2} \int_0^\ell dx (\partial_x^2 u)^2 + \tau \Delta\ell + \frac{1}{2} k \Delta\ell^2, \quad (3.2)$$

where $\Delta\ell$ is the amount of the length of the filament taken up by its undulations – see Eq. 3.1. For notational convenience, the spring constant k used here is equal to $4k$ in Ref. [71]. The first term is the usual worm-like chain model, with the restriction of no overhangs. The second term represents the contribution due to tension. The third and novel term is due to a Hookean spring at the boundary. Since ΔL depends quadratically on the normal modes of the filament, this final term is nonlinear. Though the nonlinearity was introduced via a boundary condition (coupling the filament to a longitudinal spring), it manifests as a contribution to the bulk Hamiltonian.

The tension $\tau = \tau_{\text{applied}} + kx_0$ can be freely adjusted using the externally applied tension τ_{applied} , or by adjusting the anchoring point of the longitudinal spring x_0 . By

a suitable choice of x_0 , it can be made to vanish. We assume that filament's ends are pinned to the x axis and torque free: u and $\partial_x^2 u$ vanish at the endpoints. This choice enables one to expand the transverse undulations in a sine expansion

$$u(x, t) = \sum_p u_p(t) \sin(px), \quad (3.3)$$

with wave numbers

$$p_n = n\pi/\ell, \quad (3.4)$$

where $n = 1, 2, \dots$

This Hamiltonian provides minimal coupling of a filament in a network to its surroundings (treated as a linear elastic solid). It is necessarily nonlinear. The assumption of instantaneous tension propagation will eventually be violated at sufficiently high wavenumber since these undulatory modes will relax faster than the tension propagation time. Accounting for tension propagation introduces other nonlinearities to the Hamiltonian, which have been extensively studied [46, 48, 50]. We return to the relation of our work to these studies in Sec. 3.4.1.

The network is overdamped, being immersed in a viscous fluid with viscosity η so that inertial effects may be ignored. We treat the hydrodynamic forces on the filament using resistive-force theory, where the drag force is linear in velocity and decomposes locally into a component perpendicular to (with coefficient ξ_\perp) and parallel to (with coefficient ξ_\parallel) the mean tangent $\hat{t} \approx \hat{x}$. In terms of the position vector of a segment of the filament: $\vec{u} = (x, u_1(x), u_2(x))$, where the 1, 2 subscripts label the coordinates transverse to the direction of the undeformed filament \hat{x} , the drag force is [158]

$$[\xi_\parallel \hat{t}\hat{t} + \xi_\perp (\mathbb{1} - \hat{t}\hat{t})] \cdot \partial_t \vec{u} = -\vec{F}_{\text{drag}}, \quad (3.5)$$

where the drag coefficients are given by $\xi_{\perp} \approx \frac{4\pi\eta}{\ln \ell/a}$, $\xi_{\parallel} \approx \xi_{\perp}/2$. We neglect any modification of the effective drag per unit length near the filaments ends, and we neglect any nonlocal hydrodynamics which produce logarithmic time corrections [33, 45]. The drag terms retained give the leading contribution to the drag forces in slender body theory, which provides a power series in $\ln(\ell/a)^{-1}$ [95] at zero Reynolds number. Lastly, if we keep the drag forces acting on the filament only to linear order in u , we may neglect the drag associated with tangential motion.

We now obtain overdamped, model A dynamics [59]

$$\xi_{\perp} \partial_t u(x, t) = -\delta H / \delta u(x, t) + \zeta(x, t). \quad (3.6)$$

We also include Gaussian white noise

$$\langle \zeta(x, t) \zeta(x', t') \rangle = 2\xi_{\perp} k_B T \delta(x - x') \delta(t - t') \quad (3.7)$$

in the stochastic equation of motion, Eq. 3.6, consistent with the fluctuation-dissipation theorem. The analysis presented here is immediately generalizable to nonequilibrium and frequency-dependent noise, as long as it remains Gaussian.

3.2.2 Spring-free results

We first review the previously studied dynamics of a filament with fixed applied tension and no coupling to springs. The Langevin equation is linear and admits a normal mode decomposition in terms of half integer wavelength sine waves discussed above. Integrating over frequencies and averaging with respect to the white noise produces the dynamic correlation function for the amplitudes of these sine waves [15] – see Eqs. 3.3, 3.4.

$$\langle u_p(t) u_p(0) \rangle = \frac{2k_B T}{\ell} \frac{e^{-\gamma_p^0 t / \xi_{\perp}}}{\gamma_p^0}, \quad (3.8)$$

where we have introduced

$$\gamma_p^0 = \kappa p^4 + \tau p^2, \quad (3.9)$$

so that γ_p^0/ξ_\perp is the wavenumber-dependent decay rate. There are no cross correlations between amplitudes of different normal modes.

There is a crossover between tension- and bending-dominated relaxational dynamics, set by the *tension length*

$$\ell_\tau = \sqrt{\kappa/\tau}. \quad (3.10)$$

In the long-wavelength $\lambda \gg \ell_t$ tension-dominated regime, modes have an approximate relaxation time $\tau_{\text{relax}} \sim \frac{\eta\lambda^2}{\tau \ln(\ell/a)}$. In the short-wavelength bending-dominated regime, modes have an approximate relaxation time $\tau_{\text{relax}} \sim \frac{\eta\lambda^4}{\kappa \ln(\ell/a)}$. With vanishing applied tension, one observes a very broad range of relaxation times due to the λ^4 -dependence. We now consider dynamics with the inclusion of the longitudinal spring, which mixes the filament's normal modes.

3.3 The longitudinal spring: perturbative expansion

We hereafter work in units such that $k_B T = 1$. At the end of any calculation, we must then input factors of $k_B T$ where units of energy are needed. In these units, we can use the Einstein relation

$$D = \xi_\perp^{-1} \quad (3.11)$$

to freely switch from ξ_\perp to D , the latter of which represents a diffusion constant times a length. We now return to the full model A equation of motion defined by Eq. 3.6. By using Eqs. 3.1 and 3.2, we find

$$\frac{\partial u_p}{\partial t} = -D\gamma_p^0 u_p - Dk\Delta\ell u_p + h_p + \zeta_p, \quad (3.12)$$

where $\zeta_p(t)$ and $h_p(t)$ represent noise and externally applied transverse force respectively, each absorbing a factor of D . From Eq. 3.7, we infer that equilibrium correlations of the Gaussian white noise obey the usual relation

$$\langle \zeta_p(t) \zeta_{p'}(t') \rangle = (4D/\ell) \delta_{pp'} \delta(t - t'). \quad (3.13)$$

The second term on the right hand side of Eq. 3.12, proportional to k , couples each mode (labeled by p) to changes in the total projected length of the filament, which depends on a sum over the square of amplitudes of all the dynamical modes. As a result, this term in the equation of motion is nonlinear. In order to systematically compute correlation functions in the presence of this nonlinearity, we make use of the MSRJD functional integral method [146, 4].

We start by introducing the moment generating MSRJD functional

$$Z[j, \bar{j}] = \int \mathcal{D}[i\bar{u}(x)] \mathcal{D}[u(x)] e^{-\int (\mathcal{A}(\bar{u}, u) - \bar{j}\bar{u} - ju) dx dt}, \quad (3.14)$$

with the action \mathcal{A} separated into: a Gaussian part \mathcal{A}_0 , which generates correlation functions of the spring-free system, the nonlinear and spring-dependent correction \mathcal{A}_{int} , and a term representing the external h -dependent forcing:

$$\mathcal{A}[u(x, t), \bar{u}(x, t)] = \mathcal{A}_0 + \mathcal{A}_{\text{int}} + D \int dx dt \bar{u} h. \quad (3.15)$$

The Gaussian part is

$$\mathcal{A}_0 = \int dt dx [\bar{u} (\partial_t + D(\kappa \partial_x^4 - \tau \partial_x^2)) u - D\bar{u}^2], \quad (3.16)$$

and the nonlinear interaction is

$$\mathcal{A}_{\text{int}} = -\frac{Dk}{2} \int dt dx dy \bar{u}(x, t) \frac{\partial^2 u(x, t)}{\partial x^2} \left(\frac{\partial u(y, t)}{\partial y} \right)^2. \quad (3.17)$$

For the nonlinear action, we have explicitly written out the spatial and time dependencies. Each field is evaluated at the same time (a consequence of instantaneous tension propagation), yet there are two independent spatial variables x and y (non-locality).

Finally, we recall that (n, \bar{n}) -point cumulants, representing response functions and correlation functions, are computed via functional derivatives of the logarithm of the MSRJD functional:

$$\left\langle \prod_{i,k}^{n,\bar{n}} u_i \bar{u}_k \right\rangle = \prod_{i,j}^{n,\bar{n}} \frac{\delta}{\delta j_i} \frac{\delta}{\delta \bar{j}_k} \ln Z[j, \bar{j}]|_{j=\bar{j}=0}, \quad (3.18)$$

where the brackets denote averages over the stochastic forces $\zeta(x, t)$. Specifically, by taking a derivative $\delta \langle u(x, t) \rangle / \delta h(x', t')|_{h(x', t')=0}$, we obtain the transverse linear response function:

$$\chi_{uu}(x, x'; t, t') = D \langle u(x, t) \bar{u}(x', t') \rangle. \quad (3.19)$$

The source field \bar{j} provides the same information as h . Hereafter we set $h = 0$. The response function is trivially related to the propagator $G(x, x'; t, t')$ of the theory via a factor of D :

$$G(x, x'; t, t') = D^{-1} \chi_{uu}(x, x'; t, t'). \quad (3.20)$$

We also define the dynamic or time-dependent correlation function

$$C(x, x'; t, t') = \langle u(x, t) u(x', t') \rangle, \quad (3.21)$$

hereafter referred to as the *correlator*. Given knowledge of $\chi_{uu}(x, x'; t, t')$, it can be found easily via fluctuation-dissipation theorem, so it need not be calculated independently, at least for the equilibrium dynamics that we study here.

We have chosen the Ito formulation of the Langevin equation, such that the Jacobian of our field transformation from $\zeta(x, t)$ to $u(x, t)$ is unity. This corresponds

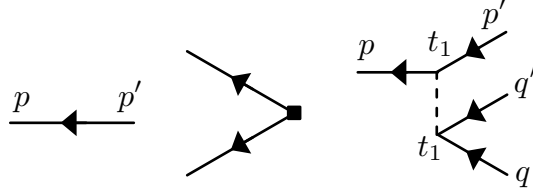


Figure 3.2: Diagrams contributing to the perturbation theory of the (u, \bar{u}) fields. The propagator (left) is a function of a single p and the time difference: $\langle u_p(t)u_{p'}(t') \rangle = \delta_{pp'}G_p^0(t - t')$. The noise vertex (middle) produces two outgoing lines, and has a coefficient D . The interaction vertex (right) is equivalent to $\frac{-Dk\ell^2}{8}p^2q^2\delta_{pp'}\delta_{qq'}$. It carries two Kronecker deltas, and depends on two wavenumbers p, q . This is a consequence of the spatial nonlocality of the nonlinear interaction. Dashed lines connect two points at equal times. In the interaction vertex (right), we associated a factor of $p^2\delta_{pp'}$ ($q^2\delta_{qq'}$) with each vertex of the dashed and solid lines, and a factor of $\frac{-Dk\ell^2}{8}$ with the dashed line itself.

to the step function continuation $\Theta(0) = 0$, and, as a result, all perturbative terms consisting of closed response loops evaluate to zero, consistent with causality. For general time ordering schemes, closed response loops can be shown to be canceled by the appropriate Jacobian factor, ensuring that the physical result is independent of discretization choice [146].

Eqs. 3.14, 3.15 enable the full machinery of diagrammatic perturbation theory in k . Expectation values with respect to the Gaussian action are denoted by the brackets $\langle \dots \rangle_0$. The diagrammatic rules are summarized in Fig. 3.2. In wavenumber space, the Gaussian propagator is proportional to a Kronecker delta $\delta_{pp'}$, and therefore depends only on a single wavenumber. The retarded (+) and advanced (-)

propagators are given by

$$G_p^{0,\pm}(t) = \frac{2}{\ell} \theta(\pm t) e^{\mp \gamma_p^0 t}, \quad (3.22)$$

and represented by a directed line from earlier to later times. The comma in the superscript emphasizes that the 0 is a label, and not related to the whether the propagator is advanced or retarded. The step function allows us to identify outgoing lines as \bar{u} fields and incoming lines as u fields.

One may further define an undirected line to be the bare correlator

$$C^0(x, y, t) = \langle u(x, t) u(y, 0) \rangle_0. \quad (3.23)$$

However, since the bare correlator is related to the transverse linear response function via fluctuation-dissipation theorem, we can avoid introducing the additional undirected propagator by treating the noise term $\sim D\bar{u}^2$ term in Eq. 3.16 as a new vertex [146] denoted by the filled square in the middle of Fig. 3.2.

The spring-induced nonlinearity generates a spatially nonlocal, but instantaneous vertex. As a result, the bare vertex shown in Fig. 3.2 carries two independent Kronecker deltas in wavenumber and a delta function in time (dashed line), as well as four factors of wavenumber. See the caption of Fig. 3.2 for further details. We can easily switch from the time domain to the frequency domain, by Fourier transforming the fields

$$u_p(t) = \int_{-\infty}^{\infty} \frac{d\omega}{2\pi} u_p(\omega) e^{-i\omega t}, \quad (3.24)$$

and imposing frequency conservation at each vertex.

Using these diagrammatic rules, we compute the k -dependent corrections to the propagator to two-loop order, which is also second order in k . Generally, in perturbation theory these corrections can be neatly grouped into a self-energy $\Sigma_p(\omega)$,

defined by the relation $\langle G_p(\omega) \rangle^{-1} = (G_p^0)^{-1}(\omega) - \Sigma_p(\omega)$ [4]. The physical interpretation of this quantity is found in the shift of the bare decay rate from Eq. 3.9, so that $\gamma_p^0 \rightarrow \gamma_p^0 - \frac{2}{D\ell}\Sigma_p(\omega)$. As such, we define the adjusted self-energy

$$\tilde{\Sigma}_p(\omega) = \frac{2}{D\ell}\Sigma_p(\omega), \quad (3.25)$$

which is precisely the shift in γ_p^0 .

All the necessary diagrams for this calculation are shown in Fig. 3.3, and we refer to them hereafter by their label in that figure, beginning with A1 at the top and continuing to D4 in the bottom right. They are individually calculated in Appendix B.1. Here, we report the full two-loop self-energy (writing out $k_B T$ explicitly for clarity):

$$\begin{aligned} \tilde{\Sigma}_{\bar{p}}(\Omega) &= -\frac{k k_B T \bar{p}^2}{\kappa} \left[\frac{1}{\bar{p}^2 + 1} + \frac{1}{2} \sum_{\bar{q}} \frac{1}{\bar{q}^2 + 1} \right] \\ &+ \frac{k^2 k_B^2 T^2}{\kappa \tau^2} \left[\frac{\bar{p}^2}{2(\bar{p}^2 + 1)^3} + \frac{3\bar{p}^4}{(\bar{p}^2 + 1)^2(-i\Omega + 3\bar{p}^2(\bar{p}^2 + 1))} \right. \\ &+ \frac{1}{2} \frac{\bar{p}^2}{(\bar{p}^2 + 1)} \sum_{\bar{q}} \frac{1}{(\bar{q}^2 + 1)^2} \left(1 - \frac{-i\Omega}{-i\Omega + 2\bar{q}^2(\bar{q}^2 + 1) + \gamma_{\bar{p}}} \right) \\ &\left. + \frac{\bar{p}^2}{4} \sum_{\bar{q}} \frac{1}{\bar{q}^2 + 1} \sum_{\bar{q}} \frac{1}{(\bar{q}^2 + 1)^2} \right]. \end{aligned} \quad (3.26)$$

We have introduced dimensionless wavenumbers $\bar{p} = p\sqrt{\kappa/\tau} = p\ell_\tau$ and frequencies $\Omega = \frac{\omega\kappa}{D\tau^2} = \omega/\omega^*$. These units are convenient, provided that the tension is not so small that $\ell_\tau \approx \ell$, but they are primarily used in order to aid in a qualitative analysis of Eq. 3.26. Physically, these units correspond to the distance from the spring-free bending-tension dominated transition. For an alternative scheme valid at small τ , see Eq. B.10.

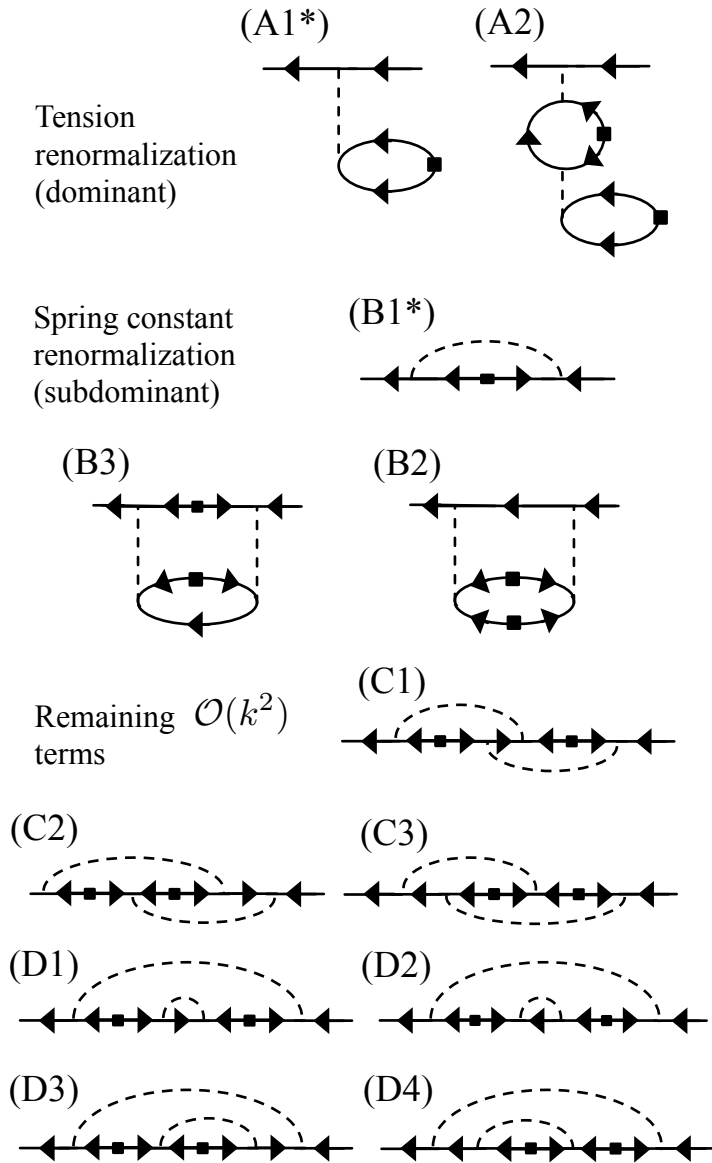


Figure 3.3: All diagrams contributing to the self-energy (see definition preceding Eq. 3.25) through $\mathcal{O}(k^2)$. There are two $\mathcal{O}(k)$ contributions marked by an asterisk. For detailed calculations, see Appendix B.1. Diagrams A1 and B1 are later used to renormalize tension (Eq. 3.34) and self-consistently compute the self-energy (Eq. 3.28).

The $\mathcal{O}(k)$ correction is negative, and proportional to \bar{p}^2 , which tells us that it renormalizes the effective tension to a larger value. This is expected, as the spring stiffens the filament to elongation, causing it relax faster. To analyze the effects of the spring beyond first order, we categorize the two-loop self-energy into three types of contributions, beginning with the most dominant. The first group consists of type A diagrams in Fig. 3.3. These are $\sim \bar{p}^2$ so they become appreciable at large wavenumber. Due to the summations, they also grow with system size, *i.e.*, filament length. As we will see in Sec. 3.4.1 (and commented on more in Appendix B.1), these correspond to a renormalization of the tension, and may be eliminated by using a self-consistent approach to the Green's function.

The second group consists of the type B diagrams in Fig. 3.3. After τ renormalization, these are the next most important class of diagrams. We will later find that they correspond to renormalization of the spring constant k . At large \bar{p} , they plateau to a constant value, and, at small \bar{p} , they decay as \bar{p}^2 . These corrections are important for $\bar{p} \leq 1$. These contributions are largest at zero frequency, where they acquire a prefactor $\sim \sum_{\bar{q}}(\bar{q}^2 + 1)^{-2}$. But this remains small when compared to the type A diagrams, which are proportional to $\sum_{\bar{q}}(\bar{q}^2 + 1)^{-1}$. In general, we will find (see Sec. 3.4.2) that any diagram containing a solid loop with n outgoing dashed lines will be proportional to a summation $\sum_{\bar{q}}(\bar{q}^2 + 1)^{-n}$, and thus represent increasingly smaller contributions.

The third and final group consists of both type C and D diagrams of Fig. 3.3. These diagrams have a single solid line with crossed (type C) or uncrossed (type D) dashed lines. At large \bar{p} , these vanish and are therefore small compared to the diagrams of the first (A) and second groups (B). At small \bar{p} , they go to zero as \bar{p}^2 , however, they lack a summation compared to the other terms in Fig. 3.3 and are

thus still smaller. At $\mathcal{O}(k^2)$, these summations are $\sim \sum_{\bar{p}} \bar{p}^{-2}$. As a result, we infer that the missing summations in type C and D diagrams cause them to be about an order of magnitude smaller than the contributions from the other $\mathcal{O}(k^2)$ diagrams. Furthermore, at high frequency, the contributions from the crossed (C) diagrams are smaller than those from non-crossing (D) diagrams. This suggests that we may ignore crossed diagrams in any self-consistent treatment of the dynamics, as described below. This distinction between the crossing and non-crossing diagrams is analogous to impurity scattering in condensed matter, where one also finds that crossing diagrams in electron impurity scattering calculations may be safely ignored [130, 163].

We now use the previous analysis to develop a self-consistent approximation for the propagator of Eq. 3.20 in frequency/wavenumber space. The principal effect of the longitudinal spring is to renormalize tension. The details of that process will be shown in Sec. 3.4.1. We account for this by defining

$$\gamma_p = \kappa p^4 + \tau_{\text{R}} p^2, \quad (3.27)$$

which everywhere replaces γ_p^0 . τ_{R} is the renormalized tension due to the longitudinal spring. We next incorporate the remaining first order correction (diagram A1), by considering it as the first term in a series of diagrams that contain a single solid line, with no crossed dashed lines (the $\mathcal{O}(k^2)$ term in this series consists of all type D diagrams in Fig. 3.3). The infinite summation can quickly be achieved by demanding that the self energy is equal to the contribution in diagram A1, so long as we replace the bare propagators by a dressed ones. This leads to the self-consistent equation

$$\tilde{\Sigma}_p^{\text{NCA}}(\omega) = -\frac{k k_{\text{B}} T p^4}{\gamma_p - \tilde{\Sigma}_p^{\text{NCA}}(\omega)}, \quad (3.28)$$

known as the non-crossing approximation (NCA). This is certainly correct to $\mathcal{O}(k)$, and as $\omega \rightarrow \infty$ becomes precise to all orders in k . Since this is a self-consistent

equation, we are free to extend k to large values where we can see its effect. Eq. 3.28 is algebraic, and we easily find the solution

$$\tilde{\Sigma}_p^{\text{NCA}}(\omega) = \frac{\gamma_p}{2} \left(1 - \sqrt{1 + \frac{4kk_{\text{B}}Tp^4}{\gamma_p^2}} \right). \quad (3.29)$$

The simplicity of this result is a direct consequence of the spatial nonlocality of our interaction; since dashed lines do not carry wavenumber, there is no summation over modes in diagram A1. From $\tilde{\Sigma}_p^{\text{NCA}}(\omega)$, we find the NCA transverse linear response function

$$\chi_p^{\text{NCA}}(\omega) = \frac{2D/\ell}{-i\omega + \frac{1}{2}D\gamma_p \left(1 + \sqrt{1 + 4kk_{\text{B}}Tp^4/\gamma_p^2} \right)} \quad (3.30)$$

Using the fluctuation-dissipation theorem and reinserting $k_{\text{B}}T$ where necessary to work in physical units, we obtain the dynamic correlator

$$C_p^{\text{NCA}}(\omega) = \frac{4k_{\text{B}}T/\xi_{\perp}\ell}{\omega^2 + \frac{\gamma_p^2}{4\xi_{\perp}^2} \left(1 + \sqrt{1 + 4kk_{\text{B}}Tp^4/\gamma_p^2} \right)^2}. \quad (3.31)$$

At low tension, we intuitively expect the effect of the longitudinal spring to be stronger. We thus seek units in which the tension can easily be taken to small values. Per the discussion of Sec. 3.2.2, at low wavenumber, the system is in a tension-dominated regime. Accordingly, we switch to a dimensionless length scale by factoring out the wavenumber of the lowest mode $p_1 = \pi/\ell$. We also adopt a dimensionless tension, spring constant, and frequency:

$$\phi = \frac{\tau\ell^2}{\kappa\pi^2}, \quad (3.32a)$$

$$\bar{k} = \frac{kk_{\text{B}}T\ell^4}{\kappa^2\pi^4}, \quad (3.32b)$$

$$\bar{\omega} = \frac{\omega\xi_{\perp}\ell^4}{\kappa\pi^4}. \quad (3.32c)$$

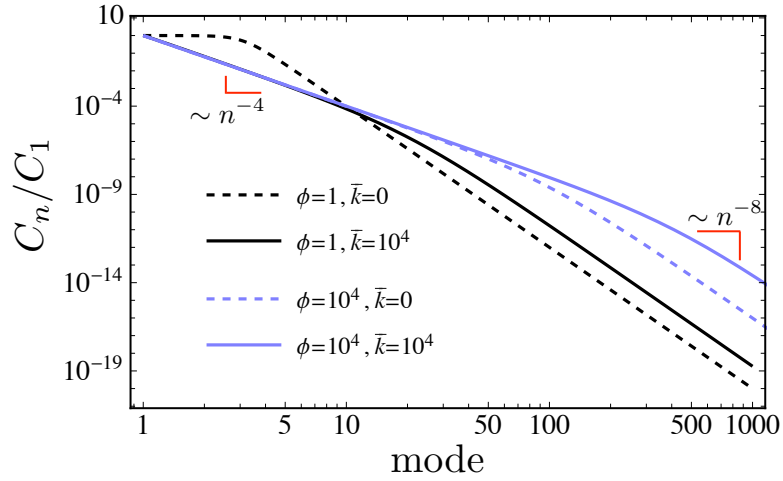


Figure 3.4: (color online) NCA dynamical correlation function normalized by its first mode at both low (black) and high (blue) tension in the presence (solid) or absence (dashed) of the longitudinal spring. $\bar{\omega} = 100$. The solid black curve overlaps with the solid blue curve at low mode numbers, indicating that the spring generates tension in the absence of any pre-existing tension, given in a nondimensionalized form as ϕ . In the presence applied tension $\phi > 0$, the spring increases the effective tension, pushing the transition from tension- to bending-governed fluctuations to higher mode numbers (blue curves).

To compute $C_p(\omega)$, we must further calculate tension renormalization. In terms of ϕ , this amounts to the replacement

$$\phi_R = \phi + \Delta\phi, \quad (3.33)$$

where $\Delta\phi$ is defined by the self-consistent equation

$$\Delta\phi = \frac{\bar{k}}{2} \sum_{n=1}^{\infty} \frac{1}{n^2 + \phi + \Delta\phi}. \quad (3.34)$$

This equation can be derived by approximating the entire self-energy correction by the dominate diagram A2 in Fig. 3.3, provided we replace the loop propagator with the dressed one. This approximation is discussed more fully in the context of the mean-field theory in Sec. 3.4.1. In terms of mode number n , we find the correlator to be

$$C_n^{\text{NCA}}(\bar{\omega}) = \frac{4k_B T \xi_{\perp} \ell^7 / \kappa^2 \pi^8}{\bar{\omega}^2 + \left(\frac{1}{2} n^2 (n^2 + \phi_R) \left(1 + \sqrt{1 + \frac{4\bar{k}}{(n^2 + \phi_R)^2}} \right) \right)^2}. \quad (3.35)$$

In Fig. 3.4, we plot the NCA correlator as a function of wavenumber. Generically there are three regimes going from low to high mode number. There is a low wavenumber plateau transitioning into a n^{-4} decay, followed by an n^{-8} decay at sufficiently high mode numbers. The effect of the spring is to shift these transitions to lower mode number. For sufficiently high spring constants, the plateau regime may disappear entirely as shown by the (blue and black) solid curves in the figure. The condition for the appearance of the plateau is that $\bar{\omega} > \max\{n^4/4, \phi/4\}$ for some $n \geq 1$. The principal effect of the spring is still tension renormalization. Even as $\phi \rightarrow 0$, the longitudinal spring ensures that the filament still behaves as if it were under tension. For finite values of the applied tension, the effect of the spring still increases the total effective or renormalized tension, moving the transition to higher-frequency, bending-dominated fluctuations to still higher modes. The fact that the

mode where the fluctuations change from being stretching- to bending-dominated moves in response to the external spring suggests that the effects of even a weak spring will be most easily observed near this tension-to-bending transition ($p = \ell_\tau^{-1}$) of the spring-free model.

In Fig. 3.5, we look at how varying the applied tension and spring constant shift the lowest mode $C_1(\omega)$. If the spring does not significantly alter $\Delta\ell$, then the tension $k\Delta\ell$ created by the spring increases linearly in k . However, due to the self-consistent condition, at high k , $\Delta\ell$ diminishes, causing tension to increase as $k^{2/3}$. We discuss this scaling more fully in Sec. 3.4.1. As a result, the correlator decays like $\bar{k}^{-4/3}$, as shown in the top panel of Fig. 3.5. The transition occurs when $k^* = \tau/\Delta\ell$, which we approximate as $k^* \approx 12\kappa\tau/k_B T\ell^2$ by replacing $\Delta\ell$ with its small tension and spring-free result [98].

We can also see the transition in the correlation function by keeping k constant and varying tension. The correlator transitions from being ϕ -independent to decaying as ϕ^{-2} with increasing ϕ , as shown in the bottom panel of Fig. 3.5. The dependence of the correlator upon applied tension is the same as in the spring-free model. The transition occurs once ϕ is greater than both $4\bar{\omega}^2$ (for the lowest mode) and the renormalized tension $\Delta\phi$, due to the spring. As a result, the spring washes out the effect of small applied tensions, replacing the overall tension with its renormalized value. We now turn to a justification of the approximations outlined above, as well as derive new results concerning projected length fluctuations. Our main tool will be functional techniques using the MSRJD formalism.

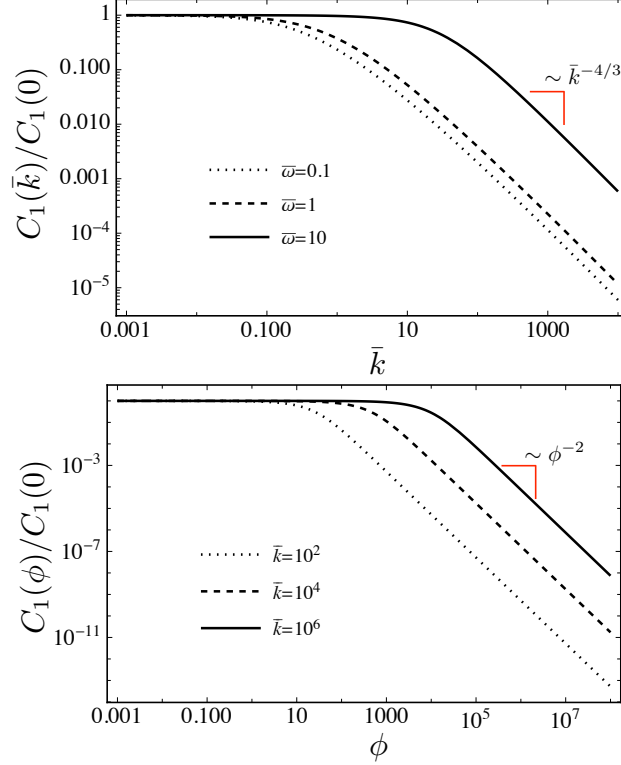


Figure 3.5: (color online) Lowest mode of the dynamic correlation function vs. (top) spring constant and (bottom) applied tension. The top panel is evaluated at low tension, $\phi = 10^{-2}$, and the bottom at $\bar{\omega} = 1$. At large \bar{k} , the effective tension grows sublinearly as $\sim \bar{k}^{2/3}$, leading to the $\bar{k}^{-4/3}$ dependence of C_1 . In the bottom panel, the lowest mode dynamic correlation function decays as ϕ^{-2} , which is identical to the spring-free $k = 0$ case. The transition to the ϕ^{-2} decay occurs at tensions higher than $\phi \approx \bar{k}\langle\Delta\ell\rangle$.

3.4 Projected length auxiliary field theory

The spatially nonlocal theory presented here was previously examined in equilibrium, where the nonlocal aspect allowed for a complete resummation of diagrams contributing to the two point function [71]. In the dynamical version, however, this resummation fails. The previous calculation of equal-time correlation functions allowed for a great simplification due to the fact that all of these diagrams collapsed into one of two groups - see Ref. [71]. The calculation of dynamical correlations here, however, introduces a time associated with each interaction. This time ordering makes all the previously identical diagrams from Ref. [71] distinct. Since, in the dynamical theory, dashed lines carry frequency, there are an infinite number of inequivalent single-line diagrams, differentiated by the arrangement of dashed-line contractions (for example, compare the class C and D diagrams in Fig. 3.3).

Despite this complication, we may still proceed along the lines of Ref. [71]. Inspection of Eq. 3.2 suggests that the Hamiltonian is more naturally expressed in terms of $\Delta\ell(t)$ rather than $u(x, t)$. This will allow us to more easily compute projected length fluctuations $\langle\Delta\ell(t)\Delta\ell(t')\rangle$, which are relevant for experiments measuring the dynamic shear modulus. As a tradeoff, solving for the two-point function, $\langle u_p(\omega)u_{p'}(\omega')\rangle$, will be harder.

In order to change functional integration variables from $u(x, t) \rightarrow \Delta\ell(t)$, we first employ a Hubbard-Stratonovich transformation to write the quartic interaction, $\frac{1}{2}k\Delta\ell^2$, in terms of an interaction with auxiliary fields $\lambda, \bar{\lambda}$. This amounts to using the identity [164]

$$e^{-\int dt \bar{z}z} = \int \mathcal{D}(\bar{\lambda}, \lambda) e^{-\int [\bar{\lambda}\lambda - \bar{z}\lambda - \bar{\lambda}z] dt} \quad (3.36)$$

in Eq. 3.14, while making the identifications $\bar{z} = -Dk \int \bar{u}u'' dx$ and $z = \Delta\ell =$

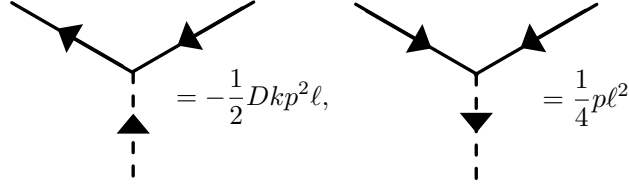


Figure 3.6: $\lambda \bar{u} u$ and $\bar{\lambda} u u$ interactions. The Hubbard-Stratonovich transformation cuts the four-point vertex into two three-point vertices. Dashed lines are now directed, with λ incoming and $\bar{\lambda}$ outgoing.

$\frac{1}{2} \int u'^2 dx$. Diagrammatically, this transformation severs the undirected dashed line into the two three-point vertices depicted in Fig. 3.6. This transformation is essentially a δ -function, acting to assign the change in projected length to the variable $\lambda(t)$. We may alternatively arrive at this step by introducing a Lagrange multiplier into the Hamiltonian, writing down the Langevin equation, then finding the MSRJD functional.

We now add additional source terms $\int dt j_\lambda(t) \lambda(t) + \bar{j}_\lambda \bar{\lambda}(t)$ to the expanded functional, which will generate correlations of the auxiliary $\lambda, \bar{\lambda}$ fields. To understand the physical meaning of these new auxiliary fields, we take the functional derivatives $\frac{\delta}{\delta j_\lambda}, \frac{\delta}{\delta \bar{j}_\lambda}$ of the generating functional before and after integration over $(\bar{\lambda}, \lambda)$, and compare the results. $\delta Z[j_\lambda, \bar{j}_\lambda] / \delta j_\lambda$ produces the moments of $\Delta \ell(t)$. As a result, there is a one-to-one correspondence between expectation values of $\lambda(t)$ and $\Delta \ell(t)$. That is, for any N -point correlation

$$\left\langle \prod_i^N \lambda(t_i) \right\rangle = \left\langle \prod_i^N \Delta \ell(t_i) \right\rangle. \quad (3.37)$$

$\bar{\lambda}$ is related to the linear response of the projected length to an applied tension.

For a small change in applied tension $\Delta\tau$, this is defined as

$$\chi_{\Delta\ell}(t, t') = \left. \frac{\delta\Delta\ell(t)}{\delta\Delta\tau(t')} \right|_{\Delta\tau=0}. \quad (3.38)$$

Eq. 3.36 shows that $\bar{\lambda}$ appears conjugate to $\Delta\ell$, in the same manner as would a time-dependent applied tension. Applying two derivatives $\left. \frac{\delta^2 \ln Z}{\delta j_\lambda \delta \bar{j}_\lambda} \right|_{j_\lambda = \bar{j}_\lambda = 0}$ before and after integration over auxiliary fields, and then comparing the results, we find the linear response is expressed in terms of the auxiliary fields as

$$\chi_{\Delta\ell}(t, t') = k^{-1}(1 - \langle \lambda(t) \bar{\lambda}(t') \rangle). \quad (3.39)$$

As a result of the Hubbard-Stratonovich transformation, the action \mathcal{A} now depends on four fields $\mathcal{A}[\bar{\lambda}, \lambda, \bar{u}, u]$. It is quadratic in the fields \bar{u}, u , so we may integrate them out. Doing so, yields the effective action

$$\mathcal{A}[\bar{\lambda}, \lambda, \bar{j}, j] = \int \bar{\lambda} \lambda dt + \frac{1}{2} \text{Tr} \ln \mathbf{G}^{-1} - \frac{1}{2} \int \mathbf{j}^T \mathbf{G} \mathbf{j} dt, \quad (3.40a)$$

$$\mathbf{G}_p^{-1} = \begin{pmatrix} -2D\mathbb{1} & (G_p^+)^{-1} \\ (G_p^-)^{-1} & -p^2 \bar{\lambda} \mathbb{1} \end{pmatrix} \quad (3.40b)$$

plus $\lambda, \bar{\lambda}$ -dependent source terms. In the above expressions, the lower case, bold letters stand for the vectors of the fields $\mathbf{u} = (\bar{u}, u)$, $\boldsymbol{\lambda} = (\bar{\lambda}, \lambda)$, and $\mathbf{j} = (\bar{j}, j)$. The trace runs over fields. It also includes a summation over wavenumbers p . We have defined the 2x2 block matrix (since its components are operators) \mathbf{G}^{-1} in terms of the advanced/retarded propagators

$$G_p^\pm(t, t') = G_p^{0,\pm}(t) e^{\mp Dkp^2 \int_{t'}^t \lambda(t'') dt''}. \quad (3.41)$$

Since \mathcal{A} retains its dependence on the source terms \mathbf{j} , we may still generate correlations of the transverse displacement field via functional differentiation, as

defined in Eq. 3.18. As expected, correlations $\langle \mathbf{u}\mathbf{u} \rangle$ depend on expectation values of operator inverses containing stochastic fields $\boldsymbol{\lambda}$. We have traded calculating a simple observable with a complex probability functional for a nonlinear observable with a simple probability functional. Correlations with respect to $\Delta\ell$, on the other hand, are evaluated at $\mathbf{j} = 0$ and are tractable, provided we can simplify the trace-log appearing in \mathcal{A} .

Since the spring constant k appears only in the combination $\sim Dkp^2\lambda$, we may shift integration variables $\lambda \rightarrow \lambda/Dk$, thereby putting all of the k dependence in \mathcal{A} into the first term $\int dt \bar{\lambda}\lambda/Dk$. As $k \rightarrow 0$, \mathcal{A} oscillates wildly, indicating that saddle-point evaluation of the functional integral becomes exact. We may then carry out a controlled small k expansion of \mathcal{A} about its saddle-point solution $(\bar{\lambda}_0, \lambda_0)$ plus fluctuations. Incidentally, the saddle-point solution λ_0 is *precisely* the average $\langle \Delta\ell(t) \rangle$, regardless of whether or not k is small.

3.4.1 Mean field theory

We investigate the saddle-point solution corresponding to the effective action Eq. 3.40a, which becomes exact as $k \rightarrow 0$. We denote the saddle point solutions for the auxiliary fields by λ_0 and $\bar{\lambda}_0$. We will find that the saddle-point solution corresponds to a type of dynamical “mean-field theory” (MFT), and henceforth refer to $\bar{\lambda}_0, \lambda_0$ as the mean-field solutions.

The saddle-point equations are

$$\delta\mathcal{A}/\delta\lambda = \delta\mathcal{A}/\delta\bar{\lambda} = 0, \tag{3.42}$$

evaluated at $\lambda = \lambda_0$ and $\bar{\lambda} = \bar{\lambda}_0$. Functional differentiation of the trace-log appearing

in \mathcal{A} is carried out in the standard way [4], using $\delta_{\bar{\lambda}} \text{Tr} \ln \mathbf{G}^{-1} = \text{Tr} \left(\hat{\mathbf{G}} \delta_{\bar{\lambda}} \hat{\mathbf{G}}^{-1} \right)$. As $\bar{\lambda}$ appears only in the (22) component of \mathbf{G}^{-1} , functional differentiation yields a matrix with one in the (22) component, and zeroes elsewhere. Taking the matrix product with \mathbf{G} and performing the trace yields the (22) component of \mathbf{G} . We emphasize again that \mathbf{G}^{-1} is really a 2x2 block matrix, with each block representing an operator. Since \mathbf{G}^{-1} is not diagonal in either the time or frequency domains, we cannot trivially invert it. Instead, we determine \mathbf{G} via its defining equation $(\hat{\mathbf{G}}^{-1})_{ik} \hat{\mathbf{G}}_{kj} = \delta_{ij} \delta(t-t')$. This yields the result $G_{22} = (\mathbb{1} - p^2 \hat{C}_p \bar{\lambda}_0)^{-1} \hat{C}_p$.

Since $\delta \hat{\mathbf{G}} / \delta \lambda = 0$, the first saddle-point equation is trivially

$$\bar{\lambda}_0(t) = 0. \quad (3.43)$$

The second saddle-point equation can now be easily found by setting $\bar{\lambda}_0 = 0$. We find the second saddle-point equation

$$\lambda_0(t) = D \sum_p p^2 \int_{-\infty}^t [G_p^+(t, t')]^2 dt', \quad (3.44)$$

where $G_p^+(t, t')$ was defined in Eq. 3.41. This depends only on λ_0 , and we call it the mean-field condition.

There are two alternative ways to interpret this result, each of which add to our physical understanding. First, in the context of the (\bar{u}, u) diagrammatic perturbation theory defined by Fig. 3.2, we can recover the mean-field condition by summing over all one-correlator loop corrections to the propagator. These contributions can be grouped into a mean-field self energy $\Sigma_p^{\text{MFT}}(t)$. We then demand that $\Sigma_p^{\text{MFT}}(t)$ is equivalent to diagram A1 in Fig. 3.3, when the loop correlator is replaced by a dressed correlator. Looking for a solution of the form $\tilde{\Sigma}_p^{\text{MFT}}(t) = -\bar{k} p^2 \lambda_0$ reproduces the mean-field condition. This observation suggests that the mean-field theory is

the leading term in an expansion of $\mathcal{A}[\bar{\lambda}, \lambda]$, determined by the maximal number of dashed lines emanating from a closed, solid line loop. We call a subdiagram with n outgoing dashed lines an *n-bubble*. The suggestion turns out to be accurate, and is elaborated on more in Sec. 3.4.2.

Second, we may arrive at Eq. 3.44 by employing a type of *mean-field* approximation, in which we make the replacement: $\Delta\ell^2 \rightarrow 2\langle\Delta\ell\rangle\Delta\ell$ in the Hamiltonian – see Eq. 3.2. The angled brackets denote averages with respect to the noise. Looking at this replacement more closely, we note that the equilibrium average $\langle\Delta\ell(t)\rangle$ must be a constant in time. Here, however, the averaging is applied with respect only to the noise, and not to the initial configuration of the filament. In that case, the average $\langle\Delta\ell(t)\rangle$ can evolve in time from any particular initial condition. The mean-field theory is capable of describing the relaxation of this variable to its equilibrium value. For example, we can consider a situation where the filament is pulled starting at time $t = 0$.

Returning to our mean field approximation, the MFT Hamiltonian is now linear. The resulting Langevin equation is also linear, and can be solved for $u_p(t)$ in terms of the noise $\zeta_p(t)$ and $\langle\Delta\ell(t)\rangle$. Imposing the self-consistency condition given by the definition in Eq. 3.1 of projected length, and identifying $\lambda_0(t) = \langle\Delta\ell(t)\rangle$, we reproduce the mean-field condition Eq. 3.44. Physically, the mean-field approximation assumes that the normal modes respond only to the change in the averaged projected length, and ignore changes in $\Delta\ell$ due to fluctuations of other normal modes. This approach is actually a mean-field *differential* equation for the function $\lambda_0(t)$. The mean-field theory is neatly summarized as the following Langevin equation

$$\frac{\partial u_p(t)}{\partial t} = -D [\gamma_p^0 + kp^2\lambda_0(t)] u_p(t) + \zeta_p(t), \quad (3.45a)$$

with the condition

$$\lambda_0(t) = \frac{\ell}{4} \sum_p p^2 \langle u_p^2(t) \rangle. \quad (3.45b)$$

Combining these two equations results in the integral equation given by Eq. 3.44 for $\lambda_0(t)$. When solving the integral equation, it is more convenient to work with the time derivative of $\lambda_0(t)$. Following the notation of Hallatschek *et al.* [46, 48, 50], we hereafter refer to Eq. 3.44 as a partial-integro differential equation (PIDE). The quantity $k\lambda_0(t)$ acts as a time-dependent tension, whose value depends self-consistently on the instantaneous conformation of the filament. Our model appears similar to those describing nonlinear tension propagation along inextensible filaments [138, 46, 48, 50]. This is true for both the ordinary and multiscale perturbation theory [48]. These authors obtain a PIDE similar to ours, where our $\lambda_0(t)$ is analogous to their stored thermal length $\langle \varrho(t) \rangle$. Our analysis differs from the previous work in that the inherent longitudinal compliance of the system is concentrated in the external longitudinal spring, rather than the extensional deformation of the filament. The longitudinal spring responds only to a particular, collective degree of freedom of the system – the end-to-end length. Moreover, the longitudinal spring constant can be changed arbitrarily for a filament with fixed elastic compliance, which provides more freedom for exploration.

When comparing our analysis to the multiscale perturbation theory PIDE, the key distinction is that our $\lambda_0(t)$ does not have spatial dependence. Theories of tension propagation in untensed and tensed filaments [138, 58, 116] allow for a finite propagation speed of tension, which requires that the longitudinal extension be spatially dependent. In either case, provided we are looking at filaments short enough that we may neglect the finite speed of tension propagation, our results should hold.

The filament length upper bound occurs roughly when the total longitudinal frictional force is equal to the forcing applied at the boundary. This, in turn, defines a time-dependent length scale $\ell_{\parallel}(t)$ beyond which filament segments are set into longitudinal motion due to tension propagation. This length scale is to be compared to the characteristic length $\ell_{\perp}(t)$ of transverse undulations. Previous authors have shown that the ratio $\ell_{\parallel}(t)/\ell_{\perp}(t) \sim (\ell_p/\ell)^{1/2}$, which in our stiff filament approximation ensures that we may neglect tension propagation [48].

In Eq. 3.53, we show the predicted response function of the end-to-end distance in the presence of prestress. While the projected length fluctuations in the absence of prestress have been studied [40, 108, 45], there has not been an explicit discussion of the problem with prestress¹. We leave details of the evaluation of $\lambda_0(t)$ to Appendix B.2, and here discuss the results. In the long time limit, $\lambda_0(t)$ must approach its equilibrium configuration, a constant λ_0 . Writing $\lambda_0(t) = Dk\lambda_0$, we find λ_0 obeys the self-consistent equation (restoring $k_B T$ for the moment for ease of comparison)

$$\lambda_0 = \frac{k_B T}{2} \sum_p \frac{1}{\kappa p^2 + \tau + k\lambda_0}, \quad (3.46)$$

which can be interpreted as a renormalization of the tension $\tau \rightarrow \tau + k\langle\Delta\ell\rangle$. In terms of the dimensionless tension ϕ (see Eq. 3.32a), this is expressed as the shift $\phi \rightarrow \phi + \Delta\phi$, where $\Delta\phi$ satisfies the MFT equation in Eq. 3.34. The MFT dynamics of a filament attached to a longitudinal spring in equilibrium are thus the same as for a semiflexible filament under tension, provided we renormalize tension.

The time-dependent $\lambda_0(t)$ solution is determined by its initial condition. We

¹The response of unstressed filaments in an equilibrium ensemble to an applied tension at $t = 0$ has been studied [45, 48], and incorrectly extended to filament fluctuations under prestress via fluctuation dissipation theorem [15]. The response is not in the linear forcing regime, and thereby the fluctuation dissipation theorem does not hold

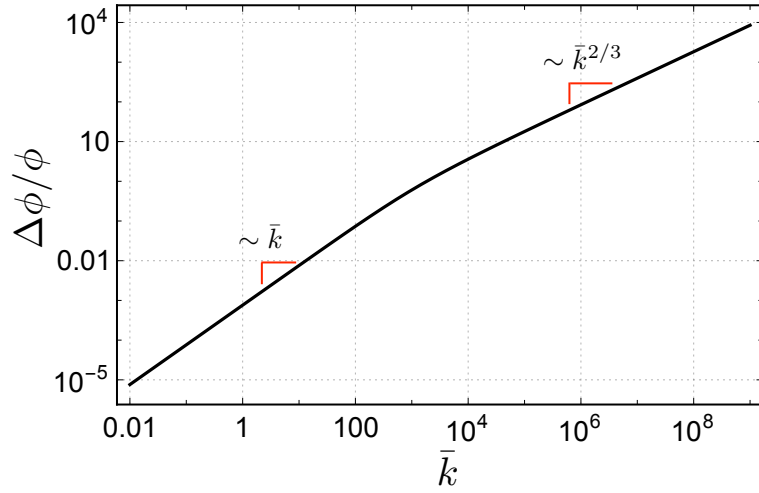


Figure 3.7: (color online) Growth of additive tension renormalization $\Delta\phi$ as a function of the dimensionless spring constant \bar{k} . $\phi = 100$. At $k = \tau/\Delta\ell_0$, we can no longer approximate $\Delta\ell$ as being k -independent. It decays like $k^{-1/3}$, leading to the shift to $\bar{k}^{2/3}$ growth in $\Delta\phi$.

consider the case where the filament is initially in equilibrium with the longitudinal spring, then at $t = 0$, we apply a small additional tension $\delta f(t)$ to an already tensed filament with tension $\tau \gg \delta f(t)$. In Appendix B.2, we derive the general solution for this situation. We define the change in the projected length from its equilibrium value,

$$\delta\lambda_0(t) = \lambda_0(t) - \lambda_0. \quad (3.47)$$

At $t = 0$, $\delta\lambda_0(t)$ vanishes, and at $t = \infty$ it must plateau to a constant as the system again reaches a new equilibrium. The Laplace transform $\delta\lambda_0(z)$ obeys the equation

$$\delta\lambda_0(z) = -\frac{\tilde{M}(z)}{1 + k\tilde{M}(z)/z}\delta F(z), \quad (3.48)$$

where the kernel $\tilde{M}(z)$ is defined in Eq. B.26. The function $\delta F(z)$ is the Laplace transform of the time-integrated applied tension defined in Eq. B.19. The negative sign arises because putting a filament under tension causes it to extend, thereby increasing total projected length, and thus decreasing $\Delta\ell$.

We now examine two cases:

$$\delta f(t) = \begin{cases} \text{oscillating:} & f \sin \omega t \\ \text{constant:} & f \end{cases}, \quad (3.49)$$

corresponding to oscillatory and constant applied tensions respectively. These lead to the Laplace-transformed integrated tensions

$$\delta F(z) = \begin{cases} \text{oscillating:} & f(z/\omega)/(z^2 + \omega^2) \\ \text{constant:} & f/z^2 \end{cases}. \quad (3.50)$$

The Laplace transform of the MFT longitudinal linear response is trivially related to $\delta\lambda_0(z)$:

$$\chi_{\Delta\ell}(z) = \delta\lambda_0(z)/f. \quad (3.51)$$

The remaining step is to take the inverse Laplace transformation in both cases.

We first discuss the oscillatory solution. In the long time limit, only residues corresponding to the purely imaginary poles will remain. The only contributing poles are due to $\delta F(z)$, which occur at $z = \pm i\omega$. We can thus substitute $\chi_{\Delta\ell}(z \rightarrow -i\omega)$ to obtain the long-time oscillatory solution. An alternative derivation is presented later in Sec. 3.4.2 using the MSRJD formalism. Comparing $\tilde{M}(-i\omega)$ with $\Pi^+(\omega)$ (defined later in Eq. 3.61), and $\chi_{\Delta\ell}(z)$ with the later MSRJD result in Eq. 3.39, we observe that the MFT Langevin equation exactly reproduces the more rigorous MSRJD analysis. We thus postulate (but do not prove in this chapter) that the MFT Langevin equation is capable of providing the exact correlations $\langle \Delta\ell(t_1)\dots\Delta\ell(t_N) \rangle$ for any product of N $\lambda_0(t)$ fields.

The p summation appearing in the kernel $\tilde{M}(z)$ (Eq. B.26) can be performed, but is unwieldy. It is easily performed numerically. We used that numerical summation to plot $\delta\langle\Delta\ell\rangle/\delta f$ in Fig. 3.8. Analytically, we look at the long and short time limits, and then comment on the transition between the two. Long/short times correspond to small/large z respectively. At long times, $\tilde{M}(z \rightarrow 0) \sim z$, while at short times $\tilde{M}(z \rightarrow \infty) \sim z^{1/4}$. The long-time limit leads to a constant value λ_0 , which is determined by the self-consistent Eq. 3.46 with τ replaced by $\tau + f$.

At short times, z is large, and so the factor of $k\tilde{M}(z)/z \sim z^{-3/4}$ is negligible compared to 1. We find the simpler expression

$$\chi_{\Delta\ell}(z \gg 1) = -\frac{\tilde{M}(z)}{z^2}. \quad (3.52)$$

The inverse Laplace transform yields

$$\chi_{\Delta\ell}(t \ll 1) = \frac{k_B T}{2} \sum_p \frac{e^{-2Dp^2 t(\kappa p^2 + \tau)} - 1}{(\kappa p^2 + \tau)^2} \quad (3.53)$$

This is precisely the spring-free result for the longitudinal linear response of a tensed filament.

To extract the short-time behavior, we replace the summation with an integration, extend the limits of integration from 0 to ∞ , and make the variable substitution $p \rightarrow p(2D\kappa t)^{1/4}$. At small t , the p^4 bending terms in the exponent are dominant, leading to

$$\chi_{\Delta\ell}(t \ll 1) \approx \frac{k_B T \ell}{2\pi\kappa^2} (2D\kappa t)^{3/4} \int_0^\infty \frac{e^{-z^4} - 1}{z^4} dz. \quad (3.54)$$

The integral is $\Gamma(1/4)/3$. From this we find the final result

$$\chi_{\Delta\ell}(t \ll 1) \approx \frac{k_B T \ell \Gamma(1/4)}{3\pi 2^{1/4} \kappa^{5/4} \xi_\perp^{3/4}} t^{3/4}. \quad (3.55)$$

The short time power law growth $t^{3/4}$ is the same as for flexible filaments [15]. However, this is only the leading term at short time. Due to the presence of τ , the filament breaks self-similarity and the function does not obey a power law.

The short-time longitudinal response is bending dominated, and independent of the spring. From Eq. 3.48, we expect the longitudinal spring to become important when $k\tilde{M}(z)/z > 1$. As $k \rightarrow \infty$, the $\tilde{M}(z)/z$ in the numerator and denominator cancel out, leaving the inverse Laplace transform of $-f/zk$, which gives a constant. Thus, the spring shortens the relaxation time. Since, in the short time limit $\tilde{M}(z) \sim z^{1/4}$, this suggests that the relaxation time to equilibrium decreases with increasing spring constant like $k^{-4/3}$.

In Fig. 3.8, we plot the response function by performing a numerical inverse Laplace transform of Eq. 3.51 using Eq. B.27, for several values of k . It exhibits the predicted $t^{3/4}$ spring-free growth. Increasing k shortens the equilibration time.

To conclude the section, we consider how the decay rates of normal modes are

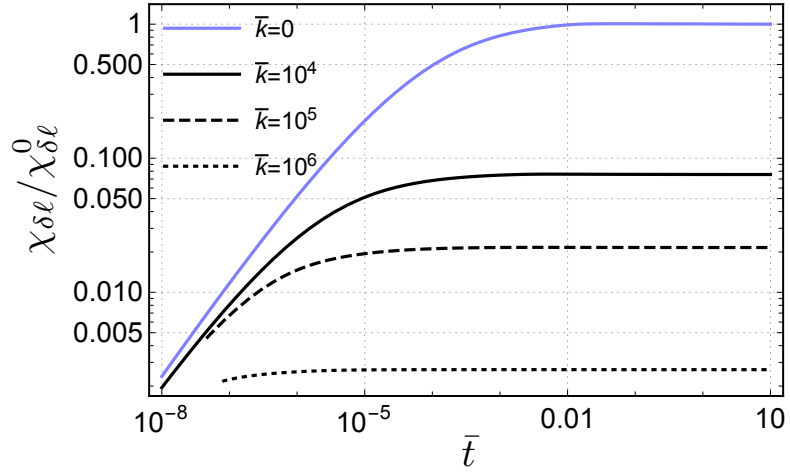


Figure 3.8: (color online) MFT longitudinal linear response normalized by the plateau value $\chi_{\Delta\ell}^0 = \chi_{\Delta\ell}(\bar{t} = \infty, \bar{k} = 0)$ of the spring-free filament. $\bar{t} = t\ell^4\xi_{\perp}/\kappa\pi^4$. At early times, there is $\bar{t}^{3/4}$ growth, but the function does not exhibit power-law behavior. The longitudinal spring decreases the relaxation time, roughly proportional to $\bar{k}^{4/3}$.

altered in the MFT. From Eq. B.12, specifying $u_p(0)$ then averaging over the noise suggests that normal modes obey a time-dependent decay rate, τ_{decay} , given by

$$\tau_{\text{decay}}^{-1}(t) = \xi_{\perp}^{-1} \left(\kappa p^4 + \tau p^2 + kt^{-1} \int_0^t \lambda_0(t') dt' \right). \quad (3.56)$$

At short times, $\lambda_0(t) \sim t^{3/4}$, which implies an additional stretched exponential prefactor $\langle u_p(t) \rangle \sim e^{-kt^{7/4}/\xi_{\perp}}$ (again, the average is over noise and $u_p(0)$ is specified). Since at small times $t > t^{7/4}$, we expect this effect to be difficult to observe in experiment.

3.4.2 Fluctuations/Random phase approximation

The saddle-point approximation, while accurately calculating $\langle \Delta\ell(t) \rangle$, does not address multipoint correlations of $\Delta\ell(t)$. This prevents us from understanding how the spring-induced nonlinearity affects dynamic fluctuations of $\Delta\ell(t)$. We define the longitudinal correlator

$$C_{\delta\ell}(t, t') = \langle \Delta\ell(t)\Delta\ell(t') \rangle - \langle \Delta\ell(t) \rangle \langle \Delta\ell(t') \rangle \quad (3.57)$$

to be the correlation functions of the end-to-end distance. This quantity is related to the dynamic shear modulus [41, 40] and informs frequency-dependent activity microscopy [97, 71].

We account for fluctuations by expanding the trace-log term $\text{Tr} \ln \mathbf{G}^{-1}(\lambda_0 + \delta\lambda, \delta\bar{\lambda})$ of the action (Eq. 3.40a) in powers of $\delta\lambda, \delta\bar{\lambda}$, about the saddle-point. In principle, one may carry out the expansion to arbitrary order. We stop at the quadratic terms. This truncation is a valid approximation for stiff filaments, where the equilibrium end-to-end contraction is small compared to contour length.

Since we are considering fluctuations about equilibrium, time-translation invariance allows us to Fourier transform to the frequency domain. In frequency/wavenumber space, the propagators and correlators appearing in the expansion refer to the saddle-point/MFT values:

$$\bar{G}_p^+(\omega) = \frac{2/\ell}{-i\omega + Dp^2(\kappa p^2 + \tau + k\lambda_0)}, \quad (3.58a)$$

$$\bar{C}_p(\omega) = \frac{4D/\ell}{\omega^2 + [Dp^2(\kappa p^2 + \tau + k\lambda_0)]^2}. \quad (3.58b)$$

In Appendix B.3, we carry out the trace-log expansion to quadratic order, yielding the Gaussian approximation to the action at the saddle point:

$$\mathcal{A}_{\text{eff}}[\delta\bar{\lambda}, \delta\lambda] = \frac{1}{2} \int \frac{d\omega}{2\pi} \delta\boldsymbol{\lambda}_\omega^T \mathbf{M}_\omega^{-1} \delta\boldsymbol{\lambda}_{-\omega}, \quad (3.59)$$

where the matrix \mathbf{M}_ω^{-1} is defined in Eq. B.36. This is our final expression for the effective action \mathcal{A}_{eff} . We are primarily concerned with the inverse \mathbf{M}_ω . It is related to fluctuations in the projected length, and its linear response to applied tension.

We compute

$$\mathbf{M}_\omega = \begin{pmatrix} 0 & \frac{1}{1+k\Pi_\omega^-} \\ \frac{1}{1+k\Pi_\omega^+} & \frac{\Pi_\omega^0}{|1+k\Pi_\omega^\pm|^2} \end{pmatrix}, \quad (3.60)$$

where the polarization functions, Π_ω^\pm and Π_ω^0 , are defined as

$$\Pi^\pm(\omega) = \sum_p \frac{Dp^4}{\gamma_p(\mp i\omega + 2D\gamma_p)}, \quad (3.61)$$

$$\Pi^0(\omega) = \sum_p \frac{2Dp^4}{\gamma_p(\omega^2 + 4D^2\gamma_p^2)}. \quad (3.62)$$

The Π^0 function is precisely the Fourier transform of the spring-free correlator [40].

The \pm functions are complex conjugates of one another, *i.e.* $\Pi^+ = (\Pi^-)^*$. They can

be related to Π^0 via a fluctuation-dissipation-like relation (Eq. B.37). Using Eq. 3.39, we relate the Π^+ function to the longitudinal linear response via

$$\chi_{\Delta\ell}(\omega) = \frac{\Pi^+(\omega)}{1 + k\Pi^+(\omega)}. \quad (3.63)$$

Comparison of the correlation function with $\chi_{\Delta\ell}$ confirms that the fluctuation-dissipation theorem is satisfied.

The ratio

$$\frac{C_{\delta\ell}(\omega)}{C_{\delta\ell}^{\text{free}}(\omega)} = \frac{1}{|1 + k\Pi^+(\omega)|^2}, \quad (3.64)$$

of projected length fluctuations in the presence/absence of a longitudinal spring, makes the effect of the spring more transparent. That ratio is plotted in Fig. 3.9. We first analyze the k dependence of the ratio. If we slowly increase k , we see that, below $|k\Pi^+(\omega)| = 1$, there is little deviation from the spring-free result. When k is large enough to exceed the bound $|k\Pi^+(\omega)| = 1$, then the end-to-end fluctuations diminish as k^{-2} . This is supported numerically – see the inset of Fig. 3.9. It is interesting that below a certain value of k , the effect of the longitudinal spring on the end-to-end distance fluctuations is *screened*. To make the connection with screening more clear, consider the low frequency limit $\Pi^+(\omega) \sim i\omega$, then inverse Fourier transform Eq. 3.64. We find exponential time decay set by the longitudinal spring constant, an effect analogous to that of the more familiar position space screening. The screening effect shows that the effect of the longitudinal spring goes beyond tension renormalization. When looking at the dynamics of the end-to-end fluctuations, we now observe the filament length stored in the various normal modes at different times interact (through the spring) to make the dynamics of the end-to-end length more complex.

The value k^* beyond which screening breaks down is, itself, frequency dependent.

Specifically, $k^* \approx |\Pi^+(\omega)|^{-1}$. Since $\Pi^+(\omega)$ is decreasing with ω , screening breaks down at smaller values k^* as ω decreases, bottoming out in the static limit ($\omega = 0$) with a minimum value $\bar{k}_{\min}^* = [\sum_{n=1}^{\infty} (n^2 + \phi)^{-2}]^{-1}$. Below this spring constant \bar{k}_{\min}^* , screening occurs at all frequencies.

The frequency dependence of the ratio of the correlators with and without the spring can be understood similarly. At $\omega = 0$, if $k > k_{\min}^*$, then the longitudinal spring shifts the longitudinal correlator to its mean-field result. In the opposite limit where $\omega \rightarrow \infty$, screening becomes perfectly effective, and there is no deviation from the spring-free result. In the main panel of Fig. 3.9, we see that the longitudinal correlator transitions from the spring-dominant, mean-field result to the spring-free result across a range of frequencies that increases with k .

By examining the saddle point analysis, we obtain further insight into which of the perturbative corrections we have taken into account in this approach. Examining the action in Eq. 3.59, we claim that it is a renormalization of the dashed line propagators of the original (\bar{u}, u) theory. Since all dashed-line renormalizations are necessarily bubble type diagrams, \mathbf{M} contains the contributions from all two-bubbles (the general n -bubble subdiagram is a solid line loop with exactly n outgoing dashed lines). Taking higher order terms in the expansion of the trace-log will result in bubbles with $n > 2$ external dashed lines, which are exactly the n -bubbles. The fluctuation expansion is not just a k expansion, but a systematic inclusion of higher number bubbles.

We can estimate the relative importance of successive terms. The one-bubble returns just the static change in projected length $\Delta\ell_0$. The two-bubble $\sim \sum_p G_p^2(\omega = 0) \sim \partial_\tau \langle \Delta\ell_0 \rangle$, is proportional to the static susceptibility $\chi_{\Delta\ell}$, with each higher order

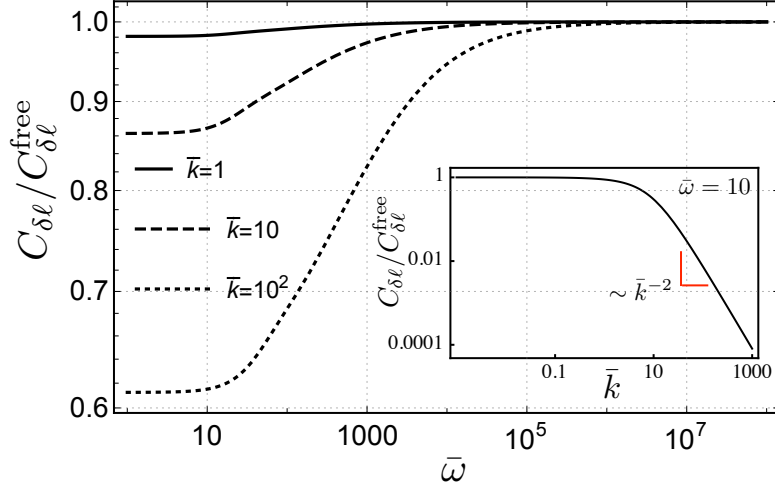


Figure 3.9: (color online) Ratio of the longitudinal correlator to its spring-free value. $\phi = 1$. At high frequency, individual modes have not relaxed to a new equilibrium that accounts for the longitudinal spring, so the ratio flattens to one. As frequency decreases, we approach the static result of Eq. 3.46, whereby we find a reduced amplitude, with zero slope. The inset shows that, for a fixed frequency ($\bar{\omega} = 10$) and zero tension $\phi = 0$, the ratio decays as \bar{k}^{-2} after passing a frequency-dependent cross-over spring constant k^* .

gaining another derivative of the projected length with respect to ∂_τ . Since each derivative lowers the summand by p^{-2} , successive terms quickly become small.

Classifying the diagrams in Fig. 3.3 of the perturbation series, to $\mathcal{O}(k^2)$ they can be divided into one-bubbles, two-bubbles, and the rest. Per the saddle-point analysis, the one/two-bubbles are the leading/subleading terms, corresponding to renormalization of the effective tension/spring constant. This is consistent with our analysis in Sec. 3.3, where our grouping of diagrams into dominant and subdominant classes was in fact a grouping into n -bubbles.

Returning to our analysis of the effective action, we observe that the resummation of bubble diagrams is an approximation known as the *random phase approximation* (RPA) [4]. The RPA applies only to the dashed line, which in any actual diagram must be attached to two solid lines according to the rules in Fig. 3.6. The two-bubble renormalized vertex is given by the diagrams in Fig. 3.10, which yield the equations:

$$M_{21}(\omega) = 1 - \frac{kD\ell^2}{4} \sum_p \int \frac{d\omega'}{2\pi} p^4 \bar{C}_p(\omega' - \omega) \bar{G}_p^+(\omega'), \quad (3.65a)$$

$$M_{22}(\omega) = |M_{21}(\omega)|^2 \sum_p \int \frac{d\omega'}{2\pi} \frac{p^4 \ell^2}{4} \bar{C}_p(\omega - \omega') \bar{C}_p(\omega'). \quad (3.65b)$$

Solving these reproduces Eq. 3.60, thus confirming our claim. Since the dashed lines appear only in combination with k , the RPA amounts to a renormalization of k . M_{21} and M_{22} represent effective vertices, whose lowest order terms reproduce diagrams B1 and B2, and B3 respectively in Fig. 3.3.

Finally, we consider the longitudinal response function given in Eq. 3.63. This provides an estimate for the high-frequency behavior of the dynamic shear modulus of semiflexible networks [58, 116], via the relation $\tilde{G}(\omega) = \frac{1}{15} \rho \ell \chi_\omega^{-1} - i\omega\eta$ [40], where

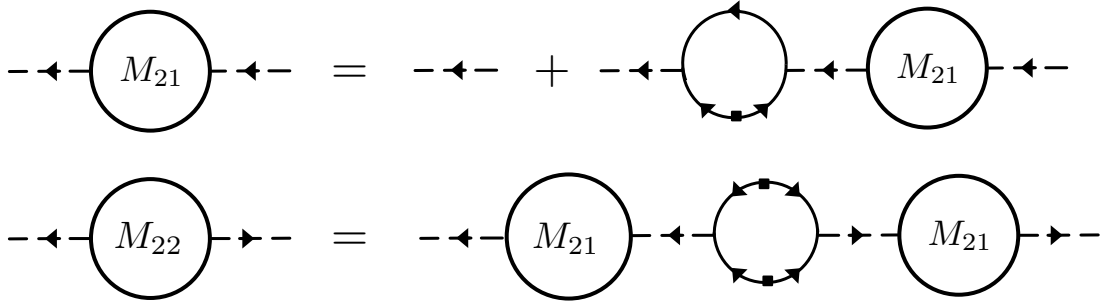


Figure 3.10: Random phase approximation for computing renormalized interaction vertex. When used in a diagram, the directed dashed lines must join to external solid lines according to Fig. 3.6. M_{ij} refers to the matrix elements of \mathbf{M} . $M_{21} = \langle \lambda \bar{\lambda} \rangle$ is directed from a vertex with two incoming lines, to one with an incoming and outgoing.

ρ denotes the density of filaments. Note that the dynamic shear modulus, $\tilde{G}(\omega)$, must be distinguished from our earlier definitions of propagators. Ignoring the viscous term, in Fig. 3.11 we plot both $J(\omega)$ and $\tilde{G}(\omega)$ for both $\bar{k} = 0$ and $\bar{k} = 10^4$. $\tilde{G}(\omega)$ possesses three distinct scaling regimes, regardless of the longitudinal spring: a low-frequency regime $\sim \omega$, an intermediate-frequency regime $\sim \omega^{1/2}$, and a high-frequency bending regime $\sim \omega^{3/4}$. The spring does not affect this scaling, but shifts the transition region to higher ω as k increases, which is consistent with our assertion that tension renormalization is the spring's main effect.

3.5 Conclusion

We have extended the static analysis of Ref. [71] to include the dynamics of the fluctuations of a filament in network, whose linear compliance is modeled as a hookean

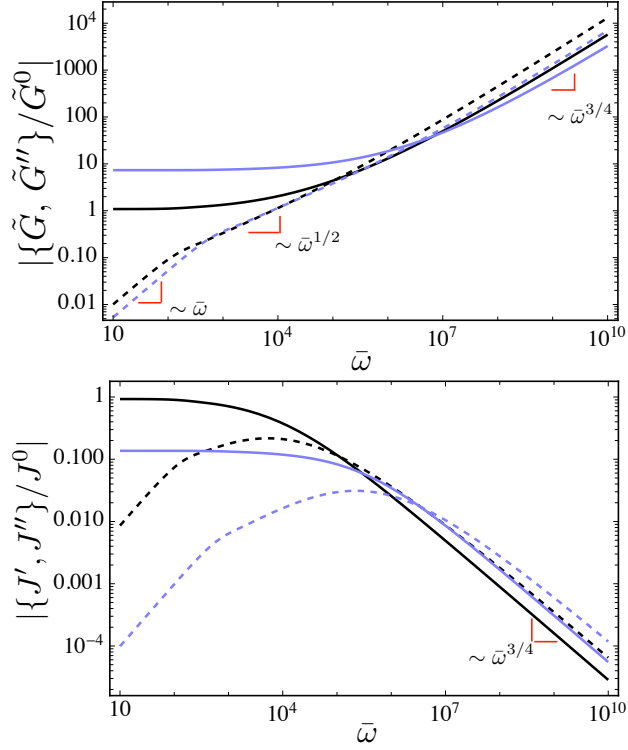


Figure 3.11: (color online) Real (solid lines) and imaginary (dashed lines) parts of the shear modulus $\tilde{G}(\omega)$ and network compliance $J(\omega)$ for $\bar{k} = 0$ (black) and for $\bar{k} = 10^4$ (blue). $\phi = 10^2$. \tilde{G} and J are normalized by their spring-free plateau values. The transition of $\tilde{G}(\omega)$ from $\omega^{1/2}$ to $\omega^{3/4}$ scaling signals the shift from tension- to bending-dominated behavior [138, 45]. The longitudinal spring does not alter the power-law dependence, but shifts the cross-over between them to higher frequencies.

spring attached to the boundary. The principal motive behind these calculations is to provide a precise prediction for the dynamical fluctuations of filaments based on κ , τ , and k , that can then be used to perform local activity microscopy.

The addition of the spring boundary condition introduces a nonlinearity into the problem, which is peculiar in the sense that it is nonlocal in space but local in time. It depends at each instant on the projected length of the whole filament. The peculiarity stems from our assumption of instantaneous tension propagation. The strength of the nonlinearity can be externally governed via the spring constant k .

For a filament bound to a larger network, the spring constant k approximates the compliance of the entire surrounding network. To get an estimate for experimentally relevant values of parameters, we use as an example an F-actin network with shear modulus $G \approx 100\text{Pa}$, and mesh spacing $\xi \approx 0.5\mu\text{m}$, which we assume is comparable to the mean distance between consecutive cross links along the same filament. Using the relation $G \sim k/\xi$ [98], we estimate a spring constant of 0.05pN/nm [71]. We further assume a persistence length $\ell_p = \kappa/k_B T$ that is approximately an order of magnitude greater than the filament segment length, and $k_B T \approx 4\text{pN nm}$. These suggest $\bar{k} \sim 10^3$. In these dimensionless units, a tension of 1pN corresponds to $\phi \sim 10^2$.

The most direct and quantitatively precise experimental test of this analysis is directly examining the dynamics of a single filament tethered to a bead in an optical (or magnetic) trap. In that case, one can independently control both the mean tension in the filament and the effective spring constant k by varying the position of the optical trap and its intensity respectively. In this setup, one may imagine two distinct types of measurements. One could observe the end-to-end length fluctuations

by tracking the bead in the trap with high spatial and temporal resolution. Or, one could observe the undulations of the filament directly, which would allow one to measure the u correlation functions computed here. In both of these cases, one might also measure the response functions by observing the response of either u or the end-to-end distance of the filament to changes in the trap's center.

We find the main effect of the spring is to renormalize tension. Even for untensed filaments, once a spring is added, the filament behaves as if it were under tension $\tau_R \approx k\langle\Delta\ell\rangle_0$. Perhaps, this blending of spring effects into an effective tension explains the success of previous theories, which have neglected nonlinearities introduced by a longitudinal boundary spring [98, 15]. We have shown that an increasing spring constant decreases the relaxation times of all the fluctuating degrees of freedom of the filament. Given a fixed external tension τ , there is a scale $k^* \approx 12 \kappa\tau/k_B T\ell^2$ of the external spring constant, above which the dominant contribution to tension comes from the spring and not the bare applied tension. Using this crossover, we estimate the minimum spring constant whose effect on filament dynamics should be observable. For typical filaments on the order of microns (with persistence lengths greater than their contour length) and tensions ~ 10 pN, we expect this transition to occur at $k \approx 1$ (pN/nm). This is achievable near the upper limit of optical trap strength (~ 100 pN/100nm), or by alternatively using a magnetic trap that can achieve higher k values.

One could alternatively use optical tweezers to exert localized forces within a network of filaments, putting some of them under tension τ . We predict that increasing τ will not affect fluctuations up until a transition tension $\tau^* \approx k k_B T\ell^2/12\kappa$, after which the amplitude of fluctuations will decrease as τ^{-2} . In the absence of the network compliance (the spring in our model), the transition occurs at a lower tension,

which is frequency-dependent. One may also look for nontrivial changes in filament tension and fluctuations as a function of network stiffness. Since the change in tension due to the spring is $\Delta\tau \sim k\Delta\ell$, for sufficiently stiff networks where the effective spring constant $k > k^*$, the change in tension switches from a linear k dependence to a weaker one $\sim k^{2/3}$, due to the shortening of $\Delta\ell$. This leads to a $k^{-4/3}$ decrease in the amplitude of transverse fluctuations.

We also considered fluctuations of the end-to-end projected length of the filament, and its response to an applied tension. We found that including the external longitudinal spring does not affect the short-time longitudinal, linear response of projected length to an abrupt change in applied tension. The change in projected length grows initially like $t^{3/4}$, but does not exhibit a power law at longer times. The longitudinal spring, does, however, shorten the relaxation time of the end-to-end length by a factor $\sim k^{-4/3}$. From the response function of the end-to-end distance of a single filament to oscillatory forcing, we can predict the collective dynamic shear modulus of the network using now standard arguments. We find that the spring shifts the transition from tension dominated, $G(\omega) \sim \omega^{1/2}$, to bending dominated, $G(\omega) \sim \omega^{3/4}$, to higher frequencies.

Finally, there is an additional frequency-dependent effect that can be observed from fluctuations in the end-to-end projected length, which arises as a result of the nonlinear interaction the spring induces on normal modes. In the static, $\omega \rightarrow 0$ limit, the amplitude of end-to-end fluctuations will be lower than that for a filament not attached to a longitudinal boundary spring. As frequency increases, however, the effect of the spring diminishes, approaching the spring-free result as $\omega \rightarrow \infty$. At high frequencies the normal modes adjust so as to screen the effect of the longitudinal spring. We report a minimum value \bar{k}_{\min}^* , below which the longitudinal spring is

screened at all frequencies. This occurs when $\bar{k}_{\min}^* = [\sum_n (n^2 + \phi)^{-2}]^{-1}$. This minimal spring stiffness necessary for complete screening grows with applied tension as $\sim \tau^{3/2}$.

Future directions for this work include a first-principles calculation of the effective spring constant k representing the network. At least, one may imagine pursuing a type of self-consistent analysis by demanding that the force extension relation of the filament coupled to the spring is identical to those of the network filaments, whose collective elasticity is represented by that spring. Secondly, one may consider how the transverse undulations of a filament in the network (represented by external springs coupled to the end of that filament) behave in response to nonequilibrium driving, such as would be experienced by the filament in a network driven by endogenous molecular motors.

CHAPTER 4

Dynamics of transiently cross-linked bundles

4.1 Introduction

Reconstituted cytoskeletal networks are a useful model for understanding the mechanics of living cells [38, 74, 157, 11, 69]. The cytoskeleton is composed mostly of filamentous biopolymer F-actin, cross-linked together to form a network [29]. Since the thermal persistence length is longer than the typical contour length between cross-links, F-actin comprises a semiflexible filamentous network. Studying the rheology of such networks is advantageous both for its ease of *in vitro* experimental fabrication, as well as its generalization to networks composed of other biopolymers such as microtubules [161, 96].

At higher concentrations, semiflexible filaments tend to coalesce into a cross-linked collections of aligned filaments called bundles, which also form a hierarchical semiflexible *bundle* network [92, 94, 93]. The viscoelasticity of these networks deviates from that of non-bundled semiflexible networks, a fact that can be traced to the difference in mechanical behavior between single filaments and bundles [123, 135, 10]. More precisely, network rheology can be extrapolated from the compliance of constituent filaments [40], which are in turn determined by their transverse undulations.

The mechanics of such bundle networks can be described by viewing each filament

as an effective worm-like bundle (WLB) [56, 57]. The WLB differs from the worm-like chain (WLC) in the introduction of a new parameter k_{\times} , representing the cross-linker stiffness, which couples bundle deformation to cross-link shear. This effect is a consequence of arclength mismatch between adjacent, bent filaments, and as shown in Fig. 4.1, is present for as few as two filaments.

For permanently bound linkers [10], linker shear leads to a stiffening of bundles at long wavelength, with a more complicated shift to the WLC model (decoupled limit) as stiffness decreases [56]. An extension to slowly deformed bundles shows an unbinding transition for highly curved bundles [54].

As cross-links are only transiently bound, their viscoelasticity cannot be fully described by the permanently bound models. Indeed, at low frequencies, semiflexible filamentous networks obey cross-link governed dynamics, exhibiting a shear modulus $G \sim \omega^{1/2}$ due to a broad spectrum of relaxation times originating from the relaxation of constraints from linker unbinding [16]. An extension of this analysis to simulations on semiflexible bundle networks, shows a similar low frequency non-Newtonian $\omega^{1/2}$ rheology, with an additional intermediate regime associated with bundle-dissolution and large-scale rearrangements of the network [111].

A full description of bundle dynamics necessitates the simultaneous consideration of both the cross-linker/bundle interaction [56], (first introduced for two filament bundles as the rail-way track model by Everaers et. al. [32]) as well as the unbinding of cross-links. In addition to the coupling scale k_{\times} , we must also consider a new parameter, the linker unbinding rate k_{off} . The combined linker-bundle system constitutes an interacting dynamical field theory, whereby bundle deformations respond to changes in cross-linker density and vice-versa.

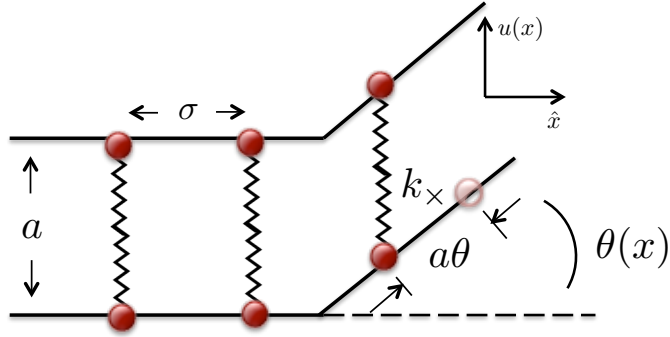


Figure 4.1: (color online) Filament bending introduces cross-linker shearing. Filaments are constrained to distance a apart, with hard rod widths σ set by the spacing of adsorption sites. Transverse displacements are labeled by $u(x)$, with x representing the distance along the mean orientation. Arc-length mismatch incurs a shear energy cost for cross-linkers attached at locations where the filament is not directed along the mean orientation.

A closer look at the railway track model shows that a single unbinding rate is insufficient to describe the full dynamics of cross-linkers. For a cross-linker to detach, it must unbind from both filaments before re-attaching. As $k_{\text{off}} \rightarrow 0$, there is an increasing probability for a linker to unbind only one filament, then reattach at an adjacent site, allowing the linker to precess along the bundle. This grants cross-linkers an alternative diffusive means of transport, in contrast to the hopping described by a single unbinding rate. The precession model shown in Fig. 4.2 introduces a new time scale τ_{walk} that competes with unbinding when ratio of on to off rates is unity.

The new time scale, τ_{walk} , signals the existence of an additional dynamical regime, where linkers remain bound to the bundle, yet are free to diffuse across it. Furthermore, long lived cross-linkers are subject to thermal Casimir attractions

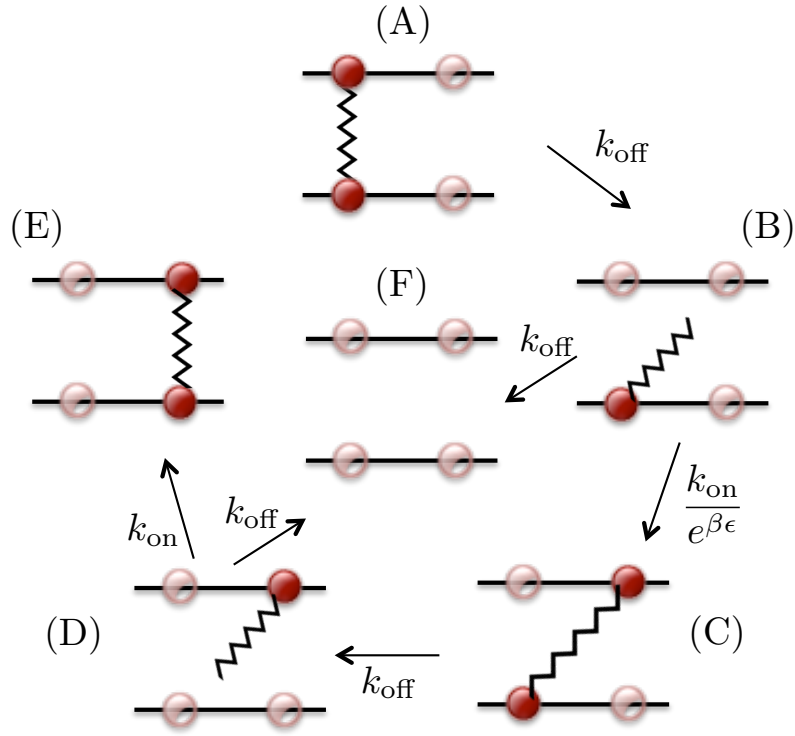


Figure 4.2: (color online) Walking cycle to traverse one lattice spacing. Reverse processes are ignored for clarity. Red bubbles indicates a bound linker, clear bubbles an unbound site. Linkers unbind according to rates $k_{\text{on/off}}$. For $k_{\text{on}} \gg k_{\text{off}}$, and for ϵ small, the linker is more likely to re-attach to an adjacent site (bottom right) than to completely unbind (center), and for small enough distances, the linkers prefer to equilibrate via walking.

between nearest neighbors [65], suggesting that the bundle must respond to the dynamics of a strongly correlated cross-linker fluid [66].

Since network properties can be extracted from the behavior of a single bundle, we focus our attention on the dynamics of the bundle, and, where possible, the viscoelastic implications. We broadly explore the mechanics of the bundle/linker system as a function of the un/binding rate $k_{\text{on/off}}$, as well as the walking rate k_{walk} . We estimate the shortest relaxation time of the problem to determine the principal dynamical features, and the appropriate dynamical model. This leads to three distinct regimes, that we model with three separate linker/bundle theories.

First, at low k_{off} , we approach the permanently cross-linked regime [56, 57, 10]. Cross-linkers are modeled as a correlated fluid. At high k_{off} , linkers quickly unbind in response to bundle deformation, approaching a collection of independent WLCs. In the intermediate regime, either τ_{walk} or τ_{off} (for τ_{off} the detachment rate) can be the dominant time scale, equilibrating on roughly the same time scales as the bundle.

The outline of this paper is as follows. First, we provide a phase space estimate for the various regions. Since bundle rigidity is mode-dependent in the presence of linkers, we find a parameter space spanned by the unbinding rate and the bundle length. The competition between walking vs. unbinding is approximated via a two-step Michaelis-Menten enzymatic precession of linkers along the bundle [114], which gives an estimate in terms of a single off and a single on rate. We then analyze the dynamics in each of the three regimes separately, before commenting on the distinguishing characteristics between these.

4.2 Overview

We focus our attention on the two-filament bundle, as our main concern is analyzing the linker/bundle interaction. The nature of the bundle cross-section can have strong effects on bundle mechanics [56], but we expect the two-filament approximation to capture the dynamical consequences of linker transience. The two-filament bundle confined to two dimensions, is known as the railway-track model [32]. This assumes the bundle is composed of two inextensible worm-like chains, in contact with a reservoir of cross-linkers inextensible in the direction transverse to the bundle axis, and compliant parallel to it. The distinguishing feature of this model (sketched in Fig. 4.1) from a mere collection of WLCs, is an energetic penalty for bending due to cross-linker shear arising from inextensibility of the constituent filaments.

The bundle is assumed to be nearly straight, with an average orientation $\theta = 0$ defined along the x -axis. Transverse displacements $u(x, t)$, and the local angle $\theta(x, t) = u'(x, t)$, are parametrized by distance along the bundle direction. This assumes no overlaps/overhangs of the filaments. For bending rigidity κ , The semi-flexible filament energy is described by the well-known WLC Hamiltonian

$$H_{\text{WLC}} = \frac{\kappa}{2} \int \left(\frac{\partial \theta}{\partial x} \right)^2 dx. \quad (4.1)$$

Cross-linkers may discretely, reversibly bind to any of N_s sites located along the bundle, with mean spacing σ between sites. The binding sites permit only a single linker to be occupied. For low occupation numbers $N/N_s \ll 1$ of linkers to sites, this distinction is unimportant. However, for larger concentrations this constraint will modify the ideal gas free energy of linkers in the bound theory, and the commutation relations of the linker Hamiltonian in the kinetic theory.

For a large number sites $N_s = \ell/\sigma \gg 1$ we may approximate bound cross-linkers via an continuous occupation density function $n(x, t)$. Due to inextensibility, bundle bending leads to an arc-length mismatch between adjacent filaments, which in turn shears cross-links, as illustrated in Fig. 4.1. Cross-links are modeled as incompressible transverse to the filament (thus fixing a), and linearly compliant to shear, with a spring coefficient k_\times . This leads to the railway-track model interaction [56, 32]

$$H_{\text{int}} = \frac{k_\times a^2}{2} \int n(x, t) \theta^2(x, t). \quad (4.2)$$

This is only strictly applicable for permanently bound cross-links. Its extension to transient linkers is one of the main goals of our paper. To understand the breakdown of Eq. 4.2 for transient linkers, consider the example process shown in Fig. 4.3. Cross-linkers that unbind in response to shear will predominantly re-bind into a zero-shear state with nonzero local angle $\theta(x, t)$ with respect to the mean orientation. In effect, linkers display a memory; they prefer the bundle to be in the same configuration as it was when they first bound.

Bundle dynamics partitions into a strongly bound small k_{off} limit given by the railway-track model, and a weakly bound large k_{off} limit, which we shall refer to as the *memory* model. The memory model is described by an appropriate generalization of Eq. 4.2 in Sec. 4.4. That such a transition occurs, consider the high k_{off} limit: if the bundle deforms slowly, cross-linkers quickly unbind and re-attach, rendering $H_{\text{int}} = 0$ (this is in contrast to Ref. [54], whereby linkers were assumed to re-bind in a sheared state).

More qualitatively, the transition from the railway track to the memory model occurs approximately when the relaxation time of the bundle is equal to the unbind-

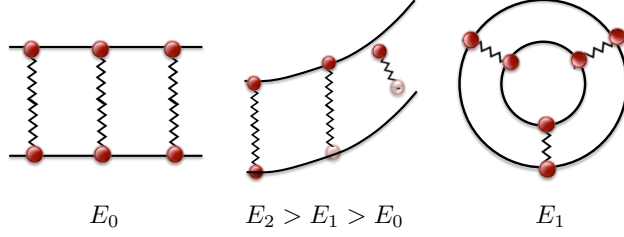


Figure 4.3: (color online) From left to right we describe a binding mediated transition to a preferred curved metastable state. The left figure is the preferred flat configuration. The center figure illustrates linker unbinding to relax stress in response to bundle induced shear. The right figure shows the linkers re-binding into a zero shear configuration, despite the bundle having curvature. The far right figure will incur a shear penalty if it tries to flatten out, and is thus a meta-stable energy minimum, compared to the global minimum on the leftmost figure.

ing time. The true relaxation time of the bundle is complicated by its coupling to the linkers. To get an estimate, we assume that linkers are permanently cross-linked. The relaxation time is mode-dependent. The lowest mode π/ℓ (for pinned boundary conditions), determines the relaxation time of a filament of length ℓ . we have the length dependent relaxation time [32]

$$\tau_{\text{WLB}} = \left(\frac{4\pi\kappa\eta}{k_{\times}^2 a^4 n_0^2 \ln(\ell/r)} \right) \frac{\bar{\ell}^4}{1 + \bar{\ell}^2}. \quad (4.3)$$

n_0 is the homogeneous part of the density $n(x, t)$, η the viscosity, and r the filament radius. We have further defined the dimensionless length $\bar{\ell} = \ell/\ell_{\times}$, where $\ell_{\times} = \sqrt{\kappa\pi^2/k_{\times}a^2n_0}$ is the length beyond which the bundle stiffens due to linker shear. Additionally, we have used the standard drag coefficient $\zeta = 4\pi\eta/\ln(\ell/r)$, describing the motion of slender bodies in viscous fluid [15]. Since the unbinding rate of linkers

is assumed to be constant up to a renormalization due to shear, there is a transition length above which the bundle relaxation time is longer than the unbinding time.

More specifically, we are interested not in the unbinding time, but the detachment time K_{off}^{-1} denoted by a capital letter, for a linker to completely unbind from both filaments. This should increase in response to shear, and contain spatial dependence. From detailed balance, we expect the detachment rate in the presence of shear to be increased by a Boltzmann factor to

$$K_{\text{off}}(x) = K_{\text{off}} e^{\beta k_{\times} a^2 \theta^2(x)/2}. \quad (4.4)$$

$\beta = (k_{\text{B}}T)^{-1}$ is the inverse temperature. We estimate a renormalized detachment rate by replacing $\theta^2(x)$ with its non-dynamical spatial and equilibrium average $\bar{\theta}^2(x) = \ell^{-1} \int_0^\ell \langle \theta^2 \rangle dx$. This leads to

$$\bar{K}_{\text{off}} = K_{\text{off}} \exp \left(\frac{1}{2n_0\ell} \sum_{n=1}^{\infty} \frac{\bar{\ell}^2}{n^2 + \bar{\ell}^2} \right). \quad (4.5)$$

\bar{K}_{off} monotonically increases from zero to a plateau value $K_{\text{off}} e^{\pi/4n_0\ell_{\times}}$. We shall thus ignore the difference between \bar{K}_{off} and K_{off} . For a given detachment rate, the condition $\tau_{\text{WLB}}(\bar{\ell}) = \bar{K}_{\text{off}}^{-1}$, determines the length above which the railway-track model transitions to the memory model.

To complete our description, we must further prescribe the dynamical equations governing cross-linkers. When viewed as a cross-linker fluid, this amounts to supplying a generalized force (derived from a grand potential or hamiltonian) and diffusion coefficient. When viewed as a non-conserved density in contact with a reservoir, this amounts to supplying the kinetic equations.

The two viewpoints correspond physically to cross-linker walking vs hopping. To describe walking, we consider the simple precession mechanism of Fig. 4.2. Linker

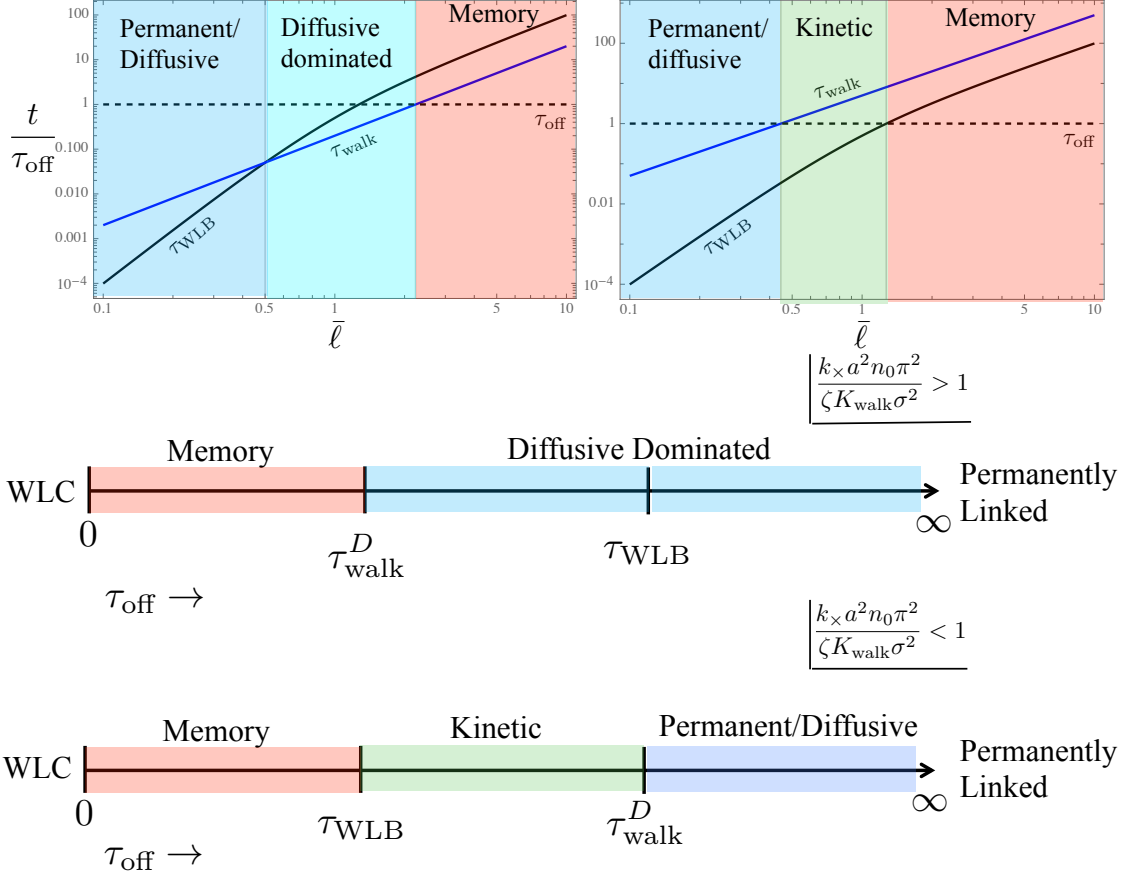


Figure 4.4: (color online) Trajectories of relaxation rates as function of dimensionless filament length. Top: $\frac{k \times a^2 n_0 \pi^2}{\zeta K_{\text{walk}} \sigma^2} = 5 > 1$. Bottom: $\frac{k \times a^2 n_0 \pi^2}{\zeta K_{\text{walk}} \sigma^2} > 1 = 0.2 < 1$. The shortest time scale determines the dominant mechanism describing dynamics, and hence the appropriate model to choose. On the right we give an alternative viewpoint, where length is fixed and the detachment rate free to change. For long enough filaments (or short τ_{off}) linker unbinding is always fastest, leading to the memory model. Conversely, at short lengths (or long unbinding time) the bundle relaxes as if linkers are permanent, while linkers respond to deformations diffusively. In the intermediate regions, precession/hopping must be considered in concert with bundle fluctuations.

unbinding is viewed as a two-step process, whereby linkers must unbind from both filaments to fully detach. When a single filament detaches (B/D), there is a possibility for it to attach to an adjacent site (C), with rate reduced by a Boltzmann factor due to linker extension. For $k_{\text{off}} \ll k_{\text{on}}$ and $\beta\epsilon < 1$, the linker prefers to walk to an adjacent site, rather than hop. We describe this walking process via Michaelis-Menten kinetics [114]. Considering only the production of states C and F, we write the rate equations



Approximating the intermediate concentration by its equilibrium value leads to the effective rate constants

$$K_{\text{off}} \approx \frac{k_{\text{off}}^2}{k_{\text{on}}}, \quad K_{\text{walk}} \approx \frac{k_{\text{off}}}{1 + e^{\beta\epsilon}}. \quad (4.8)$$

The phenomenological parameter ϵ is no more fundamental than K_{walk} and we henceforth assume that K_{walk} has been specified. The diffusion coefficient for walking is thus given by $D_{\times} = K_{\text{walk}}\sigma^2$, from which we find the Thouless time to diffuse a distance ℓ ,

$$\tau_{\text{walk}}^D = \left(\frac{\kappa\pi^2}{K_{\text{walk}}k_{\times}a^2\sigma^2n_0} \right) \bar{\ell}^2. \quad (4.9)$$

The superscript D emphasizes that this is different than the adjacent site walking time $\tau_{\text{walk}} = K_{\text{walk}}^{-1}$. This determines the time scale for diffusive relaxation via precession. Like for the WLB, we have a length dependent transition condition

$\tau_{\text{walk}}^D = K_{\text{off}}^{-1}$. This sets a scale $\ell \approx \sigma \sqrt{k_{\text{on}} K_{\text{walk}} / k_{\text{off}}^2}$ below which linkers prefer to walk, and above which they prefer to hop.

System dynamics are determined by the shortest of the three relaxation times τ_{off} , τ_{WLB} , and τ_{walk}^D , which in turn corresponds to a maximum of three transition lengths. We plot the length dependent relaxation times in Fig. 4.4, which reveals that there are either two or three intersections, depending on whether or not τ_{WLB} and τ_{walk}^D cross. Comparison of Eq. 4.9 to Eq. 4.3 shows that for $\frac{k_{\times} a^2 n_0 \pi^2}{\zeta K_{\text{walk}} \sigma^2} > 1$, τ_{walk}^D is always greater than τ_{WLB} .

These two "phase" portraits are shown in Fig. 4.4. At low $\bar{\ell}$, the system tends to the permanently cross-linked railway-track model. Due to the vanishing of τ_{walk} with length, the short $\bar{\ell}$ region always relaxes its linkers diffusively (assuming $\sigma \ll \ell$), preferring to re-arrange locally. As length increases, both the bundle and walking mechanisms require more time to relax, while the linker unbinding time remains fixed. At long enough lengths the system tends to the memory model, which at infinite length or unbinding rate reaches the decoupled limit, whereby the bundle behaves as a collection of independent WLCs. The diffusive region and the memory model can both be understood as perturbative expansions from the permanently linked and decoupled bundles respectively.

At intermediate lengths, the situation is slightly more complicated. If τ_{walk}^D intersects τ_{WLB} , then there is a region where τ_{walk}^D is the shortest relaxation time, and linkers prefer to diffuse rather than hop. In this region, linker diffusion can be expected to have a noticeable impact on bundle relaxation, and we call it the diffusive dominated regime.

If τ_{walk}^D does not intersect τ_{WLB} , then the diffusive dominated regime vanishes.

Instead, there is a region where linkers prefer to hop rather than diffuse, and both the unbinding time and bundle relaxation time are of the same order. Here, the linkers cannot unbind fast enough to relax shear, yet they are also not long enough lived to be considered permanently linked. The system still obeys the railway track model, but with transient linkers. This regime is governed by what we call the kinetic railway track model.

In summary, there are essentially four regimes. The first is the $k_{\text{off}} = 0$ permanently linked railway-track model. As k_{off} increases, linkers begin to diffuse with diffusion coefficient D_{\times} , which can be considered as a perturbative parameter. If $\frac{k_{\times} a^2 n_0 \pi^2}{\zeta K_{\text{walk}} \sigma^2} < 1$, then upon further increasing k_{off} the system will reach a region where τ_{walk}^D is the shortest length scale of the problem, and we are in the diffusion dominated regime. If not, the system will encounter a crossover length $\ell = \sigma \sqrt{k_{\text{on}} K_{\text{walk}} / k_{\text{off}}^2}$ at which point linkers prefer to hop rather than diffuse. Increasing k_{off} we enter the kinetic railway track model, which can be obtained perturbatively from the permanently linked model via the parameter $1/\tau_{\text{off}}$. Eventually, we reach a point where τ_{off} is the shortest relaxation time, the memory model. Pushing $\tau_{\text{off}} \rightarrow 0$ we recover the WLC. The memory model is found by slowly raising τ_{off} back up to finite values, and can be considered a perturbative expansion about the WLC.

Experimentally, it is difficult to resolve the distribution of cross-linkers. Undulations of the bundle on the other hand, can easily be observed via confocal imaging. Cross-linker dynamics can be indirectly observed via its effect on the response of the bundle to either an applied load, or measurement of thermal fluctuations. The linear response of $u(x, t)$ to a transverse, sinusoidal/harmonic applied load, $\chi_p(\omega) = \delta u_p(\omega) / \delta F_p(\omega)$ is diagonal in frequency and wavenumber. Coupling to a spatio-temporal linker density results in nonlinear corrections that can be grouped

into a renormalized bending rigidity $\kappa_R(p, \omega)$. The response to transverse loads can be written

$$\chi_p(\omega) = \frac{1}{-i\omega\zeta + \kappa_R(p, \omega)p^4}. \quad (4.10)$$

The determination of $\kappa_R(p, \omega)$ is our main focus. Using the fluctuation dissipation theorem, we can easily determine the power spectrum

$$C_p(\omega) = \frac{2k_B T}{\omega} \chi_p''(\omega) \quad (4.11)$$

from the imaginary part of the response function. The high frequency shear modulus of a material can be related to the longitudinal response function $\alpha(\omega)$ of an individual bundle, via $G(\omega) = \frac{\rho\ell}{15\alpha(\omega)} - i\omega\eta$ [40]. In terms of the transverse response function, the longitudinal response function can be expressed as (see Chapter 3)

$$\alpha(\omega) = 2\zeta \sum_q \int \frac{d\omega'}{2\pi} q^4 \chi_q(\omega') C_q(\omega - \omega'). \quad (4.12)$$

We now turn our attention to analyzing the dynamics in each of the three models discussed. Afterwards, we compare/contrast the results in the final section. We begin with the intermediate kinetic regime, as it is the most natural extension of the previously studied railway track model.

4.3 Kinetic railway track model

The kinetic railway-track model is an intermediate regime that arises provided $\frac{k \times a^2 n_0 \pi^2}{\zeta K_{\text{walk}} \sigma^2} < 1$, and the detachment rate is comparable to the inverse of the bundle relaxation time.

It can be accessed by beginning with the permanently linked railway track model, then slowly decreasing τ_{off} .

Since the bundle relaxes as fast or faster than cross-linkers, any linker memory of its initial bound state is quickly erased and averaged out. The railway track coupling H_{int} remains intact, but we must further account for cross-linkers detachment in response to bundle deformation. As sketched in Fig. 4.5, this implies that cross-linkers tend to aggregate near flat sections of the bundle. Through a quick application of the static barometric law $\frac{n(x)}{n_0} \sim e^{-\frac{1}{2}\beta k_{\times} a^2 \theta^2(x)}$ and expanding $\theta(x_0+x)$ near $\theta(x_0) = 0$, we see that linker density is Gaussian distributed around flat bundle sections. It exhibits a skin depth $\xi = \sqrt{T/k_{\times} a^2 R(x_0)^2}$, with $R(x_0)$ the local radius of curvature at x_0 .

The extension of the railway track model to include cross-linker mobility was first studied for slow bundle deformations in Ref. [54], ignoring the feedback of linker rearrangement on bundle configuration. Here we extend the analysis to an interacting field theory by allowing both linkers and bundle to equilibrate simultaneously.

The bundle is the main driver of linker rearrangement, and so we ignore linker-linker interactions (arising for example from hard rod repulsions or thermal Casimir forces [65, 66]). We also ignore the two-step unbinding mechanism, and consider only a detachment and attachment rate $K_{\text{off/on}}$. Binding now refers to the simultaneous attachment to both filaments. The analysis is greatly simplified, and it suffices to examine the density at a particular location, say the i^{th} site, along the bundle. Linker-concentration is described via a simple birth-death kinetic process $n_i \xrightleftharpoons[K_{\text{on}}]{K_{\text{off}}} \emptyset$ between the bound and unbound states. Coupling is introduced via a modification of the off rate as described in Eq. 4.4. We further define the on rate in terms

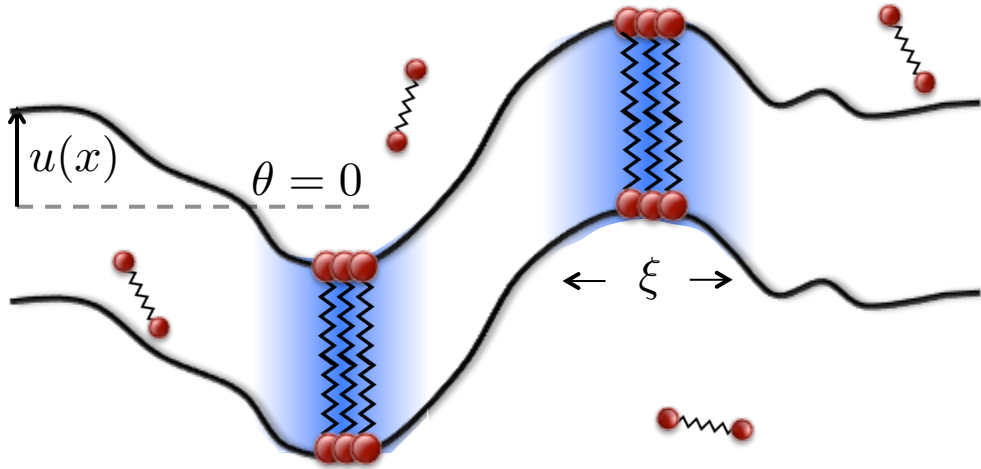


Figure 4.5: (color online) Railway track model at fixed $u(x, t)$. Bundle deformation causes bound cross-linkers to shear, regardless of when they first attached, driving them to cluster along regions locally aligned with the mean bundle orientation. Linker concentration (indicated by blue shading) near these wells is Gaussian distributed, with boundary layer length $\xi = \sqrt{T/k_{\times}a^2}|R|^{-1}$, for R the local radius of curvature.

of the off rate via $K_{\text{off}}(\theta = 0) = K_{\text{on}}z^{-1}$ and the parameter z . For an equilibrium system, we infer from detailed balance that z is the fugacity $z = e^{\beta\mu}$.

The condition $\varnothing + n_i = 1$ allows us to eliminate the function \varnothing . To extend the single site analysis to a field description, we consider the number of linkers on a particular site as a density per unit lattice spacing. This can be enacted easily by replacing $n(x, t) = n_i(t)/\sigma$ in the single site equation, which is equivalent to a density function $n(x, t) = \frac{1}{\ell} \sum_{i=1}^{N_s} \theta(\sigma - |x - x_i|)n_i(t)$. The number of sites N_s is related to the lattice spacing via $N_s = \ell/\sigma$. We arrive at the kinetic equation

$$\frac{1}{zK_{\text{off}}}\frac{\partial n}{\partial t} = - \left(1 + z^{-1}e^{\frac{1}{2}\beta k \times a^2 \theta^2(x,t)}\right) n + N_s/\ell. \quad (4.13)$$

This must be supplemented with dynamics for the angle field $\theta(x, t)$, governed by the Hamiltonian terms Eqs. 4.1, 4.2. Forces act on the transverse displacement field $u(x, t)$, and thereby indirectly on the angle field $\theta(x, t) = \partial_x u(x, t)$.

We use slender body resistive-force theory to describe overdamped dynamics of the bundle, in terms of fluctuations of the transverse displacement field $u(x)$. For individual filaments in viscous fluid whose length ℓ is much greater than its radius r , hydrodynamic interactions due to finiteness of the filament are accounted for via the drag coefficient ζ defined in the paragraph following Eq. 4.3, and we may neglect longitudinal friction terms.

Consequently, $u(x)$ obeys model A dynamics [59]. That is, $\partial_t u = -D\delta H/\delta u + \xi(x, t)$. We have introduced the parameter $D = \zeta^{-1}$, which is a diffusion coefficient times a length. The field $\xi(x, t)$ represents a white noise force with variance $\langle \xi^2 \rangle = 2DT\delta(x - x')\delta(t - t')$. Taking a functional derivative of the Hamiltonian found from

the sum of Eqs. 4.1 and 4.2, we find the Langevin equation

$$\frac{\partial u}{\partial t} = -D (\kappa u'''' - k_{\times} a^2 (nu)') + \xi. \quad (4.14)$$

This, together with Eq. 4.13, define the kinetic railway track model. The coupled equations are highly nonlinear. The $K_{\text{off}} \rightarrow 0$ limit implies that $n(x, t)$ is a constant, and reproduces the permanently linked railway track model as expected.

Slowly increasing K_{off} from infinity to a finite value, $u(x, t)$ relaxes much faster than $n(x, t)$, and remains near its equilibrium value $\theta(x, t) = 0$. This implies $\theta(x, t)$ is small as well, and suggests we Taylor expand the Boltzmann weight of Eq. 4.13. The lowest order solution for $n(x, t)$ is time-independent, given by

$$n_0 = N_s \ell^{-1} (1 + z^{-1})^{-1}. \quad (4.15)$$

This expresses the linker density of the permanently-linked railway-track model in terms of the fugacity. The permanent linker limit is also approached as $\beta k_{\times} a^2 \rightarrow 0$, as in the absence of coupling, the linkers have no preferred binding location and distribute equally.

In App. C.1, we decompose $n(x, t) = n_0 + \delta n(x, t)$, and Taylor expand the dynamical equations in $\delta n(x, t)$, $\theta(x, t)$. We then compute perturbative corrections to $\kappa_R(p, \omega)$. The validity of the expansion is justified a posteriori by inspecting the terms that appear. We find the perturbative series is regulated by the small parameter

$$\epsilon = \frac{\tau_{\text{WLC}}}{\tau_{\text{off}}} = \frac{\zeta \ell^4}{\tau_{\text{off}} \kappa \pi^4}, \quad (4.16)$$

which is a ratio of the relaxation times of the linkers to the bundle. Clearly, taking the limit $\epsilon = 0$ reproduces the permanently linked railway track model, indicating that for small but finite ϵ , linkers acquire a long but finite binding lifetime. We

are thus computing perturbative correction in ϵ about the permanently linked limit. This corresponds to moving leftward from $\tau_{\text{off}} = \infty$ in the lower right timeline in Fig. 4.4.

The ϵ expansion is most easily computed in Fourier space. We assume periodic boundary conditions, leading to the Fourier series/transform

$$\delta n(x, t) = \sum_p \int \frac{d\omega}{2\pi} \delta n_p(\omega) e^{i(px - \omega t)} \quad (4.17)$$

$$u(x, t) = \sum_{p \neq 0} \int \frac{d\omega}{2\pi} u_p(\omega) e^{i(px - \omega t)}. \quad (4.18)$$

Wave-numbers are quantized to $p_n = 2\pi n/\ell$, for $n \in \mathbb{Z}$. We have further removed bulk translations of the bundle, setting the $p = 0$ component of $u(p, \omega)$ to zero. The $p = 0$ component of $\delta n(x, t)$ is not zero, as the bundle can shift the homogeneous part of the density. Alternatively, one can assume that n_0 represents the measured linker density, and then omit the $p = 0$ modes. Here, we do the former, and retain the zero modes, since for high enough ϕ we will find that the bundle undergoes an unbinding transition. In simulations/experiment we do the latter, assuming that n_0 represents the homogeneous part of the bundle renormalized density.

The first two corrections to the bending rigidity $\kappa_R(p_n, \omega) = \kappa + \Delta\kappa_n^{(1)}(\omega) + \Delta\kappa_n^{(2)}$ are

$$\frac{\Delta\kappa_n^{(1)}(\omega)}{\kappa} = -\frac{\epsilon\phi^2}{2n^2N} \sum_{m=1}^{\infty} \frac{(4m^2 + \phi)^{-1}}{-i\bar{\omega} + 4m^2(4m^2 + \phi) + \epsilon(1+z)} \quad (4.19)$$

$$\frac{\Delta\kappa_n^{(2)}}{\kappa} = -\frac{\phi^2}{4n^2Nl(1+z)} \sum_{m=1}^{\infty} \frac{1}{4m^2 + \phi} \quad (4.20)$$

We have used the dimensionless force

$$\phi = \bar{\ell}^2 = \frac{k_{\times} a^2 n_0 \ell^2}{\kappa \pi^2}, \quad (4.21)$$

and frequency

$$\bar{\omega} = \omega \ell^4 / D \kappa \pi^4. \quad (4.22)$$

The latter is equivalent to rescaling time to units of τ_{WLC} . $N = n_0 \ell$ is the total number of bound linkers. Both corrections are negative, indicating that linker transient allows the bundle to relax shear by unbinding, thereby reducing the effective bending rigidity.

At fixed ϵ , $|\Delta \kappa_n^{(1)}|$ is monotonically increasing in ϕ , with $\lim_{\phi \rightarrow \infty} \Delta \kappa_n^{(1)} = \frac{\epsilon \pi^2}{48 n_0 \ell}$ suggesting a large radius of convergence $\epsilon < \frac{48 n_0 \ell}{\pi^2}$. Similarly, in the limit $\epsilon \rightarrow \infty$, $\Delta \kappa_1 < \infty$ and more specifically $\Delta \kappa_n^{(1)} = 2 \Delta \kappa_n^{(2)}$. This is expected as $\epsilon \rightarrow \infty$ corresponds to the static limit, in which all first order corrections must be identical. The parameter ϵ can be alternatively viewed as controlling the transition from statics to dynamics.

$\Delta \kappa_n^{(2)}$, is problematic, since it violates our assumption that $\kappa_R(p, \omega)$ is expressible as a power series in ϵ . It is a purely static contribution, arising precisely at zero frequency transfer (Eq. C.6), i.e. when $\delta n(x, t)$ is time-independent. Its survival at $\epsilon = 0$ is a consequence of non-commutativity of the limits $\epsilon \rightarrow 0$ and $\bar{\omega} \rightarrow 0$. First taking the limit $\bar{\omega} \rightarrow 0$, and then $\epsilon \rightarrow 0$, ensures that there is a finite time for linkers to unbind, and reproduces the correct static result. We can thus retain the ϵ power series provided we are able to systematically account for all zero-frequency static corrections. These corrections will renormalize $n_0 \rightarrow n_R$, and are consistent with the non-conservation of linker number. Replacing $n_0 \rightarrow n_R$ accounts for all contributions that are ϵ -independent and we can thus set $\Delta \kappa_n^{(1)}$ to zero.

In App. C.1, we exactly calculate all ϵ -independent diagrams to find the self-

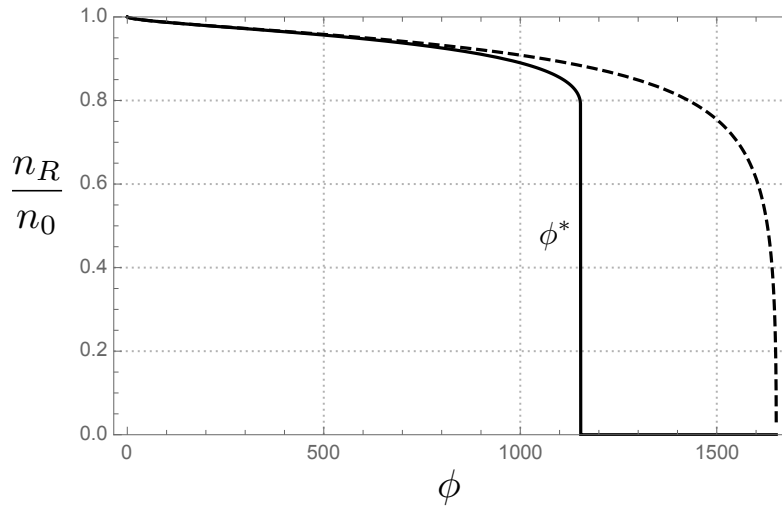


Figure 4.6: Renormalization of linker density with respect to linker stiffness. $L = \pi$, $n_0 = 20$, $z = 10$. Solid line represents self-consistent solution, while the dashed line the bare solution, whereby the right side of Eq. 4.23 uses $n_R = n_0$. At high ϕ the bundle undergoes a discontinuous unbinding transition at $\phi^* \approx 2\sqrt{2}(N+1)^2/\pi^2$.

consistent renormalized density equation

$$n_R = \frac{N_s/\ell}{1 + 1/z_R(\phi n_R/n_0)}, \quad (4.23)$$

where

$$z_R(\phi) = z \left(1 - \frac{1}{n_0 \ell} \left(\frac{\pi \sqrt{\phi}}{2} \coth \left(\frac{\pi \sqrt{\phi}}{2} \right) - 1 \right) \right)^{1/2}. \quad (4.24)$$

$z_R(\phi)$ represents a renormalized fugacity. To reiterate, the linker density n_0 corresponds to the density of linkers bound to a rigidly flat bundle. Numerical investigation of the self-consistent equation shows that n_R is well approximated by the "bare" solution, where we replace $z_R(\phi n_R/n_0) \rightarrow z_R(\phi)$. This holds, up until an unbinding transition at $\phi^* \approx 2\sqrt{2}(N+1)^2/\pi^2$ as shown in Fig. 4.6. The bare solution predicts an unbinding transition at $\sqrt{2}\phi^*$, and the reduction factor of $1/\sqrt{2}$ was found numerically to predict the transition for a variety of parameters. The unbinding transition is solely a property of the nonlinear interaction, which is in contrast to earlier studies on dynamic linkers that predict an unbinding transition as the number of filaments in the bundle grows [54]. The transition grows $\sim N^2$ for N the total number of bound linkers, and this effect is likely unobservable for typical bundles sizes.

Summarizing our results, we find the renormalized bending rigidity of the m^{th} mode

$$\frac{\kappa_R(p_m, \bar{\omega})}{\kappa} = 1 + \frac{\phi_R}{m^2} - \frac{\Delta\kappa_n^{(1)}(\bar{\omega}, \phi_R, n_R)}{\kappa}, \quad (4.25)$$

where $\Delta\kappa^{(1)}$ is a function of the renormalized density, $\phi_R = \phi n_R/n_0$, subject to the constraints $\phi < \phi^*$, and $\epsilon < 48n_0\ell/\pi^2$. At any particular frequency and wavenumber, the inhomogeneous rigidity correction is much smaller than the permanent linker correction ϕ_R/m^2 , and justifies previous neglect of linker dynamics [56]. At large wavenumber however, there is a transition mode n^* where the power spectrum $C_m(\omega)$

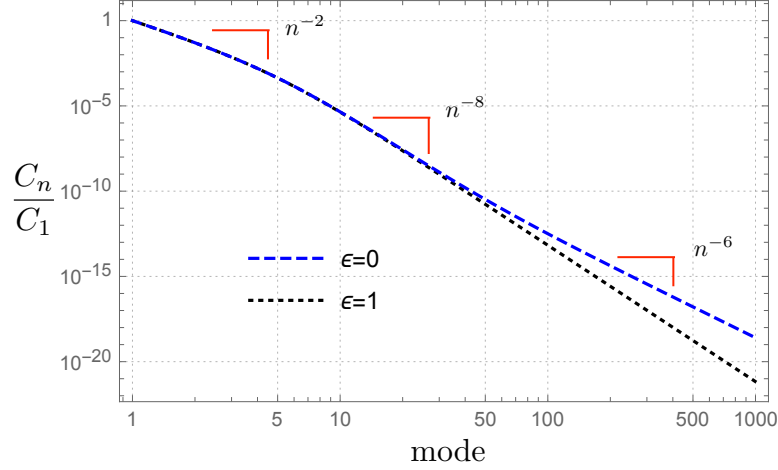


Figure 4.7: (color online) $C_n(\bar{\omega})$ as function of the n^{th} mode, normalized by the first mode: $\bar{\omega} = 1$, $\epsilon = 1$, $\phi = 100$, $N = 20$, $z = 10$. Below $n^* \approx 52$, $C_n(\bar{\omega})$ exhibits the usual transition from tension to bending like behavior. Above n^* , linker dynamics become important, causing $C_n(\bar{\omega})$ decay more slowly as $\sim n^{-6}$.

decays as $\sim m^{-6}$, as opposed to the usual $\sim m^{-8}$. This is a consequence of the frequency dependence of $\Delta\kappa^{(1)}$, with the transition number occurring at

$$n^* = \left[\frac{2\epsilon\phi^2}{N} \sum_{m=1}^{\infty} \frac{(4m^2 + \phi)^{-1}}{\bar{\omega}^2 + (4m^2(4m^2 + \phi) + \epsilon(1+z))^2} \right]^{-1/2}. \quad (4.26)$$

4.4 Memory model

We start with the WLC limit $\tau_{\text{off}} = 0$, given by the left endpoint on the timelines of Fig. 4.4. As the unbinding time raised from zero, cross-linkers develop a finite lifetime, shearing in response to bundle deformation. This allows them to couple to the bundle with an interaction strength set by $1/\epsilon$, with ϵ as defined in Eq. 4.16. In

this section, we develop a perturbative expansion at large ϵ , naming the resulting dynamical equations the memory model.

Cross-linkers interact based on previous configurations of the bundle, remembering the local angle when they first bound (hence the name *memory* model). The memory model transitions to the WLC at $\epsilon = \infty$, and at $\epsilon = 1$, it begins to transition to either the kinetic railway track model (Sec. 4.3) or the diffusive dominated model (Sec. 4.5).

In order to account for cross-linker memory of the bundle configuration, we introduce a continuous species index s , labeling the local angle $s = \theta(x, t_{\text{bind}})$ of the bundle for a cross-linker attached at position x at time t_{bind} . The density now carries a species subscript $n(x) \rightarrow n_s(x)$. As a result, we modify the interaction Hamiltonian of Eq. 4.2 to

$$H_{\text{int}} = \frac{k_{\times} a^2}{2} \int dx \int_{-\pi/2}^{\pi/2} ds n_s(x, t) (\theta(x, t) - s)^2. \quad (4.27)$$

To complete our model, we must also prescribe the dynamical equation(s) describing multi-species linkers. Here, we present a quick derivation based on kinetic equations. This is justified in App. C.3 where we give a microscopic derivation of Eq. 4.31 beginning with the master equation written in terms of many-body theory raising and lowering operators [146, 17].

As in the kinetic railway track model, linkers are non-interacting, and it suffices to examine the density at a particular location along the bundle. Linker-concentration now obeys the s dependent birth-death kinetic process $n_s \xrightleftharpoons[\beta_s]{\mu_s} \emptyset$ between the bound and unbound states. In setting up the dynamical equations, we briefly use β and μ with subscripts to refer to birth/death rates, in line with the literature. The

appropriate generalization of Eq. 4.4 gives the birth and death rates respectively

$$\beta_s = K_{\text{on}}\delta(\theta - s), \quad \mu_s = K_{\text{on}}z^{-1}e^{\frac{1}{2}\beta k \times a^2(\theta-s)^2}. \quad (4.28)$$

$\theta(x, t)$ is a time and spatially dependent function, and so *both* on/off rates are now configuration dependent. We have also made use of the relation $K_{\text{off}} = K_{\text{on}}z^{-1}$. The binding rate is assumed constant, and we have imposed that linkers always bind in a non-sheared configuration. The latter constraint can, in principle, be generalized. However, due to the exponential increase of the off rate of sheared linkers, we have assumed binding into a sheared configuration to be negligible. Inserting the θ dependent rates we arrive at the kinetic equations governing the probability distribution \varnothing of the unbound state, and n_s of the s-type bound state

$$\frac{d\varnothing}{dt} = -\beta_s\varnothing + \int ds' \mu_{s'} n_{s'} ds' \quad (4.29)$$

$$\frac{dn_s}{dt} = -\mu_s n_s + \beta_s \varnothing. \quad (4.30)$$

Adding the two equations gives the additional the conservation of probability relation $\varnothing + \int ds n_s = 1$. As a result, we can eliminate the \varnothing function and write in terms of n_s only. Extending from the single site to a density we find

$$\frac{1}{K_{\text{off}}} \frac{dn_s}{dt} = -z\delta_{\theta s} \int n_{s'} ds' - e^{\frac{1}{2}\alpha(\theta-s)^2} n_s + z \frac{N_s}{\ell}. \quad (4.31)$$

The equation has a simple interpretation; the first two terms on the right side represent the s -dependent unbinding rate, accounting for penalties due to misalignment of species index with bundle configuration. The the last term on the right is constant pumping rate of new linkers driven by the reservoir. In the single species limit, we recover the kinetic equations of Sec. 4.3

Let us consider the solution $n_s^{(0)}$ corresponding to the limit $K_{\text{off}} \rightarrow \infty$. This amounts to setting the left hand side to zero. $n_s^{(0)}$ is solved by the ansatz

$$n_s^{(0)}(x, t) = \frac{N_s}{\ell} \frac{\delta(s - \theta(x, t))}{1 + z^{-1}} = n_0 \delta(s - \theta(x, t)). \quad (4.32)$$

This solution pins the species to the preferred configuration. The time derivative $dn_s^{(0)}/dt \sim d\theta/dt$, the latter of which is zero on the time scale (infinitely fast) of linker rearrangement. This implies $d\theta/dt$ must be zero as well, and the solution $n_s^{(0)}$ represents a steady state configuration, approximately valid for very slow bundle deformations. Inserting $n_s^{(0)}$ into the Hamiltonian, we find that the interaction term in Eq. 4.27 vanishes. As expected, the bundle behaves like a collection of decoupled WLCs.

In the opposite limit, where the bundle equilibrates much faster than the linkers, we can average Eq. 4.32 with respect to θ , which yields a Gaussian like profile $n_s \sim e^{-s^2/2\langle\theta^2\rangle}$. As this distribution respects the symmetry $\theta \rightarrow -\theta$, it cannot create an energy cost due to species index. This is consistent with our neglect of species index in the kinetic railway-track model.

The notion of slow deformations is made precise by examining the bundle dynamical equation. This is derived similarly following the procedure leading to Eq. 4.14. In terms of the dimensionless time $\tau = K_{\text{off}}t$, the bundle Langevin equation

$$\frac{\partial u}{\partial \tau} = -\frac{1}{\epsilon} \frac{\ell^4}{\pi^4} u'''' + \frac{1}{\epsilon} \frac{\phi \ell^2}{n_0 \pi^2} \int ds (n_s(u' - s))' + \tau_{\text{off}} \xi \quad (4.33)$$

is proportional to the small parameter ϵ^{-1} , as claimed in the beginning of the section. The $\epsilon = \infty$ solution, $n_s^{(0)}$, decouples the filaments and linkers, generating no nontrivial solution. As ϵ decreases, bound linkers will develop a finite lifetime, interacting

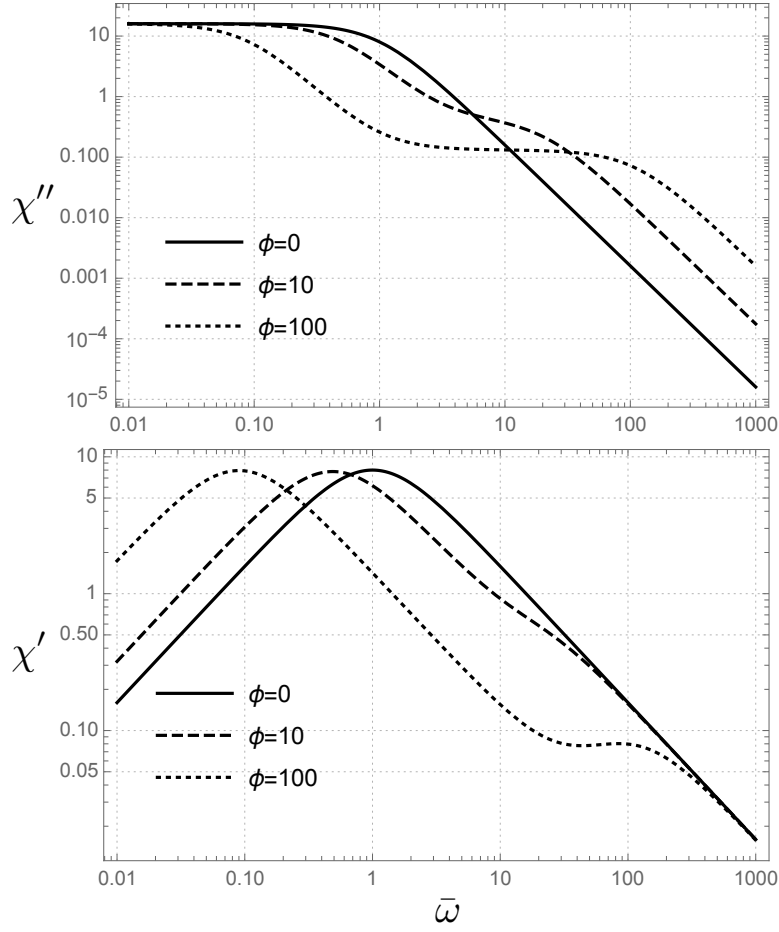


Figure 4.8: Transverse load response function of $n = 1$ mode in high K_{off} limit, normalized by the plateau response $\chi(\omega = 0)$. $\epsilon = 10$. The solid curve corresponds to the WLC result. There are two transition frequencies, when $\bar{\omega} = \epsilon, \phi$.

with the bundle through shear deformations. This suggests the density is expressible as a power series in ϵ :

$$n_s(x, t) = \sum_{m=0}^{\infty} n_s^{(m)}(x, t) \epsilon^{-m}, \quad (4.34)$$

with the leading order term given in Eq. 4.31. Inserting this into the kinetic equation, we find at $\mathcal{O}(1/\epsilon)$

$$\frac{\partial n_s^{(1)}}{\partial \tau} = -z \delta_{\theta s} \int n_{s'}^{(1)} ds' - e^{\frac{1}{2}\alpha(\theta-s)^2} n_s - \epsilon z n_0 \frac{\partial \theta}{\partial \tau}. \quad (4.35)$$

This equation is solved by a similar ansatz to that used for the steady state solution: $n_s^{(1)}(x, t) = \delta'(\theta(x, t) - s) \tilde{n}_s^{(1)}$. Time derivatives acting on the delta function produce terms with an additional $1/\epsilon$ factor, and are discarded at this order. An overall factor of $\delta'(\theta - s)$ drops out and we are left with the single-species equation

$$\frac{\partial \tilde{n}_s^{(1)}}{\partial \tau} = -e^{\frac{1}{2}\alpha(\theta-s)^2} \tilde{n}_s^{(1)} - \epsilon z n_0 \frac{\partial \theta}{\partial \tau}. \quad (4.36)$$

Inputting the $n_s^{(1)}$ ansatz into the Langevin equation, we find that the interaction force depends only on the $s = \theta$ component in the form $-\epsilon^{-2} \frac{\phi \ell^2}{n_0 \pi^2} \partial_x n_\theta^{(1)}$. The differential equation obeyed by n_θ is linear, and can be readily solved by Fourier transformation $n_s^{(1)} = -\frac{\epsilon z}{1+z^{-1}} \frac{-i\tilde{\omega}}{-i\tilde{\omega}+1}$, with $\tilde{\omega} = \omega \tau_{\text{off}}$. Upon insertion into the bundle Langevin equation we obtain for the m^{th} mode

$$-i\tilde{\omega} u_m = -\frac{1}{\epsilon} m^4 u_m - \frac{1}{\epsilon} \phi \frac{-i\tilde{\omega}}{-i\tilde{\omega}+1} m^2 u_m + \tau_{\text{off}} \xi. \quad (4.37)$$

We have here assumed pinned and torque free boundary conditions as opposed to periodic. These are both satisfied by the sine Fourier series

$$u(x, t) = \sum_p u_p(t) \sin(px) \quad (4.38)$$

with $pn\pi/\ell$, and n the positive definite integers. To compare with the kinetic model, we convert to the dimensionless frequency $\bar{\omega} = \omega\tau_{\text{WLC}}$ by substituting $\tilde{\omega} \rightarrow \bar{\omega}/\epsilon$. This gives

$$-i\bar{\omega}u_m = -m^2 \left(m^2 + \frac{-i\bar{\omega}}{-i\bar{\omega} + \epsilon} \phi \right) u_m + \tau_{\text{WLC}}\xi. \quad (4.39)$$

This suggests the simple renormalized bending rigidity

$$\frac{\kappa_R(p_n)}{\kappa} = 1 + \frac{\phi}{m^2} \frac{-i\bar{\omega}}{-i\bar{\omega} + \epsilon}, \quad (4.40)$$

and accordingly the transverse response function

$$\chi_m^{\text{memory}}(\omega) = \frac{\ell^4}{\kappa\pi^4} \frac{1}{-i\bar{\omega} + m^4 + m^2 \frac{-i\bar{\omega}}{-i\bar{\omega} + \epsilon}} \quad (4.41)$$

Unbinding has caused the "tension" induced by the cross-linkers to become frequency dependent. At low frequencies, the bundle behaves like a collection of WLCs, and at high frequencies it behaves like the permanently linked railway-track model. There is a transition between the two at frequency $\omega = \tau_{\text{off}}^{-1}$, i.e. when the applied frequency is equal to the unbinding time.

The mode dependence of the power spectrum can be significantly altered by linker unbinding even for small off rates (large ϵ). As shown in Fig. 4.9, the bundle behaves as a WLC up until a transition wavenumber

$$n^* = \sqrt{\frac{\epsilon^2 + \omega^2}{\epsilon\phi}}, \quad (4.42)$$

beyond which the power spectrum decays only as n^{-6} in contrast to the n^{-8} behavior of the WLC. This behavior was also found in the kinetic railway track model, though for the memory model, the transition can occur at much lower modes.

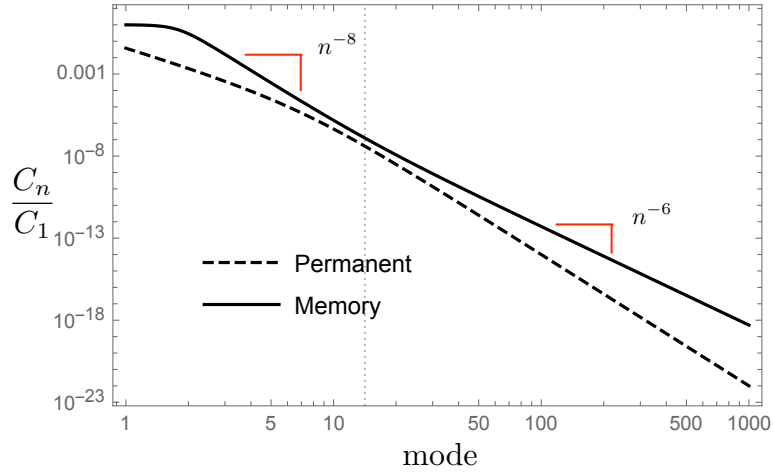


Figure 4.9: (color online) Mode dependence of power spectrum, normalized by first mode: $\epsilon = 10^4$, $\phi = 50$, $\bar{\omega} = 10$. Solid line is the memory model, and the dashed line the permanently-linked railway track model for comparison. The memory model behaves like the WLC with $C_n \sim n^{-8}$ up until a transition wavenumber n^* denoted by the gridline, whereby it only decreases as n^{-6} .

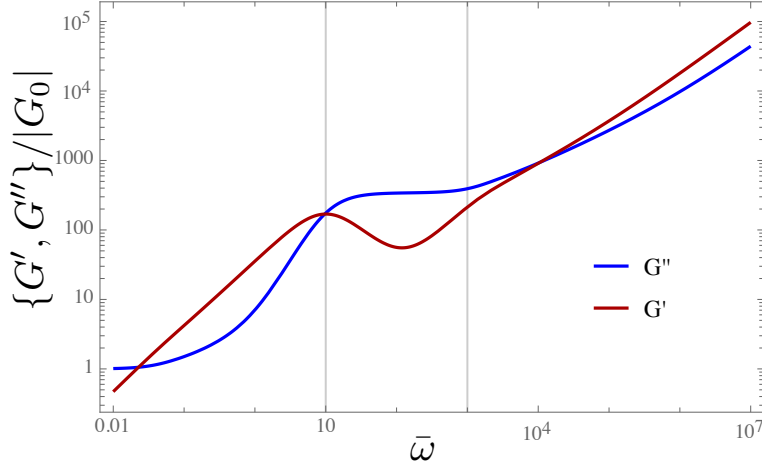


Figure 4.10: (color online) Dynamic shear modulus normalized by $G^0 = G(\bar{\omega} = 0)$: $\epsilon = 10$, $\phi = 10^3$. Gridlines at $\bar{\omega} = \epsilon, \phi$ show where the power-law self averaging behavior of the bundle is destroyed by linker unbinding, similar to that observed in Ref. [111].

Linker unbinding can dramatically effect the shear modulus $G(\omega)$ for frequencies near τ_{off}^{-1} . To calculate, we begin with the longitudinal response function defined in Eq. 4.12. Inspection of χ^{memory} shows that it has two poles in $\bar{\omega}$ in the lower half plane, which are easily found via the quadratic formula. We can perform the $\bar{\omega}'$ integration by summation of the residues of the two complex conjugate poles in the upper half plane. The result is exceedingly long, and we omit it here. The remaining summation over wavenumber can then be performed numerically, and the results are plotted in Fig. 4.10.

Qualitatively, our model captures the results of previous numerical simulations of bundle networks [111], for all but the lowest frequencies, where the network stability assumptions relating $\alpha(\omega)$ to $G(\omega)$ breakdown. Typical bundles consist of many

more than two filaments, which can drastically alter the power-law high/low $\bar{\omega}$ dependences. We expect that a more accurate extension of our model to include more filaments would accurately match the observed power-laws as well.

4.5 Diffusive cross-linkers

Due to the vanishing of τ_{walk}^D with respect to length, at short enough scales (with lower bound set by the lattice spacing σ), walking becomes the preferred method of cross-linker rearrangement. For fixed rates, this preference persists up to a length $\ell^* \approx \sigma \sqrt{k_{\text{on}} K_{\text{walk}} / k_{\text{off}}^2}$, at which point linkers prefer to hop. In the permanent/diffusive regime highlighted in dark blue in Fig. 4.4, the bundle behaves as if the linkers are fixed, while linkers locally diffuse. If $\frac{k_{\text{on}} a^2 n_0 \pi^2}{\zeta K_{\text{walk}}} > 1$, then for the low detachment rate (but not necessarily low unbinding rate) or for lengths $\ell < \ell^*$, then cross-linker diffusion is the shortest time scale and we are in the diffusive dominated regime.

In the diffusive regime, cross-linkers are long lived and can begin to interact with each other. In addition to a hard-core repulsion due to the discreteness of binding sites, thermal Casimir forces arising from filament fluctuations, cause an attractive force between adjacent linkers [65]. This motivates the description of bound cross-linkers as a one-dimensional fluid with attractive nearest-neighbor Casimir forces and a repulsive hard rod potential at distances less than the site spacing σ . Casimir interactions are not necessarily negligible, as at sufficiently low chemical potential the bundle can undergo a discontinuous unbinding transition [66].

We assume periodic boundary conditions. The linker-bundle interaction (Eq. 4.2) breaks translational symmetry, meaning that for non-constant $\theta(x, t)$, the linker density will be nonuniform. Since the interaction hamiltonian is of the form $H_{\text{int}} \sim$

$\int dx n(x, t) V[\theta(x, t)]$ (for some function V), cross-linkers may be viewed as an inhomogeneous fluid in an external potential. This situation is aptly described by dynamic density functional theory (DDFT) [100, 101, 6, 24]. The dynamical equation governing linker density can be written as

$$\frac{\partial n(x, t)}{\partial t} = \frac{D_{\times}}{T} \frac{\partial}{\partial x} \left(n(x, t) \frac{\partial}{\partial x} \frac{\delta \mathcal{F}[n(x, t)]}{\delta n(x, t)} \right), \quad (4.43)$$

where the intrinsic Helmholtz free energy is given by

$$\begin{aligned} \mathcal{F}[n(x, t)] &= T \int n(x, t) (\ln(\Lambda n(x, t)) - 1) dx \\ &+ \mathcal{F}_{\text{ex}}[n(x, t)] + \frac{1}{2} k_{\times} a^2 \int \theta^2(x, t) n(x, t) dx. \end{aligned} \quad (4.44)$$

The density $n(x, t)$ has already been averaged over internal noise, leading to the appearance of the walker diffusion coefficient $D_{\times} = K_{\text{walk}} \sigma^2$. The linker fluid responds deterministically to bundle configurations. The DDFT is a generalized Smoluchowski equation, with driving force determined by the gradient of an inhomogeneous chemical potential $\mu(x, t) = \delta \mathcal{F} / \delta n(x, t)$. The intrinsic free energy contains three contributions.

The first is an ideal gas term (Λ denotes the thermal wavelength), and ensures diffusive behavior. We have represented bound linkers as an ideal gas, assuming that if we are in the diffusive regime, jamming must be negligible.

The third term is simply a driving force due to an external potential. This arises due to bundle-induced linker shear, and is obtained by a functional derivative of the interaction Hamiltonian.

The second term is the excess over ideal free-energy. It encodes linker-linker interactions. Determination of \mathcal{F}_{ex} is the most difficult step of formulating the DDFT.

Since bundle fluctuations erase any long lived potential minima and restore translational invariance, we expect that density will not aggregate at any preferred location along the bundle. This suggests we proceed analogously to our treatment of the kinetic railway track model in Sec. 4.3, and decompose $n(x, t) = n_0 + \delta n(x, t)$ into a homogeneous n_0 , and a spatially varying $\delta n(x, t)$ with the same symmetry as $\theta(x, t)$. n_0 represents the density of linkers at vanishing stiffness ($\phi = 0$). At finite ϕ , $\delta n(x, t)$ acquires a homogeneous part δn , that renormalizes n_0 to the liquid density $n_l = n_0 + \delta n$. n_l merely represents the measured equilibrium concentration of linkers. We first replace n_0 with n_l and omit the zero wavenumber mode from the Fourier series of $\delta n(x, t)$, later returning to the question of renormalization of n_0 . Like in the kinetic railway track model, at sufficiently high ϕ , bundle fluctuations can push n_l to zero, signifying an unbinding transition. For now, we focus on dynamical properties, assuming we are below the transition.

The amplitude of fluctuations $\delta n(x, t)$ decrease with $\theta(x, t)$, and can be driven arbitrarily low by suppressing thermal fluctuations/reducing the applied load. We thus approximate ¹ \mathcal{F}_{ex} by its Taylor expansion to second order in density about the $\theta(x, t) = 0$ excess free energy. This is equivalent to the method of direct integration [53, 28], replacing correlations with their $\theta(x, t) = 0$ values. This procedure gives the Ramakrishnan-Yussouff excess free-energy [129, 128]

$$\mathcal{F}_{\text{ex}} = -\frac{T}{2} \int \delta n(x, t) c^{(2)}([n_0]; x - x') \delta n(x', t) dx dx', \quad (4.45)$$

where $c^{(2)}([n_0]; x - x')$ denotes the equilibrium direct correlation function at $\theta(x, t) = 0$. The difficulty has now been shifted onto solving for the direct correlation function

¹The exact expression \mathcal{F}_{ex} in the presence of arbitrary $\theta(x)$, in fact, admits a formal solution as given in Ref. [124]. It is valid for any one dimensional fluid with nearest neighbor interactions; however, the resulting expressions are analytically intractable.

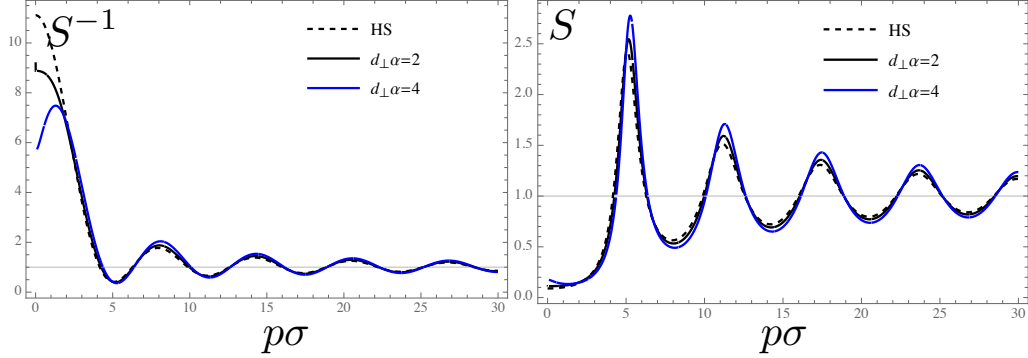


Figure 4.11: (color online) Structure function for unhinged ($d_{\perp}\alpha = 2$) and hinged ($d_{\perp}\alpha = 4$) cross-linkers at a packing fraction of $n_0\sigma = 0.7$. HS denotes the hard rod solution without Casimir interactions. Wavenumber is in units of lattice spacing.

of an interacting fluid, in general a formidable task.

Casimir forces act only between nearest neighbors [65]. The statistical mechanics of a one dimensional fluid with nearest neighbor interactions is, in fact, an exactly solvable system [36, 134, 124], and so we can calculate $c^{(2)}([n_0]; x - x')$ without approximation. The details are presented in App. C.2, where we derive the equation of state [66], the radial distribution function, and the direct/total correlation functions. The radial distribution function $g(r)$ can be found experimentally by counting the number of linkers within a shell of width dr at a radius r away from a reference linker, then ensemble averaging.

The dynamical equation for δn is given by linearization of Eq. 4.43 [6]. Furthermore, we implement periodic boundary conditions, taking the Fourier series

$$\delta n(x, t) = \sum_{p \neq 0} \delta n_p(t) e^{ipx} \quad (4.46)$$

and likewise for $u(x, t)$, again, omitting the zero mode by assumption. p is restricted

to nonzero values $p = 2\pi n/\ell$, $n \in \mathbb{Z}$. This gives the dynamical equation

$$\frac{\partial \delta n_p}{\partial t} = -D_\times p^2 S_p^{-1} \delta n_p - \frac{1}{2} D_\times k_\times a^2 n_0 p^2 \sum_{p'} \theta_{p-p'} \theta_{p'}. \quad (4.47)$$

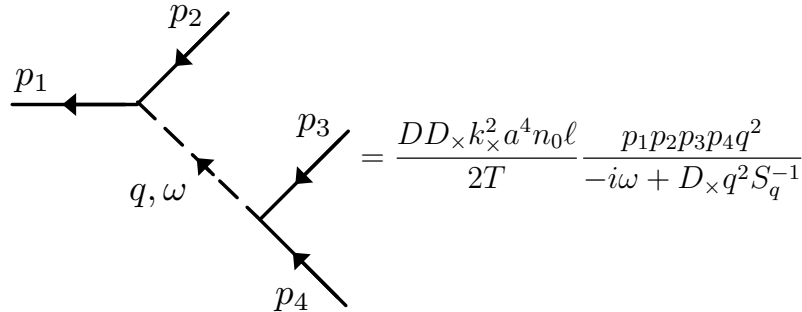
We have further defined the structure function of the homogeneous fluid [51]

$$S_p = \frac{1}{1 - n_l c_p}, \quad (4.48)$$

where c_p are the Fourier coefficients $c^{(2)}([n_0]; x) = \sum_p c_p e^{ipx}$. S_p is plotted in Fig. 4.11 with and without Casimir forces. We find that to a good approximation, we can ignore Casimir forces and consider only the hard core repulsion.

Eq. 4.47, in combination with the bundle Langevin equation (Eq. 4.14), completes our diffusive linker model. The $k_\times = 0$ equation predicts a mode dependent relaxation time $\tau_{\text{walk}} \sim D_\times p^2$ (S_p tends to unity with p and is negligible) consistent with our predicted $\bar{\ell}^2$ growth given by simple diffusive arguments in Sec. 4.2.

Fourier transforming $\delta n_p(t) = \int \frac{d\omega}{2\pi} e^{-i\omega t} \delta n_p(\omega)$, we can solve for δn and insert into the bundle equation, leading to an effective $u(x, t)$ theory with a nonlinear interaction proportional to D_\times . A perturbative expansion is thus applicable as the linker diffusion coefficient approaches zero. The nonlinear term can be represented diagrammatically by the vertex



$$= \frac{DD_\times k_\times^2 a^4 n_0 \ell}{2T} \frac{p_1 p_2 p_3 p_4 q^2}{-i\omega + D_\times q^2 S_q^{-1}}, \quad (4.49)$$

At first order, there is only a single contribution to the self energy (see the discussion preceding Eq. C.5)

$$\tilde{\Sigma} = \frac{D_{\times} k_{\times}^2 a^4 n_0}{\ell} \sum_q \frac{p^2 q^2 (p - q)^2}{\gamma_{q-p} (-i\omega + D\gamma_q + D_{\times} k_{\times} a^2 q^2 S_q^{-1})}, \quad (4.50)$$

which leads to the correction of the n^{th} mode

$$\frac{\Delta\kappa_n}{\kappa} = \frac{-\eta\phi^2}{4n^2 N} \sum_{m \neq n} \frac{m^2 (4(n - m)^2 + \phi)^{-1}}{-i\bar{\omega} + 4m^2 (4m^2 + \phi) + 4\eta\phi m^2 S_m^{-1}}. \quad (4.51)$$

We have defined the small parameter

$$\eta = \frac{D_{\times}}{Dn_0}, \quad (4.52)$$

which regulates the perturbation series. When $\eta > 1$, we enter the diffusive dominated regime highlighted by light blue in Fig. 4.4. The n^{-2} prefactor of $\Delta\kappa_n$ indicates that diffusion renormalizes ϕ .

Overall, the correction is negligible. This can be seen by graphing numerically for a large range of parameters, as well as by examining each parameter dependence individually. For small η , $\Delta\kappa_n$ is trivially small. At low ϕ , $\Delta\kappa_n$ falls off as ϕ^2 , and at large ϕ it tends to a constant, indicating it is small at all ϕ . It is also monotonically decreasing with respect to frequency, number of bound linkers, and mode number. The latter can be inferred by setting $\bar{\omega} = 0$ and $\eta = 0$ in the denominator, then performing the summation over m . We find the summation transitions from n -independent to n^{-2} decay at large n . This is in contrast to the kinetic railway track model, and as such the response function does not gain a new power law mode decay at large wavenumber.

In the permanent/diffusive regime, the bundle is impervious to linker diffusion. To probe the diffusion dominated regime, we must look at large η , which is technically

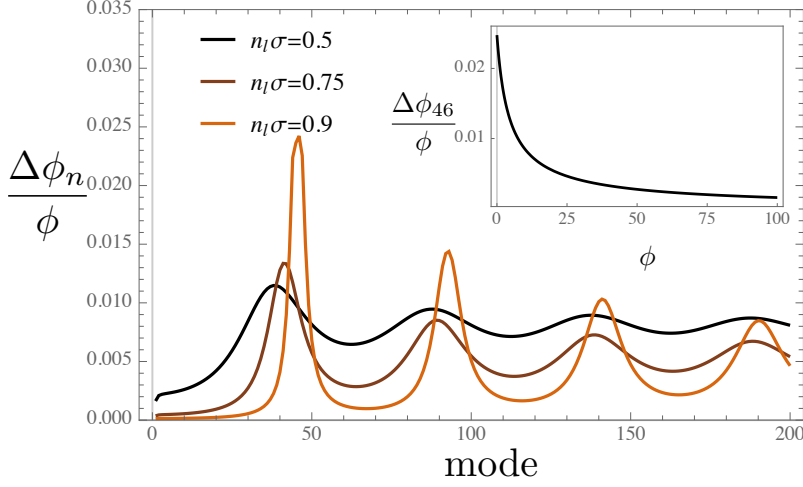


Figure 4.12: (color online) Mode-dependent ϕ renormalization to first order in the diffusion dominated $\eta = \infty$ regime ($\phi = 0.1$). At increased packing fraction, linker induced corrections increase, localizing around peaks in the structure function. The inset shows ϕ dependence of the mode $n = 46$, corresponding to the first peak. More generally, for all modes $\Delta\phi_n$ decreases with respect to ϕ .

beyond the perturbation theory. Physically, as η approaches infinity, linkers diffuse instantaneously on the scale of bundle relaxation. Due to the η appearing in the denominator of $\Delta\kappa_n$, the $\eta \rightarrow \infty$ limit is well-defined, and we can extend our result. In this limit we find the correction

$$\frac{\Delta\phi_n^{\eta=\infty}}{\phi} = \frac{-1}{4n\ell} \sum_{m \neq 0, n} \frac{S_m}{4(n-m)^2 + \phi}. \quad (4.53)$$

Where we have defined $\Delta\phi_n = 4n^2\Delta\kappa_n/\kappa$ to emphasize that this is a ϕ correction. The structure function acts like a two-body interaction between $\theta^2(x, t)$ at different locations on the bundle. It is plotted in Fig. 4.11. It has a principal peak at low wavenumber, followed by decaying oscillations about unity with increasing wavenum-

ber.

For a given mode n , the summand reaches its largest values for m near n , and m near the peaks of the structure function. This tells us that the dominant contributions to $\Delta\phi_n^{\eta=\infty}$ from modes n near the mode corresponding to the maximum of S_n . In Fig. 4.12, we compute $\Delta\phi_n^{\eta=\infty}$ through the first 200 modes. We find that linker diffusion is still a small correction, at most %2.5 of ϕ , and peaks with the structure function. At increasing ϕ , $\Delta\phi_n^{\eta=\infty}$ grows slower than linear, leading to a vanishing contribution.

The principle dynamical effect, is a small reduction in the effective stiffness of linkers for bundle deformations with wavenumber coinciding with peaks of the cross-linker structure function. As the linkers approach full packing however, these peaks become infinitely sharp delta functions, making the reduction more pronounced.

Lastly, we return to the question of the zero mode, and renormalization of n_l . For packing fractions not close to unity, this is the principle effect. It is a non-dynamical calculation, and so our starting point is the DFT grand potential $\Omega[n(x, t)]$, obtained from the free energy functional by Legendre transformation

$$\Omega_\theta[n(x, t)] = \mathcal{F}[n(x, t)] - \int dx (\mu - V(\theta(x, t)))n(x, t)dx. \quad (4.54)$$

Minimization with respect to $n(x, t)$ determines the density profile for a specific configuration $\theta(x, t)$. Since $\theta(x, t)$ is itself a fluctuating field, the bundle averaged grand potential is given by

$$\langle \Omega[n(x, t)] \rangle = -k_B T \ln \int \mathcal{D}\theta(x) e^{-\beta\Omega_\theta[n(x, t)]} e^{-\beta H_{\text{WLC}}[\theta(x, t)]}. \quad (4.55)$$

Averaging demands that $n(x, t)$ is spatially homogeneous, and so we look for solutions of the form $n = n_l + \delta n$. Inserting the RY free energy and WLC Hamiltonian,

we find that functional integral is Gaussian, and can easily be performed. This leads to the grand potential

$$\begin{aligned}
\Omega[n] &= \Omega_0[n_l] + \frac{1}{2} \ln \left(\frac{\sinh \sqrt{n\phi/n_l}}{\sqrt{n\phi/n_l}} \right) \\
&+ n\ell \ln(n/n_l) - (n - n_l)\ell \\
&- \frac{1}{2} c_0^{(2)} (n - n_l)\ell^2.
\end{aligned} \tag{4.56}$$

Stability demands $c_0^{(2)}$, which is satisfied for the models we consider. We minimize with respect to n , allowing us to discard $\Omega_0[n_l]$. The logarithm in the first line is the effective potential due to bundle fluctuations combined with linker shear. It is monotonically increasing and shifts the minimum to $n < n_l$.

Given a measured value of the linker density for some value ϕ , Fig. 4.13 shows how the density renormalizes as ϕ increases. Eventually $n = 0$ is reached, indicating a shear induced unbinding transition. This can occur independently of both the Casimir force mediated transition [66], and the number of filaments in the bundle [54].

4.6 Conclusion

We have explored the dynamics of semiflexible filament bundles with transiently bound cross-linkers for a broad range of unbinding times τ_{off} . We found that the dynamics can be segmented into two types of behavior, based on whether or not the cross-linkers prefer to relax via diffusion or unbinding. Linkers that prefer to unbind exhibit a frequency dependent stiffness. At high frequency, the cross-linkers do not have time to relax in response to changes in the bundle configuration, and we thereby recover the permanently linked railway-track model. At low frequencies, the linkers unbind quickly in response to bundle deformation and therefore have

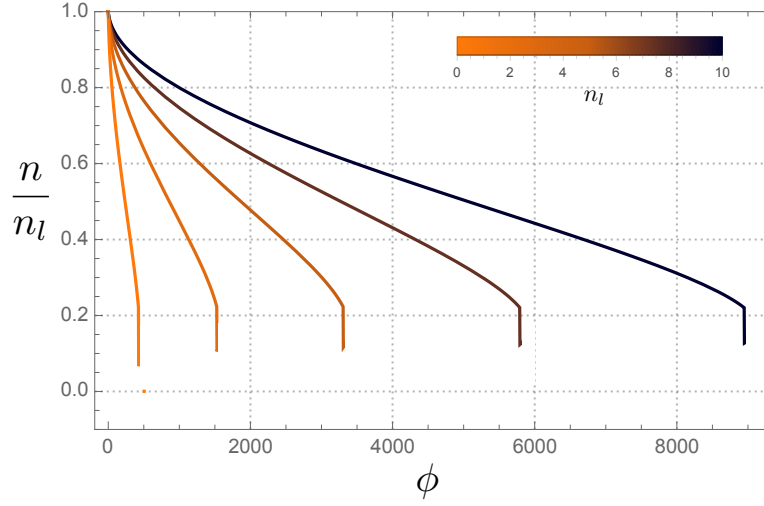


Figure 4.13: Renormalization of measured density n_l with respect to stiffness force. $L = 1$ and σ is adjusted to keep the packing fraction at 0.25 for each curve. At high ϕ , the density vanishes, indicating a unbinding transition.

vanishing effective stiffness. The transition between these two regimes occurs for frequencies near the unbinding rate $\omega \sim \tau_{\text{off}}^{-1}$. This picture explains qualitatively previous numerical findings of a non-self averaging viscoelasticity regime.

In the diffusive crosslinker regime, we find that effective linker stiffness is reduced for bundle wavenumbers corresponding to peaks in the cross-linker fluid structure function. Finally, we found a shear mediated unbinding transition at high enough linker stiffness for both diffusive and unbinding linkers.

Part II

Membranes and rods

CHAPTER 5

Effects of curvature on the propagation of undulatory waves in lower dimensional elastic materials

5.1 Introduction

Lower dimensional elastic structures are materials in which one (or more) of their characteristic length scales is small, while the others are not. Examples include biopolymer filaments [15] (two such small lengths and one large one), ribbons [75], and membranes or shells (one small length and two large ones) [112]. The physics of lower dimensional elastic structures is broadly applicable to problems ranging from nanometer lengths in carbon nanotubes [155, 14] to $\sim 10^6$ meters when discussing continental plates [70]. In the purely biological context, lower dimensional elastic structures are central to several systems, including viral capsids [91, 103, 73, 142], and cell membranes [156, 120, 121], as well as filaments and their bundles.

Due to their having one (or more) microscopic dimensions, lower dimensional elastic structures have a large separation of energy scales associated with deformation along the “thin” directions as compared to the directions normal to them [83]. This is well known in the study of flat elastic shells, in which the out-of-plane motion

of the sheet, that arises due to bending deformations, requires low energies when compared to in-plane deformations. For a shell of lateral extent L and thickness $h \ll L$, this separation of energy scales can be parameterized by the Föppl-von Kármán number $\nu K \sim (L/h)^2 \gg 1$ [115, 133]. For a flattened shell (i.e. a plate) and within linear elasticity theory, these soft bending modes decouple from the stiff in-plane deformations. When the elastic reference (stress-free) state of the shell is not flat, these modes are coupled by the local curvature. The result is that shells with complex geometry have significantly different elastic behavior [87, 13, 77]. For example, thin shells with local positive Gauss curvature in their stress-free state inhibit bending undulations [153]. Previous studies of the dynamics of undulatory waves on curved shells have shown that, in the geometric optics limit, these waves are reflected and refracted by changes in the local curvature. They can even undergo total internal reflection when propagating from regions of negative to positive Gaussian curvature [31]. Such effects have measurable implications for the spatial distribution of thermal undulations on red blood cells, which have regions of both positive and negative Gauss curvature [30].

The coupling of bending to stretching by curvature alters the normal-mode frequency spectrum by mixing in-plane and out-of-plane deformations. One may ask whether one could, in effect, “hear” the curvature of a shell by examining its eigenfrequencies of vibration. Famously, such a question was posed with regard to hearing the shape of drum [64], which was in the negative [43]. We suggest by an example discussed below, that one can, in fact, hear the shape of a bent rod; this has implications for understanding the phonon structure of some carbon nanotubes [9].

In this manuscript, we study the propagation of elastic waves on an undamped filament, where the elastic reference state couples bending and stretching deforma-

tions within the framework of linear elasticity. Our goal is go beyond the geometric optics analysis of undulatory waves and produce the analog of the Fresnel equations, allowing one to understand the transmission and reflection of elastic energy intensity at various geometric interfaces. The simplest model that retains the geometric coupling of in-plane deformation and bending is the elastic rod. While we believe that these results will inform work on membranes with more complex curvature, the theory is directly applicable to a wide variety of filaments. After introducing the elastic Hamiltonian in Sec. 5.2, we analyze in Sec. 5.3 the effect of uniform curvature on the eigenmodes of a rod, addressing the question of whether one can, in this instance, observe the effect of curvature on the mode spectrum. In Sec. 5.4, we look at the scattering of elastic waves on an infinite rod by localized regions of curvature, where we find that undulations can tunnel through curved regions that do not support such undulations in the bulk. Finally, we summarize our results and comment on their implications in Sec. 5.5.

5.2 Model

We consider the elastic dynamics of a thin curved rod embedded in two dimensions. We neglect twisting/torsional modes of deformation. Neglect of twisting is justified by our treatment of the rod as infinitesimal, and lacking internal structure. Naively, we may neglect torsion as it does not exist for surfaces of codimension one, and therefore is not a general feature of all lower dimensional elastic structures. A more detailed explanation is given following Eq. 5.5. We do not consider the elastic deformation of the material in the rod's cross section. Where applicable, we will state the results for a rod of uniform cross section and composed of isotropic elastic continuum

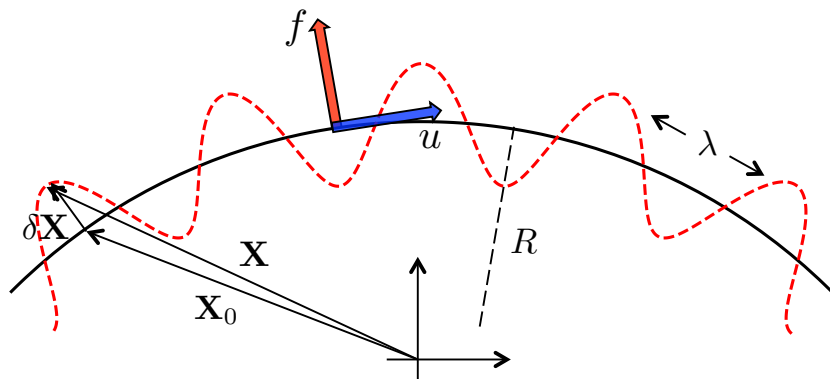


Figure 5.1: (color online) Schematic representation of an undulatory wave on a curved rod. The (black) solid line is the space curve of the undeformed rod with radius of curvature R supporting a sinusoidal wave (not to scale) shown as the (red) dashed line. Deformations about the undeformed state are decomposed locally into a displacement u (wide blue arrow) along the local tangent, and a displacement f (wide red arrow) along the local normal. The weak curvature approximation assumes that the radius of curvature R of the stress-free state (solid black line) is much larger than wavelength λ of characteristic deformations (dashed red line).

with uniform elastic constants.

We develop the mechanics of curved rods by determining the action, from which the equations of motion are derived. We work in the weak curvature limit shown schematically in Fig. 5.1. The weak curvature limit is equivalent to the inequalities $h \ll \lambda \ll R$, where h represents the cross sectional radius, λ the length of characteristic deformations, and R the local radius of curvature. This is a one-dimensional version of the linearized shallow shell theory approximations [115, 31].

The stress-free configuration of the rod, shown in Fig. 5.1, is described by a two-dimensional space curve $\mathbf{X}_0(s)$, where s denotes the arclength. The local tangent is

given by $\hat{\mathbf{t}} = d\mathbf{X}_0/ds$. One may also compute the local normal (and binormal, which is trivial for the rod embedded in the plane) vectors via the well-known Frenet-Serret relations [143]. We may write these relations as

$$\frac{d\hat{\mathbf{t}}}{ds} = \kappa(s)\hat{\mathbf{n}}, \quad \frac{d\hat{\mathbf{n}}}{ds} = -\kappa(s)\hat{\mathbf{t}}, \quad (5.1)$$

where $\kappa(s)$ is the arclength dependent curvature (equivalent to the inverse radius of curvature $R(s)$), $\hat{\mathbf{n}}$ the local normal vector, and bold-face symbols refers to two-dimensional vectors.

Due to our assumption of weak curvature, we may neglect self-intersections of the rod so that its elastic energy density is determined solely by its local state of deformation. For small deformations $\delta X(s)$, the space curve describing the deformed state is then

$$\mathbf{X}(s) = \mathbf{X}_0(s) + \delta\mathbf{X}(s). \quad (5.2)$$

Translational invariance demands that the elastic energy, \mathcal{U} , be function of $\frac{d\mathbf{X}_0}{ds}$, $\frac{d\mathbf{X}}{ds}$ and their derivatives. Given the curved stress-free state of the rod, we also require that \mathcal{U} vanishes when $\mathbf{X} = \mathbf{X}_0$. We obtain the elastic energy

$$\mathcal{U} = \frac{1}{2} \int ds \left[aU^2 + bK^2 \right], \quad (5.3)$$

where a and b represent phenomenological parameters governing stretching and bending respectively. We have introduced the one-dimensional longitudinal strain tensor

$$U = \frac{1}{\sqrt{2}} \left[\left| \frac{d\mathbf{X}}{ds} \right|^2 - \left| \frac{d\mathbf{X}_0}{ds} \right|^2 \right]^{1/2} = \hat{\mathbf{t}} \cdot \frac{d\delta\mathbf{X}}{ds} + \mathcal{O}(\delta X^2), \quad (5.4)$$

and the bending tensor

$$K = \frac{1}{\kappa\sqrt{2}} \left[\left| \frac{d^2\mathbf{X}}{ds^2} \right|^2 - \left| \frac{d^2\mathbf{X}_0}{ds^2} \right|^2 \right]^{1/2} = \hat{\mathbf{n}} \cdot \frac{d\delta\mathbf{X}}{ds} + \mathcal{O}(\delta X^2). \quad (5.5)$$

The appearance of these terms, including using square roots in the definitions of U and K , is chosen to align with the generalized representations of elasticity in higher dimensions. They are equivalent to the more familiar bending and stretching elastic energy terms [26, 82].

For rods (and generally for objects of codimension greater than one), there exist additional torsion degrees freedom that may contribute to the elastic energy [22]. These consist of displacements normal to both the local tangent, as well as the unique bending normal orthonormal to the covariant derivative of a local geodesic. The generalized Serret-Frenet relations tell us that each additional normal vector is proportional to a power $m > 1$ of the local tangent. For weakly curved rods, these torsion terms constructed out of higher order derivatives may thus be neglected in comparison to the aforementioned bending and stretching contributions.

Deformations are parametrized in normal coordinates [112]

$$\delta\mathbf{X} = u\hat{\mathbf{t}} + f\hat{\mathbf{n}}, \quad (5.6)$$

where u represents the local in-plane stretching, and f the local out-of-plane bending. Rewriting U and K in terms of normal coordinates, we find (using primes to denote arclength derivatives)

$$U = u' - \kappa f, \quad (5.7)$$

and

$$K = f'' + 2\kappa u' + \kappa' u - \kappa^2 f. \quad (5.8)$$

In the weak curvature limit, the second and fourth terms are negligible. The third term is more subtle. It can certainly be discarded for rods with constant curvature, which we study here, but also may be discarded provided R'/R is small. We thus find $K \approx f''$.

To determine the action, we introduce the kinetic energy, taking the mass density (mass per unit length) of the rod to be ρ . In the weak curvature limit, the kinetic energy density can be approximated by its flat rod result, as corrections are higher order in curvature. Using dots (primes) for time (spatial) derivatives, we obtain the action

$$S = \frac{1}{2} \int ds \left\{ \rho \dot{f}^2 + \rho \dot{u}^2 - a(u' - \kappa f)^2 - b f''^2 \right\}. \quad (5.9)$$

For a uniform elastic rod with Young's modulus Y , cross sectional area A , and moment of inertia I , the two phenomenological elastic constants can be expressed in terms of these more microscopic ones as: $a = YA$ and $b = YI/2$ [83]. We may eliminate the dependence on a, b by a suitable rescaling of length and time, introducing dimensionless independent variables: $s \rightarrow s/\ell^*$ and $t \rightarrow t/t^*$, where

$$\ell^* = \sqrt{\frac{b}{a}} \quad (5.10)$$

$$t^* = \frac{\sqrt{b\rho}}{a}. \quad (5.11)$$

Variations with respect to u and f yield the equations of motion

$$\partial_t^2 f + \partial_s^4 f + M^2 f = M \partial_s u \quad (5.12a)$$

$$\partial_t^2 u - \partial_s^2 u = -\partial_s(Mf), \quad (5.12b)$$

where we have defined the dimensionless curvature

$$M(s) = \ell^*/R(s), \quad (5.13)$$

in terms of the the arclength dependent stress-free radius of curvature $R(s)$. Eqs. 5.12a and 5.12b are one-dimensional versions of the linearized shallow shell equations governing thin shells [115].

The boundary conditions are also obtained by variation of the action. In addition to continuity of u , f , and f' across the boundary, we find three force balance equations. These equations require the continuity

$$\Delta(u' - Mf) = 0 \tag{5.14}$$

$$\Delta(f'') = 0 \tag{5.15}$$

$$\Delta(f''') = 0, \tag{5.16}$$

across an interface where the curvature of the rod changes, say at $s = 0$. In the above equations we use the notation $\Delta(\phi) = \lim_{s \rightarrow 0^+} \phi - \lim_{s \rightarrow 0^-} \phi$ to represent the discontinuity of some variable ϕ across a boundary. At a boundary where the curvature changes discontinuously, there is a subtlety in that κ' is not well defined, suggesting that we are not justified in discarding the term $\kappa'u$ in the bending tensor K – see Eq. 5.8. However, in the presence of discontinuous curvature, our assumptions leading to the derivation of K cease to hold as well. Physically, the boundary conditions Eqs. 5.14–5.16 represent longitudinal force balance, transverse force balance, and torque balance across the interface. Within the linearized shallow shell theory [115] approximation $K \approx f''$, these boundary conditions still provide the correct physical continuity of force and torque. Eqs. 5.12 and boundary conditions Eqs. 5.14–5.16 represent the minimal coupling of an elastic rod to curvature.

5.3 Eigenmodes and frequencies

We consider the case of constant curvature, which corresponds to the replacement $M(s) \rightarrow M$. Eqs. 5.12a, 5.12b now constitute a set of linear partial differential equations. In the frequency domain, these equations can be made to appear like the

time-independent Schrödinger equation for a spinor-valued state ket $|\psi\rangle$:

$$\hat{H}|\psi\rangle = \omega^2|\psi\rangle, \quad (5.17)$$

which may be written in the s or arclength basis

$$\langle s|\psi\rangle = f(s)|f\rangle + u(s)|u\rangle, \quad (5.18)$$

in terms of basis spinors $|f\rangle = (1\ 0)^T$ and $|u\rangle = (0\ 1)^T$, and two “wavefunctions” $f(s)$ and $u(s)$, which correspond to the amplitude of bending and stretching deformation respectively. In terms of this spinor fu basis, the Hamiltonian is given by

$$\hat{H} = \begin{pmatrix} \partial_s^4 + M^2 & -M\partial_s \\ M\partial_s & -\partial_s^2 \end{pmatrix}. \quad (5.19)$$

Note that the f and u problems decouple on a straight rod ($M = 0$) as expected – see below. We look for traveling wave solutions of the form $e^{iks}|\psi_k\rangle$, where the spinor $|\psi_k\rangle$ is s -independent. The Hamiltonian acting on such a state becomes

$$\hat{H}(k, M) = \begin{pmatrix} k^4 + M^2 & -iMk \\ iMk & k^2 \end{pmatrix}. \quad (5.20)$$

5.3.1 Zero curvature

We briefly review the case of zero curvature ($M = 0$). The Hamiltonian is diagonal, with eigenfrequency and eigenstate pairs

$$(\omega = k) \leftrightarrow |u\rangle, \quad (\omega = k^2) \leftrightarrow |f\rangle. \quad (5.21)$$

f and u waves have quadratic and linear dispersion relations respectively. In their mode spectrum there are three points of degeneracy: $k = 0, \pm 1$.

For a finite rod of length ℓ , boundary conditions restrict the allowed values of wavenumber k , producing a discrete spectrum of eigenvalues or frequencies. We consider a clamped rod, requiring that u , f , and f' vanish at the boundary. The eigenvalue equation (Eq. 5.17) has a solution of the form $|\psi(s)\rangle = e^{iks} |\psi_k\rangle$, provided that $\det(\omega^2 \mathbb{1} - \hat{H}(k)) = 0$. This is satisfied for any wavenumber k that fulfills the condition

$$(\omega^2 - k^2)(\omega^2 - k^4) = 0. \quad (5.22)$$

There are six solutions. These include two propagating u waves of the form $e^{\pm i\omega s} |u\rangle$, two propagating f waves of the form $e^{\pm i\sqrt{\omega} s} |f\rangle$, and two exponential (evanescent) f waves corresponding to imaginary solutions of wavenumber. These are given by $e^{\pm \sqrt{\omega} s} |f\rangle$.

We determine the allowed frequencies by first projecting $|\psi\rangle$ onto the wavenumber basis

$$\psi(k) = \sum_{\sigma=\pm} c_{\sigma}^u e^{\sigma i\omega s} |u\rangle + \left(c_{\sigma}^f e^{\sigma i\sqrt{\omega} s} + c_{\sigma}^{E,f} e^{\sigma \sqrt{\omega} s} \right) |f\rangle, \quad (5.23)$$

in terms of the undetermined coefficients $c_{\pm}^u, c_{\pm}^f, c_{\pm}^{E,f}$. The six boundary conditions (three at each end) produce a set of six equations for the six coefficients. A solution exists provided the determinant of the coefficient matrix vanishes, yielding the eigenfrequency condition

$$[\cos(\sqrt{\omega}\ell) \cosh(\sqrt{\omega}\ell) - 1] \sin(\omega\ell) = 0. \quad (5.24)$$

Frequencies ω_f that cause the bracketed expression to vanish correspond to purely $|f\rangle$ bending modes, whereas frequencies ω_u that cause the sine to vanish are purely $|u\rangle$ stretching modes. Since the function $\cosh(x)$ grows exponentially with its argument, to good approximation, we may use the approximate f -mode frequency condition

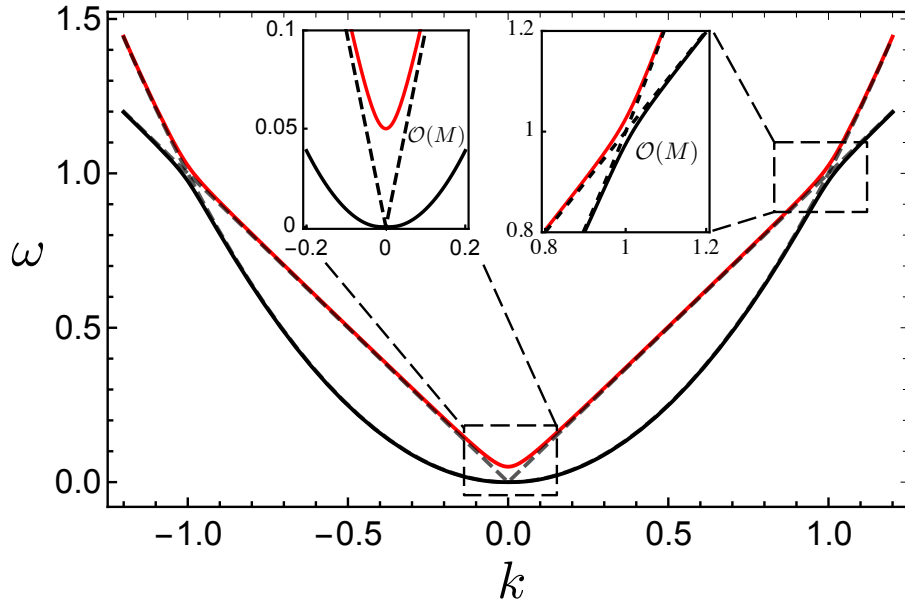


Figure 5.2: (color online) Dispersion relation of a uniformly curved rod. $M = 0.05$. The degeneracy between the $M = 0$ dispersion curves (dashed black lines) is lifted due to curvature. Level splitting between the upper branch (red) and lower branch (black) is $\mathcal{O}(M)$ near wavenumbers $k = \pm 1$ and $k = 0$.

$\cos(\sqrt{\omega_f}\ell) = 0$ when $\sqrt{\omega_f}\ell > 1$. This leads to the (approximate) solutions for the bending-mode eigenfrequencies

$$\omega_f \approx \left(\frac{(n + 1/2)\pi}{\ell} \right)^2, \quad (5.25)$$

for positive integers n . The stretching eigenfrequencies, which correspond to vanishing of $\sin(\omega_u\ell)$, are easily found to be

$$\omega_u = \frac{n\pi}{\ell}. \quad (5.26)$$

5.3.2 Uniform curvature

In the presence of uniform curvature M , the eigenfrequencies of Eq. 5.20 split into two branches:

$$\omega_{\pm}^2 = \frac{1}{2} \left[(k^4 + k^2 + M^2) \pm \sqrt{(k^4 + k^2 + M^2)^2 - 4k^6} \right], \quad (5.27)$$

where the (+) subscript refers to the upper branch, and the (-) subscript to the lower. In the limit $M \rightarrow 0$ and $|k| > 1$, these reduce to $\omega_+ = k^2$ and $\omega_- = k$, indicating that the upper branch corresponds to a bending mode, and the lower branch to a stretching mode. For $|k| < 1$, the identification is reversed, with $\omega_+ = k$ and $\omega_- = k^2$. These identifications are further supported by looking at the (unnormalized) eigenmodes, which may be written as

$$|+\rangle = |f\rangle + \frac{-ikM}{k^2 - \omega_+^2(k, M)} |u\rangle \quad (5.28)$$

$$|-\rangle = |u\rangle + \frac{ikM}{k^4 + M^2 - \omega_-^2(k, M)} |f\rangle. \quad (5.29)$$

For $|k| > 1$, the $M \rightarrow 0$ limit recovers the zero-curvature results $|+\rangle = |f\rangle$ and $|-\rangle = |u\rangle$. Again, the identifications are reversed for $|k| < 1$.

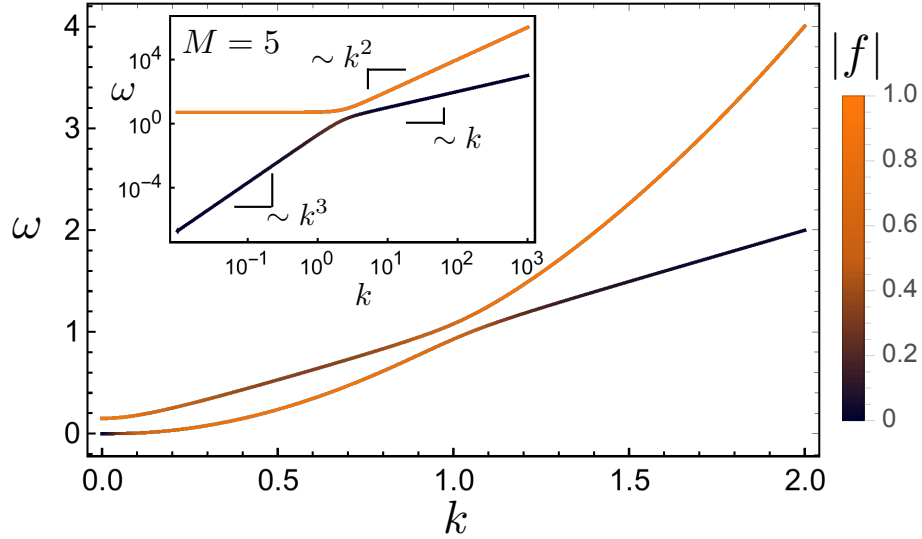


Figure 5.3: (color online) The dispersion relation of a rod with uniform curvature, color-coded according to the normalized amplitude of its corresponding $|f\rangle$ eigenstate. $M = 0.15$ and $\ell = 1$. Mode mixing is strongest near the degeneracy points of the $M = 0$ case. In the inset, we show the behavior for larger curvature $M > 1$. At small k , the upper branch is essentially flat, while the lower branch develops an $\omega_- \approx |k|^3/M$ power law, in contrast to its quadratic dispersion relation at small curvature.

In Fig. 5.2, we plot the dispersion relations of elastic waves on the rod at fixed $M \neq 0$. Curvature lifts the degeneracies at wavenumbers $k = 0, \pm 1$. The magnitude of the level splitting is $\mathcal{O}(M)$. The upper branch is gapped; it does not tend to zero with wavenumber, but instead to $\omega(k = 0) = M$. In this sense, the upper branch acts as if it has acquired a *mass* due to curvature, hence our use of the notation M . If the system possess frequencies $\omega < M$, they must have complex wavenumber and are necessarily bound. At finite M , in the limit $k \rightarrow 0$, the eigenmode of the upper branch becomes a pure $|f\rangle$ mode. Bending modes are gapped in the presence of curvature, which can be viewed as the one-dimensional analog of the suppression of undulations on thin shells at areas of positive Gauss curvature [153, 31]. In the case of shells, this suppression is due to a change in character of the elasticity equations from hyperbolic to elliptic upon changing the sign of Gauss curvature [115]. Here, the effect manifests as a gap in the dispersion.

In the absence of curvature, the linear and quadratic dispersion corresponded to directly to $|u\rangle$ and $|f\rangle$ normal modes. In the presence of curvature, these normal modes are mixed. In Fig. 5.3, we show the same free dispersion relation color coded by normal mode amplitude. The amplitudes obey the normalization constraint $|u|^2 + |f|^2 = 1$, which implies that $|f| = 1$ when $|u| = 0$, and vice-versa. The effects of mode-mixing are most prevalent at wavenumbers near level splitting. At these points, the normal mode amplitudes of the two branches switch character between u and f dominated. This ensures that only bending (stretching) dominated normal modes exhibit quadratic (linear) dispersion at large wavenumber. For wavenumber $k < 1$, the lower branch $\omega_- \sim |k|^3/M$, in contrast to the zero curvature quadratic dispersion.

At fixed k , the frequencies on the upper (lower) branch of Eq. 5.27 increase (decrease) with increasing M . At large k , the frequencies on the lower branch decrease

$\sim M^{-1}$, while those on the upper branch are hyperbolic and approach the asymptote $\omega = M$. As a result, frequencies ω_+ may never fall below M . This is due to the $k = 0$ band gap shown in Fig. 5.2 (see the inset of that figure).

The large curvature limit of Eqs. 5.28, 5.29 shows that the eigenstates that mix bending and stretching modes once again decouple so that $|+\rangle \rightarrow |f\rangle$ and $|-\rangle \rightarrow |u\rangle$. Interestingly, this is the same result as for $M \rightarrow 0$. Since at large M the $|+\rangle$ states become pure bending modes, we deduce that bending dominated modes may not have frequencies $\omega < M$. Moreover, by increasing the curvature, one can identify which eigenfrequencies are related to primarily bending (stretching) dynamics, by seeing if they increase (decrease) with M . At larger curvature, due to the frequency gap, these frequencies are separated by the line $\omega = M$.

We now turn from the case of an infinite rod to a finite one. For a finite rod, we must impose boundary conditions at the ends, which generally lead to a quantized set of eigenfrequencies ω_n . To study how the frequency spectrum changes with respect to curvature, we fix clamped boundary conditions at the ends and vary only the curvature M . Thus, we demand that u , f , and f' vanish at the endpoints $s = 0, \ell$.

Following the steps of Sec. 5.3.1 to determine the eigenfrequencies involves solving a cubic characteristic equation for k^2 as a function of ω , followed by finding the roots of an analytically complicated transcendental equation. Instead, we compute the eigenfrequencies and eigenfunctions directly in position space numerically, using collocation methods on a Chebyshev grid [148]. The eigenmode amplitudes are determined via numerical integration $\frac{\int_0^\ell |f|^2 ds}{\int_0^\ell (|f|^2 + |u|^2) ds}$, performed via quadrature.

In the upper panel of Fig. 5.4, we plot the eigenfrequencies as a function of curvature for a rod of length $\ell = 20$, color coded so that an increasing ratio of

bending to stretching amplitude runs from dark to light. Broadly, frequencies that increase with respect to curvature are associated with bending f -modes, and such modes are still restricted to frequencies $\omega > M$. The lower frequency modes show more mixing of bending and stretching.

Due to changing the rod's curvature, spectral lines (frequencies) corresponding to different modes cross. There are three regimes, dictated by the strength of interaction between different harmonics. At high frequency (and accordingly high $|k|$), curvature-induced coupling between bending and stretching is negligible. The spectral curves can be well approximated by using the zero-curvature k values, Eq. 5.25 and Eq. 5.26, in the equations for the ω_+ and ω_- branches. As for the infinite rod, bending (stretching) modes increase (decrease) with increasing curvature. At low frequencies, curvature significantly affects the rod, and the free dispersion relation gives a poor fit.

At intermediate frequencies (approximately $1 < k < 1.75$ in the upper panel of Fig. 5.4), frequencies exhibit oscillatory behavior, due to level splitting between other harmonics. To understand this effect, we expand the state $|\psi\rangle$ of Eq. 5.17 in the basis of zero curvature eigenmodes

$$|\psi\rangle = \sum_n c_n(M) |\psi_n^{(0)}\rangle, \quad (5.30)$$

for some M -dependent coefficients. This leads to an equation for the coefficients c_n :

$$[\omega^2(M) - \omega_n^2] c_n = \sum_m \langle \psi_n^{(0)} | \hat{V} | \psi_m^{(0)} \rangle c_m, \quad (5.31)$$

where we have introduced the $M = 0$ eigenfrequencies ω_n corresponding to the

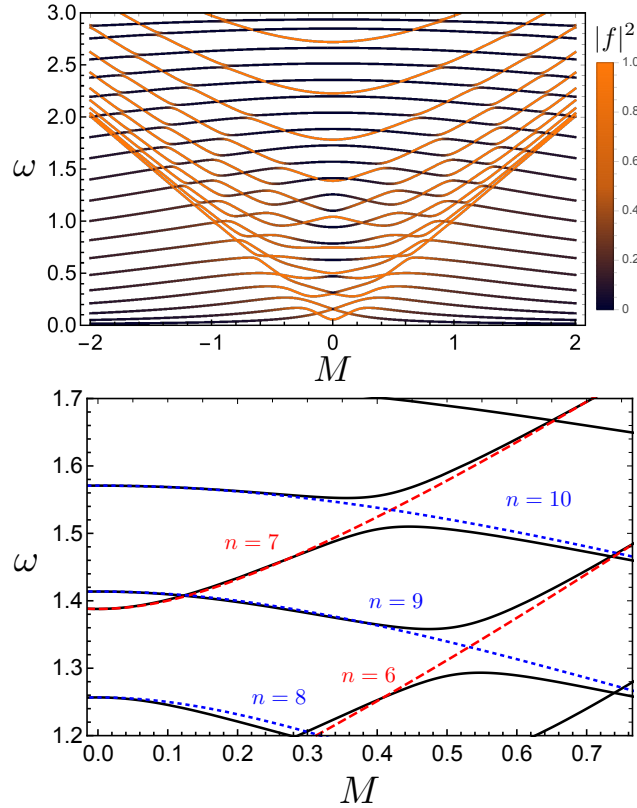


Figure 5.4: (color online) The frequency spectrum of a clamped rod of length $\ell = 20$ as a function of curvature M . Top: the M -dependence of the frequency spectrum, color coded by the relative amplitude of its f to u mode, where lighter colors represent more bending f -amplitude. Due to parametric M -dependence, each curve represents one eigenmode. We find three distinct regimes: high ω where the curves look like their infinite-rod counterparts, intermediate ω , where they spectrum is approximated by free dispersion curves with level splitting, and low ω where curvature strongly distorts the spectrum. Bottom: a close up view of the frequency spectrum (black solid lines) overlaid with the infinite rod dispersion curves for several modes labeled by n in the figure (dashed lines). Level splitting occurs between even and odd numbered modes, as explained in the text.

eigenmodes $|\psi_n\rangle$, and we have defined the perturbation operator

$$\hat{V} = \begin{pmatrix} M^2 & -M\partial_s \\ M\partial_s & 0 \end{pmatrix}. \quad (5.32)$$

The perturbed eigenfrequencies $\omega(M)$ retain implicit dependence on the curvature M . For the infinite rod, the direct solution of Eq. 5.30 leads to the frequencies and states ω_{\pm} , $|\pm\rangle$. We do not try to recover this result, but instead look at the possible straight-rod states coupled by the perturbation operator. Evaluating the off diagonal matrix elements of V_{mn} we find

$$\langle m|\hat{V}|n\rangle_{m\neq n} = -2M \int_0^\ell f_m \partial_s u_n ds, \quad (5.33)$$

where f_m and u_m represent the zero curvature eigenfunctions corresponding to the m^{th} and n^{th} eigenfrequencies – see Eqs. 5.25, 5.26. The zero-curvature Hamiltonian \hat{H}_0 , is invariant under a parity transformation $\hat{H}_0(s) = \hat{H}_0(-s)$. As a result, the eigenfunctions f_n and u_n are either even or odd. Since the operator ∂_s is odd under parity, the operator \hat{V} connects states of opposite parity. The coupling $V_{m\neq n}$ is non-vanishing only when m is even and n is odd, or vice-versa. In the lower panel of Fig. 5.4, we show a close-up view of the frequency spectrum overlaid with the free dispersion curves labeled by their harmonic. Level splitting occurs precisely between odd and even harmonics, which leads to the oscillatory-like behavior.

5.4 Scattering

We study the transmission and reflection of undulatory and compression waves through regions of nonzero curvature. We imagine the scattering problem as follows. Two semi-infinite straight rod segments are appended to the left and right

sides of a region of constant curvature M (*i.e.* the arc of a circle), such that both the rod and its tangents are everywhere continuous. We choose a coordinate system so that the center $s = 0$ is the symmetry point of the figure and note that the circular arc has length ℓ . The curvature jumps discontinuously from $0 \rightarrow M$ on the left, and $M \rightarrow 0$ on the right. See Fig. 5.5.

In the straight domains $|s| > \ell/2$, waves are defined by the eigenmodes and eigenfrequencies of Sec. 5.3.1. Radiative incoming and outgoing states are thus determined solely by the basis of plane wave solutions, *i.e.*, values k that satisfy the infinite rod dispersion relation. After demanding the solution be finite at $\pm\infty$, each semi-infinite rod has five such solutions: an incoming/outgoing f -wave, an incoming/outgoing u -wave, and one evanescent f -wave.

In the curved domain $s \in [-\ell/2, \ell/2]$, k can take complex values. This differs from the well-known transmission through a barrier in quantum mechanics, where the allowed k values are either purely real or imaginary [132]. In general, states with real k correspond to propagating solutions, and facilitate transmission. We refer to the number of propagating solutions in the curved region as the number of *channels*, whereby a wave may be transmitted through the curved domain. Before computing transmission/reflection coefficients for an incoming plane wave, we study how the number of available channels is set by the combination of both the curvature of the rod and the frequency of an incoming plane wave.

The characteristic equation is found by demanding that the eigenvalue problem defined by Eq. 5.17 with Hamiltonian given by Eq. 5.20 has a solution. This is ensured provided

$$\det \left[\omega^2 \mathbf{1} - \hat{H}(k, M) \right] = 0. \quad (5.34)$$

We find the characteristic equation for $\kappa = k^2$ is cubic:

$$\kappa^3 - \omega^2 \kappa^2 - \omega^2 \kappa - \omega^2 (M^2 - \omega^2) = 0. \quad (5.35)$$

Real solutions $\kappa < 0$ and $\kappa > 0$ correspond to evanescent and propagating waves respectively. Complex κ corresponds to damped propagating waves.

The number of channels is twice the number of real, positive roots κ . These roots are a function of frequency and curvature. At zero curvature ($M = 0$), there are three roots at $\kappa = \pm\omega, \kappa = \omega^2$, leading to four channels (two pure f -waves, and two pure u -waves). At nonzero M , Descartes' rule of signs states that the number of positive (negative) roots is equal to or less than (by an even number) the number of sign changes of the coefficients when ordered in decreasing powers of κ ($-\kappa$).

For $M > \omega$, the polynomial coefficients undergo one sign change. There is only one positive root. When $0 \leq M < \omega$, Descartes' rule determines that there are either two or zero positive roots. In the limit $M = 0$, we already know that the characteristic equation contains two positive roots, and has a positive y -intercept. Increasing M will only serve to shift the characteristic polynomial downward, while keeping the y -intercept positive for $0 \leq M < \omega$. This shift cannot remove the two positive roots. We conclude that for $0 \leq M < \omega$ the characteristic polynomial has two positive roots.

In summary, there are four available channels when $0 \leq M < \omega$, but for $M > \omega$ there are only two available channels. The reduction in the number of channels with decreasing frequency can be traced back to the vanishing of f dominated eigenmodes for frequencies $\omega < M$. However, the two available channels are not pure u -modes, but instead some combination of f and u displacements. This mixing of the modes allows pure f or u modes to interconvert in the presence of curvature, which has

implications for phonon transmission through curved regions.

5.4.1 Transmission/reflection through constant curvature

We consider the case of an incoming, purely f mode wave $e^{i\sqrt{\omega}s}|f\rangle$, or a purely u mode wave $e^{i\omega s}|u\rangle$. In both cases, we take the incident wave to have unit amplitude far to the left of the circular arc. The wave, scattered by the curved region, produces two transmitted f and u waves with transmission amplitudes t_f and t_u , two reflected waves with amplitudes r_f and r_u , and two evanescent waves with amplitudes r_f^E and t_f^E , which decay exponentially away from $s = \pm\ell/2$. The situation is summarized in Fig. 5.5.

The transmission (reflection) coefficient, denoted by a capital letter T (R), is defined as the ratio of the outgoing flux of amplitude to the incoming flux. The flux is given by the product of the amplitude squared times the group velocity. For an incoming f wave of unit amplitude, the f -mode transmission/reflection coefficients are

$$T_f = |t_f|^2, \quad R_f = |r_f|^2. \quad (5.36)$$

However, since bending and compression waves obey different dispersion relations, we must account for their difference in group velocity. Compression u -waves have unit velocity, while bending waves have a group velocity of $d\omega/dk = 2\sqrt{\omega}$. For an incoming f wave, the transmitted/reflected u waves are given by

$$T_u = \frac{|t_u|^2}{2\sqrt{\omega}}, \quad R_u = \frac{|r_u|^2}{2\sqrt{\omega}}. \quad (5.37)$$

To solve for the transmission/reflection coefficients, we must explicitly solve Eq. 5.17 at nonzero M , and then employ the boundary conditions – Eqs. 5.14-5.16 – to stitch together solutions at the boundaries $s = \pm\ell/2$.

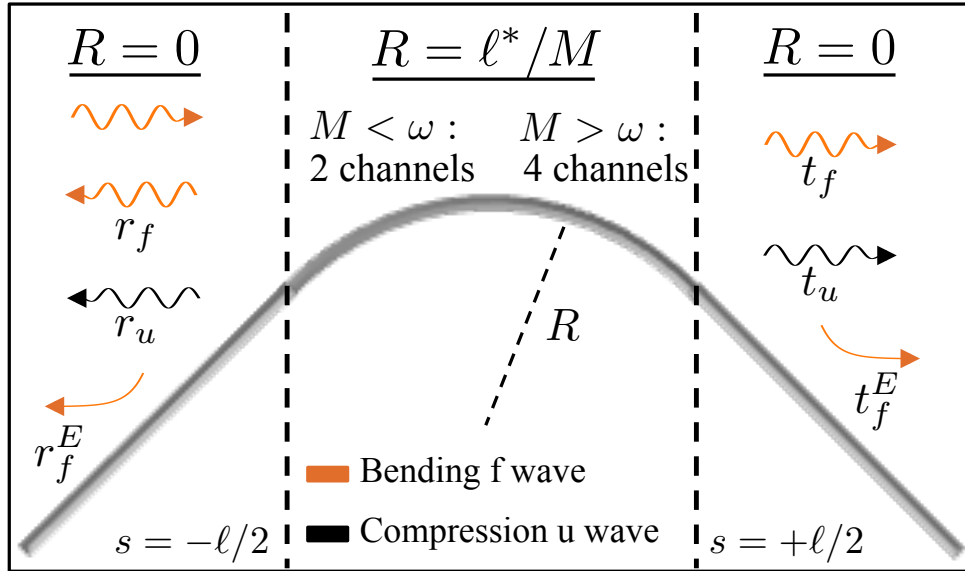


Figure 5.5: (color online) Schematic representation of an elastic rod (solid gray line) formed by adjoining two semi-infinite straight rods at the (black) dashed lines to the left ($s = -\ell/2$) and right ($s = \ell/2$) of the curved rod segment (arc of a circle with radius R), such that the rod and its tangent are everywhere continuous. We consider the scattering of an incoming bending f wave from the left, through the region of constant curvature M . Curvy arrows correspond to propagating asymptotic states, and decaying arrows to evanescent states. The darker (lighter) colors refer to u (f) modes. There are six unknown transmission/reflection amplitudes. In the curved region, there are either two or four propagating channels, determined by the value of M .

Since we are looking for plane wave solutions of the form $|\psi(s)\rangle = e^{iks} |\psi_k\rangle$, we shall reformulate Eq. 5.17 as an eigenvalue problem of the operator ∂_s at fixed ω . This is accomplished by reducing all higher order derivatives ∂_s through the introduction of new fields $f_a \equiv \partial_s^a f$ and $u_a = \partial_s^a u$, for integers $a \geq 0$. The resulting system of equations may be written as a vector differential equation

$$\partial_x |\chi\rangle = \hat{A} |\chi\rangle \quad (5.38)$$

for six-dimensional vector

$$|\chi\rangle = \begin{pmatrix} u_0 \\ u_1 \\ f_0 \\ f_1 \\ f_2 \\ f_3 \end{pmatrix} \quad (5.39)$$

and matrix

$$\hat{A} = \begin{pmatrix} 0 & 1 & 0 & 0 & 0 & 0 \\ -\omega^2 & 0 & 0 & M & 0 & 0 \\ 0 & 0 & 0 & 1 & 0 & 0 \\ 0 & 0 & 0 & 0 & 1 & 0 \\ 0 & 0 & 0 & 0 & 0 & 1 \\ 0 & M & \omega^2 - M^2 & 0 & 0 & 0 \end{pmatrix}. \quad (5.40)$$

The boundary conditions are now algebraic relations amongst all these fields. For a trial solution of the form $e^{iks} |\chi_k\rangle$, there are six possible solutions in the curved region, one for each value k that is a root of the characteristic polynomial – see Eq. 5.35. The full solution is given by a linear superposition these trial solutions with six undetermined coefficients. We also have six more undetermined coefficients

associated with the incident, reflected, and transmitted waves, giving a total of twelve undetermined coefficients. These are fixed by imposing the continuity of u , f , and f' at $s = \pm\ell/2$ (six conditions), as well as the three force balance conditions –Eq. 5.14 –at $s = \pm\ell/2$ (six conditions). Thus, we have a system of twelve linear equations that can be solved for the scattering amplitudes.

We solve these equations numerically. In Fig. 5.6, we plot the transmission and reflection coefficients for an f wave of unit amplitude incident on an interval of length $\ell = 10$, with uniform curvature $M = 3$. In the upper panel of Fig. 5.6, we show both the bending and compression transmission coefficients separately. Due to conservation of energy, we can define a total transmission coefficient $T_{\text{tot}} = T_f + T_u$, and reflection coefficient $R_{\text{tot}} = R_f + R_u$, such that their sum $T_{\text{tot}} + R_{\text{tot}} = 1$ is unity. Though we consider only an incoming bending wave, we find that curvature allows the rod to convert bending into stretching deformations, leading to the production of compression waves.

At low frequencies, $\omega < M$, the circular arc of the rod cannot support bending-dominant modes. The nonzero transmission coefficient for incident bending waves indicates that the f -waves can, in effect, tunnel through the curved region via conversion to compression u -waves, which then convert back into outgoing bending f -waves in the righthand straight segment of the rod. In the curved domain, the incoming bending mode propagates through one of the two available channels. As frequency increases through $\omega = M$, the number of available channels in the curved domain jumps from two to four. This leads to a dramatic increase in the transmission coefficient.

For higher frequencies, $\omega > M$, the circular arc can support bending-dominant

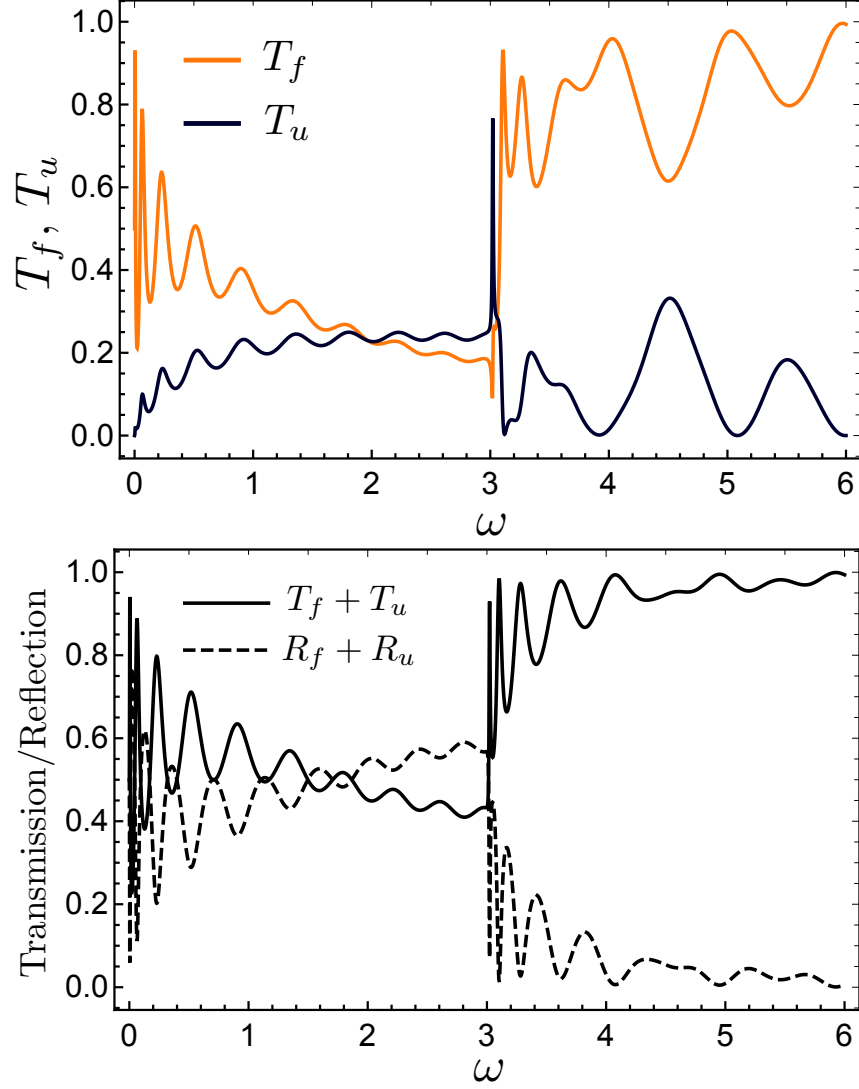


Figure 5.6: (color online) Transmission and reflection coefficients for a bending wave of unit amplitude incident on a region of length $\ell = 10$, with uniform curvature $M = 3$. Top: the transmission coefficients for bending (orange) and compression (black) waves. Bottom: the total transmission and reflection coefficients. Due to conservation of energy, the coefficients obey $T_f + T_u + R_f + R_u = 1$. Curvature mixes eigenmodes, converting the incident pure bending wave into a linear combination of bending and compression waves.

modes. As a result, the transmission coefficient for f -waves in the upper panel of Fig. 5.6 is much larger than that for u -waves, and tends to one as $\omega \rightarrow \infty$. The two principal effects of curvature – conversion from bending to compression and suppression of bending modes – diminish at high frequency.

In addition to these jumps, the transmission coefficients are oscillatory. It is well-known that peaks in the scattering amplitude correspond to bound states under a change of sign of the eigenvalue $\omega^2 \rightarrow -\omega^2$ [44]. Since f has these peaks, they must correspond to eigenmodes in the curved region, which we know to be u -dominant. Therefore, the incident bending wave uses these u -dominant modes to “tunnel” through the curved region.

When $\omega < M$, the upper panel of Fig. 5.6 shows T_f and T_u oscillating in phase. This supports idea that bending modes propagate via compression-dominated eigenmodes in the curved domain. Alternatively, for $\omega > M$, T_f and T_u oscillate out of phase. Peaks in T_f occur at frequencies corresponding to bending-dominated bound states. The fact that T_f and T_u are now out of phase shows that bending f waves are not traversing the curved region by conversion into compression u waves.

Finally, we observe that T_f is a decreasing function of frequency in the domain $0 \leq \omega < M$, while T_u is an increasing function of frequency on that same domain. Transmission of bending waves is a minimum for frequencies just below $\omega = M$. This suggests that bending waves are most effective at tunneling through curvature for both small and large frequencies.

In Fig. 5.7 we show the transmission and reflection coefficients for the case of an incoming u -wave. We find similar results. The main difference lies at frequencies $\omega < M$. Bending waves arise only if they are produced via mode coupling in the

curved domain. We find that T_f follows T_u , decreasing as frequency goes to zero, in contrast to its behavior for a purely bending incoming wave.

5.5 Conclusion

We investigate the interplay of bending and stretching in a curved, one-dimensional elastic rod. This is the simplest model that retains both bending and stretching deformations, and allows their coupling via the geometry of the unstressed state [7]. In the limit of small deformations, we find a set of two coupled equations for out-of-plane deformations f and in-plane deformations u , corresponding to bending and stretching respectively. These equations are the one-dimensional analog of the linearized shallow shell equations for a thin elastic shell. In fact, those equations reduce to the ones we study here in the limit of a membrane in which spatial variations occur along one direction only.

We find that there are two principal effects of curvature. The first is the opening of a frequency gap in the dispersion relation. This prevents bending f -modes with frequencies $\omega < M$, with ω and M being the dimensionless frequency and curvature respectively. This is the simpler one-dimensional equivalent of the suppression of bending undulations on membranes at areas of positive Gauss curvature [153, 31]. For a finite rod with discrete frequency spectrum, the restriction of $\omega > M$ for bending eigenfrequencies causes eigenfrequencies to cross with increasing curvature. By slowly bending a ringing rod, one can, in effect, “hear” the effects of curvature by noting the modes split into an upper branch tending to the curve $\omega = M$, and a lower branch tending to zero. In this restricted sense, one can indeed hear changing curvature in a rod. We also note that one observes an oscillation of eigenfrequencies

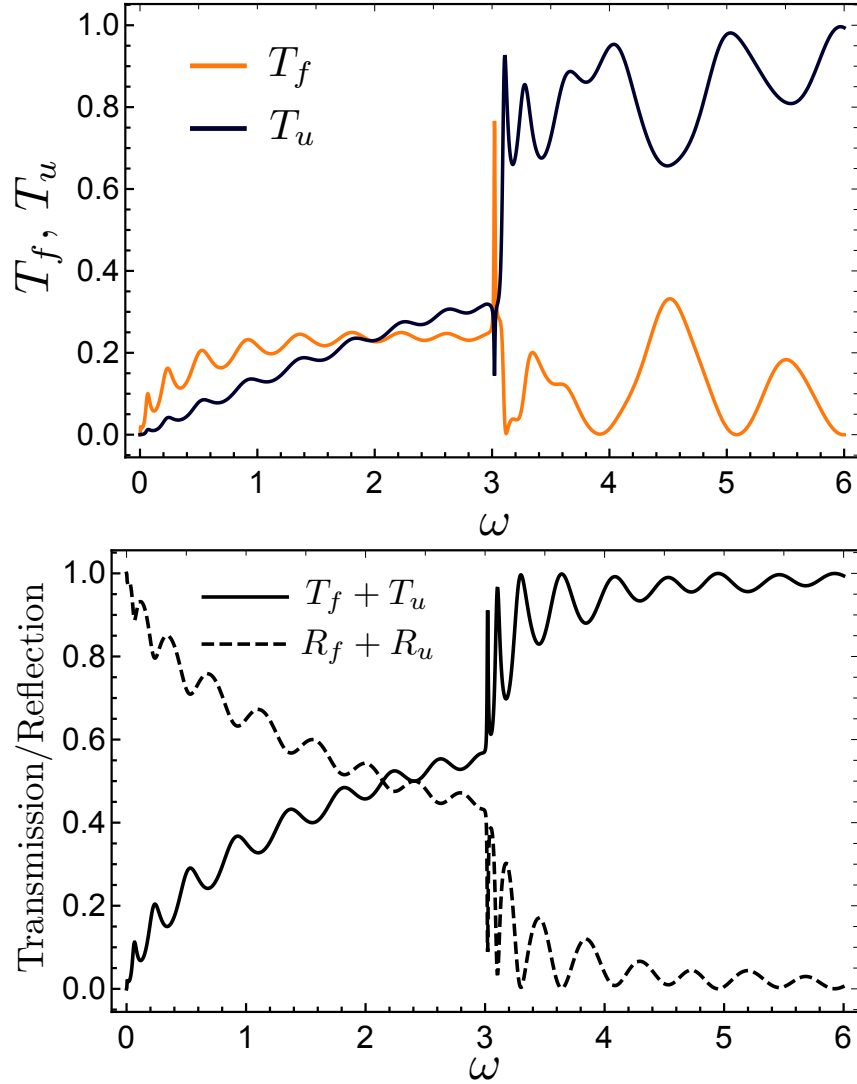


Figure 5.7: (color online) Transmission and reflection coefficients for a compression wave of unit amplitude incident on a region of length $\ell = 10$, with uniform curvature $M = 3$. Top: the transmission coefficients for bending (orange) and compression (black) waves. Bottom: the total transmission and reflection coefficients. In contrast to an incident bending wave, see Fig. 5.6, the transmission coefficients vanish as $\omega \rightarrow 0$.

with respect to M , as consequence of level splitting among harmonics.

The second principal effect of curvature is the ability for undulatory f -waves with frequency ω , to tunnel through regions of curvature $M > \omega$. Though the curved region cannot support such bending waves, by coupling to in-plane modes, these undulatory waves can convert to compression waves in order to tunnel through curvature. This tunneling effect may be significant for understanding the propagation of flexural (bending) phonons over large distances in rods or membranes with complex curvature in their stress-free state. Physical examples should include the propagation of phonons in bent carbon nanotubes or ribbons, as well as the propagation of membrane undulations along cell membranes [30].

One may inquire if multiple scattering of bending waves from randomly curved surfaces can lead to localization, and then consider how the “tunneling” of bending waves may affect this result. We provide answers to such questions in Chapter 6.

CHAPTER 6

Geometrical diffusion of undulatory waves on a warped membrane

6.1 Introduction

Thin, elastic shells, whose lateral size is much larger than their thickness, arise in a diverse array of contexts and across systems spanning several orders of magnitude in length [70, 155, 14]. Though the initial theory was formulated more than a century ago, shells that retain curvature in the stress-free state exhibit complex solutions due to geometrically induced nonlinearity, which has continued to inspire research [153, 87, 13]. The mechanical properties of shells with curved stress-free states is vital to the functionality of a number of biological applications, including red blood cells [156, 120, 121], viral capsids [91, 61, 81, 103, 73], and plant morphogenesis [25]. Though these latter examples lack well defined elastic continua, they have nevertheless been successfully studied using thin shell theory.

The mechanics of thin shells are determined by geometry, and shells of different curvature in the stress-free state can exhibit wildly different characteristics [127, 110, 126, 89]. Due to Gauss' *theorema egregium*, Gaussian curvature couples the typically soft bending undulations to the much stiffer stretching deformations. As a result,

areas of positive Gauss curvature suppress bending undulations [153], which can lead to spatially heterogeneous pockets of large undulations separated by boundary curves of zero normal curvature, as has been observed in the fluctuations of red blood cells [30]. As undulations typically represent the softest elastic modes, these can have serious consequences on the ability for shells to equilibrate, which has applications for the stability of cell membranes with actively driven pumps.

An examination of undulatory waves in the geometric optics limits shows that Gauss curvature scatters undulatory waves, and can even lead to total internal reflection at boundaries where the sign changes [31]. This suggests that for thin shells with random stress-free curvature, energy transport could be severely slowed, if not localized, purely as a consequence of geometry.

In this manuscript, we present an analysis of the propagation of undulatory waves through randomly curved thin shells that, in contrast to the large literature of wave propagation in random media [60], is driven entirely by geometry. Wave propagation in random media has been extensively studied [3, 130, 151, 140, 20] across a broad array of subjects [19, 76, 12], which we use as a guide.

The outline of this paper is as follows. First, a general consequence of random scattering is to shift energy propagation from ballistic to diffusive, which we quantitatively compute in the weak scattering limit. This is done via a hydrodynamic derivation, looking at the long length/time limits of energy transport [140, 154, 8]. In Appendix D.4, we present an alternative diagrammatic derivation in terms of the well-known ladder diagram approximation [3, 130, 151, 140, 20]. Time reversal invariant systems possess an additional contribution in the hydrodynamic limit, *weak localization* [2, 160, 149], that serves to inhibit diffusion. After computing the weak

localization correction, we consider the behavior of waves in the strong scattering regime. At strong scattering, waves can undergo a localization transition [5, 147], whereby they are spatially localized even in the absence of energy barriers. We extend our weak localization result to the strong scattering limit via a self-consistent condition [154], where we find that undulatory waves exhibit the same exponentially large localization length endemic to other two dimensional systems, such as electrons in a random potential [140].

Finally, we attempt to summarize our results in the limits of waves propagating through large/small disorder where the weighty expressions simplify.

6.2 Generalized Donnel-Mushtari-Vlasov (DMV) linearized shallow shell theory

We define membranes as a particular class of thin shells. Membranes are elastic media with two internal dimensions describing in-plane stretching deformations, and d_c surface normals describing the direction of bending undulations, embedded in a $d_c + 2$ dimensional space. Throughout this manuscript, we employ the convention that Greek indices correspond to the d_c normal directions, and Latin indices to the two internal dimensions. Bold-face letters refer to vectors in the $(d_c + 2)$ dimensional embedding space.

The purpose of this generalization to arbitrary embedding dimension is to later allow us to use the self-consistent screening approximation (SCSA) to partially resum perturbation series encountered upon disorder averaging (see Appendix D.1) [77, 78]. Ultimately, we are interested in the physically realizable case of $d_c = 1$, which we

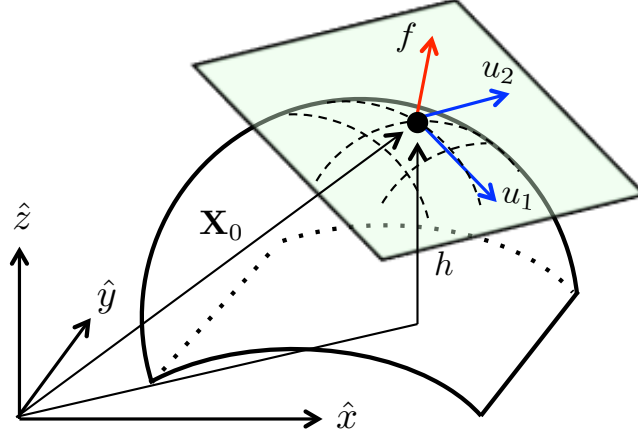


Figure 6.1: (color online) parametrization of a physical membrane middle surface \mathbf{X}_0 in the Monge representation, with small deformations f , u_1 , and u_2 given in normal coordinates. Displacements u_1, u_2 (in blue) are along the local surface tangent of the curved background surface, while displacements f (in red) are in the direction of the local surface normal. Misalignment of the local surface normal with the global \hat{z} direction is responsible for additional curvature terms in the strain (see Eq. 6.8).

hereafter refer to as physical membranes.

To isolate the role of geometry, we focus our analysis on warped membranes [77, 78] (for behavior of these membranes under thermal fluctuations see Refs [127, 126, 110, 89]); these are nearly flat membranes of internal volume L^2 , with stress-free local height configuration that can be given in the Monge representation [112] by a quenched, random background height field $h_\beta(\mathbf{x})$. Specifically, the stress-free membrane is described by the vector

$$\mathbf{X}_0(x_a) = x_a \mathbf{t}_a + h_\beta \mathbf{n}_\beta, \quad (6.1)$$

where \mathbf{t}_a represent the local surface tangents, and \mathbf{n}_β the local surface normals. See Fig. 6.1 for details. The total displacement field after small deformation is denoted $\mathbf{X}(x_a)$. The quenched height field is a random variable, whose Fourier coefficients

$$h(\mathbf{p}) = \frac{1}{L^2} \int d^2x h(\mathbf{x}) e^{-i\mathbf{p}\cdot\mathbf{x}}, \quad (6.2)$$

are sampled from a Gaussian distribution with zero mean, and variance

$$\langle h_\alpha(\mathbf{p}) h_\beta(\mathbf{p}') \rangle = \frac{\gamma \delta_{\alpha\beta} \delta_{\mathbf{p}, -\mathbf{p}'}}{L^2 \mathbf{p}^{2d_H}}. \quad (6.3)$$

The parameter γ specifies the amplitude of the quenched height field and determines the strength of disorder. We focus on the experimentally relevant cases $d_H = 0, 2, 4$, which may be realized in biological contexts by rapid polymerization of fluctuating lipid bilayers [84, 131, 78].

To quadratic order, the change in potential energy about a particular configuration $\mathbf{X}(x_a)$ is [77]

$$\mathcal{U} = \frac{1}{2} \int d^2x \{ 2\mu(U_{ab})^2 + \lambda(U_{cc})^2 + \kappa(K_{cc})^2 \}. \quad (6.4)$$

The tensors U_{ab} and K_{ab} represent the variation in the metric tensor and generalized bending tensor respectively, from their background configurations;

$$U_{ab} = \partial_a \mathbf{X} \cdot \partial_b \mathbf{X} - \delta_{ab}, \quad \mathbf{K}_{ab} = \partial_a \partial_b \mathbf{X} - \mathbf{d}_{ab}, \quad (6.5)$$

and we have defined the quenched background curvature tensor

$$\mathbf{d}_{ab} = (\partial_a \partial_b h_\beta) \mathbf{n}_\beta. \quad (6.6)$$

Ignoring small deformations of $\mathcal{O}((\partial_a h_\beta)^2)$, the background metric tensor is flat (δ_{ab}). The background curvature tensor (second fundamental form [115, 37]) then encodes all effects of the disordered geometry.

We decompose the deformation vector $\mathbf{X} = \mathbf{X}_0 + \delta\mathbf{X}$ into a background configuration \mathbf{X}_0 plus small deformation $\delta\mathbf{X}$. The latter is parametrized in normal coordinates [112], separating local strain into in-hyperplane displacements, $u_a(x_a)$, and out-of-hyperplane displacements, $f_\beta(x_a)$, via

$$\delta\mathbf{X} = u_a \mathbf{t}_a + f_\beta \mathbf{n}_\beta. \quad (6.7)$$

The equations of motion derived from Eq. 6.4 are formidable. We work in the limit where variations in curvature are slow on the scale of characteristic deformation wavelength. This is summarized as the condition $w \ll \lambda \ll |R|$, for w the membrane thickness, λ the characteristic deformation wavelength, and R the average radius of curvature. Utilizing the definition of the tangent vector, $\mathbf{t}_a = \partial_a \mathbf{X}$, this leads to the linearized strain fields

$$U_{ab} = \frac{1}{2}(\partial_a u_b + \partial_b u_a) - f_\alpha \partial_a \partial_b h_\alpha, \quad \mathbf{K}_{ab} = (\partial_a \partial_b f_\alpha) \mathbf{n}_\alpha. \quad (6.8)$$

This is the lowest order coupling of bending undulations to Gauss curvature. Deformations f_β are considered small compared to h_β , and hence nonlinear terms may be neglected. In terms of the fields u_a, f_β , the elastic energy now reads:

$$\begin{aligned} \mathcal{U} = \frac{1}{2} \int d^2x \left\{ \kappa (\nabla^2 f_\beta)^2 + u_a \nabla^2 \left((\lambda + 2\mu) \hat{P}_{ab}^L + \mu \hat{P}_{ab}^T \right) u_b \right. \\ \left. + 2\mu \text{Tr} \left(\left(\hat{P}_{ab}^T f_\alpha \partial_b \partial_c h_\alpha \right)^2 \right) + \lambda \left(\hat{P}_{ab}^T f_\alpha \partial_a \partial_b h_\alpha \right)^2 \right. \\ \left. + 2\lambda \partial_a u_a \left(\hat{P}_{bc}^T f_\alpha \partial_b \partial_c h_\alpha \right) \right\}, \end{aligned} \quad (6.9)$$

where we have defined the projection operators

$$\hat{P}_{ij}^L = \nabla^{-2} \partial_i \partial_j, \quad \hat{P}_{ij}^T = \delta_{ij} - \hat{P}_{ij}^L. \quad (6.10)$$

The first line of Eq. 6.9 is the elastic energy of a flat plate. In-hyperplane deformations split into longitudinal and transverse components. The second line penalizes bending in regions of positive Gauss curvature. The third line is the linear coupling between bending and stretching, which can allow undulations to *tunnel* through regions of positive Gauss curvature. Only the longitudinal component of $u_a(x_a)$ couples.

To find dynamical solutions, we must form an action by including a kinetic energy density. Since in-hyperplane displacements relax much faster than bending undulations, we approximate that the u_a fields respond instantaneously to deformation. We therefore only include an undulatory kinetic energy density $(\sigma/2)(\partial_t f_\beta)^2$, for σ the surface mass density. Furthermore, since u_a is simply a constraint field, we may eliminate it by setting it equal to its equation of motion, yielding an effective action describing the dynamics of undulatory waves subject to a long range potential. As the membrane length L is considered large, its bulk properties do not depend on boundary condition, which we will assume to be periodic. We switch to and from Fourier space via

$$f(\mathbf{x}) = \sum_{\mathbf{p}} f_{\mathbf{p}} e^{i\mathbf{p}\cdot\mathbf{x}}, \quad (6.11a)$$

$$f_{\mathbf{p}} = \frac{1}{L^d} \int d^d x f(\mathbf{x}) e^{-i\mathbf{p}\cdot\mathbf{x}}. \quad (6.11b)$$

Here, and for the remainder of the manuscript, bold face refers to vectors in the internal two-dimensional space. The summations run over $p_1, p_2 = 2\pi n/L$, for $n \in \mathbb{Z}$. In Fourier space we find the effective undulation action [127, 78]

$$S = S_0 + S_{\text{int}}, \quad (6.12)$$

$$S_0 = \frac{L^2}{2} \sum_{\mathbf{q}} (\kappa q^4 - \sigma \omega^2) f_{\mathbf{q}} f_{-\mathbf{q}}, \quad (6.13)$$

$$S_{\text{int}} = \sum_{\substack{\mathbf{q}_2 + \mathbf{q}_4 = -\mathbf{q} \\ \mathbf{q}_1 + \mathbf{q}_3 = \mathbf{q}}} \frac{L^2}{d_c} \mathbf{q}_1^i \mathbf{q}_1^j R_{ij,kl}(\mathbf{q}) \mathbf{q}_2^k \mathbf{q}_2^l h_{\mathbf{q}_1}^\alpha h_{\mathbf{q}_2}^\beta f_{\mathbf{q}_3}^\alpha f_{\mathbf{q}_4}^\beta, \quad (6.14)$$

where we have defined the interaction tensor

$$\hat{R}_{ij,kl} = \frac{\tilde{\mu}}{2} \left(\hat{P}_{ik}^T \hat{P}_{jl}^T + \hat{P}_{il}^T \hat{P}_{jk}^T + \frac{2\tilde{\lambda}}{\tilde{\lambda} + 2\tilde{\mu}} \hat{P}_{ij}^T \hat{P}_{kl}^T \right). \quad (6.15)$$

This form is valid for arbitrary internal dimension. For physical membranes with two internal dimensions, the indices are irrelevant and we can write the simpler form

$$R_{ij,kl}(q) = \frac{Y}{2d_c} P_{ik}^T(q) P_{jl}^T(q), \quad (6.16)$$

where Y is the two dimensional Young's modulus

$$Y = \frac{4\mu(\lambda + \mu)}{\lambda + 2\mu}. \quad (6.17)$$

The equations of motion are typically written including the displacements u_a , and are derived by variation of the elastic energy in Eq. 6.9. These, in turn, are further reduced by eliminating u_a in terms of a scalar Airy stress function χ , defined by its relation to the stress tensor $\delta\mathcal{U}/\delta U_{ab} = \epsilon_{ac}\epsilon_{bd}\partial_c\partial_d\chi$. In terms of χ and f , we find the Donnell-Mushtari-Vlasov (DMV) linearized shallow shell equations [115, 31, 153]

$$\frac{1}{Y} \nabla^4 \chi + \hat{\mathcal{L}} f = 0 \quad (6.18)$$

$$\kappa \nabla^4 f - \sigma \frac{\partial^2 f}{\partial t^2} - \hat{\mathcal{L}} \chi = 0. \quad (6.19)$$

The operator

$$\hat{\mathcal{L}} = \epsilon_{ac}\epsilon_{bd}(\partial_a\partial_b h)\partial_c\partial_d, \quad (6.20)$$

contains the quenched random height field, and encodes undulatory scattering due to curvature. Though for elastic continua Y represents a Young's modulus and κ a bending rigidity, these may alternatively be viewed as phenomenological parameters governing the strength of stretching and bending respectively when the membrane is not derivable from elastic continua. Eqs. 6.18, 6.19 represent the main equations of motion for physical membranes in linearized shallow shell theory.

By formally integrating out the fields χ , we find the f field experiences an effective potential $\hat{V} = \hat{\mathcal{L}}\nabla^{-4}\hat{\mathcal{L}}$. Via the Gauss-Bonnet theorem [112], the Riemann curvature is equal to twice the Gauss curvature. Since the metric is flat, the total Gauss curvature is then given by the determinant of the total bending tensor $\mathbf{d}_{ab} + \mathbf{K}_{ab}$ (these are $d_c + 2$ dimensional vectors). To linear order in f , $\delta R(\mathbf{x}, t) = \hat{\mathcal{L}}f$ represents the local change in Gauss curvature. Geometry can be viewed as inducing a two-body ∇^{-4} potential acting between different regions of Gauss curvature, attractive/repulsive between opposite/same sign, as a response to the membrane trying to flatten [113].

6.3 Signatures of localization

We now illustrate several quantities that measure the degree of localization and diffusion for undulatory waves. Conserved quantities are particularly useful, as they retain information about an initial injected disturbance at both long times and after disorder averaging, and have the potential for diffusive dynamics. Their propagation through the membrane (or lack thereof) acts as a marker for the spatial localization of waves.

We give two examples. First, the equations of motion are time reversal invariant, indicating total energy is conserved. Transport of energy across the membrane gives information on heat transfer and the thermal conductivity of the system, both of which are of interest in mechanics of cellular membranes [30]. Second, the Gauss-Bonnet theorem stipulates that the integral of the Riemann curvature over the membrane is a fixed, topological value, identical over all instances of disorder. For physical membranes, the Gauss curvature is proportional to the Riemann curvature and hence can play the role of a conserved quantity.

An additional quantity to study is the kinetic energy, which for monochromatic waves is proportional to the disorder averaged local intensity $\langle |f_\beta(\mathbf{x})|^2 \rangle$. We will find that undulation intensity obeys diffusive dynamics, and is the primary cause of diffusive energy/curvature transport. We thus focus our efforts on intensity, which is fortunate, as working with the total energy is analytically challenging.

In order to describe wave propagation, we translate the problem into the language of Green's functions [63, 72]. We consider a physical membrane ($d_c = 1$) for ease of notation, with generalization to higher dimensionality straightforward. Without loss of generality, the equation of motion may be written as $(\partial_t^2 - \hat{A})f(\mathbf{x}, t) = j(\mathbf{x}, t)$, for some operator \hat{A} derived from minimization of the action in Eq. 6.12, and arbitrary undulation source $j(\mathbf{x}, t)$. Associated with this is a Green's function, $G(x, x'; t, t')$, that satisfies the equation $(\partial_t^2 - \hat{A})G(x, x'; t, t') = \delta(x - x')\delta(t - t')$.

We are interested in the source-free situation where at times $t < 0$, the membrane is in mechanical equilibrium ($f(\mathbf{x}, 0) = 0$), then at $t = 0$ it is plucked ($\partial_t f(\mathbf{x}, 0) = 1$) with unit velocity at the origin, thereby injecting energy into the system localized at the origin. This is accomplished in the Green's function formalism by imposing

initial conditions [72]

$$\partial_t G^+(\mathbf{x}, \mathbf{x}'; 0) = \delta(\mathbf{x} - \mathbf{x}'), \quad (6.21)$$

$$G^+(\mathbf{x}, \mathbf{x}'; t < 0) = 0. \quad (6.22)$$

Provided the initial pluck is truly δ -like, the main result is that we can everywhere replace the time-dependent amplitude by a Green's function via

$$f(\mathbf{x}, t) = G^+(\mathbf{x}, 0; t). \quad (6.23)$$

We now define the disorder averaged quantity $\phi(\mathbf{x}, t)$, which represents the intensity of undulations across the membrane in response to an initial pluck at the origin:

$$\phi(x, t) = \langle G^+(\mathbf{x}, 0; t) G^-(0, \mathbf{x}; t) \rangle. \quad (6.24)$$

Here and throughout, angular brackets refer to disorder averaging over the quenched random height field. Our principle object of study is the four-point function

$$\phi_{pp'}(\mathbf{q}, \Omega) \equiv \langle G_{\omega_+}^+(\mathbf{p}_+, \mathbf{p}'_+) G_{\omega_-}^-(\mathbf{p}_-, \mathbf{p}'_-) \rangle, \quad (6.25)$$

which gives the Fourier components of $\phi(\mathbf{x}, t)$ upon summation over p, p' and integration of ω . We have introduced the shorthand $p_{\pm} \equiv p \pm q/2$ and $\omega_{\pm} \equiv \omega \pm \Omega/2$. We refer to ω as the *internal* frequency, and Ω as the *external* frequency. The four-point function is the product of an advanced and retarded propagator, and has the necessary phase cancellation to propagate across multiple scattering processes. In terms of the four-point function, the disorder averaged kinetic energy density is

$$T(\mathbf{x}, \Omega) = \frac{1}{2} \int \frac{d\omega}{2\pi} (\omega^2 + \Omega^2/4) \sum_{pp'q} e^{i\mathbf{q}\cdot\mathbf{x}} \phi_{pp'}(\mathbf{q}, \Omega). \quad (6.26)$$

We measure the degree of localization by the normalized spatial variance of kinetic energy in the long-time limit. For diffusive waves, the variance grows linearly in time,

while for propagating waves it grows quadratically. This leads us to define the kinetic energy diffusion coefficient [63]

$$D_E = \lim_{t \rightarrow \infty} \frac{1}{t} \frac{\int x^2 T(x, t) dx}{\int T(x, t) dx}. \quad (6.27)$$

We enact the long time limit by means of the identity [102]

$$\lim_{t \rightarrow \infty} f(t) = \lim_{\eta \rightarrow 0} \eta \int f(t) e^{-\eta t} dt. \quad (6.28)$$

Upon Fourier transform, we obtain

$$D_E = \lim_{\eta \rightarrow 0} \frac{-2\eta^2 \int \frac{d\omega}{2\pi} \omega^2 \nabla_{\mathbf{q}}^2 |_{q=0} \sum_{kk'} \phi_{kk'}(q, -2i\eta)}{\eta \int \frac{d\omega}{2\pi} \omega^2 \sum_{kk'} \phi_{kk'}(q, -2i\eta)} \quad (6.29)$$

In general, the frequency integrations will diverge as a consequence of the δ -function singularity of the initial spike. This can be regulated by replacing the δ -function with a Gaussian impulse at $t = 0$ of width Δt . The integrations are regulated by simply adjusting the measure $d\omega \rightarrow d\omega e^{-\frac{1}{2}\omega^2 \Delta t}$. If the disorder is short-ranged, corresponding to $d_H = 0$, high frequencies are cutoff as a consequence of finite lattice spacing, and this may be the more relevant cutoff for short impulses.

We can further simplify D_E by anticipating that at small frequency Ω , the four-point function is diffusive. Indeed, borrowing the later result in Eq. 6.55,

$$\sum_{pp'} \phi_{pp'} = \frac{\pi\nu/(2\sigma^2\omega^2 L^2)}{-2\eta + D(\omega)q^2}. \quad (6.30)$$

we obtain the much simpler form

$$D_E = 4 \frac{\int d\omega \nu(\omega) D(\omega)}{\int d\omega \nu(\omega)}, \quad (6.31)$$

where the frequency dependence of ν has been made explicit. The function ν represents the density of states, and suggests the quantity $D(\omega)$ is a frequency dependent intensity diffusion coefficient.

In fact, $D(\omega)$ corresponds precisely to the diffusion coefficient of intensity in response to a harmonic, transverse load applied at the origin. To show this, we note that the four-point function corresponding to harmonic loading at the origin is equivalent to that of Eq. 6.25, so long as we take $\Omega \rightarrow -2i\eta$ and pin the internal frequency to ω as opposed to integrating. The variance in intensity is then given by Eq. 6.29 if we apply the same conditions, which after simplification yields the frequency dependent diffusivity

The calculation of $D(\omega)$ is a point of contact with numerical simulations that are solved in the frequency domain. Specifically, given knowledge of the solution $f(\mathbf{x}, \omega)$ in response to harmonic loading, one identifies

$$D(\omega) = -\frac{1}{2} \lim_{\eta \rightarrow 0} \eta \frac{\int d^2x x^2 |f(\mathbf{x}, \omega - i\eta)|^2}{\int d^2x |f(\mathbf{x}, \omega - i\eta)|^2}. \quad (6.32)$$

6.4 Hydrodynamics

The four-point function defined in Eq. 6.25 is the fundamental quantity governing diffusion/localization. In this section we present a derivation of its diffusive behavior at long length/time scales.

The four point function is a disorder averaged object, which may in general be decomposed into a sum of independently averaged Green's functions, plus all connected averages. Implementing this procedure leads to the Bethe-Salpeter (BS) equation [154]

$$\phi_{pp'}(q, \Omega) = \langle G_{p_+}^+(\omega_+) \rangle \langle G_{p_-}^-(\omega_-) \rangle \times \quad (6.33)$$

$$\left(\delta_{pp'} + \sum_k U_{pk}(q, \Omega) \phi_{kp'}(q, \Omega) \right).$$

The lack of a summation over frequencies is a consequence of quenched disorder. The frequency dependence can be grouped into a single three-vector (\mathbf{p}, ω) . When not explicitly written, the three-vector is implied. The function $U_{pk}(q, \Omega)$ represents the irreducible vertex, and contains all information on connected averages between retarded/advanced Green's functions.

The utility of the BS equation, is that it allows us to work in terms of only disorder averaged Green's functions. Thus, for ease of notation, we shall drop the $\langle \rangle$ brackets, and assume that all Green's functions are replaced with their disorder averaged values, unless otherwise specified.

$\langle \hat{G} \rangle$ is the Green's function corresponding to the full action of Eq. 6.12. In order to compute this, we first separate S into a part S_0 whose Green function is readily solvable, plus a perturbative piece S_{int} that contains the disorder field. It is well known that the configurational average of a translationally invariant Green's function for such a system can then be written in the Fourier basis as the inverse of the sum of the bare Green's function pertaining to S_0 , and a self energy operator $\hat{\Sigma}$, as [140]

$$\langle G_{p_{\pm}}^{\pm}(\omega_{\pm}) \rangle^{-1} = L^2 (\kappa p_{\pm}^4 - \sigma \omega_{\pm}^2) - \Sigma_{p_{\pm}}^{\pm}(\omega_{\pm}). \quad (6.34)$$

We have not yet solved for $\langle \hat{G} \rangle$. Instead, all effects of disorder averaging have been moved onto $\langle \hat{\Sigma} \rangle$. The real part of $\hat{\Sigma}$ renormalizes the phase velocity, while the imaginary part introduces a mean free path length, beyond which the phase information of a single monochromatic wave has been erased by scattering processes. We will find that the self-energy does, in fact, have an imaginary part, which implies that $\langle \hat{G} \rangle$ is a short range object, *i.e.* its disorder average vanishes exponentially with re-

spect to length. For the remainder of the manuscript, unless otherwise specified, we assume that we are in the weak scattering limit, whereby the imaginary part of the self energy is small.

The self energy obeys the useful relation $\hat{\Sigma}^+ = \left(\hat{\Sigma}^-\right)^*$. Using this in combination with the identity $AB = (A^{-1} - B^{-1})^{-1}(B - A)$, we can rewrite the BS equation to arrive at the Boltzmann equation [154]

$$\begin{aligned} \left(-\Omega + (\mathbf{v}_p \cdot \mathbf{q}) - \frac{1}{L^2} \frac{\Delta \Sigma_p(q)}{2\sigma\omega}\right) \phi_{pp'}(q) = \\ -\frac{\Delta G_p(q)}{2\sigma\omega L^2} \left(\delta_{pp'} + \sum_k U_{pk}(q) \phi_{kp'}(q)\right). \end{aligned} \quad (6.35)$$

The velocity

$$\mathbf{v}_p = \frac{2\kappa p^2}{\sigma\omega} \mathbf{p}, \quad (6.36)$$

contains an additional term $\sim q^2 \mathbf{q}$ that we have discarded in anticipation of later taking the diffusive limit. The Δ symbol means the difference between retarded and advanced quantities. We will only be concerned with its action on the self-energy and Green's function, namely

$$\Delta \Sigma_p(q) = \Sigma_{p+}^+(\omega_+) - \Sigma_{p-}^-(\omega_-), \quad (6.37a)$$

$$\Delta G_p(q) = G_{p+}^+(\omega_+) - G_{p-}^-(\omega_-). \quad (6.37b)$$

For ease of notation, when the q dependence of a quantity is not explicitly written, it is evaluated at $q = 0$, but not at $\Omega = 0$. For example, $\Delta G_p = G_p^+(\omega + \Omega/2) - G_p^-(\omega - \Omega/2)$.

We may also consider the group velocity of undulatory waves. This depends on the self energy and can be written

$$\mathbf{v}_p^G = \mathbf{v}_p \frac{1 - \delta_1}{1 + \delta_2}, \quad (6.38)$$

where we have defined the dimensionless quantities

$$\delta_1 = \frac{1}{4\kappa p^3} \frac{\partial \text{Re}\Sigma}{\partial p}, \quad (6.39)$$

and

$$\delta_2 = \frac{1}{2\sigma\omega} \frac{\partial \text{Re}\Sigma}{\partial \omega}. \quad (6.40)$$

We will encounter the function δ_1 frequently in our calculations.

Inspecting Eq. 6.35, we see that the p' index can be freely summed. Doing so allows us to work with the simpler function

$$\phi_p(q) \equiv \sum_{p'} \phi_{pp'}(q). \quad (6.41)$$

The right hand side of Eq. 6.35 is proportional to ΔG_p . In the weak scattering limit, the imaginary part of $\hat{\Sigma}$ is small and so ΔG_p as a strongly peaked Lorentzian around some value $p = p_F$ determined by the condition

$$\text{Re}G_{p_F}^{-1} = 0. \quad (6.42)$$

In alignment with the terminology appearing in hard condensed matter [4], we refer to this wavenumber p_F as the *Fermi wavenumber*, though our system is purely classical. From Eq. 6.36, we additionally define the associated Fermi velocity $v_F = 2\kappa p_F^3 / \sigma\omega$. The sharpness of ΔG_p around p_F suggests that we may approximate it as a δ -function pinning the wavenumber magnitude to $p = p_F$. Using the large L limit to replace summations with integrations, we find the identity

$$\sum_p \Delta G_p(\dots) \xrightarrow{\text{weak scattering}} \frac{i\pi\nu}{\sigma\omega} \int_0^{2\pi} \frac{d\theta}{2\pi} (\dots)|_{p=p_F}, \quad (6.43)$$

which we will make extensive use of. We have further defined the density of states per unit volume

$$\nu = \frac{p_F}{2\pi v_F (1 - \delta_1)}. \quad (6.44)$$

Combining Eqs. 6.33 and 6.43, we notice that $\phi_p(q)$ is strongly peaked around the forward direction, *i.e.* $\hat{\mathbf{p}} \cdot \hat{\mathbf{q}} = 0$. This suggests that $\phi_p(q)$ is approximately given by the first couple moments of its Legendre expansion. We define

$$S \equiv \sum_p \phi_p(q), \quad \mathbf{J} \equiv \sum_p \mathbf{v}_p \phi_p(q). \quad (6.45)$$

These represent the intensity propagation density S , and current density \mathbf{J} . The velocity \mathbf{v}_p is the zero curvature group velocity of undulations. It is proportional to, yet not necessarily equal to, the transport velocity, *i.e.* the average velocity of intensity across the membrane. Solutions S and \mathbf{J} are found by taking the first two moments of the Boltzmann equation (Eq. 6.35).

The first moment is found by summing both sides of the Boltzmann equation over p, p' . We obtain

$$\begin{aligned} -\Omega S + \mathbf{q} \cdot \mathbf{J} &= \frac{\pi\nu}{i\sigma\omega L^2} + \\ &+ \frac{1}{2\sigma\omega L^2} \sum_{pp'k} (\Delta\Sigma_p(q)\delta_{pk} - \Delta G_p(q)U_{pk}(q)) \phi_{kp'}(q). \end{aligned} \quad (6.46)$$

In order for S to exhibit diffusive behavior, all terms $\sim S$ in the equation must vanish in the limit $q, \Omega \rightarrow 0$. The existence of a diffusive solution is thus contingent on the vanishing of the final term. This is indeed the case, as is ensured by the Ward identity (WI)

$$\Delta\Sigma_p(q) = \sum_{p'} U_{pp'}(q)\Delta G_{p'}(q). \quad (6.47)$$

In the limit $q, \Omega \rightarrow 0$, we can replace $\Delta\Sigma_p \rightarrow 2i\text{Im}\Sigma_p$, so that the WI relates the imaginary part of the forward scattering amplitude to the total cross section. The WI is thus a generalized optical theorem [140], and depends on the type of wave equation studied [80, 150, 152]. The derivation of the WI is nontrivial and presented in Appendix D.3.

Implementing the WI yields the continuity equation

$$-i\Omega S + i\mathbf{q} \cdot \mathbf{J} = \frac{\pi\nu}{\sigma\omega L^2} + O(q^2). \quad (6.48)$$

In position space, Eq. 6.48 is of the form $\partial_t S + \nabla \cdot \mathbf{J} = \pi\nu/\sigma\omega L^2$, hence the name *continuity equation*.

In order to obtain a closed set of hydrodynamic equations, we must relate \mathbf{J} to S . If the intensity is to exhibit diffusive behavior, then the current \mathbf{J} must obey Fick's law $\mathbf{J} = -D\nabla S$, with $D(\omega)$ some diffusion coefficient to be determined. The coefficient D can, and will, depend on the internal frequency ω .

We begin by taking the second moment of the Boltzmann equation, *i.e.* applying $\sum_p (\mathbf{v}_p \cdot \hat{\mathbf{q}})(\dots)$ to both sides of Eq. 6.35. As we are interested in the long length/time limit, we retain only the lowest terms through $\mathcal{O}(\Omega, q)$. We obtain

$$q \sum_p (\mathbf{v}_p \cdot \hat{\mathbf{q}})^2 \phi_p(q) = \frac{1}{2\sigma\omega L^2} \sum_{pk} (\mathbf{v}_p \cdot \hat{\mathbf{q}}) \left(\Delta \Sigma_p(q) \delta_{pk} - \Delta G_p(q) U_{pk}(q) \right) \phi_k(q). \quad (6.49)$$

The left hand side (LHS) is the third moment of $\phi_p(q)$, and prevents a closed solution in S and \mathbf{J} . This is remedied in the usual way, by everywhere replacing $\phi_p(q)$ with its truncated Legendre expansion

$$\phi_p(q) = \frac{\Delta G_p}{i\pi\nu/(\sigma\omega)} \left(S + \frac{2}{v_p^2} (\mathbf{v}_p \cdot \hat{\mathbf{q}})(\hat{\mathbf{q}} \cdot \hat{\mathbf{J}}) \right). \quad (6.50)$$

The LHS is evaluated using the identity $\Omega_d^{-1} \int d\Omega_d (\mathbf{a} \cdot \hat{\mathbf{p}})(\mathbf{b} \cdot \hat{\mathbf{p}}) = d^{-1} \mathbf{a} \cdot \mathbf{b}$, valid for arbitrary vectors \mathbf{a} and \mathbf{b} , in any dimension d , with solid angle Ω_d . As a result, this term is simply

$$\text{LHS} = q \frac{v_F^2}{2} S. \quad (6.51)$$

The right hand side (RHS) is more difficult to simplify than it was when deriving the continuity equation, as the angular dependence in $(\mathbf{v}_p \cdot \hat{\mathbf{q}})$ prevents direct application of the WI. Inserting the Legendre expansion of $\phi_k(q)$ and using Eq. 6.43 to perform the k summation, we find that the term $\sim S$ on the RHS vanishes by means of the WI. Computing the remaining terms we find

$$\text{RHS} = \left(\frac{i\text{Im}\Sigma_{p_F}}{\sigma\omega L^2} - M_0 \right) (\hat{\mathbf{q}} \cdot \mathbf{J}) \quad (6.52)$$

where

$$M_0 = \frac{1}{i\pi\nu v_F^2 L^2} \sum_{pp'} \Delta G_p(\mathbf{v}_p \cdot \hat{\mathbf{q}}) U_{pp'}(\mathbf{v}_{p'} \cdot \hat{\mathbf{q}}) \Delta G_{p'}. \quad (6.53)$$

Collecting all terms and trivially rearranging, we arrive at Fick's Law

$$\mathbf{J} = -i\mathbf{q} \left(\frac{L^2\sigma\omega}{\text{Im}\Sigma_{p_F}} \frac{v_F^2/2}{1 - \sigma\omega L^2 M_0 / (i\text{Im}\Sigma_{p_F}(\omega))} \right) S. \quad (6.54)$$

The term M_0 in the denominator encodes the effects of coherent scattering, and is also responsible for weak/strong localization. Eqs. 6.48, 6.50 and 6.54, and complete the hydrodynamic description.

6.5 Diffusion and weak/strong localization

The hydrodynamical equations contain a wealth of information about undulatory wave propagation, whose physical meanings are opaquely hidden in M_0 and $\hat{\Sigma}$. Before directly computing the diffusion coefficient and weak localization correction, we briefly discuss computation of disorder averages in general. This has the additional benefit of laying the groundwork for analysis beyond the average intensity, for example, computing the fluctuations in intensity transport known as speckle correlations [151].

The well-known particle/wave duality in quantum mechanics affords a fruitful language for describing the propagation of undulatory on a membrane. A single undulatory wavepacket can be viewed as a *particle* that is scattered by a random *potential* resulting from Gauss curvature. In this language, the disorder averaged retarded (advanced) Green's function, $\langle \hat{G}^\pm(\mathbf{x}, \mathbf{x}'; t) \rangle$, gives the amplitude for one particle initially at position \mathbf{x}' to propagate forward (backward) in time t to point \mathbf{x} . In the weak scattering limit, this average can be computed by considering the path as consisting of a series of scattering events with the random potential. The perturbative series is ordered by the number of scatterings, which at a fixed distance $|\mathbf{x} - \mathbf{x}'|$ becomes smaller at weak curvature.

In the particle formulation, $\langle \hat{G}^\pm \rangle$ contains only single-particle information. Scattering events are independent, and there are no interference effects between undulatory waves. In contrast, the four-point function defined in Eq. 6.25 contains two-particle information. It is the disorder average of two particles, one moving forward in time and one moving backward in time (called a *hole* or *anti-particle*) to the same initial/final positions. The two particles have the potential to constructively interfere with one another, which is the source of the long-range nature of the four-point function. Viewed as waves, two-particle information encodes coherence effects in the system.

Schematically, the two particles interfere constructively when they encounter the same sequence of scattering paths. This results in a long range object for intensity transport called the *diffuson*. In the special case of return to the origin ($\mathbf{x} = \mathbf{x}'$), time reversal invariance in the action permits another solution whereby one of the particles is traversed backwards in time. This leads to another long range object that reduces diffusion, called the *cooperon*. Analysis of intensity transport in terms

of diffusons/cooperons is given in Appendix D.4, where we provide a diagrammatic derivation of the hydrodynamical equations in section 6.4. The diagrammatical analysis allows one to extend beyond the level of analysis in this manuscript. In particular, one can use the formalism to describe fluctuations in intensity, which arise from diffuson-diffuson scattering [3].

All of the information regarding diffusion is contained in the long length/time limit of the four-point function, to which we now turn. By combining the continuity equation with Fick's law (Eqs. 6.48, 6.54), we arrive at

$$\phi_{pp'}(q) = \left(\frac{-1}{2\pi\nu L^2} \right) \frac{\Delta G_p \Delta G_{p'}}{-i\Omega + Dq^2}, \quad (6.55)$$

which has the diffusive form postulated in section 6.3. The coefficient D is precisely that appearing on the righthand side of Eq. 6.31. From our hydrodynamic analysis, we further obtain

$$D^{-1} = D_0^{-1} + D_0^{-1} i\tau M_0, \quad (6.56)$$

where D_0 is the Drude-Boltzmann diffusion coefficient¹, given by

$$D_0 = \frac{1}{2} v_F^2 \tau, \quad (6.57)$$

and τ is the scattering time given by

$$\tau^{-1} = \frac{\text{Im}\Sigma_{pF}}{\sigma\omega L^2}. \quad (6.58)$$

The diffusion coefficient of Eq. 6.57 takes the standard form, implying the intensity transport velocity, v_t , is equivalent to the group velocity evaluated at the Fermi wavenumber:

$$v_t = v_F. \quad (6.59)$$

¹This name was chosen to agree with the nomenclature used for this approximation in computing the conductivity of a metal. See Ref. [3] for more details

Both D_0 and τ depend only on the self-energy, which can be obtained by computing the disorder average of only a single Green's function. By combining v_t and τ , we determine the mean free path

$$\ell = v_t \tau = v_F \tau. \quad (6.60)$$

The scattering time and mean free path represent the average time/length before an undulation wavepacket is scattered by Gaussian curvature. In position space, this corresponds to an exponential decay $\langle G^+(\mathbf{x}, 0; \omega) \rangle \sim e^{-|\mathbf{x}|/\ell}$.

Per Eq. 6.57, D^{-1} is a sum of two pieces: single-particle effects coming from D_0 , and two-particle effects mediated via the irreducible vertex $U_{pp'}$. Setting $U_{pp'}(q) = 0$ (and thereby M_0), is the Drude-Boltzmann approximation, whereby $\langle \hat{G}^+ \hat{G}^- \rangle$ is replaced by the product of its averages $\langle \hat{G}^+ \rangle \langle \hat{G}^- \rangle$.

In order to proceed further, we must further specify the irreducible vertex. Our arguments at the beginning of the section suggest coherent scattering will primarily lead to two effects: diffusion and weak localization. Anticipating this, we decompose $U_{pp'}(q)$ into the sum of two terms

$$U_{pp'}(q) \approx U_{pp'}^0(q) + U_{pp'}^{(\text{MC})}(q), \quad (6.61)$$

called the *bare* vertex $U_{pp'}^0(q)$, and the *maximally crossed* vertex $U_{pp'}^{(\text{MC})}(q)$. These are responsible for diffusion and weak localization respectively. Likewise, we decompose the diffusion coefficient into a sum of two pieces

$$D^{-1} = D_c^{-1} + D_\times^{-1}. \quad (6.62)$$

D_c represents the coherent diffusion coefficient found by choosing $\hat{U} = \hat{U}^0$. Inserting \hat{U}^0 into Eq. 6.56 and rearranging, we identify

$$D_c = D_0(1 + \delta_c)^{-1}, \quad (6.63)$$

where we have defined the reduction factor

$$\delta_c = i\tau M_0|_{U_{pp'}(q)=U_{pp'}^0}. \quad (6.64)$$

The calculation of δ_c is presented in Appendix D.2.

D_\times is the maximally crossed diffusion coefficient found by choosing $\hat{U} = \hat{U}^{(\text{MC})}$, and ignoring the D_0^{-1} contribution that has already been counted. It is explicitly given by

$$D_\times^{-1} = D_0^{-1} i\tau M_0|_{\hat{U}=\hat{U}^{(\text{MC})}}. \quad (6.65)$$

We begin by first studying the \hat{U}^0 contribution to D^{-1} .

The bare vertex is defined as the minimally disorder averaged vertex connecting two pairs of retarded and advanced propagators. For an explicit representation of $U_{pp'}^0(q)$ in terms of diagrammatic perturbation theory (Appendix D.1) see Fig. D.5. The bare vertex represents a single particle-hole scattering event. Inputting $U_{pp'}^0(q)$ into the BS equation generates all trajectories where the particle and hole scatter off the same sites, in the same order. In the diagrammatic derivation of Appendix D.4, these trajectories correspond to summing over the set of all box diagrams with uncrossed disorder lines, the so-called ladder approximation [3].

The hydrodynamic analysis has thus shown that long-range contributions to the four-point function come from summations over ladder-type diagrams, or in the position space representation, a summation over scattering events where the particle and hole traverse the same trajectory in the same order. If the system is time-reversal invariant (as is the case here) there exists an additional long-range contribution to the four-point function, found by reversing the order of scattering for one of the particles (*i.e.* running backwards in time). Using time-reversal symmetry, we can

additionally change the signs of the hole wavenumber to obtain the identity

$$\phi(p_+, p'_+; p_-, p'_-) = \phi(p_+, p'_+; -p'_-, -p_-), \quad (6.66)$$

where we have explicitly written the dependence on all four wavenumbers. Reducing to a function of only three wavenumbers we find

$$\phi_{pp'}(q) = \phi_{\frac{1}{2}(p-p'-q), \frac{1}{2}(p'-p-q)}(p + p'). \quad (6.67)$$

This identity trivially allows us to sum over all maximally crossed diagrams, by mapping them onto a summation over uncrossed diagrams. Furthermore, we know that this must be a long-range object that becomes divergent for some combination of \mathbf{p} , \mathbf{p}' and \mathbf{q} as $\Omega \rightarrow 0$, and hence can have an appreciable effect.

In Fig. 6.2, we compute $\hat{U}^{(\text{MC})}$ diagrammatically. The procedure is as follows: write the maximally crossed irreducible vertex by crossing two bare irreducible vertices and inserting the full four point function between them, uncross the diagram, then use time-reversal symmetry to reverse wavenumbers bringing it into a standard form. We find the equation [140]

$$U_{pp'}^{(\text{MC})}(q) = \sum_{k, k'} U_{\tilde{p}k}(Q) \phi_{kk'}(Q) U_{k'\tilde{p}'}(Q), \quad (6.68)$$

where \tilde{p}, \tilde{p}' and Q are defined in Fig. 6.2. As expected, $\hat{U}^{(\text{MC})}$ diverges as $\Omega, Q \rightarrow 0$, per Eq. 6.55. Working in the divergent limit where $\hat{U}^{(\text{MC})}$ is appreciable, we discard all terms $\mathcal{O}(Q)$ and perform the summations using the WI (Eq. 6.47) to obtain

$$U_{pp'}^{(\text{MC})}(Q, \Omega) = \left(\frac{-1}{2\pi\nu L^2} \right) \frac{\Delta\Sigma_{\tilde{p}}\Delta\Sigma_{\tilde{p}'}}{-i\Omega + D_c Q^2}. \quad (6.69)$$

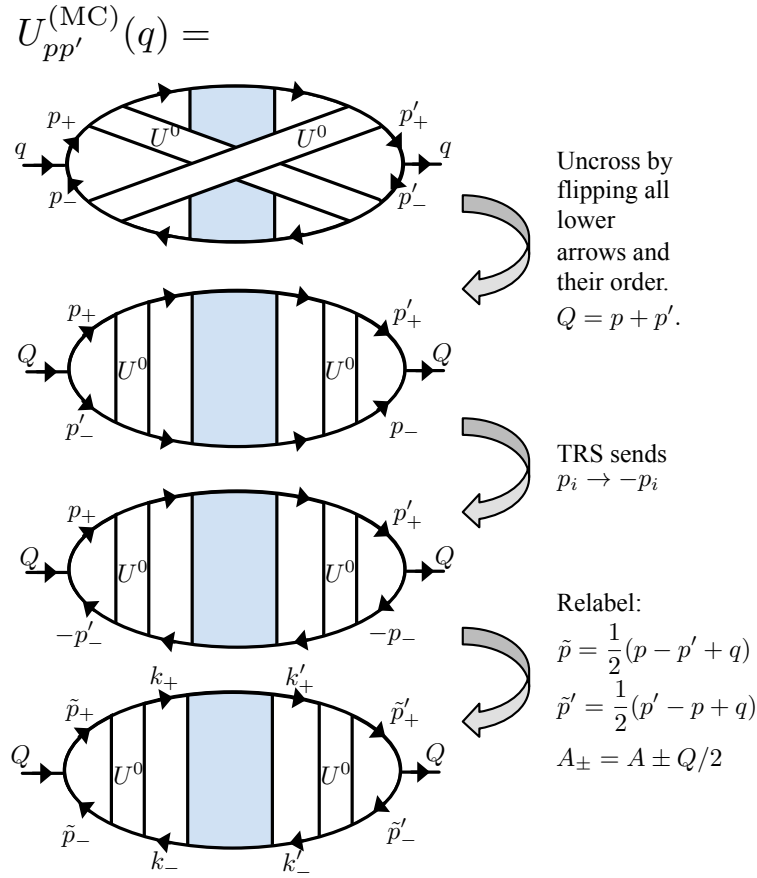


Figure 6.2: (color online) diagrammatic construction of the maximally crossed irreducible vertex. White boxes represent the bare irreducible vertex \hat{U}^0 ; the shaded box represents the diffusive four-point function in Eq. 6.55. *Crossing* refers to overlap of \hat{U}^0 vertices. The summation over maximally crossed diagrams can alternatively be viewed as summation over uncrossed diagrams with all lines on the lower rung reversed. Time-reversal symmetry allows us to flip arrow orientation bringing it to standard form.

The definition of Q tells us that $\hat{U}^{(\text{MC})}$ is maximal when $p' \approx -p$. In the wavenumber representation, p and p' correspond to the incoming and outgoing wavenumbers for an initial wave incident on the disordered media. $p \approx -p'$ thus corresponds to backscattering, which in position space corresponds to particle trajectories that return to the point of departure.

We continue the calculation of D_\times by inserting $\hat{U}^{(\text{MC})}$ into M_0 (Eq. 6.53). We work in the $Q \rightarrow 0$ limit, approximating the summation by everywhere replacing $p' = -p$. This yields the intermediate expression

$$M_0 = \frac{1}{2i\pi^2 L^4 \nu^2 v_F^2} \sum_{p, Q} (\Delta G_p)^2 (\mathbf{v}_p \cdot \hat{\mathbf{q}})^2 \frac{\Delta \Sigma_{\tilde{p}} \Delta \Sigma_{\tilde{p}'}}{-i\Omega + D_c Q^2}. \quad (6.70)$$

In the weak scattering approximation, we may ignore terms containing $(\hat{G}^\pm)^2$ inside the summation, allowing us to use $(\Delta G_p)^2 \approx -2\Delta G_p / \Delta \Sigma_p$ [140, 3]. In the diffusive limit, q is also small and we can replace \tilde{p}, \tilde{p}' with p, p' . Using Eq. 6.43 to perform the p summation and adding a factor of $(1/2)$ from the remaining angular integration we find

$$M_0 = \frac{1}{2\pi\nu} \frac{\Delta \Sigma_{pF}}{\sigma\omega L^4} \sum_Q \frac{1}{-i\Omega + D_c Q^2}. \quad (6.71)$$

Inserting M_0 into Eq. 6.65 and using the definition of τ (Eq. 6.58) we obtain the maximally crossed diffusion coefficient

$$D_\times^{-1} = D_0^{-1} \frac{1}{\pi\nu L^2} \sum_Q \frac{1}{-i\Omega + D_c Q^2}, \quad (6.72)$$

and from Eq. 6.57, the total diffusion coefficient [154]

$$D^{-1} = D_c^{-1} + D_0^{-1} \frac{1}{\pi\nu} \int \frac{d^2 Q}{(2\pi)^2} \frac{1}{-i\Omega + D_c Q^2}. \quad (6.73)$$

In the last line we have taken the continuum limit. The limits of integration over Q must be limited to the domain where diffusive transport is applicable. The upper

bound is set by the inverse mean free path ℓ^{-1} defined in Eq. 6.60, while the lower bound is set by the inverse system size L^{-1} .

In the weak disorder limit, $D \approx D_c$, and so the rightmost term of Eq. 6.73 may be considered small. Taking the long time $\Omega \rightarrow 0$ limit, performing the integration, and using the definition of ν in Eq. 6.44 we find

$$D = D_c - \delta D, \tag{6.74}$$

where we have defined the weak localization correction

$$\delta D = \frac{2\kappa p_F^2(1 - \delta_1)}{\pi\sigma\omega(1 + \delta_c)} \ln\left(\frac{L}{\ell}\right). \tag{6.75}$$

This is one of our main results. The summation of maximally crossed diagrams has led to a reduction in the diffusion coefficient, which diverges like $\ln L$ as $L \rightarrow \infty$. The logarithmic dependence on system size is a universal result for 2D mesoscopic systems [3], and appears in our model as well. Formally, in the $L \rightarrow \infty$ limit all states are localized, however, since the weak localization correction is only logarithmic, it may be difficult for finite systems to localize.

All of the quantities appearing in δD have been computed elsewhere already (ℓ , p_F , and δ_1 in Appendix D.1, δ_c in Appendix D.2), and can be determined immediately. In Appendix D.5 we give the full analytic expressions in $d_H = 0, 1, 2$ for δD , as well as the other main quantities in this manuscript.

The weak localization correction breaks down near the localization transition ($\delta D \approx D_c$). In order to probe the onset of localization, we treat Eq. 6.73 self-consistently, replacing D_c under the integration on the right side with the full diffusion coefficient D [154]. This has the effect of renormalizing each of the two-particle propagators appearing in the ladder diagrams of D_c with maximally crossed vertices,

and vice versa for those appearing in D_\times . In the diagrammatic language, this corresponds to renormalizing the diffuson with all numbers of insertions of cooperons. In the localized regime, we expect the diffusion coefficient to vanish at long times. We can then posit a localization length [154, 140]

$$\xi^2 = \lim_{\Omega \rightarrow 0} \frac{D(\Omega)}{-i\Omega}. \quad (6.76)$$

The localization length ξ determines the length beyond which all states are localized. Assuming such a length exists in the system, we no longer need to restrict the wavenumber integration over Q to be larger than L^{-1} , as ξ will regulate the low wavenumber divergence. Solving the self-consistent extension of Eq. 6.73 we find

$$\xi/\ell = \left(e^{4\pi^2\nu D_0} - 1 \right)^{1/2}. \quad (6.77)$$

The localization length describes transport in the strong scattering regime. This result, combined with the weak localization solution of Eq. 6.75, and the coherent diffusion coefficient D_c of Eq. 6.63, completes our description of undulatory transport on a warped membrane.

6.6 Results

Table 6.1: Dimensionless scattering time $\tau = \omega / \text{Im}\bar{\Sigma}_{p_F}$, and dimensionless transport velocity v_t , in each of $d_H = 0, 1, 2$. These are calculated within the SCSA (see Appendix D.1 for more details). We have further used the weak-scattering approximation to determine $\text{Im}\bar{\Sigma}_{p_F}$, and hence τ . For $d_H < 2$, the continuum picture breaks down and quantities depend on the underlying lattice. This is taken into account by restricting wavenumbers to lie below an upper cutoff $\Lambda \sim 1/a$, for a the lattice spacing.

	τ	v_t
$d_H = 0 :$	$\left(\frac{3}{2}\right)^{2/3} \frac{\Lambda^{4/3}}{\pi\omega^2\alpha^{1/3}}$	$2\sqrt{\omega} \sqrt{\frac{2}{3\alpha\Lambda^2}}$
$d_H = 1 :$	$\frac{6}{19\pi\alpha^2\omega} \left(1 + \frac{3\alpha/2 + 12\alpha \ln(\Lambda/\sqrt{\omega}) + 1}{\sqrt{3\alpha + 12\alpha \ln(\Lambda/\sqrt{\omega}) + 1}}\right)$	$2\sqrt{\omega} \left(\frac{2}{1 + \sqrt{12\alpha \ln\left(\frac{\Lambda}{\sqrt{\omega}}\right) + 3\alpha + 1}}\right)^{3/4}$
$d_H = 2 :$	$\frac{2\omega}{3\pi\alpha^2} \left(1 + \frac{3}{2} \ln\left(1 + \frac{\alpha}{\omega}\right)\right)$	$2\sqrt{\omega} \left(\sqrt{\frac{9\alpha^2}{4\omega^2} + 1} - \frac{3\alpha}{2\omega}\right)^{3/2}{}^a, \quad 2\sqrt{\omega} \left(\frac{2\sqrt{2}}{(6 \ln\left(\frac{\alpha}{\omega}\right) + 7)^{3/4}}\right)^b$

^a $\alpha \ll \omega$, ^b $\alpha \gg \omega$

There are two fundamental quantities to compute: the self-energy $\hat{\Sigma}$ and the coherent diffusion reduction factor δ_c , from which, all other quantities may be derived. Calculation of these quantities must be done starting directly from the DMV equations for physical membranes, Eqs. 6.18 and 6.19, or the action in Eq. 6.12, if working with generalized membranes. Computation of $\hat{\Sigma}$ is lengthy, so to simplify matters we shall immediately switch to working with dimensionless quantities.

We measure lengths in units of $\sqrt{\kappa/Y}$ and time in units of $\sqrt{\kappa\sigma}/Y$. Henceforth, we redefine wavenumber and frequency

$$p \rightarrow p/\sqrt{\kappa/Y}, \quad (6.78a)$$

$$\omega \rightarrow \omega/\sqrt{\kappa\sigma}/Y, \quad (6.78b)$$

so that p, ω refer to the dimensionless wavenumber and frequency. These, in turn, lead us to define the dimensionless self energy

$$\bar{\Sigma}_p = \frac{\Sigma_p}{\kappa L^2 (Y/\kappa)^2}, \quad (6.79)$$

and disorder amplitude

$$\alpha = \frac{\gamma}{16\pi} \left(\frac{Y}{\kappa} \right)^{2-d_H}. \quad (6.80)$$

This choice of length and time conveniently allows us to set $Y, \kappa, \sigma = 1$ in the DMV equations.

From Eq. 6.34, the self-energy is found via a disorder average of the DMV Green's function. For any given realization of the quenched background height field, the DMV equations represent a well-defined, albeit intractable, pair of partial differential equations. To overcome this, one typically decomposes the Green's function into a zero disorder contribution with known solution, plus corrections that tend to zero as the amplitude of the quenched height field vanishes.

In Appendix D.1.1 we compute the first order correction to $\bar{\Sigma}_p$. We find that the perturbation series is governed by a d_H -dependent parameter $Yh_{\text{eff}}^2(p)/\kappa$ (defined in Eq. D.7) [77], that is system size dependent for $d_H \leq 1$ and divergent at $p = 0$ for $d_H > 1$. The perturbation series fails, and any perturbative computation must include a partial re-summation of some set of terms.

To remedy the failure of the perturbation series, we employ the self-consistent screening approximation (SCSA) [88, 126, 162, 39]. In terms of generalized membrane with two internal dimensions and d_c normals, the SCSA provides the leading order term in a d_c^{-1} expansion of the self-energy. The SCSA has found success in determining the renormalized elastic constants of both athermal [77] and thermal [78] warped membranes.

The self-energy is computed in Appendix D.1, where we also develop the diagrammatic perturbation theory. The remaining quantity to calculate, the reduction coefficient δ_c , is computed in Appendix D.2. We hereafter discuss only the results, and refer the reader to the appropriate appendix for further details.

Beginning with one-particle quantities, in Tab. 6.1 we present results for v_t and τ in $d_H = 0, 1, 2$. The Drude-Boltzmann diffusion coefficient and mean free path can easily be found from these two quantities using Eqs. 6.57 and 6.60 respectively.

For membranes that are flat in the stress-free state, the transport velocity is equal to the group velocity $2\sqrt{\omega}$. The frequency dependence is a consequence of the biharmonic ∇^4 term appearing in the DMV equations. For all values d_H , and at fixed frequency, both the transport velocity and scattering time decrease due to geometrical disorder. The former is a consequence of random scattering, which prevents undulatory waves from propagating along a straight line. The latter is due

to an increased density of scatters with increasing disorder. Generally, the slowing down of waves due to multiple scattering gives rise to diffusive transport.

In Fig. 6.2, we give asymptotic results at small/large α for the mean free path ℓ . We find at small α , that $\ell \sim \alpha^{-5/6}$ in $d_H = 0$ and $\ell \sim \alpha^{-2}$ for both $d_H = 1, 2$. As expected, increased disorder leads to a reduction in ℓ , and as a result, phase information of an undulatory wave is lost at shorter distances from the point of force application.

The frequency dependence of ℓ is more interesting. For $d_H = 2$, $\ell \sim \omega^{3/2}$ increases with frequency, while for $d_H \neq 2$ it decreases. Waves with high frequency can better resolve the geometry of the surface, as their characteristic wavelengths are smaller. One would expect that at higher frequency the effective curvature is smaller, leading to fewer scattering events and a longer mean free path.

The breakdown of this explanation for $d_H < 2$ is due to the lack of a well-defined curvature, which depends on two spatial derivatives of the quenched height field. There is no meaningful derivative that can be assigned to the quenched height field, as the derivatives of the height field become arbitrarily large as the lattice spacing tends to zero. The continuum picture breaks down and quantities depend on the underlying lattice spacing a . This is taken into account by restricting wavenumbers to lie below an upper cutoff $\Lambda \sim 1/a$ (this is an inverse length, and per Eq. 6.78a, written in units of $\sqrt{\kappa/Y}$). The decrease in mean free path with respect to frequency for $d_H \leq 1$ can be understood as the wave scattering off the now-resolved short-distance roughness, which would otherwise be smoothed over.

$d_H = 1$ is the marginal case; the system develops logarithm dependence on Λ . The $d_H = 0$ case (white noise disorder) however, is more extreme. We find that Λ

dominates the behavior of the system; indeed, from Tab. 6.2, the coherent diffusion coefficient $D_c \sim (\alpha^2 \Lambda)^{-2/3}$. Though we have studied the properties of the $d_H = 0$ membrane (and list the corresponding results), we shall restrict our analysis to the more physical cases of $d_H = 1, 2$. We now consider two-particle quantities, *i.e.* the diffusion coefficient and localization length.

In Appendix. D.5, we list the full analytic expressions for D_c , δD , ξ , ℓ and ν , which in combination with the contents of Tab. 6.1, comprise the main results of our manuscript. In Tab. 6.2 we give asymptotic limits at small/large α of the quantities of interest, namely the coherent diffusion coefficient and weak localization correction.

Beginning with $d_H = 2$, in Fig. 6.3 we plot the total diffusion coefficient D as a function of both α and ω . D depends only on the ratio α/ω , and so its frequency dependence is trivially inverse to that of its disorder dependence. Focusing on the case of fixed disorder, we see that at low ω the diffusion coefficient sharply drops to zero. This occurs near $D_c \approx \delta D$ and corresponds to the localization transition. The localization transition frequency grows linearly with α , telling us that as disorder increases low frequency states are first to localize. In the weak disorder regime, we find that D decreases $\sim \alpha^{-2}$ and, conversely, at fixed α increases $\sim \omega^2$. The increase of D with ω indicates disorder acts like a high-pass filter, trapping low frequency undulatory waves.

In Fig. 6.4, we plot the $d_H = 1$ diffusion coefficient versus both α and ω . As a function of α , $d_H = 1$ behaves similarly to $d_H = 2$. $D \sim \alpha^{-2}$ at low α , and there is a localization transition at high disorder. In contrast, $d_H = 1$ has only logarithmic frequency dependence. Increasing the frequency by orders of magnitude marginally decreases the value α at which the wave localizes. The logarithmic frequency depen-

Table 6.2: Asymptotic limits of the primary quantities contributing to localization: the coherent diffusion coefficient D_c , the weak localization correction δD , and the mean free path ℓ , in each of $d_H = 0, 1, 2$.

$\alpha \ll 1$			
	D_c	δD^a	ℓ
$d_H = 0 :$	$\frac{2}{\pi} \frac{(2/3)^{1/3}}{\alpha^{4/3} \omega \Lambda^{2/3}}$	$\frac{1}{\pi} \left(\frac{3}{2}\right)^{4/3} \alpha^{1/3} \Lambda^{2/3} \ln\left(\frac{L}{\ell}\right)$	$\frac{(96)^{1/6}}{\pi} \frac{\Lambda^{1/3}}{\alpha^{5/6} \omega^{3/2}}$
$d_H = 1 :$	$\frac{48}{(11+76\pi)\alpha^2}$	$\left(\frac{152}{11+76\pi} + \mathcal{O}(\alpha \ln \Lambda)\right) \ln\left(\frac{L}{\ell}\right)$	$\frac{12}{19\pi\alpha^2\sqrt{\omega}}$
$d_H = 2 :^c$	$\frac{16\omega^2}{3(1+4\pi)\alpha^2}$	$\frac{8}{1+4\pi} \ln\left(\frac{L}{\ell}\right)$	$\frac{4\omega^{3/2}}{3\pi\alpha^2}$
$\alpha \gg 1$			
	D_c	δD^a	ℓ
$d_H = 0 :$	$_b$	$_b$	$_b$
$d_H = 1 :$	$\sim \alpha^{-9/4} \ln^{-1/4}\left(\frac{\Lambda}{\sqrt{\omega}}\right)$	$\sim \frac{\ln(L/\ell)}{\alpha^{1/8} \ln^{1/8}(\Lambda/\sqrt{\omega})}$	$\sim \frac{\ln^{5/8}(\Lambda/\sqrt{\omega})}{\alpha^{11/8} \sqrt{\omega}}$
$d_H = 2 :^c$	$\sim \frac{\omega^2}{\alpha^2}$	$\sim \ln\left(\frac{L}{\ell}\right)$	$\sim \frac{\omega^{3/2}}{\alpha^2}$

^a The weak localization correction δD is only defined for $L > \ell$, *i.e.* when the argument of \ln is greater than one.

^b These are the same as the $\alpha \ll 1$ limit, as Λ is the dominant parameter.

^c The precise limits here are instead $(\alpha/\omega) \ll 1$ and $(\alpha/\omega) \gg 1$

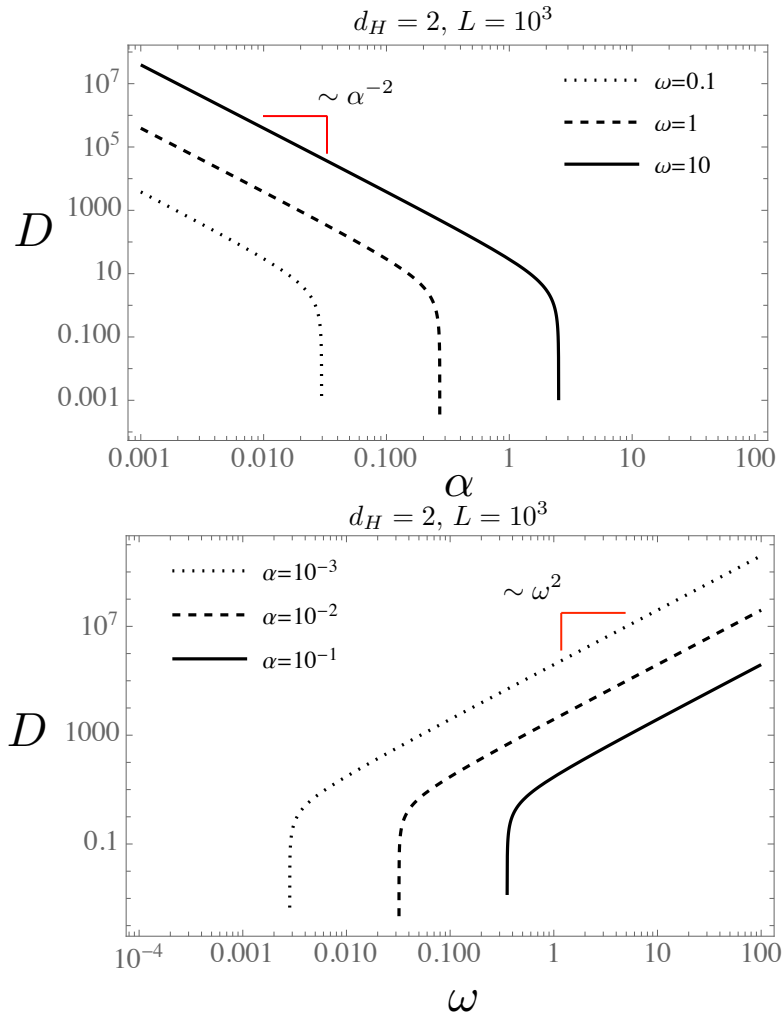


Figure 6.3: (color online) diffusion coefficient as a function of both disorder α (top) and frequency ω (bottom). D decays $\sim \alpha^2$ at small α , and grows like ω^2 at large α . At low ω there is a localization transition where D vanishes. At smaller system size L , the localization transition is pushed to smaller/larger frequencies/disorder.

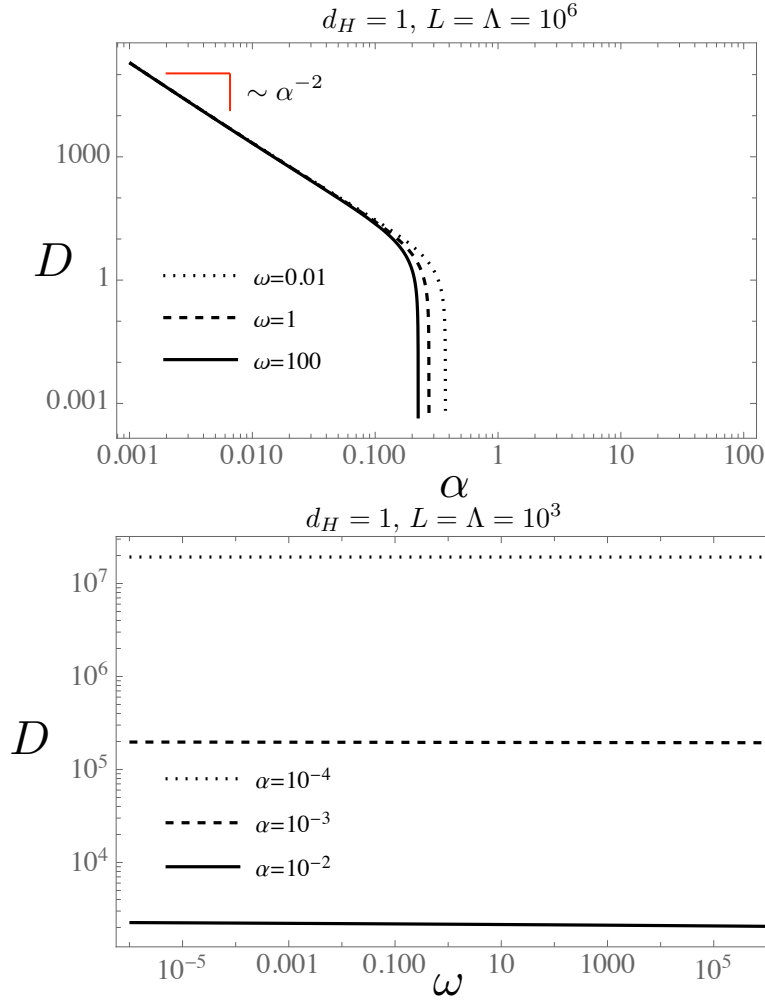


Figure 6.4: (color online) diffusion coefficient in $d_H = 1$ versus both disorder amplitude (top) and frequency (bottom). As for $d_H = 2$, $D \sim \alpha^{-2}$ at low alpha, and reaches a localization transition at large α . The transition decrease logarithmically in frequency. If the system localizes, it occurs first at high frequency. In the lower panel, the weak frequency dependence of D is shown to hold ten orders of magnitude, and even up to the upper limit $\omega \approx \Lambda^2$.

dence of D is shown clearly in the lower panel of Fig. 6.4, where in a log-log plot it appears as a flat line. At fixed α , increasing the frequency over several orders of ten orders of magnitude does not significantly alter D , even as ω approaches its upper limit Λ^2 . D is not entirely independent of frequency however, as in the upper panel of Fig. 6.4 we see that increasing ω lowers the disorder amplitude at the localization transition. Though the transition point only decreases logarithmically with frequency, this behavior is still in contrast to that observed in $d_H = 2$, where increasing frequency raises the localization transition disorder amplitude. This analysis at large α is circumspect however, as the calculation of D assumes we are in the weak scattering regime. Despite this, a strong scattering calculation of the localization length (shown in Fig. 6.6) confirms that for $d_H = 1$, high frequency waves are first to localize.

The computation of D is only valid in the weak scattering approximation, $\alpha \ll 1$. The vanishing of D in both $d_H = 1, 2$ above a certain value of α signals a transition to the localization regime. To probe this, we consider the localization length ξ defined in Eq. 6.77, and its size relative to the mean free path ℓ .

In Fig. 6.5 we plot ξ and ℓ as functions of both α and ω for $d_H = 2$. Localization occurs approximately when $\xi < \ell$: in other words, when the wave has not yet had a chance to scatter before being localized. In agreement with the high α prediction of Fig. 6.3, at large enough disorder, the localization length becomes shorter than the mean free path. When frequency is decreased, the the disorder amplitude at the localization transition decreases as well. The lower panel of Fig. 6.5, shows that ξ transitions from $\sim \omega^{5/2}$ to $\sim e^{\omega^2}$ dependence near the transition. The exponential increase of localization length tells us that undulatory waves are sharply divided between extended and localized.

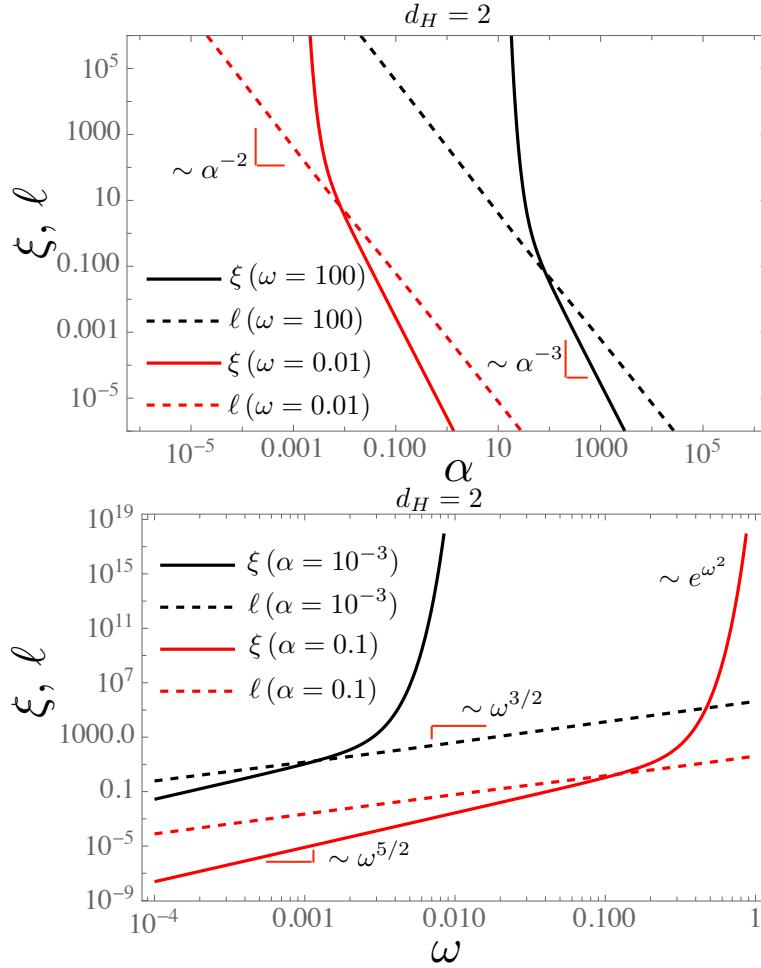


Figure 6.5: (color online) top: localization length and mean free path as a function of disorder in $d_H = 2$. Solid (dashed) lines refer to ξ (ℓ). Black is for $\omega = 10^{-3}$, red is for $\omega = 0.1$. Bottom: ξ and ℓ as a function of frequency at fixed $\alpha = 10^{-3}$ (black) and $\alpha = 0.1$ (red). Localization occurs at both high disorder and low frequency.

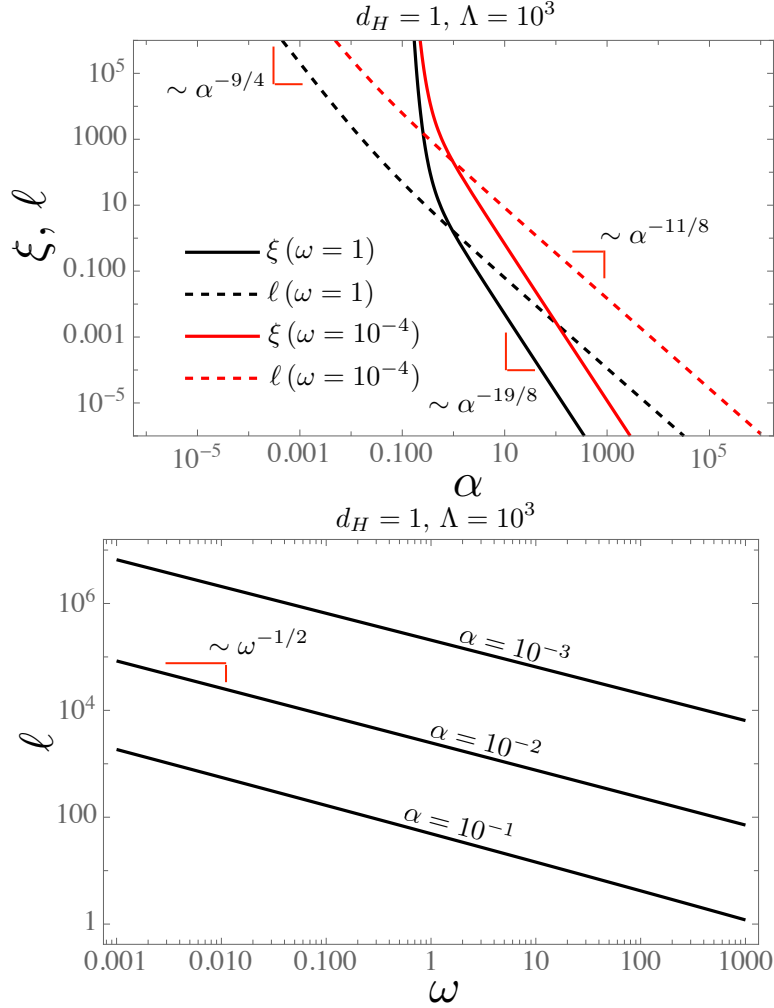


Figure 6.6: (color online) localization length ξ and mean free path ℓ in $d_H = 1$ as a function of both disorder amplitude (top) and frequency (bottom). In the top panel, black (red) lines correspond to $\omega = 1$ ($\omega = 10^{-4}$). Solid (dashed) lines refer to ξ (ℓ). The wave localizes when ξ falls below ℓ . This occurs at weaker disorder (smaller α) with increasing frequency. In the lower panel, we show the $\omega^{-1/2}$ decay of the mean free path. The localization length is ω -independent, and not shown.

In Fig. 6.6, we perform the same analysis of ξ and ℓ in $d_H = 1$ as we did for $d_H = 2$. As expected, the localization length decays with increasing disorder ($\sim \alpha^{-19/8}$) faster than the mean free path at both small ($\sim \alpha^{-9/4}$) and large ($\sim \alpha^{-11/8}$) disorder. In contrast to $d_H = 2$, the ratio ξ/ℓ is frequency independent in $d_H = 1$. The lower panel of Fig. 6.6 shows the mean free path is a decreasing function of frequency ($\sim \omega^{-1/2}$). At fixed disorder, $\xi \sim \ell$ and so the localization length will run parallel to the mean free path. Frequency does not affect the localization transition.

Though we can take the strong scattering limit via our self-consistent treatment of D leading to ξ , these results should be interpreted with caution for two reasons. First, at high α , the quenched height field may produce stronger curvature. Our derivation of the warped membrane equations assume that derivatives $|\nabla h|^2$ were small, thus allowing us to use the flat metric. A proper extension to strong curvature would require the use of covariant derivatives and a non-flat metric, significantly increasing the difficulty. Second, the underlying DMV equations assume that the characteristic wavelength of deformations is much smaller than the radius of curvature (see discussion following Eq. 6.7. When this does not hold, there are additional contributions to the change in the curvature tensor \mathbf{K}_{ab} (see the definition in Eq. 6.8) that couple stretching to bending [115].

6.7 Conclusion

We analyze the transport of undulatory waves on a membrane whose stress-free state is curved. Due to Gauss' *theorema egregium*, curvature couples in-plane stretching deformations to the much softer our-of-plane bending undulations. As a result, undulatory wave are scattered by changes in Gauss curvature, a purely geometric

mechanism.

We study a particular class of curved surfaces called warped membranes [77]. The stress-free state of these membranes is nearly flat, and can be parametrized by a quenched height field $h(\mathbf{x})$ drawn from a Gaussian ensemble with variance set by Eq. 6.3. By considering ensemble averages over membrane realizations, we can compute general transport quantities, independent of a particular realization of disorder.

The elastic equations of a nearly flat membrane are described using the linearized DMV equations. This isolates the effects of curvature, which can be appreciable before nonlinearities need be accounted for. Typically, membranes are much stiffer to stretching than bending, and so the in-plane deformations relax on a time scale much shorter than undulations. Integrating out these in-plane modes, we arrive at an effective, linear field theory of undulatory waves. The resulting undulatory equations of motion appear similar to those describing wave propagation in random media, albeit with a complicated nonlocal potential and biharmonic term.

As undulations obey a linear partial differential equation, the amplitude of undulations in response to a transverse applied load can be described by a Green's function. We consider an experiment whereby an initially undeformed membrane is suddenly plucked at the origin, thereby injecting energy into the system. On average, the amplitude at any point is the sum of many random phases, and averages to zero. The disorder averaged Green's function is thus a short range quantity. In contrast, the energy is a conserved quantity, and it must survive disorder averaging. Its propagation through (or lack thereof) the membrane is an indicator for diffusion/localization. We find that the kinetic energy alone, and more specifically the

undulation intensity (a product of a retarded and advanced Green's function), is a long-range object capable of describing diffusion/localization. We focus on studying undulation intensity transport in response to an applied transverse load of fixed frequency at the origin. This defines a frequency dependent diffusion coefficient $D(\omega)$, from which we can determine the diffusion coefficient of any finite sized wavepacket.

Our theory obeys a Ward identity (WI) relating the self-energy to the irreducible four-point function. Using the WI, we derive diffusive dynamics of undulation intensity for long times and lengths. The resulting expression for the diffusion coefficient is found to depend critically on the type of noise under consideration, as well as the frequency of the applied load. For Gaussian noise with power law variance in wavenumber space, we find that only membranes with variance $\langle |h_q|^2 \rangle \sim q^{-2d_H}$ with $d_H > 1$ are well defined and independent of the short distance cutoff, with $d_H = 1$ the marginal case.

For all types of noise, geometry is found to decrease both the transport velocity and scattering time. The strength of the effect increases with amplitude of the quenched height field. The combination of random scattering and slowed propagation is responsible for diffusive behavior of disorder averaged intensity transport.

Considering the effect of coherent scattering on intensity transport, we compute the diffusion coefficient and its weak localization correction in the limit of weak scattering (small quenched height field amplitude). The weak localization correction is found to behave similar to those in other 2D systems, lowering the diffusion coefficient $\sim \ln L$, which is logarithmically dependent on the system size. [140, 3, 154]

For membranes belonging to the $d_H = 2$ ensemble, we find at fixed frequency the diffusion coefficient decrease like α^{-2} , for α the dimensionless amplitude of the

quenched height field. At large enough α , the system undergoes a localization transition, whereby the diffusion coefficient vanishes. The weak scattering prediction is confirmed by self-consistently extending the weak localization correction to the strong scattering regime, where we find the localization length ξ to decrease with α . At fixed α , waves first localize at low frequency. Away from the localization transition, the diffusion coefficient grows $\sim \omega^2$ with increasing frequency. This effects of random geometry are mitigated at high frequency.

For $d_H = 1$, the diffusion coefficient decreases $\sim \alpha^{-2}$ until a localization transition at high α , just like for $d_H = 2$ membranes. However, for $d_H = 1$, both the diffusion coefficient and localization are only logarithmically frequency dependence. Increasing the frequency over n orders of magnitude, we observe that the value α at the localization transition is reduced by a factor of n . In contrast to $d_H = 2$, this suggests that the localizing effects of random geometry are enhanced at high frequency (though exponentially small).

For $d_H = 0$, we find that transport is completely determined by the short-distance cutoff of the theory, where the continuum description breaks down. Upon further analysis, this failure can be traced back to the unphysical nature of $d_H = 0$ membranes. Since there is no correlation in amplitude of the quenched height field between arbitrarily close points in space, derivatives can become arbitrarily large as the lattice spacing goes to zero, resulting in a lack of a well-defined curvature. We can still analyze the theory, however, and we find the diffusion coefficient to be $\sim \omega^{-1}$. This supports the claim that $d_H = 1$ is the marginal case; for short range disorder ($d_H < 1$) geometry acts as a high-pass filter, and for longer range disorder ($d_H > 1$) it acts as a low-pass filter.

The unphysical dependence on Λ plaguing the $d_H = 0$ case, also appears to an extent for $d_H = 1$. An alternative way to express the claim that $d_H = 1$ represents the marginal case, is by looking at its Λ dependence. Membranes belonging to the $d_H = 0$ ensemble exhibit are $\sim \Lambda^2$, in the $d_H = 1$ ensemble $\sim \ln \Lambda$, and in the $d_H = 2$ ensemble Λ -independent.

In all cases of disorder, the localization length is found to depend exponentially on α and ω . This is a feature of two dimensional systems, and indicates that the divide between localized/extended states is sharp.

In future work we would like to explore fluctuation corrections to our results. In particular, it would be interesting to look at intensity fluctuations in the diffusive limit, and see if the system obeys a type of geometrical speckle-correlation. Additionally, we would like to understand the sensitivity of our results to inelastic scattering. In biological applications, membranes are immersed in viscous fluid. Whether or not localization effects persist in the overdamped limit is a question of interest.

APPENDIX A

Appendices for equilibrium fluctuations of a semiflexible filament cross linked into a network

A.1 Real space MFT Green's functions

The Green's function satisfies the equation of motion

$$[\kappa\partial_x^4 - (\tau + 4k_{\parallel}\langle\Delta\ell\rangle)\partial_x^2] G(x, x') = \delta(x - x'). \quad (\text{A.1})$$

To make the equations more readable, we define:

$$\lambda \equiv 2\langle\Delta\ell\rangle. \quad (\text{A.2})$$

We solve for the Green's function by first finding solutions of Eq. [A.1](#) in the regions $x \neq x'$. We then fix the undetermined coefficients according to the prescribed boundary conditions and the jump discontinuity at $x = x'$ necessary to generate the delta function. The general solutions on the left (L) and right (R) of this discontinuity are

$$u_{L,R}(x) = A + Bx + C \cosh(px) + D \sinh(px), \quad (\text{A.3})$$

where

$$p \equiv \sqrt{\tau + 2k_{\parallel}\lambda/\kappa}, \quad (\text{A.4})$$

and $\{A, B, C, D\}$ are, as yet, undetermined coefficients. We require that $u_L(x)$ and $u_R(x)$ be equal through the second derivative. The jump discontinuity then gives $u_R'''(x') - u_L'''(x') = 1/\kappa$. Applying the boundary conditions at the discontinuity as well as at the prescribed boundaries yields an algebraic system of equations from which the undetermined coefficients may be found. We obtain:

$$G(x, x)_{\text{pinned}} = \frac{\sqrt{\kappa} \left(\coth \left(\sqrt{\frac{2k_{\parallel}\lambda + \tau}{\kappa}} \right) \sinh^2 \left(x \sqrt{\frac{2k_{\parallel}\lambda + \tau}{\kappa}} \right) \right)}{(2k_{\parallel}\lambda + \tau)^{3/2}} \quad (\text{A.5})$$

$$- \frac{\sqrt{\kappa} \left(\sinh \left(2x \sqrt{\frac{2k_{\parallel}\lambda + \tau}{\kappa}} \right) - (x - 1)x \sqrt{\frac{2k_{\parallel}\lambda + \tau}{\kappa}} \right)}{2(2k_{\parallel}\lambda + \tau)^{3/2}}$$

$$G(x, x)_{\text{free}} = \frac{\sqrt{\kappa}}{(2k_{\parallel}\lambda + \tau)^{3/2}} \left[\coth \left(\sqrt{\frac{2k_{\parallel}\lambda + \tau}{\kappa}} \right) \sinh^2 \left(x \sqrt{\frac{2k_{\parallel}\lambda + \tau}{\kappa}} \right) \right.$$

$$\left. - \frac{1}{2} \sinh \left(2x \sqrt{\frac{2k_{\parallel}\lambda + \tau}{\kappa}} \right) + x \sqrt{\frac{2k_{\parallel}\lambda + \tau}{\kappa}} \right] \quad (\text{A.6})$$

$$G(x, x)_{k_{\perp}} = \frac{x(k_{\perp}(-x) + k_{\perp} + 2k_{\parallel}\lambda + \tau)}{(2k_{\parallel}\lambda + \tau)(k_{\perp} + 2k_{\parallel}\lambda + \tau)} - \frac{\sqrt{\kappa} \text{csch} \left(\sqrt{\frac{2k_{\parallel}\lambda + \tau}{\kappa}} \right) \cosh \left(\sqrt{\frac{2k_{\parallel}\lambda + \tau}{\kappa}} \right)}{2(2k_{\parallel}\lambda + \tau)^{3/2}} \quad (\text{A.7})$$

$$+ \frac{\sqrt{\kappa} \text{csch} \left(\sqrt{\frac{2k_{\parallel}\lambda + \tau}{\kappa}} \right) \cosh \left((1 - 2x) \sqrt{\frac{2k_{\parallel}\lambda + \tau}{\kappa}} \right)}{2(2k_{\parallel}\lambda + \tau)^{3/2}}$$

To write the final answer, we must determine λ . The self-consistency condition is

$$\lambda = \int_0^L dx \lim_{x' \rightarrow x} \partial_x \partial_{x'} G(x, x'). \quad (\text{A.8})$$

For each of the three cases we find

$$\lambda_{\text{free}} = \frac{\kappa \sqrt{\frac{2k_{\parallel} \lambda + \tau}{\kappa}} + (2k_{\parallel} \lambda + \tau) \coth \left(\sqrt{\frac{2k_{\parallel} \lambda + \tau}{\kappa}} \right)}{2\sqrt{\kappa}(2k_{\parallel} \lambda + \tau)^{3/2}} \quad (\text{A.9})$$

$$\lambda_{\text{pinned}} = \frac{(2k_{\parallel} \lambda + \tau) \coth \left(\sqrt{\frac{2k_{\parallel} \lambda + \tau}{\kappa}} \right) - \kappa \sqrt{\frac{2k_{\parallel} \lambda + \tau}{\kappa}}}{2\sqrt{\kappa}(2k_{\parallel} \lambda + \tau)^{3/2}} \quad (\text{A.10})$$

$$\lambda_{\text{spring}} = \frac{\kappa \sqrt{\frac{2k_{\parallel} \lambda + \tau}{\kappa}} + (2k_{\parallel} \lambda + \tau) \coth \left(\sqrt{\frac{2k_{\parallel} \lambda + \tau}{\kappa}} \right)}{2\sqrt{\kappa}(2k_{\parallel} \lambda + \tau)^{3/2}} - \frac{k_{\perp}}{(2k_{\parallel} \lambda + \tau)(k_{\perp} + 2k_{\parallel} \lambda + \tau)}. \quad (\text{A.11})$$

APPENDIX B

Appendices for dynamics of undulatory fluctuations of semiflexible filaments in a network

B.1 Diagrammatic perturbation theory to $\mathcal{O}(k^2)$

We compute the adjusted self energy given in Eq. 3.25 to $\mathcal{O}(k^2)$. For readability, in this section we drop the 0 superscript, with γ_p referring to γ_p^0 . When we refer to diagrams appearing in Fig. 3.3, we are including not only the diagram, but also its combinatorial factor for contracting the legs. We also include a factor of $(-Dk\ell^2/8)^n/n!$ at $\mathcal{O}(k^n)$. Diagram B1 has combinatorial factor 2, A1 has 1, all C and D diagrams have 2^3 , B2 has 2^2 , B3 has 2^3 , and A2 has 2^2 .

We calculate for the $\mathcal{O}(k)$ diagrams:

$$A1 = -\frac{1}{2}kp^2 \sum_q \frac{q^2}{\gamma_q}, \quad (\text{B.1})$$

and

$$B1 = -k \frac{p^4}{\gamma_p}. \quad (\text{B.2})$$

For the D diagrams, $D1$ and $D2$ vanish due to a closed response loop. $D3$ and $D4$ give identical contributions, leading us to write the D contribution

$$D3 + D4 = \frac{k^2 p^8}{\gamma_p^3}. \quad (\text{B.3})$$

All three of the C diagrams give the same contribution. Summing these gives

$$C1 + C2 + C3 = k^2 \frac{3Dp^8}{\gamma_p^2(-i\omega + 3D\gamma_p)}. \quad (\text{B.4})$$

Lastly, for the B diagrams,

$$B2 = k^2 \frac{p^4}{\gamma_p} \sum_q \frac{Dq^4}{\gamma_q(-i\omega + 2D\gamma_q + D\gamma_p)}, \quad (\text{B.5})$$

and

$$B3 = k^2 p^4 \sum_q \frac{Dq^4}{2\gamma_q^2(-i\omega + 2D\gamma_q + D\gamma_p)}. \quad (\text{B.6})$$

Taking the sum, we simplify to

$$B2 + B3 = \frac{k^2 p^4}{2\gamma_p} \sum_q \frac{q^4}{\gamma_q^2} \left(1 - \frac{-i\omega}{-i\omega + D(2\gamma_q + \gamma_p)} \right). \quad (\text{B.7})$$

The last diagram is

$$A2 = k^2 p^2 \left(\sum_q \frac{q^2}{2\gamma_q} \right) \left(\sum_q \frac{q^4}{2\gamma_q^2} \right). \quad (\text{B.8})$$

The adjusted self-energy is simply the sum of these contributions. Altogether we find

$$\begin{aligned} \tilde{\Sigma}_p(\omega) &= -k \left(\frac{p^4}{\gamma_p} + \frac{p^2}{2} \sum_q \frac{q^2}{\gamma_q} \right) + k^2 \left[\frac{p^8}{\gamma_p^2} \left(\frac{1}{\gamma_p} + \frac{3D}{-i\omega + 3D\gamma_p} \right) \right. \\ &+ \left. \frac{p^4}{2\gamma_p} \sum_q \frac{q^4}{\gamma_q^2} \left(1 - \frac{-i\omega}{-i\omega + D(2\gamma_q + \gamma_p)} \right) + \frac{1}{4} p^2 \left(\sum_q \frac{q^2}{\gamma_q} \right) \left(\sum_q \frac{q^4}{\gamma_q^2} \right) \right] \\ &+ \mathcal{O}(k^3). \end{aligned} \quad (\text{B.9})$$

We may rewrite this in terms of the dimensionless tension, $\phi = \frac{\tau \ell^2}{\pi^2 \kappa}$, and dimen-

sionless frequency, $\bar{\omega} = \omega \ell^4 / (D\kappa\pi^4)$, as

$$\begin{aligned}
\tilde{\Sigma}_n(\omega) &= -\frac{k k_{\text{B}} T}{\kappa} \left(\frac{n^2}{n^2 + \phi} + \frac{n^2}{2} \sum_m \frac{1}{m^2 + \phi} \right) \\
&+ \frac{k^2 \ell^4 k_{\text{B}}^2 T^2}{\kappa^3 \pi^4} \left[\frac{n^2}{(n^2 + \phi)^3} + \frac{3n^4}{-i\bar{\omega} + 3n^2(n^2 + \phi)} \right. \\
&+ \frac{1}{2} \frac{n^2}{n^2 + \phi} \sum_m \frac{1}{(m^2 + \phi)^2} \left(1 - \frac{-i\bar{\omega}}{-i\bar{\omega} + 2m^2(m^2 + \phi) + n^2(n^2 + \phi)} \right) \\
&\left. + \frac{n^2}{4} \sum_{m, m'} \frac{1}{(m^2 + \phi)(m'^2 + \phi)^2} \right], \tag{B.10}
\end{aligned}$$

where m , m' , and n are positive integers, and we have restored factors of $k_{\text{B}}T$.

Rewriting $\tilde{\Sigma}_p(\omega)$ in terms of the dimensionless wavenumber $\bar{p} = p\sqrt{\kappa/\tau}$ instead leads to Eq. 3.26. We can categorize several of the diagrams in terms of the n -bubble expansion. Diagrams of type A contain one-bubbles, and generate a shift in the effective tension. Diagrams of type B contain two-bubbles, and generate a shift in the effective spring constant k . The remaining diagrams are single line topologies.

B.2 Mean-field theory solution in time-domain

Our starting point is Eq. 3.45. We begin by defining the integrated projected length

$$\Lambda(t) = \int^t \lambda_0(t') dt', \tag{B.11}$$

as the antiderivative of $\lambda_0(t)$. The differential equations of motion (Eq. 3.45a) governing the normal modes can be solved in terms of $\lambda_0(t)$. We find

$$u_p(t) = u_p(0) \tilde{\chi}_p(t, 0) + \int_0^t dt' \tilde{\chi}_p(t, t') \zeta_p(t'), \tag{B.12}$$

where we defined

$$\tilde{\chi}_q(t, t') = e^{-D(\kappa q^4 + \tau q^2)(t-t') - Dkq^2(\Lambda(t) - \Lambda(t'))}, \tag{B.13}$$

in agreement with the notation of Refs. [58, 116]. The initial condition $u_p(0)$ may either be specified, or treated as a random variable. Using Eq. 3.45b, we can eliminate the normal modes in favor of a single PIDE governing $\lambda_0(t)$. We obtain

$$\frac{d\Lambda}{dt} = \frac{\ell}{4} \sum_q q^2 \left\{ \chi_q^2(t, 0) \langle u_q^2(0) \rangle + \frac{4D}{\ell} \int_0^t \chi_q^2(t, t') dt' \right\}. \quad (\text{B.14})$$

The brackets around $u_p(0)$ indicate an average over these initial amplitudes. Since the average over the initial amplitudes (u_q^2) may be taken with respect to any ensemble, this equation can describe the relaxation of a nonequilibrium state. In this section however, we will be concerned with the case where $u_p(0)$ is sampled from the equilibrium ensemble.

We begin our analysis with the long-time or equilibrium limit. We implement the long-time limit by removing the initial condition and setting the lower limit of integration to $-\infty$. This gives the long-time limit PIDE

$$\frac{d\Lambda}{dt} = D\ell \sum_p p^2 \int_{-\infty}^t e^{-2D\gamma_p^0(t-t') - 2Dkp^2(\Lambda(t) - \Lambda(t'))} dt'. \quad (\text{B.15})$$

In the long-time limit, we expect the system to reach equilibrium. Accordingly, we seek a solution of the form $\Lambda(t) = \lambda_0 t$, *i.e.*, constant $\lambda_0(t)$. $\chi_q(t, t')$ then depends only on the time difference $(t - t')$, and we are free to Fourier transform. The right hand side of the PIDE can be viewed as the Fourier transform of $\tilde{\chi}_q^2(t, 0)\Theta(t)$ evaluated at zero frequency, which leads us immediately to Eq. 3.46.

As expected, this reproduces the equilibrium mean-field theory equation of Ref. [71]. While, the sum can be performed in closed form, we approximate the summation by an integration in order to understand its k -dependence. Since deviations in λ_0 from the spring-free result occur at larger values of k , the distinction between the summation and integration is immaterial. In terms of the k -independent change in

projected length λ_0^{free} (found by setting $k = 0$ in Eq. 3.46), we find the equation

$$\frac{\lambda_0}{\lambda_0^{\text{free}}} = \left[1 + \frac{k\lambda_0^{\text{free}}}{\tau} \left(\frac{\lambda_0}{\lambda_0^{\text{free}}} \right) \right]^{-1/2}. \quad (\text{B.16})$$

The most interesting result is found at high k , where the solution to this equation demands $\lambda_0/\lambda_0^{\text{free}} \sim k^{-1/3}$. Consequently, the effective tension $k\lambda_0 \sim k^{2/3}$. The transition occurs when $k\lambda_0/\tau \approx 1$. These results are confirmed by Fig. 3.7.

We now consider the short-time limit, where the behavior is dependent on the initial condition. We treat the case where $u_p(0)$ is averaged over the $k \neq 0$ equilibrium ensemble, and at $t = 0$ a small, additional time-dependent tension

$$\tau(t) = \tau + \delta f(t)\Theta(t), \quad (\text{B.17})$$

is applied. For reference, in equilibrium

$$\langle u_p^2(0) \rangle_{\text{eq}} = \frac{2k_B T/\ell}{\kappa p^2(p^2 + \tau + k\lambda_0)}, \quad (\text{B.18})$$

which can be inferred from the long-time MFT solution. $\delta f(t)$ has magnitude f , and is superimposed on top of a prestress τ . In analogy with defining the time-integrated projected length, we find it useful to introduce the time-integrated applied tension

$$\delta F(t) = \int_0^t \delta f(t') dt'. \quad (\text{B.19})$$

Upon turning on the additional tension $\delta f(t)$, the projected length will change an amount $\delta \langle \Delta \ell(t) \rangle = \langle \Delta \ell(t) - \Delta \ell(0) \rangle$, and the integrated projected length will change by an amount $\Lambda(t) = \Lambda_0 + \delta \Lambda(t)$, where $\Lambda_0 = \lambda_0^\infty t$ is the long-time constant solution. Comparing the two, we can identify

$$\partial_t \delta \Lambda = \delta \langle \Delta \ell \rangle. \quad (\text{B.20})$$

This relates $\delta\Lambda$ to the projected length response (which is not necessarily linear). Decomposing $\Lambda = \Lambda_0 + \delta\Lambda$, we redefine

$$\tilde{\chi}_q(t, t') = e^{-Dq^2(\kappa q^2 + \tau + k\lambda_0)(t-t')} e^{-Dq^2(\delta A(t) + \delta A(t'))}, \quad (\text{B.21})$$

where we have grouped the two perturbations $\delta\Lambda(t)$ and $\delta F(t)$ into a single function

$$\delta A(t) = k\delta\Lambda(t) + \delta F(t). \quad (\text{B.22})$$

This can similarly be accomplished by setting $\tau \rightarrow \tau + k\lambda_0 + \delta f(t)$ and replacing $\Lambda(t) \rightarrow \delta\Lambda(t)$ in Eq. B.13. Substituting and averaging over the initial condition yields the PIDE

$$\frac{d\delta\Lambda}{dt} = \frac{k_B T}{2} \sum_q \left\{ \frac{\tilde{\chi}_q^2(t, 0) - 1}{\kappa q^2 + \tau + k\lambda_0} + \frac{2q^2}{\xi_\perp} \int_0^t \tilde{\chi}_q^2(t, t') dt' \right\}. \quad (\text{B.23})$$

We are interested in the short-time solution to this equation. Since the projected length must be finite at $t = 0$, this implies that at, short times, $\delta\Lambda(t) \sim t^\eta$ for some $\eta > 1$. The prestress ensures that $\delta F(t)$ can be made small (by reducing the amplitude of applied tension) relative to τ at all values q , allowing one to expand $\delta F(t)$ in the exponential of $\tilde{\chi}_q(t, t')$ as $t \rightarrow 0$ [116]. Consequently, the change $\delta\Lambda(t)$ will be small as well, since it vanishes at $f = 0$. These considerations suggest that we can expand $\tilde{\chi}_q(t, t')$ in a power series about $\delta\Lambda(t)$ and $\delta F(t)$. Doing so, we find

$$\frac{d\delta\Lambda}{dt} = - \int_0^t M(t-t') [k\delta\Lambda(t') + \delta F(t')] dt', \quad (\text{B.24})$$

where we have defined the kernel

$$M(t) = \sum_p \left[\frac{Dp^2 \delta(t)}{\kappa p^2 + \tau + k\lambda_0} - 2D^2 p^4 e^{-2Dp^2(\kappa p^2 + \tau + k\lambda_0)t} \right]. \quad (\text{B.25})$$

This may be solved by Laplace transformation. The Laplace transform of the kernel is

$$\tilde{M}(z) = \sum_p \frac{zDp^2}{(\kappa p^2 + \tau + k\lambda_0)[z + 2Dp^2(\kappa p^2 + \tau + k\lambda_0)]}. \quad (\text{B.26})$$

In terms of the dimensionless tension ϕ , the shift $\Delta\phi$ defined in Eq. 3.34, \bar{k} , and the dimensionless Laplace variable $\bar{z} = z\ell^4/D\kappa\pi^4$, we can equivalently write this as

$$\tilde{M}(\bar{z}) = \sum_{n=1}^{\infty} \frac{Dn^2\bar{z}/\kappa}{(n^2 + \phi + \Delta\phi)[\bar{z} + 2n^2(n^2 + \phi + \Delta\phi)]} \quad (\text{B.27})$$

Solving, the transformed change in projected length $\delta\Lambda(z)$ is

$$\delta\Lambda(z) = -\frac{\tilde{M}(z)/z}{1 + k\tilde{M}(z)/z} \delta F(z). \quad (\text{B.28})$$

Since $F(z)$ is proportional to f , we may divide both sides by f , then use Eq. B.20 to obtain the Laplace transform of the projected length linear response

$$\chi_{\Delta\ell}(z) = -z \frac{\tilde{M}(z)/z}{1 + k\tilde{M}(z)/z} \frac{\delta F(z)}{f}. \quad (\text{B.29})$$

B.3 Polarization function calculation

It is computationally easier to begin by working in the time domain. We decompose $\mathbf{M}^{-1}(t, t')$ in terms of its $k = 0$ and $k \neq 0$ pieces via

$$\mathbf{M}^{-1}(t, t') = \boldsymbol{\sigma} + Dk\boldsymbol{\Pi}(t, t'), \quad (\text{B.30})$$

where $\boldsymbol{\sigma}$ represents the 2x2 block matrix with zeros along the diagonal, and identity matrices on the off diagonal. We call the additional contribution, $\boldsymbol{\Pi}(t, t')$, the polarization matrix, in analogy to electron screening in metals [4]. It encodes fluctuation corrections, and is determined by the trace-log. Specifically, it is given by the

second-order term in the Taylor expansion of $\text{Tr} \ln(\mathbb{1} + Dkp^2 \hat{G} \delta \hat{\lambda})$ about the small matrix

$$\delta \hat{\lambda}(t) = \begin{pmatrix} 0 & \delta \lambda(t) \\ \delta \lambda(t) & -\delta \bar{\lambda}(t) \end{pmatrix}. \quad (\text{B.31})$$

\hat{G} is the saddle-point, matrix-valued Green's function

$$\hat{G}(t, t') = \begin{pmatrix} 0 & \bar{G}_p^-(t - t') \\ \bar{G}_p^+(t - t') & \bar{C}_p(t - t') \end{pmatrix}, \quad (\text{B.32})$$

with components given by the time representation of Eq. 3.58a,

$$\bar{G}_p^\pm(t) = \Theta(\pm t) e^{\mp D \gamma_p t}, \quad (\text{B.33})$$

and Eq. 3.58b,

$$\bar{C}_p(t, t') = 2D \int d\tau G^+(t - \tau) G^-(\tau - t'). \quad (\text{B.34})$$

The modified function $\gamma_p = \gamma_p^0 + kp^2 \lambda_0$, includes the saddle-point value λ_0 . The logarithm of matrices is defined via its Taylor series, whose quadratic term is $\frac{-1}{2} \text{Tr} \hat{G} \delta \hat{\lambda} \hat{G} \delta \hat{\lambda}$. The factor of 1/2 can be factored out, per the definition of $\mathbf{\Pi}$. Products of the form $\hat{G}^\pm(t) \hat{G}^\pm(-t)$ have vanishing support due to the θ functions and are zero. Carrying out the matrix products, we find that $\mathbf{\Pi}(t, t') = \mathbf{\Pi}(t - t')$ is a function only of the time difference, with the result

$$\mathbf{\Pi}(t) = \sum_p p^4 \begin{pmatrix} -C_p^2(t) & 2G_p^+(t)C_p(t) \\ 2G_p^-(t)C_p(t) & 0 \end{pmatrix}. \quad (\text{B.35})$$

Since each of the operators depend on only the time difference $t - t'$, we may Fourier transform to frequency space. Including the σ contribution we find the effective functional matrix

$$\mathbf{M}_\omega^{-1} = \begin{pmatrix} -\Pi_\omega^0 & \Pi_\omega^+ + 1 \\ \Pi_\omega^- + 1 & 0 \end{pmatrix}. \quad (\text{B.36})$$

The individual components are given by Eqs. 3.61 and 3.62. We have chosen the \pm notation to emphasize the similarity of Π^\pm to Green's functions, and Π^0 to the spring-free correlator. Indeed, $\Pi^+ = (\Pi^-)^*$, and, as a consequence of the fluctuation-dissipation, the Π functions obey the relationship

$$\text{Im}\Pi_\omega^+ = \frac{\omega}{2k_B T} \Pi_\omega^0. \quad (\text{B.37})$$

We thus need only compute Π^+ to fully specify the polarization matrix.

B.4 Transverse spring only

For completeness, we report the solution of the problem for a purely transverse spring attached at the endpoint (*i.e.*, no longitudinal component). To incorporate both the longitudinal and transverse springs simultaneously, we simply replace the decay rates below with those calculated in the main text in the presence of a longitudinal spring. We follow the method of Ref. [71] for dealing with inhomogeneous boundary conditions in Fourier space. In this section, primes refer to spatial derivatives.

The homogeneous boundary conditions are pinned, with zero torque at both endpoints: $u(x_S) = u''(x_S) = 0$, and $x_S = 0, \ell$. Wavenumbers are set to $p_n = n\pi/\ell$, for n a positive integer. The transverse spring replaces the pinned boundary condition $u(\ell) = 0$ with the new condition

$$-\kappa u''''(\ell) + \tau u''(\ell) = -k_\perp u(\ell). \quad (\text{B.38})$$

In the bulk, we still have the linear Langevin equation

$$\partial_t u + D\kappa u'''' - D\tau u'' = \zeta(x, t), \quad (\text{B.39})$$

subject to the aforementioned boundary conditions. In order to implement the boundary condition, we add an additional force operator that is non-diagonal in wavenumber and regulated by a parameter ϵ that we take to zero at the end of the calculation [71]. We write:

$$\left[\delta_{nm} (\partial_t + D\kappa p_n^4 + D\tau p_n^2) + \frac{1}{4\epsilon} \psi_n \psi_m \right] u_m = \delta_{nm} \xi_m, \quad (\text{B.40})$$

where we have defined the infinite dimensional vector

$$\psi_n = (-1)^n \left(\frac{\gamma_n}{p_n} + \frac{1}{2} k_\perp \sin 2n\pi \right). \quad (\text{B.41})$$

This is solved by the method of Green's functions. We replace ζ on the right side with a δ -function in time and a Kronecker delta δ_{nk} , and $u_m(t)$ by the Green's function $\chi_{mk}^\perp(t-t')$. The response is still given by a sum over sines

$$\chi^\perp(x, x'; t) = \sum_{m,n=1}^{\infty} \chi_{mn}^\perp(t) \sin(p_n x) \sin(p_m x'). \quad (\text{B.42})$$

Next, we Laplace transform the χ version of Eq. B.40, take the inverse of the left side, and finally take the $\epsilon \rightarrow 0$ limit to find

$$\chi_{mk}^\perp(s) = \chi_{mk}^D(s) + \chi_{mk}^{BC}(s), \quad (\text{B.43})$$

which has decomposed into a homogeneous part plus boundary term. The homogeneous part is

$$\chi_{nm}^D(s) = \chi_n^0(s) \delta_{nm} = \frac{\delta_{nm}}{s + \gamma_n}, \quad (\text{B.44})$$

where for this section we have defined

$$\gamma_n = D\kappa p_n^4 + D\tau p_n^2. \quad (\text{B.45})$$

The boundary term is given by

$$\chi_{mk}^{BC}(t) = \frac{-(\chi_n^0 \psi_n)^2}{\sum_{n=1}^{\infty} \psi_n \chi_n^0 \psi_n}. \quad (\text{B.46})$$

. The numerator is

$$\text{numerator} = -\frac{(-1)^{n+m}}{p_n p_m} \left[\frac{\gamma_n \gamma_m}{(s + \gamma_n)(s + \gamma_m)} \right]. \quad (\text{B.47})$$

The denominator is a divergent sum. It has two main pieces

$$\sum_{n=1}^{\infty} \left\{ \frac{\gamma_n^2}{p_n^2 (s + \gamma_n)} + k_{\perp} \frac{\gamma_n \sin 2\pi n}{p_n (s + \gamma_n)} + \text{convergent} \right\} \quad (\text{B.48})$$

The third piece is a convergent sum proportional to $\sin 2\pi$, and can be safely set to zero. We rewrite the series by subtracting out the divergent pieces as

$$\sum_{n=1}^{\infty} \left\{ \frac{-s\gamma_n}{p_n^2 (s + \gamma_n)} + \frac{\gamma_n}{p_n^2} + \frac{-s \sin 2\pi n}{p_n (s + \gamma_n)} + \frac{k_{\perp} \sin 2\pi n}{p_n} \right\} \quad (\text{B.49})$$

The first and third are now convergent, so the third can immediately be set to zero. The second and fourth need regularization. These sums were computed previously [71], with the results $-\tau/2$ and $-k_{\perp}\ell/2$ respectively. We then have

$$\text{denominator} = -\frac{1}{2}(\tau + k_{\perp}\ell) - \sum_{n=1}^{\infty} \frac{s(\kappa p_n^2 + \tau)}{s + \kappa p_n^4 + \tau p_n^2}. \quad (\text{B.50})$$

Combining, we find the boundary response

$$\chi_{mn}^{\text{BC}}(s) = \frac{2(-1)^{n+m}\gamma_n\gamma_m}{p_n p_m (\tau + k_{\perp}\ell + F(s))(s + \gamma_n)(s + \gamma_m)}, \quad (\text{B.51})$$

where

$$F(s) = 2 \sum_{n=1}^{\infty} \frac{s(\kappa p_n^2 + \tau)}{s + \kappa p_n^4 + \tau p_n^2}. \quad (\text{B.52})$$

The sum of Eqs B.44 and B.51 gives the final result for the Laplace-transformed response function for a purely transverse spring at the boundary. To obtain the space/time domain solution, one can numerically perform the inverse transform and sum over modes according to Eq. B.42.

APPENDIX C

Appendices for dynamics of transiently cross-linked bundles

C.1 Perturbative ϵ expansion of kinetic railway track model

Insertion of $n(x, t) = n_0 + \delta n(x, t)$ into Eq. 4.13 gives the equation of motion for $\delta n(x, t)$. Our calculation begins with the two dynamical equations

$$\left[\frac{1}{K_{\text{off}}} \frac{d}{dt} + (1 + z) + V(\theta) \right] \delta n = -n_0 V(\theta) \quad (\text{C.1a})$$

$$\frac{\partial u}{\partial t} = -D(\kappa u'''' - k_{\times} a^2 n_0 u'' - k_{\times} a^2 (\delta n u)') + \xi, \quad (\text{C.1b})$$

where we have defined the Mayer-function like potential

$$V(\theta) = e^{\frac{1}{2} \beta k_{\times} a^2 \theta^2(x, t)} - 1. \quad (\text{C.2})$$

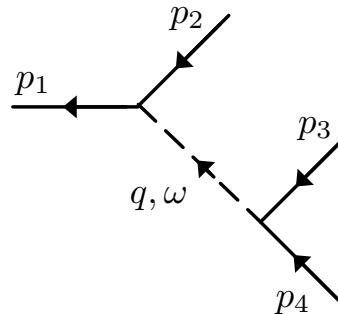
To develop the perturbation theory, we must identify a small parameter. Near the boundary between the transient and permanently linked railway track models, the bundle relaxes much faster than the cross-linkers. This suggests a ratio of the relaxation times of linkers to the bundle is small, approaching zero in the permanently linked limit. In this regime, the bundle is dominated by its $\bar{\ell}^4$ scaling, and so we approximate $\tau_{\text{WLB}} \approx \tau_{\text{WLC}}$, where $\tau_{\text{WLC}} = \frac{\kappa \pi^4}{\zeta \bar{\ell}^4}$. Rescaling units of time to $\tau = t/\tau_{\text{WLC}}$, we find that $d\delta n/d\tau \sim \epsilon$, where $\epsilon = \frac{\tau_{\text{off}}}{\tau_{\text{WLC}}}$ as defined in Eq. 4.16.

The potential $V(\theta) \sim \epsilon$ as well, and so the third term on the right side of Eq. C.1b can be treated perturbatively. The potential $V(\theta)$ however, remains highly nonlinear. Performing a pre-average of the Boltzmann factor as in Eq. 4.5, we find that the argument of the exponential is small for all values k_\times . We thus expand $V(\theta)$ in a power series with respect to θ , yielding the lowest order result

$$\left[\frac{1}{K_{\text{off}}} \frac{d}{dt} + (1+z) \right] \delta n(x, t) = -\frac{n_0 \alpha}{2} \theta^2. \quad (\text{C.3})$$

We have additionally defined the dimensionless ratio $\alpha = \beta k_\times a^2$ (not to be confused with the longitudinal response, which we do not reference in this section). Formally solving for $\delta n(x, t)$ and substituting into the Langevin equation gives the nonlinear generalized force $\frac{1}{2} D \alpha k_\times a^2 n_0 \left(u' \frac{K_{\text{off}}}{\partial_t + K_{\text{off}}(1+z)} u'^2 \right)'$. The nonlinearity can be treated graphically in terms of Feynman diagrams. To do so, we first assume periodic boundary conditions and represent $u(x, t)$, $\delta n(x, t)$ by their Fourier series/transforms defined in Eqs. 4.17, 4.18. Our normalization requires a factor of $1/\ell$ for the inverse Fourier series. We have further removed the zero mode of $u(x, t)$, fixing the midline of the bundle to lie along the \hat{x} -axis. This, in combination with Eq. C.1a, eliminates the zero mode from the δn Fourier series as well. This does not preclude a zero frequency component though.

The nonlinear interaction can be viewed diagrammatically as the vertex



$$= \frac{D k_\times^2 a^4 n_0 \ell}{2 k_B T \tau_{\text{off}}} \frac{p_1 p_2 p_3 p_4}{-i\omega + (1+z)/\tau_{\text{off}}}. \quad (\text{C.4})$$

The delta functions conserving wavenumber and frequency at each vertex are implied. Each leg with wavenumber p_i also carries a frequency ω_i , and $q = p_1 - p_2$, $\omega = \omega_1 - \omega_2$. Directed solid lines denote the $\delta n(x, t) = 0$ Green's function $G_0(p, \omega) = (1/\ell)(-i\omega + D(\kappa p^4 + k_\times a^2 p^2))^{-1}$. Undirected solid lines denote the correlator $C_0(p, \omega) = (2Dk_B T/\ell)(\omega^2 + D^2\gamma_p^2)^{-1}$, which has accounted for a factor of $2D$ coming from noise averaging. As usual, the Green's function is determined by the set of one particle irreducible connected diagrams Σ , via the relation $G^{-1}(p, \omega) = G_0^{-1}(p, \omega) - \Sigma(p, \omega)$ [?]. We focus on calculating $\tilde{\Sigma} = -\frac{1}{D\ell}\Sigma$, such that the renormalized stiffness is $\kappa_R(p, \omega) = \kappa + \tilde{\Sigma}(p, \omega)p^{-4}$. There are two diagrams at lowest order, given by

$$\tilde{\Sigma}_1(p, \omega) = 2 \begin{array}{c} \text{---} \leftarrow \text{---} \leftarrow \text{---} \leftarrow \\ \text{---} \leftarrow \text{---} \leftarrow \text{---} \leftarrow \\ \text{---} \leftarrow \text{---} \leftarrow \text{---} \leftarrow \end{array} = -\frac{p^2}{\ell} \sum_q \frac{q^2 k_\times^2 a^4 n_0}{\gamma_q(-i\omega\tau_{\text{off}} + D\tau_{\text{off}}\gamma_q + (1+z))} \quad (\text{C.5})$$

$$\tilde{\Sigma}_2(p, \omega) = \begin{array}{c} \text{---} \leftarrow \text{---} \leftarrow \\ \text{---} \leftarrow \text{---} \leftarrow \\ \text{---} \leftarrow \text{---} \leftarrow \end{array} = -\frac{p^2 k_\times^2 a^4 n_0}{2\ell(1+z)} \sum_q \frac{q^2}{\gamma_q}. \quad (\text{C.6})$$

Rearranging in terms of dimensionless quantities leads to the bending rigidity corrections $\Delta\kappa_1(p_n, \omega)$ and $\Delta\kappa_2(p_n, \omega)$ given in Eqs. 4.19 and 4.20 of the main text.

We now compute the n_0 renormalization. All ϵ -independent terms are represented diagrammatically by tadpoles, where cutting any dashed line will disconnect the diagram. Higher order terms require us to also expand $V[\theta(x, t)]$ to higher orders in well. We can, in fact, sum over all tadpole that appear when using the full nonlinear potential $V[\theta(x, t)]$.

This is done by first starting at Eq. C.1a without the small α approximation. We formally solve for the basis independent $\hat{\delta}n$, expressing it in terms of the operator inverse $\hat{G}_n = (K_{\text{off}}^{-1}\partial_t + (1+z))^{-1}$. This gives the formal result

$$\hat{\delta}n = -n_0(\mathbb{1} + \hat{G}_n\hat{V})^{-1}\hat{G}_n\hat{V}. \quad (\text{C.7})$$

Insertion into Eq. C.1b and taking the power series $\hat{\delta}n = n_0 \sum_{m=1}^{\infty} (-\hat{G}_n\hat{V})^m$ tells us the types of diagrams that appear. The first order term in the Fourier basis, $(-\hat{G}_n\hat{V})$, is precisely the vertex of Eq. C.4. \hat{G}_n generates dashed lines connecting the function on its right to that on its left, representing the propagator for a density excitation. In general, the m^{th} term of the series consists of a string of m vertices V connected by m dashed lines. The vertex V is itself represented by its own power series $V(\theta) = \sum_{m=1}^{\infty} c_m(\alpha\theta^2)^m$ which can be depicted Fourier space diagrammatically as the sum over all diagrams

$$\begin{aligned} & \text{Diagram with } p_1, p_2, q, \omega \text{ and shaded circle} \\ &= c_1 \alpha \text{ (Diagram with } p_1, p_2, p_3, p_4 \text{)} + c_2 \alpha^2 \text{ (Diagram with } p_1, p_2, p_3, p_4, p_5, p_6 \text{)} + \dots \end{aligned} \quad (\text{C.8})$$

with one incoming and one outgoing line connected by a dashed line to a vertex consisting of any even number of incoming lines. The coefficients c_n can be determined from the Taylor expansion, but the exact form will ultimately be irrelevant. The full $\hat{\delta}n$ contribution, is then given by the sum over such effective vertices chained together in a row by m dashed lines. We omit diagrams that transfer frequency, as

they will be proportional to ϵ . The remaining diagrams are the zero-frequency tadpoles. These correspond to contracting each V vertex independently of the rest, so that every dashed line in the diagram carries zero frequency; the latter corresponds to replacing G_n with $(1+z)^{-1}$.

For any given diagram of the V vertex series, all contractions are identical, forming a closed loop. The single loop contraction was already computed in Eq. C.6. Each contraction thus gives a factor of the static value

$$\langle \theta_p^2 \rangle_{\text{st}} = \sum_{m \neq 0} \frac{T\ell/\kappa\pi^2}{4m^2 + \phi} = \frac{1}{N} \left(\frac{\pi\sqrt{\phi}}{2} \coth \left(\frac{\pi\sqrt{\phi}}{2} \right) - 1 \right). \quad (\text{C.9})$$

The rest is now a combinatorics problem. Taking into account the number of ways to contract vertices, we find

$$\langle V \rangle = \sum_n (2n-1)!! c_n (\alpha \langle \theta^2 \rangle_{\text{st}})^n. \quad (\text{C.10})$$

The series is Borel summable and we may replace $(2n-1)!!$ by its representation as a Gaussian integral $(2\pi)^{-1/2} \int s^{2n} e^{-s^2/2} ds$. This introduces no new combinatorial factors, so we can group the dummy integration variable s with $\langle \theta^2 \rangle_{\text{st}}$ and trivially re-sum the series to get back the original function. The net result of these manipulations, is the replacement

$$V(\theta^2) \rightarrow (2\pi)^{-1/2} \int ds e^{-s^2/2} V(s^2 \langle \theta^2 \rangle_{\text{st}}). \quad (\text{C.11})$$

The integral is still Gaussian, and we find the main result

$$V(\theta) \xrightarrow{\text{tadpoles}} \sqrt{1 - \alpha \langle \theta^2 \rangle} - 1. \quad (\text{C.12})$$

To determine the renormalization, we again solve for $\delta n(x, t)$ (which is now a constant) and insert back into Eq. C.1b. Simplifying, we find that the bundle Langevin

equation maintains the same form provided we make the replacement

$$n_0 \xrightarrow{\text{tadpole}} \frac{N_s/\ell}{1 + z_R(\phi)^{-1}}. \quad (\text{C.13})$$

where

$$z_R(\phi) = z \left(1 - \frac{1}{N} \left(\frac{\pi\sqrt{\phi}}{2} \coth \left(\frac{\pi\sqrt{\phi}}{2} \right) - 1 \right) \right)^{1/2} \quad (\text{C.14})$$

To complete our calculation, we must also account for diagrams where the propagators themselves are renormalized by tadpoles. This is accomplished by making the self-consistent extension of replacing n_0 on the right hand side of Eq. C.13, with the fully renormalized n_R . Doing so yields the self-consistent Eqs. 4.23, 4.24 in the main text.

Finally, the non self-consistent value for n_R predicts that the linker density vanishes at $z_R(\phi^*) = 0$. Assuming N is large, this must occur at large ϕ as well, allowing us to replace the coth with 1 and find the unbinding condition $\phi^* = (2(N + 1)/\pi)^2$.

C.2 One dimensional nearest-neighbor free energy

Our exposition closely follows reference [134]. Our primary task is to calculate the radial distribution function $g(r)$, which gives the probability density of a particle located at radius r , provided there is a particle at the origin. From there, we can recover the full statistical mechanics.

We first define $p_1(x)$, the probability that if a particle is at some location x_0 , its nearest neighbor will be located at position $x_0 + x$. Due to translational invariance, this is a function only of the separation x between neighbors. The related probability $p_N(x)$, that the N^{th} nearest neighbor is located distance x away, satisfies the recursion

relation

$$p_N(x) = \int_0^x p_{N-1}(x-x')p_1(x')dx'. \quad (\text{C.15})$$

Due to the convolution, Laplace transform yields the solution

$$p_N(s) = p_1^N(s). \quad (\text{C.16})$$

Our remaining job is to determine $p_1(s)$. We consider an arbitrary configuration of the N particle system, extending from $x = 0$ to $x = L$, and at pressure P . Due to the one-dimensional nature of the problem, each particle is uniquely determined by its ordering on the line. The $N + 1$ particle system is built recursively by inserting an additional particle bounded from the left by 0 and on the right by the N^{th} particle, then integrating over positions of the last two particles. As a result, we may write

$$p_1(r) \sim \int_r^\infty dL e^{-\beta PL} \prod_{i=2}^N \int_{x_{i-1}}^L dx_i e^{-\beta V(x_i - x_{i-1})}. \quad (\text{C.17})$$

with boundary conditions $x_1 = r$ and $x_N = L$. Here, $\beta = (k_B T)^{-1}$ and P is the pressure.

Effecting the change of variables $x_i \rightarrow x_i - x_{i-1}$, the upper limits become $L - r$, $L - r - r_1$, $L - r - r_1 - r_2 - \dots$. Sending $L \rightarrow L + r$ renders the iterated integrals independent of r , and so we can set it to a constant c . This gives

$$p_1(r) = c e^{-\beta Pr} e^{-\beta V(r)}. \quad (\text{C.18})$$

Next, we define the function

$$\Omega(s) = \int dr e^{-sr} e^{-\beta V(r)}, \quad (\text{C.19})$$

which is the Laplace transform of the Boltzmann weight. In terms of $\Omega(s)$, the Laplace transform of the nearest neighbor distribution is then given by $p_1(s) =$

$c\Omega(s + \beta P)$. The constant c is determined by enforcing the normalization condition $\int dr p_1(r) = 1$, which is equivalent to $p_1(0) = 1$. As a result,

$$c = 1/\Omega(\beta P). \quad (\text{C.20})$$

We can now determine the radial distribution function. Summing the geometric series for the Laplace transform $g(s) = \frac{1}{n_l} \sum_{i=1}^{\infty} p_1(x)^i$ gives

$$\hat{g}(s) = \frac{1}{n_l} \frac{\Omega(s + \beta P)}{\Omega(\beta P) - \Omega(s + \beta P)}. \quad (\text{C.21})$$

The density n_l , and as a result the equation of state, is determined by requiring that as $r \rightarrow \infty$, particles are uncorrelated. This implies that the total number of particles a distance r away is given simply by the average density n_l . This corresponds to the condition $1 = \lim_{s \rightarrow 0} s\hat{g}(s)$, leading to the equation of state

$$n_l = -\frac{\Omega(\beta P)}{\Omega'(\beta P)}. \quad (\text{C.22})$$

The right hand side is the inverse of a logarithmic derivative with respect to pressure. In combination with the thermodynamic relations $\ell = \left(\frac{\partial \mathcal{G}}{\partial P}\right)$ and $\mathcal{G} = \mu N$, we identify the chemical potential

$$\mu = Nk_B T \ln \left(\frac{\Lambda}{\Omega(\beta P)} \right). \quad (\text{C.23})$$

Here, Λ is the thermal de Broglie wavelength. The total correlation function $h(r)$ is related to the radial distribution function via $h(r) = g(r) - 1$. In Fourier space, h_q given by

$$h_q = \hat{g}(iq) + \hat{g}(-iq). \quad (\text{C.24})$$

The zero mode is treated separately. It is given by the limit $\lim_{s \rightarrow 0} 2(R(s) - s^{-1})$, which yields

$$h_0 = 2 \left(\frac{\Omega'(\beta P)}{\Omega(\beta P)} - \frac{\Omega''(\beta P)}{2\Omega'(\beta P)} \right). \quad (\text{C.25})$$

From the density and total correlation function, we can determine a number of other quantities. Of special interest is the structure function

$$S_q = 1 + n_l h_q. \quad (\text{C.26})$$

From the Ornstein-Zernicke equation [134] we can relate the total correlation to the direct correlation function. In Fourier space this relation is

$$c_q^{(2)} = \frac{h_q}{1 + n_l h_q}. \quad (\text{C.27})$$

This concludes the main results we will need for one-dimensional nearest neighbor systems. We now apply this to hard rods interacting via Casimir forces. The Boltzmann factor pertaining to Casimir interactions is given by [66]

$$e^{-\beta V} = (r/\lambda_c)^{-\beta d_\perp \alpha} \Theta(|x| - \sigma), \quad (\text{C.28})$$

where d_\perp is the number of transverse directions, α is the number of degrees of freedom constrained at the boundary (one for pinned and two for pinning position plus angle), and λ_c is an inconsequential phase space volume. We focus on the cases $d_\perp \alpha = 2, 4$. The special case $d_\perp \alpha = 0$ is the hard rod only model. Performing the Laplace transform, we calculate the fundamental quantity

$$\Omega(s) = (\beta P)^{-1+d_\perp \alpha} \Gamma(1 - d_\perp \alpha, \beta P \sigma), \quad (\text{C.29})$$

where Γ denotes the upper incomplete gamma function. From this, we find the equation of state [66]

$$n_l = \beta P \sigma \frac{\Gamma(1 - d_\perp \alpha, \beta P \sigma)}{\Gamma(2 - d_\perp \alpha, \beta P \sigma)}. \quad (\text{C.30})$$

Generally, one must prescribe either the density n_l , or the pressure per temperature βP , then determine the other via the equation of state. The total correlation

function is

$$h_k = \frac{2}{n_l} \text{Re} \left[\left(-1 + \frac{E_{d_\perp \alpha}(\beta P)}{E_{d_\perp \alpha}((\beta P + iq)\sigma)} \right)^{-1} \right], \quad (\text{C.31})$$

and the structure function

$$S_q = 1 + 2 \text{Re} \left[\left(-1 + \frac{E_{d_\perp \alpha}(\beta P)}{E_{d_\perp \alpha}((\beta P + iq)\sigma)} \right)^{-1} \right]. \quad (\text{C.32})$$

We have written these in terms of the exponential integral function, defined as

$$E_d(z) = \int_1^\infty e^{-zt} t^{-d} dt. \quad (\text{C.33})$$

For the special case of hard rods ($d_\perp \alpha = 0$), these take can be expressed in terms of trigonometric functions. We remove the pressure from the equation of state, and σ by defining the packing fraction $n\sigma = \bar{\eta}$ and dimensionless wavenumber $\bar{q} = q\sigma$. The packing fraction is necessarily less than or equal to one. We write

$$S_{\bar{q}}^{(HS)} = \frac{\bar{q}^2 (\bar{\eta} - 1)^2}{\bar{q}^2 (\bar{\eta} - 1)^2 - 2\bar{q}\bar{\eta} (\bar{\eta} - 1) \sin \bar{q} - 2\bar{\eta}^2 \cos \bar{q} + 2\bar{\eta}^2}. \quad (\text{C.34})$$

For completeness, in Fig. C.1 we plot both the direct correlation function and radial distribution function in real space. The positive correlation tail for distances $x > \sigma$ is responsible for the density-density interaction in the RY free energy of Eq. 4.45, and is in contrast to hard rods. Peaks in radial distribution function are dampened by Casimir interactions.

C.3 Master equation for linker hopping

A particular state of bound/unbound linkers is given by the set of numbers $\{n_1, \dots, n_{N_s}\}$ denoting the number of linkers bound at any of the N_s binding sites.

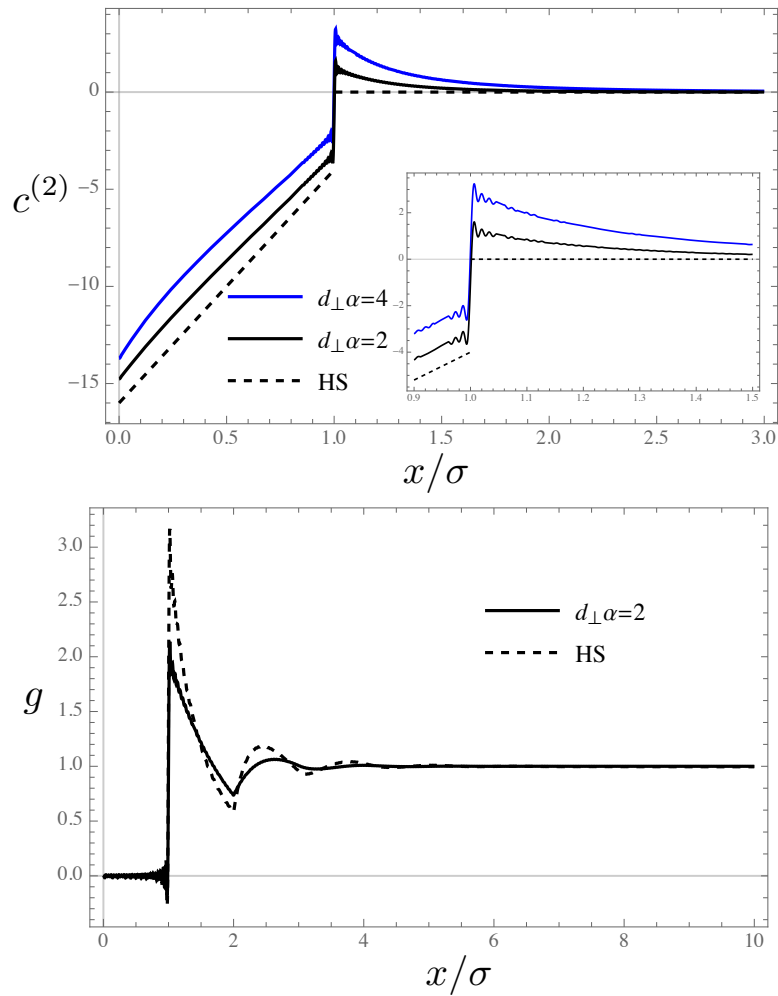


Figure C.1: Top: direct correlation function of cross-linker fluid. $\sigma = 1$, $\beta P = 1$ and 3000 modes were summed over in the Fourier series. The inset shows a close up of the transition at $x = \sigma$. Bottom: radial distribution function for the physically relevant case $d_{\perp}\alpha = 2$ compared to hard rods. Packing fraction is 0.5 and we summed over 1000 Fourier modes.

We work in a continuum picture whereby the number of binding sites per unit length is dense and we can replace lattice index i with a smooth position x . In doing so, we must take care to maintain the hard-core repulsion property of cross-linkers, that is, at every site there can be only one particle ($n_i = 0, 1$). Since the particles are non-interacting, it is sufficient to first examine our theory for a single site, then later add in position.

We shall build a field theory by using the second-quantized Doi-Peliti operator method [27, 122]. We postulate a Fock-space with vacuum $|\emptyset\rangle$ and integer valued occupation numbers. The so-called hard-core bosonic theory can be explicitly constructed in the species space [118, 119]. We denote the vacuum state of no cross-linkers by $|\emptyset\rangle$, and the state of a single species of type s as $|s\rangle$. We define then the creation and annihilation operators

$$a_s = |\emptyset\rangle \langle s|, \quad \bar{a}_s = |s\rangle \langle \emptyset|. \quad (\text{C.35})$$

Using this, it's not hard to confirm that $\bar{a}_s |\emptyset\rangle |s\rangle$ and $a_s |s'\rangle = \delta_{ss'} |\emptyset\rangle$. Furthermore, we have the hard core exclusion identities

$$a_s a_{s'} = \bar{a}_s \bar{a}_{s'} = 0, \quad (\text{C.36})$$

which tells us that only one species occupy a site at a given time. Finally, our operators obey the anti-commutation relation

$$\{a_s, \bar{a}_s\} = \mathbb{1} - \sum_{s' \neq s} a_{s'} \bar{a}_{s'}. \quad (\text{C.37})$$

The second-quantized operators are only useful provided we have a state ket to

act on. We introduce the second-quantized state ket

$$|\Psi\rangle = P_\emptyset |\emptyset\rangle + \sum_s P_s(t) |s\rangle, \quad (\text{C.38})$$

where each of the $P_i(t)$ functions represent the probability for the system to be in state $|i\rangle$. In general, we would like to compute expectation values in this formalism. The expectation of some operator A given in the Fock-space basis, is given by $\langle A \rangle = A_\emptyset P_\emptyset + \sum_s P_s A_s$. We define the projection bra $\langle \cdot | = \langle \emptyset | + \sum_s \langle s |$ which sums over each possible state. Applying the projection operator, we can succinctly write the expectation value $\langle A \rangle = \langle \cdot | A | \Psi(t) \rangle$. Conservation of probability leads to the identity $\langle \cdot | \Psi(t) \rangle = \sum_s P_s = 1$.

In order to build a dynamical theory, we must provide microscopic input. Our starting point is the master equation

$$\frac{\partial P_\beta}{\partial t} = \sum_\alpha (w(\alpha \rightarrow \beta) P_\alpha - w(\beta \rightarrow \alpha) P_\beta). \quad (\text{C.39})$$

To describe cross-linker binding/unbinding, we must now re-introduce the spatial coordinate. Assuming for a moment that the operators were defined on a lattice, we identify the annihilation operator at site j by the operator $a_j = \mathbb{1} \otimes \dots \otimes a_j \otimes \dots \otimes \mathbb{1}$. Clearly, all of the operators commute at different positions, hence the bosonic part of the hard-core boson nomenclature.

We restrict our attention to to the probability that after one time step, a single location is occupied by a cross-linker of type α . Locally, there are two ways to do so. We can begin from the vacuum state and bind an α particle, or we can start with an α particle already bound and stay that way. To describe the full transition probability though, we must also sum over configurations where binding/unbinding transitions occur at all other locations along the bundle (synchronous updating).

In order to circumvent this difficulty, we adopt an asynchronous model, whereby at each time step only one cross-linker may bind/unbind at a time. This is a similar procedure to the linear Glauber model for spin flips in a kinetic Ising model [42]. With this restriction, we lose information on rare events whereby a large number of linkers simultaneously bind/unbind. However, for smooth bundle fluctuations we expect such sharp transitions to be negligible.

Lastly, we consider the form of the rates $w_{\alpha \rightarrow \beta}$. To account for different linker species, we must adjust the interaction Hamiltonian of Eq. 4.2 by replacing $\theta(x, t) \rightarrow \theta(x, t) - s$. Accordingly, we must also slightly adjust the detailed balance condition of Eq. 4.4 by the same $\theta(x, t)$ transformation. For notational simplicity, we identify the fugacity $z = e^{\beta\mu}$. Furthermore, since only one binding constant is required, we redefine $K_{\text{on}} = k$ and $K_{\text{off}}(x, t; s) = kz^{-1}e^{\frac{1}{2}\beta k \times a^2(\theta(x, t) - s)^2}$.

We only allow binding to occur to the lowest possible configuration at any given time. That is, a cross-linker will never choose to bind in a sheared state. This is imposed by defining $k_{\text{bind}}(x, s; t) = k\delta(\theta(x, t) - s)$. The off and on rates define a birth/death process. Particularly, this is a multi-species form of the simple telegraph model. The death rate at a particular site is proportional to the number of particles n , while the birth rate is proportional to the number of empty sites $1 - n$. We now find the master equation

$$\begin{aligned} \frac{\partial P_{\{n_i\}}(t)}{\partial t} = & \sum_i -k_{\text{on}}(1 - n_i)P_{n_i^+} - k_{\text{off}}n_iP_{n_i} + \\ & + k_{\text{on}}(1 - n_i^-)P_{n_i^-} + k_{\text{off}}(n_i^+)P_{n_i^+}. \end{aligned} \tag{C.40}$$

We have used the notation $n_i^\pm = n_i \pm 1$, the species and spatial dependence of the kinetic coefficients is suppressed for clarity, and on the right hand side it is

understood that all other sites are held fixed with the subscripted site changed. The master equation in ket space takes the form of a linear Schrodinger like equation

$$\frac{\partial |\Psi(t)\rangle}{\partial t} = -\hat{H} |\Psi(t)\rangle \quad (\text{C.41})$$

governed by the pseudo-Hamiltonian \hat{H} . We make use of the definition of the number operator $\hat{n}_s(x) = \bar{a}_s(x)a_s(x)$, to express H in second-quantized form

$$\hat{H}_s(\bar{a}, a) = \beta_s - \beta_s \bar{a}_s - \mu_s a_s - (\beta_s - \mu_s) \bar{a}_s a_s. \quad (\text{C.42})$$

With the x, t dependence of β_s and μ_s not explicitly shown. Particularly, they are

$$\beta_s(x, t) = k\delta(\theta(x, t) - s), \quad \mu_s(x, t) = kz^{-1}e^{\frac{1}{2}\beta k \times a^2(\theta-s)^2}. \quad (\text{C.43})$$

The Hamiltonian obeys $\langle \cdot | \hat{H} = 0$, and so probability is conserved. We may then write all expectations in terms of the commutator $\langle A \rangle = \langle [H, A] \rangle$. Particularly, we are interested in computing the cross-link density function $n_s(x, t) = \langle \bar{a}_s a_s \rangle$, which due to occupancy limit is equivalent to the density probability distribution. Using Eqs. C.35-C.37, we compute $\langle [\hat{H}, \bar{a}_s a_s] \rangle$ to find the kinetic equations

$$\frac{\partial n_s}{\partial t} = -kz^{-1}e^{\frac{1}{2}g(\theta-s)^2} n_s + k\delta_{\theta s} \langle \emptyset | \Psi(t) \rangle. \quad (\text{C.44})$$

$$\frac{d}{dt} \langle \emptyset | \Psi(t) \rangle = -k\delta_{s\theta} \langle \emptyset | \Psi(t) \rangle + \int ds' \mu_{s'} n_{s'} \quad (\text{C.45})$$

Utilizing probability conservation $\langle \emptyset | \Psi(t) \rangle + \int ds n_s = 1$, we may eliminate the unbound probability to write

$$\frac{\partial n_s}{\partial t} = -k\delta_{\theta s} \int ds' n_{s'} - kz^{-1}e^{\frac{1}{2}g(\theta-s)^2} n_s + k\delta_{\theta s}, \quad (\text{C.46})$$

which reproduces Eq. 4.31.

APPENDIX D

Appendices for geometrical diffusion of undulatory waves on a warped membrane

D.1 Self-energy calculation

The reader primarily interested in the results, is encouraged to skip directly to Tab. D.2.

We compute the disorder averaged Green's function $\langle G^+ \rangle$ and thereby, via Eq. ??, the self-energy. The field theory is defined by the action in Eq. 6.12, and the perturbation theory by the subsequent decomposition of S into a Gaussian piece S_0 , and an interacting piece S_{int} . The dimensionless parameter regulating the perturbation series is determined post factum after computing the first order correction. The elementary propagators and vertices are shown diagrammatically in Fig. D.1. All calculations are performed using the large L limit, whereby we replace summations $L^{-2} \sum_p(\dots)$ with integrations $\int \frac{d^2 p}{(2\pi)^2}(\dots)$. The projection operators appearing in the disorder vertex can alternatively be written as the cross product of two two-dimensional vectors projected in to three dimensions as

$$p_i P_{ij}^T(q) p_j = \frac{|p \times q|^2}{q^2}, \quad (\text{D.1})$$

which will prove useful. Since p and q are not actually vectors, we omit the bold

$$\begin{aligned}
& \begin{array}{c} (q, \omega, \alpha) \\ \text{~~~~~} \\ (q', \omega', \beta) \end{array} = \frac{\gamma}{L^2} \frac{\delta_{\mathbf{q}, -\mathbf{q}'} \delta_{\alpha\beta}}{q^{2d_H}} \\
& \begin{array}{c} (q, \alpha) \\ \text{—————} \\ (q', \beta) \end{array} = \frac{1}{L^2} \frac{\delta_{\mathbf{q}, -\mathbf{q}'} \delta_{\omega, -\omega'} \delta_{\alpha\beta}}{\kappa q^4 - \sigma \omega^2} \\
& \begin{array}{c} \begin{array}{c} q_i^1 \\ \text{~~~~~} \\ \alpha' \end{array} \\ \begin{array}{c} \text{~~~~~} \\ \text{~~~~~} \\ \alpha \end{array} \\ \begin{array}{c} q_j^2 \\ \text{~~~~~} \\ \text{~~~~~} \end{array} \end{array} \begin{array}{c} \text{-----} \\ q \end{array} \begin{array}{c} \begin{array}{c} q_l^4 \\ \text{~~~~~} \\ \beta' \end{array} \\ \begin{array}{c} \text{~~~~~} \\ \text{~~~~~} \\ \beta \end{array} \\ \begin{array}{c} q_k^3 \\ \text{~~~~~} \\ \text{~~~~~} \end{array} \end{array} = \frac{Y L^2}{d_c} \delta(\sum_i \mathbf{q}_i) \delta_{\mathbf{q}, -\mathbf{q}'} \delta_{\alpha\beta} \\
& \quad \times \mathbf{q}_i^1 \mathbf{q}_j^2 \mathbf{q}_k^3 \mathbf{q}_l^4 P_{ij}^T(q) P_{kl}^T(q)
\end{aligned}$$

Figure D.1: Straight (wavy) lines represent propagators for the undulation (disorder) fields. The effective disorder vertex corresponding to Eq. 6.14, is on the third line. The vertex carries factors of wavenumber that can be accounted for by the following rule: each line (both wavy and solid) carries one factor wavenumber for each intersection that it terminates at. Only diagrams that remain connected when disorder lines are cut contribute to disorder averages.

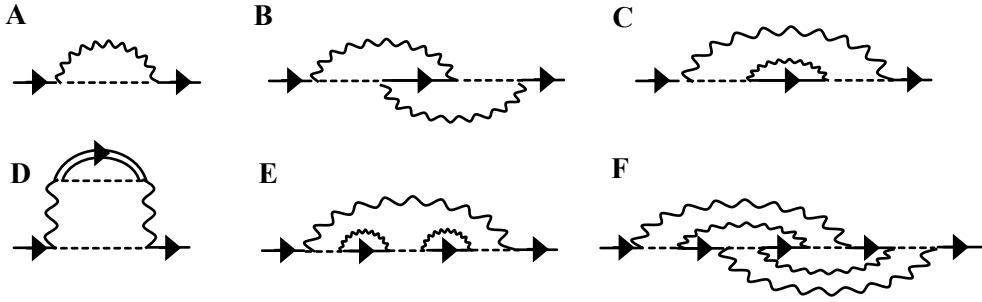


Figure D.2: A: The first order correction to the self-energy and Green's function. The absence of an internal propagator makes this contribution purely real. B: Second order correction of higher order $\mathcal{O}(1/d_c^2)$. C: Second order term in SCSA and first order term for the imaginary component of self energy. D: An example of forbidden diagrams, in which a horizontal cut across disorder lines leaves the graph disconnected. Double solid lines indicate fully dressed Green's function. E: Third order term in SCSA, but left out by the NCA. F: An example of a crossed diagram, whose phase space is restricted, leading to a result of higher order in $1/(p_F\ell)$. These diagrams are small in both the SCSA and NCA approximations.

face, with the understanding that cross products are evaluated according to Eq. D.1

The rule for contracting lines is slightly different than for typical field theories due to the nature of the disorder average. In any diagram, one must first contract all solid lines in order to build the propagators \hat{G}^+ , \hat{G}^- , then afterwards contract the remaining wavy lines to perform the disorder average. This is accounted for by implementing the additional rule that only diagrams that remain fully connected when all disorder lines are cut may contribute to any given calculation. An example of a particular class of forbidden diagrams is shown in Fig. D.2D.

As usual, the self energy is given by the set of one-particle irreducible diagrams,

i.e. diagrams that remain connected after an solid line is removed. Per the disorder rules, dashed lines and solid lines count toward connectivity, but wavy lines do not.

D.1.1 perturbation series

The lowest order term for the self-energy, shown in Fig. D.2A, is equal to the equation

$$\Sigma_p^{(1)} = \frac{-\gamma Y L^2}{d_c} \int \frac{d^2 q}{(2\pi)^2} \frac{|p \times q|^4}{q^4 (q-p)^{2d_H}}. \quad (\text{D.2})$$

Since there is no imaginary part or ω dependence, there is no distinction between advanced/retarded and we thus omit the \pm index. Counting powers of q we see that the integrand $\sim q^{2-2d_H}$, which indicates a divergence at high (low) wavenumber for d_H less (greater) than one. We regulate the high wavenumber divergence by imposing an upper cutoff Λ beyond which the continuum model breaks down. If the membrane possess an underlying lattice structure, Λ is on the order of the inverse lattice spacing (or grid spacing in numerical calculations). Integrating the angular components we find

$$\Sigma_p^{(1)} = \frac{-\gamma Y L^2 p^{6-2d_H}}{4\pi^2 d_c} \int_0^{\Lambda/p} q I_{d_H}(q) dq, \quad (\text{D.3})$$

where we have defined the commonly occurring function

$$I_{d_H}(p) = \int_0^{2\pi} \frac{\sin^4 \theta d\theta}{(p^2 + 1 - 2p \cos \theta)^{d_H}}. \quad (\text{D.4})$$

I_{d_H} is easily solved by substitution $z = e^{i\theta}$, followed by a contour integration around the unit circle. The results for $d_H = 0, 1, 2$ are summarized in Tab. D.1.

Substituting and performing the radial integration we find

$$\Sigma_p^{(1)} = \frac{-3\gamma Y L^2 p^4}{16\pi d_c} \times \begin{cases} \Lambda^2/2 & d_H = 0 \\ \frac{p^2}{6\Lambda^2} + \ln\left(\frac{\Lambda}{p}\right) + \frac{1}{4} & d_H = 1 \\ \frac{1}{p^2} - \frac{1}{2\Lambda^2} & d_H = 2 \end{cases}. \quad (\text{D.5})$$

Table D.1: Values of $I_{d_H}(q)$ for $d_H = 0, 1, 2$.

	$d_H = 0$	$d_H = 1$	$d_H = 2$
$I_{d_H}(q)$	$\frac{3\pi}{4}$	$\frac{3\pi}{4 \max(q,1)^2} \left(1 - \frac{\min(q,1)^2}{3 \max(q,1)^2}\right)$	$\frac{3\pi}{4 \max(q,1)^2}$

The Λ divergence is due to the lack of a well-defined curvature tensor for surfaces $d_H < 2$, which can be inferred from the large p limit of $\langle |\nabla^2 h| \rangle \sim p^{2-d_H}$. This suggests that the weak scattering approximation is only realizable (and physically meaningful) for $d_H \geq 1$.

We infer that the perturbation series is regulated by the d_H -dependent parameter [77]

$$\frac{Y h_{\text{eff}}^2}{\kappa} < 1, \quad (\text{D.6})$$

where h_{eff} denotes an effective averaged height field

$$h_{\text{eff}}^2(q) \sim \begin{cases} q^{2-2d_H} & d_H \geq 2 \\ \ln \Lambda/q & d_H = 1 \\ \Lambda^{2-2d_H} & d_H < 1 \end{cases} . \quad (\text{D.7})$$

The strong dependence on d_H has dramatic consequences for the effective elastic constants of warped membranes, leading to a system size dependent rigidity $\kappa \sim L$ for $d_H = 2$, compared to only a weak logarithmic $\kappa \sim \ln L$ and system size independent scaling for $d_H = 1$ and $d_H = 0$ respectively [77].

Keeping only the lowest order contribution to the self energy is plagued by two issues. The first is the dependence on the of short distance cutoff Λ , which causes the perturbation series to diverge. The second, and more important, is the lack of an imaginary component, which is necessary to describe scattering. The lowest order contribution to $\text{Im}\Sigma$ occurs at two loop order (see Figs. D.2B and D.2C).

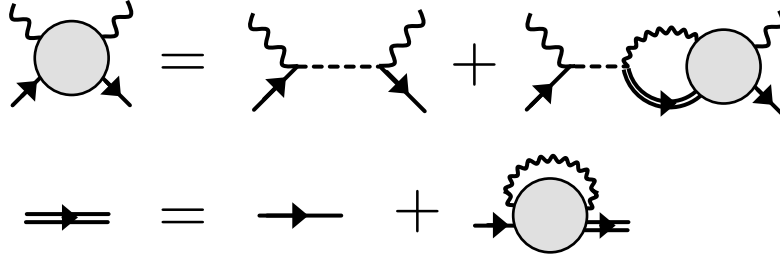


Figure D.3: The full disorder averaged propagator is represented by a double solid line, and the full vertex by a shaded bubble with two wavy lines and two solid lines attached. Top: The SCSA for the fully dressed Green's function. Bottom: The SCSA for the renormalized vertex function

Both of these problems are treated by performing a partial resummation of the perturbation series known as the self-consistent screening approximation (SCSA) [88, 77, 78]. We now turn to a calculation of the SCSA self energy

D.1.2 self-consistent screening approximation

The SCSA has proven successful in describing the thermal fluctuations of warped membranes [88, 77, 78]. It is exact in the limit $d_c \rightarrow \infty$, and corresponds to the resummation of all diagrams at $\mathcal{O}(d_c^{-1})$. In the example diagrams shown in Fig. D.2, C and E are $\mathcal{O}(d_c^{-1})$ and contribute to the SCSA, while B and F are $\mathcal{O}(d_c^{-2})$ and $\mathcal{O}(d_c^{-4})$ respectively, and do not. The latter two admit crossed disorder lines. The SCSA can be viewed as a generalization of the non-crossing approximation used in electron transport calculations [130].

The resummation of all $\mathcal{O}(d_c^{-1})$ diagrams is done diagrammatically in Fig. D.3. This is equivalent to the set of self-consistent equations

$$G_p^\pm = L^{-2}(\kappa p^4 - \sigma\omega^2 \mp i\epsilon)^{-1} - \frac{2d_c^{-1}L^{-2}}{\kappa p^4 - \sigma\omega^2 \mp i\epsilon} \sum_q \frac{p_i p_j R_{ij,kl}^{\text{SCSA}}(q) p_k p_l}{(q-p)^{2d_H} (\kappa p^4 - \sigma\omega^2 - L^{-2}\Sigma_p^\pm)}, \quad (\text{D.8a})$$

$$R_{ij,kl}^{\text{SCSA}}(q) = R_{ij,kl}(q) - \sum_p \frac{2L^2 R_{ij,mn}(q) p_m p_n p_r p_s R_{rs,kl}^{\text{SCSA}}(q)}{(p-q)^{2d_H} (\kappa p^4 - \sigma\omega^2 - \Sigma_p^\pm)}, \quad (\text{D.8b})$$

describing the dressed propagator and vertex.

We simplify these equations as follows. We first rewrite Eq. D.8a in terms of the self energy by multiplying both sides by $L^2(\kappa p^4 - \sigma\omega^2 \mp i\epsilon)(G_p^\pm)^{-1}$ and using the definition in Eq. ???. Rearranging leads to

$$\Sigma_p^\pm = \frac{-2}{d_c L^2} \sum_p \frac{p_i p_j R_{ij,kl}^{\text{SCSA}}(q) p_k p_l}{(p-q)^{2d_H}}. \quad (\text{D.9})$$

The tensor indices appearing in $R_{ij,kl}^{\text{SCSA}}$ are removed by assuming a solution of the form

$$R_{ij,kl}^{\text{SCSA}}(q) = Y_R(q) P_{ij}^T(q) P_{kl}^T(q), \quad (\text{D.10})$$

which amounts to a renormalization of the Young's modulus Y . Insertion into Eq. D.8b immediately yields the solution

$$Y_R(q) = \frac{Y}{1 + \Pi_q}, \quad (\text{D.11})$$

where we have defined the function

$$\Pi_q = \frac{\gamma Y}{L^2} \sum_{q'} \frac{[q'_i P_{ij}^T(q) q'_j]^2}{(q-q')^{2d_H} (\kappa q'^4 - \sigma\omega^2 - \Sigma_{q'} L^{-2})}. \quad (\text{D.12})$$

Inputting Eq. D.10 into Eq. D.9 we complete our setup of the SCSA. This has been reduced to solving the set of self consistent equations

$$\Sigma_p = \frac{-\gamma Y}{d_c} \sum_q \frac{|p \times q|^4}{q^4 (q-p)^{2d_H} (1 + \Pi_q)}, \quad (\text{D.13a})$$

$$\Pi_q = \frac{\gamma Y}{L^2} \sum_{q'} \frac{|q \times q'|^4}{q^4 (q - q')^{2d_H} (\kappa q'^4 - \sigma \omega^2 - L^{-2} \Sigma_{q'})}, \quad (\text{D.13b})$$

where we have made use of Eq. D.1. These equations must be solved for each of the cases $d_H = 0, 1, 2$.

For the remainder of the section, ω, p refer to their dimensionless versions defined in Sec. 6.6, Eq. 6.78. We further work with the dimensionless self-energy $\bar{\Sigma}_p$ defined in Eq. 6.79 and the dimensionless disorder amplitude α defined in Eq. 6.80. The upper cutoff has units of inverse length and is also nondimensionlized. The dimensionless SCSA equations are now

$$\Pi_p = 16\pi\alpha \int \frac{d^2q}{(2\pi)^2} \frac{|p \times q|^4}{p^4 (p - q)^{2d_H} (q^4 - \omega^2 - \bar{\Sigma}_q)} \quad (\text{D.14a})$$

$$\bar{\Sigma}_p = \frac{-16\pi\alpha}{d_c} \int \frac{d^2q}{(2\pi)^2} \frac{|p \times q|^4}{q^4 (p - q)^{2d_H} (1 + \Pi_q)}. \quad (\text{D.14b})$$

We can further perform the angular integrations, to arrive at

$$\Pi_p = \frac{4\alpha}{\pi} \int_0^{\Lambda/p} \frac{q^{5-2d_H} I_{d_H}(q) dq}{q^4 - \omega^2 - \bar{\Sigma}_q} \quad (\text{D.15a})$$

$$\bar{\Sigma}_p = \frac{-4\alpha p^{4-2d_H}}{\pi d_c} \int_0^{\Lambda/p} \frac{q I_{d_H}(q) dq}{1 + \Pi_q}. \quad (\text{D.15b})$$

This form is suited for numerical evaluation, and is used to provide a check on our analytical solutions. The imaginary part of the self energy

$$\text{Im} \bar{\Sigma}_p = \frac{-4\alpha p^{4-2d_H}}{\pi d_c} \int_0^{\Lambda/p} \frac{q I_{d_H}(q) \text{Im} \Pi_q}{|1 + \Pi_q|^2} dq, \quad (\text{D.16})$$

is Π -dependent. In the weak scattering limit, we expect $Y_R(p_F)$ is not significantly renormalized, which implies that $\Pi(p_F)$ is small. We thus approximate $\text{Im}(1 + \Pi)^{-1} \approx \text{Im} \Pi$. This approximation ignores vertex renormalization and is equivalent to the

self-consistent diagrammatic equation

$$\text{Im}\bar{\Sigma}_p \approx \text{Im} \left[\text{Diagram} \right]. \quad (\text{D.17})$$


In the weak scattering approximation, $\text{Im}\Pi(q)$ can be simplified using Eq. 6.43 to eliminate the radial q' integration. We focus on the particular solution when $p = p_F$ which is relevant for the scattering time and mean free path. We obtain

$$\text{Im}\bar{\Sigma}_{p_F} = \frac{-4\alpha^2 p_F^{8-4d_H}}{\pi d_c (1 - \delta_1)} \int_0^{\Lambda/p_F} q I_{d_H}^2(q) dq. \quad (\text{D.18})$$

Explicitly for $d_H = 0, 1, 2$:

$$\text{Im}\bar{\Sigma}_{p_F} = \frac{\pi\alpha^2}{d_c(1 - \delta_1)} \times \begin{cases} 9\Lambda^2 p_F^6 / 8 & d_H = 0 \\ 19p_F^4 / 12 & d_H = 1 \\ 3/2 & d_H = 2 \end{cases} \quad (\text{D.19})$$

The fermi wavenumber p_F and δ_1 both depend on the real part of the self-energy, and hence must be checked to be consistent with the SCSA.

In the following sections we solve the SCSA equations to determine the self energy. The main results are collected in Tab. D.2.

Table D.2: We tabulate the main results of the SCSA. The imaginary part of the self energy is given in the weak scattering limit.

d_H	p_F	$\text{Re}\bar{\Sigma}_p$	$\text{Im}\bar{\Sigma}_{p_F}$
0	$\omega^{1/2}(3\alpha\Lambda^2/2)^{-1/6}$	$-(3\alpha\omega/2)^{1/2}\Lambda p^3$	$\frac{9\pi\alpha^2\Lambda^2 p_F^6/8}{1+\frac{1}{2}(3/2)^{3/2}\Lambda\alpha^{1/2}\omega^{1/2}/p_F^2}$
1	$\frac{2^{1/4}\sqrt{\omega}}{(1+\sqrt{1+12\alpha(\ln(\Lambda/\sqrt{\omega})+1/4)})^{1/4}}$	$\frac{q^4}{2}\left(1-\sqrt{1+12\alpha(\ln(\Lambda/q)+1/4)}\right)$	$\frac{19\pi\alpha^2 p_F^4/6}{1+\frac{3\alpha/2+12\alpha\ln(\Lambda/p_F)+1}{\sqrt{3\alpha+12\alpha\ln(\Lambda/p_F)+1}}}$
2	$\sqrt{\omega}^1, \frac{\sqrt{\omega}}{\sqrt[4]{\frac{3}{2}\ln(\frac{\alpha}{\omega})+\frac{7}{4}}}^2$	$\frac{-3\alpha p^2}{2}\left(1-\frac{\alpha}{p^2}\ln\left(1+\frac{p^2}{\alpha}\right)+\frac{p^2}{\alpha}\ln\left(1+\frac{\alpha}{p^2}\right)\right)$	$\frac{3\pi\alpha^2/2}{1+\frac{3}{2}\ln(1+\alpha/p_F^2)}$

D.1.2.1 iterative solution

In principle, the SCSA Eqs. D.15b, D.15a can be solved via iteration. This is done by first guessing zeroth order solutions (we say order, though there is no formal order parameter governing the iteration) $\bar{\Sigma}_p^{(0)}, \Pi^{(0)}$, then performing the integrations on the right hand side to obtain new solutions $\bar{\Sigma}_p^{(1)}, \Pi_p^{(1)}$. These, in turn, are put into the right hand side and integrated over yielding another set of solutions $\bar{\Sigma}_p^{(2)}, \Pi_p^{(2)}$. The process is repeated ad infinitum until a stationary solution is reached, *i.e.* the n^{th} order solution is equal to the $(n-1)^{\text{th}}$ to within some desired tolerance. We make use of this method to develop an approximate solution after only a couple of iterations.

Our first task is to determine a reasonable zeroth order solution. The simplest function we can construct is a power law $\bar{\Sigma}_q^{(0)}, \Pi_q^{(0)} \sim q^{\eta_s, \eta_p}$. The solution is ω -independent, and the exponents η_s, η_p can be determined by power counting. If $0 \leq \eta_s \leq 4$, then Eq. D.14a implies $\Pi_q^{(0)} \sim q^{2-2d_H}$, *i.e.* $\eta_p = 2 - 2d_H$.

For $d_H \geq 1$, $\Pi_q^{(0)}$ is a decreasing function which does not contribute to power counting on the right side of Eq. D.14b at large q . Since the integral is peaked around the value $\mathbf{q} \approx \mathbf{p}$, the small q divergence of $\Pi_q^{(0)}$ will not significantly alter the integration so long as p is not much less than one. The scaling of $\bar{\Sigma}$ is then $\bar{\Sigma}_q^{(0)} \sim q^{6-2d_H}$, which is indeed self-consistent.

For $d_H < 1$, the integration on the right side of Eq. D.14a diverges unless $\eta_s > 4$. However, since the integration on the right side of Eq. D.14b cannot push η_s greater than four, it must be the case that $\Pi_q^{(0)}$ depends on the upper cutoff as $\Pi_q^{(0)} \sim \Lambda^{2-2d_H}$. Likewise, the integration on the right side of Eq. D.14b also depends on the upper cutoff $\sim \Lambda^{2-2d_H}$. We then find the set of self-consistent solutions $\bar{\Sigma}_q^{(0)} \sim q^4 \Lambda^{2-2d_H}$ and $\Pi_q^{(0)} \sim \Lambda^{2-2d_H}$.

Table D.3: The zeroth order trial solutions in the iterative method of solving the SCSA equations (Eq. D.14). Imaginary parts appear at first order in the iterative solution.

d_H	$\bar{\Sigma}_q^{(0)}$	$\Pi_q^{(0)}$
0	$\sim q^4 \Lambda^2$	$\sim \Lambda^2$
1	$\sim q^4$	$\sim \ln \Lambda/q$
2	$\sim q^2$	$\sim q^{-2}$

The zeroth order solutions for each case of d_H are summarized in Tab. D.3. Next we insert these into Eq. D.14 and perform the integrations to obtain the first order solutions $\bar{\Sigma}_q^{(1)}, \Pi_q^{(1)}$, at which point we terminate the iteration. This step is performed individually for each of the three cases $d_H = 0, 1, 2$. Finally, the first order solutions are inserted into Eq. D.15 numerically evaluated to assess how closely they satisfy the SCSA.

D.1.2.2 $d_h = 2$

Per Tab. D.3, we use $\Pi_q^{(0)} \sim q^{-2}$ and $\bar{\Sigma}_q^{(0)} \sim q^2$. Since $\Sigma_q^{(0)}$ does not scale with a power higher than q^4 , we expect the evaluation of the integrand in Eq. D.14a to depend only weakly on $\bar{\Sigma}_q^{(0)}$, and thus solve for $\Pi_q^{(1)}$ by setting $\bar{\Sigma}_q^{(0)} = 0$. The second term in the denominator of Eq. D.14a is a completed square, which we factorize into

$$\Pi_q^{(1)} = \frac{16\pi\alpha}{p^4} \int \frac{d^2q}{4\pi^2} \frac{p_a p_b p_c p_d \epsilon_{ai} \epsilon_{bj} \epsilon_{cm} \epsilon_{dn} q_i q_j q_m q_n}{(q-p)^4 (q^2 - \omega \mp i\epsilon)(q^2 + \omega \pm i\epsilon)}. \quad (\text{D.20})$$

Here, ϵ_{ij} represents the two-dimensional antisymmetric Levi-Civita symbol, and $i\epsilon$ an infinitesimal imaginary parameter taken to zero at the end of the calculation that keeps track of the retarded/advanced distinction. The remaining integral can now

be performed via the method of Feynman parameters [137]. We obtain

$$\Pi_q^{(1)} = \frac{3\alpha\omega}{4q^4} \left(i\pi + \frac{2q^2}{\omega} + \left(\frac{q^4}{\omega^2} - 1 \right) \ln \left(\frac{q^2 + \omega}{q^2 - \omega} \right) \right) \quad (\text{D.21})$$

The zeroth order divergence at small q is now cured at first order, with $\text{Re}\Pi_{q \rightarrow 0}^{(1)} \sim q^2/\omega^2$. For large q , the leading term is $\text{Re}\Pi_{q \rightarrow \infty}^{(1)} = 3/q^2$. This has the same behavior as the zeroth order ansatz, and we shall use this to fix the proportionality constant, *i.e.* $\Pi_q^{(0)} = 3/q^2$.

The integral in Eq. D.14b is performed using the same techniques as before, with the result

$$\text{Re}\bar{\Sigma}_q^{(1)} = \frac{-3\alpha q^2}{2d_c} \left[1 - \frac{\alpha}{q^2} \ln \left(1 + \frac{q^2}{\alpha} \right) + \frac{q^2}{\alpha} \ln \left(1 + \frac{\alpha}{q^2} \right) \right] \quad (\text{D.22})$$

From this, we may solve for renormalized group velocity and Fermi wavenumber (see Eqs. 6.38 and 6.42 respectively). Trivially, $\delta_2 = 0$ and

$$\delta_1 = \frac{-3}{2d_c} \ln \left(1 + \frac{\alpha}{q^2} \right). \quad (\text{D.23})$$

The Fermi wavenumber, p_F , is given by the solution to the nonlinear equation $p_F^4 - \omega^2 = \text{Re}\bar{\Sigma}_{p_F}$. We can find a solution in two limits. For $\alpha \ll \omega$, $\text{Re}\bar{\Sigma} = -3\alpha p^2$ yielding a quadratic equation for p_F^2 . In this limit, we use

$$p_F(\alpha \ll \omega) = \sqrt{\frac{1}{2} \left(\sqrt{9\alpha^2 + 4\omega^2} - 3\alpha \right)}. \quad (\text{D.24})$$

In the opposite limit, we find that $\text{Re}\Sigma_p \rightarrow \frac{-3}{4} (q^4 + 2q^4 \ln(\alpha/q^2))$. This yields an approximate solution

$$p_F(\alpha \gg \omega) = \frac{\sqrt{\omega}}{\sqrt[4]{\frac{7}{4} + \frac{3}{2} \ln \left(\frac{\alpha}{\omega} \right)}}. \quad (\text{D.25})$$

D.1.2.3 $d_H = 1$

Per Tab. D.3, we use zero order solutions

$$\Pi_q^{(0)} = (c_\pi - 1), \quad \bar{\Sigma}_q^{(0)} = (1 - c_s^4)q^4, \quad (\text{D.26})$$

for some constants c_π, c_s to be determined. Both integrals of the SCSA are logarithmically divergent and depend on the upper cutoff Λ . Assuming $\Lambda \gg 1$, we discard terms $O(\Lambda^{-1})$. $\bar{\Sigma}_q^{(1)}$ is evaluated easily from Eq. D.15b, giving

$$\bar{\Sigma}_q^{(1)} = \frac{-3\alpha q^4}{c_\pi d_c} (\ln(\Lambda/q) + 1/4). \quad (\text{D.27})$$

$\Pi_q^{(1)}$ is calculated from Eq. D.14a using the method of Feynman parameters as was done for the $d_h = 2$ case. We find

$$\Pi_q^{(1)} = \frac{3\alpha}{c_s^4} \int_0^1 (1 - x_1) \left(\ln \left(\frac{c_s^2 \Lambda^2}{\Delta^2 \omega} \right) - \frac{3}{2} \right) dx_1 dx_2, \quad (\text{D.28})$$

where we have defined

$$\Delta^2 = (1 - x_1) \left(\frac{c_s^2 q^2}{\omega} x_1 + (2x_2 - 1) \right). \quad (\text{D.29})$$

The remaining integrations over Feynman parameters x_1 and x_2 , may be carried out to give

$$\begin{aligned} \Pi_1^{d_H=1}(y) = \frac{\alpha}{4c_s^4 y^4} & \left[-\ln(y^4 - 1) - 6y^2 \tanh^{-1}(y^2) + y^4 \left(3 \ln \left(\frac{c_s^4 \Lambda^4 / \omega^2}{y^4 - 1} \right) + 5 \right) \right. \\ & \left. - 2y^6 \coth^{-1}(y^2) + i\pi(1 - 6y^2) \right] \end{aligned} \quad (\text{D.30})$$

with $y = c_s q / \omega^{1/2}$. We only use this expression insofar as to perform numerical checks on our calculation, since we are principally interested in the calculation of $\bar{\Sigma}_p$. We can construct an approximation of this function as follows.

First, we note that the integrand of Eq. D.28 is most strongly peaked at $q = 0$ and at $q = \Lambda$. In the former limit, the integrand is determined primarily by the larger of q^2, ω . This suggests that we may approximate $\Pi_1(q)$ as a piecewise function transitioning from the low q to high q behavior near $q \sim \omega^{1/2}$. Specifically, Taylor expanding Eq. D.28 at low/high q then solving for the value q^* at which the difference between the two solutions is minimized, we find a transition point $q^* = 6^{1/4} \omega^{1/2}$. This yields the approximate solution

$$\text{Re}\Pi_q^{(1)} \approx \frac{3\alpha}{c_s^4} \begin{cases} \ln(c_s \Lambda / \omega^{1/2}) - \frac{c_s^4 q^4}{24\omega^2} & q < 6^{1/4} \omega^{1/2} / c_s \\ \ln(\Lambda/q) + 1/4 & q \geq 6^{1/4} \omega^{1/2} / c_s \end{cases} \quad (\text{D.31})$$

The constants c_π, c_s are determined by matching the first order solution to the zeroth order solution, which is most easily accomplished in limit $q \rightarrow \Lambda$. Critically, our power law analysis of the zeroth order solution omitted non-analytic functions. Eq. D.31 suggests c_π, c_s are not strictly constant, but can admit logarithmic dependence on q . Matching the $q \rightarrow \Lambda$ limit of Eqs. D.31 and D.27 to Eq. D.26 yields the set of equations

$$c_\pi - 1 = \frac{3\alpha}{d_c c_s^4} (\ln(\Lambda/q) + 1/4), \quad (\text{D.32a})$$

$$1 - c_s^4 = \frac{-3\alpha}{d_c c_p} (\ln(\Lambda/q) + 1/4). \quad (\text{D.32b})$$

These have the solution

$$c_s^4 = \frac{1}{2} \left(1 \pm \sqrt{1 + 12\alpha d_c^{-1} (\ln(\Lambda/q) + 1/4)} \right). \quad (\text{D.33})$$

The condition $c_s^4 = 1$ at $\alpha = 0$ requires that we choose the (+) solution. Finally, we can quickly find $\bar{\Sigma}_q^{(1)}$ by using the matching condition $\bar{\Sigma}_q^{(1)} = (1 - c_s^4)q^4$ to find

$$\text{Re}\bar{\Sigma}_q^{(1)} = \frac{q^4}{2} \left(1 - \sqrt{1 + \frac{12\alpha}{d_c} (\ln(\Lambda/q) + 1/4)} \right). \quad (\text{D.34})$$

We solve for the Fermi wavenumber by evaluating $\text{Re}\bar{\Sigma}_p$ at $p = \omega^{1/2}$. This approximation is increasingly accurate as either $\alpha \rightarrow 0$ and/or $\Lambda \rightarrow \infty$. We obtain

$$p_F = 2^{1/4}\omega^{1/2} \left(1 + \sqrt{1 + \frac{12\alpha}{d_c} (\ln(\Lambda/\omega^{1/2}) + 1/4)} \right)^{-1/4}. \quad (\text{D.35})$$

The group velocity constant $\delta_2 = 0$, and

$$\delta_1 = \frac{1}{2} - \frac{3\alpha/2 + 12\alpha \ln\left(\frac{\Lambda}{\omega^{1/2}}\right) + 1}{2\sqrt{3\alpha + 12\alpha \ln\left(\frac{\Lambda}{\omega^{1/2}}\right) + 1}}. \quad (\text{D.36})$$

In the numerical calculations of Fig. D.4, the obtained value for c_s is input back into Eq. D.30 to determine $\Pi_q^{(1)}$.

D.1.2.4 $d_H = 0$

We start with Eqs. D.15a and D.15b. The zero order solutions are

$$\Pi_q^{(0)} = c_\pi, \quad \bar{\Sigma}_q^{(0)} = c_s q^4, \quad (\text{D.37})$$

as for $d_H = 1$. The integrations are quadratically divergent, and dominated by the upper wavenumber cutoff. To lowest order in Λ^{-1} we find the SCSA equations

$$c_\pi = \frac{3\alpha\Lambda^2}{2} \frac{1}{1 - c_s}, \quad (\text{D.38a})$$

$$c_s = \frac{-3\alpha\Lambda^2}{2} \frac{1}{d_c(1 + c_p)}. \quad (\text{D.38b})$$

These have the solution

$$c_s^\pm = \frac{1}{2d_c} \left(1 - \frac{3\Lambda^2\alpha\omega}{2q^2}(1-d_c) \pm \sqrt{\left(1 - \frac{3\Lambda^2\alpha\omega}{2q^2}(1-d_c) \right)^2 + \frac{6\Lambda^2\alpha\omega}{q^2}d_c} \right). \quad (\text{D.39})$$

In order to choose the correct branch, we consider the limit $\alpha \rightarrow 0$. This corresponds to zero disorder, *i.e.* $\gamma \rightarrow 0$. In this limit, the self energy should vanish and so $c_s \rightarrow 0$. This uniquely singles out the (-) solution c_s^- .

Now we consider the limit $\Lambda \gg 1$. For physical membranes we also set $d_c = 1$, which we do first, noting that the limits $d_c \rightarrow 1$ and $\Lambda \rightarrow \infty$ do not commute. To leading order in Λ we find

$$c_s = \begin{cases} \frac{-\Lambda}{q} \sqrt{\frac{3\alpha\omega}{2}} & : d_c = 1 \\ \frac{1}{2d_c} & : d_c \neq 1 \end{cases} \quad (\text{D.40})$$

c_s is a renormalization of the bending rigidity $\kappa \rightarrow \kappa(1 + c_s)$. Since by definition $\Lambda > q$ for all q , c_s dominates the effective bending rigidity for all but very small disorder and very low frequency. Assuming that $q \ll \Lambda$ (which is consistent with linearized shallow shell theory), the renormalized dimensionless propagator is

$$(G_q^\pm)^{-1} \sim \frac{1}{\sqrt{3\alpha\omega/2\Lambda q^3 - \omega^2 - i\text{Im}\Sigma_q^\pm}}. \quad (\text{D.41})$$

We easily determine the Fermi wavenumber

$$p_F = \omega^{1/2} \left(\frac{2}{3\alpha\Lambda^2} \right)^{1/6}. \quad (\text{D.42})$$

The assumption $p_F \ll \Lambda$ is self consistent, as p_F is dampened by a factor of $\Lambda^{1/3}$.

The group velocity can be found directly,

$$\mathbf{v}_G = (12\alpha)^{1/3} \Lambda^{2/3} \mathbf{q}. \quad (\text{D.43})$$

The function

$$\delta_1 = \frac{-3}{4} \left(\frac{3\alpha\omega}{2} \right)^{1/2} \frac{\Lambda}{q}, \quad (\text{D.44})$$

in combination with Eq. D.19, gives the intermediate expression for the imaginary part of the self-energy

$$\text{Im}\bar{\Sigma}_{p_F} = \frac{9\pi\alpha^2\Lambda^2 p_F^6/8}{1 + \frac{3}{4} \frac{\Lambda}{p_F} \sqrt{\frac{3\alpha\omega}{2}}} \quad (\text{D.45})$$

Inputting Eq. D.42 for p_F then taking the large Λ limit we obtain

$$\text{Im}\bar{\Sigma}_{p_F} = (2/3)^{2/3} \pi\omega^3 \alpha^{1/3} \Lambda^{-4/3}. \quad (\text{D.46})$$

D.1.2.5 numerical checks

In Fig. D.4 we numerically test the accuracy of the first order SCSA solutions. This is done by inputting $\bar{\Sigma}_q^{(1)}, \Pi_q^{(1)}$ into Eq. D.15 for the real part of the self-energy, and using Eq. D.19 for the imaginary part. The numerical integration is performed at fixed p and compared to the analytic solution. With the exception of $d_H = 0$, the self-energy is a p -dependent function, so the comparison is done over a range of wavenumbers. For $d_H = 0$, we find a single value for c_s, c_π , in good agreement with the analytical result. For $d_H = 1, 2$ we find good agreement in the weak scattering approximation for $\alpha = 10^{-3}$, with increasing precision for wavenumbers $q > \sqrt{\omega}$ on the order of a percent difference.

D.2 δ_c calculation

We begin with the definition of the coherent diffusion coefficient D_c in Eq. 6.63. The parameter δ_c is

$$\delta_c = i\tau M_0. \quad (\text{D.47})$$

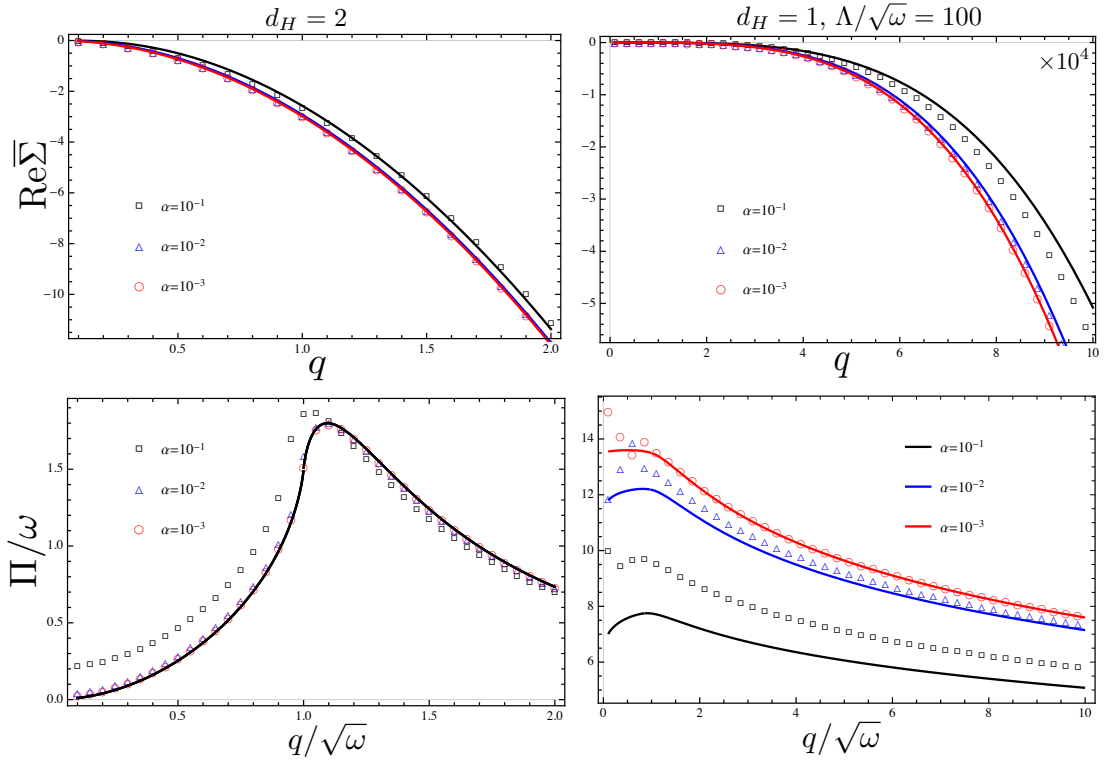


Figure D.4: Data points represent the numerical integration result for $\text{Re}\bar{\Sigma}_q$ and Π_q , using the numerical integrations defined in Eqs. D.15a D.15b. Curves represent the analytic result. We consider the cases $d_H = 1, 2$, where the solutions for $\bar{\Sigma}_q, \Pi_q$ are nontrivial functions. Beyond weak scattering we find our analytic approximations to be inaccurate, however, the shape of the curves is still accurate, which we need for deriving the diffusion coefficient.

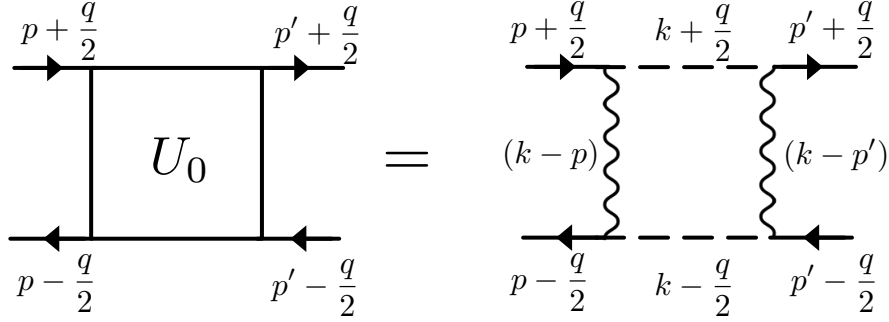


Figure D.5: The bare irreducible vertex. This is the simplest four-point vertex that can be constructed that remains fully connected after cutting all wavy lines.

The scattering time τ was found earlier in Appendix D.1 (and tabulated in Tab. 6.1), so we need only evaluate M_0 , which was defined in Eq. 6.53.

D_c is found by replacing the irreducible vertex U with the bare vertex U^0 , defined in Fig. D.5. U^0 is evaluated at $q = 0$ and affords the simpler representation

$$U_{pp'}^0 = \frac{\gamma^2 Y^2}{2d_c} \sum_k \frac{|p \times k|^4 |k \times p'|^4}{(k - p)^{2d_H} (k - p')^{2d_H} k^8}, \quad (\text{D.48})$$

where the cross product is as defined in Eq. D.1. We insert this into the definition of M_0 then evaluate the corresponding integrals. In the weak scattering approximation, the radial integrations are performed using Eq. 6.43, leaving only the angular integrations:

$$M_0 = \frac{i\pi\nu}{\sigma^2\omega^2} \int_0^{2\pi} d\hat{p}d\hat{p}' (\hat{\mathbf{q}} \cdot \hat{\mathbf{p}}) U_{\hat{p}\hat{p}'}(\hat{\mathbf{q}} \cdot \hat{\mathbf{p}}'), \quad (\text{D.49})$$

and $d\hat{p}$ is understood to mean the angular integration on \hat{p} . There are four unit vectors to consider, and a total of $4!$ angles to consider. We define angles according to Fig. D.6.

The angles β, β' can be eliminated in favor of ϕ, θ, θ' , allowing us to use $\hat{\mathbf{q}} \cdot \hat{\mathbf{p}} = \cos(\phi - \theta)$ and $\hat{\mathbf{q}} \cdot \hat{\mathbf{p}}' = \cos(\phi - \theta')$. Simplifying Eq. D.49 according to Fig. D.6, we

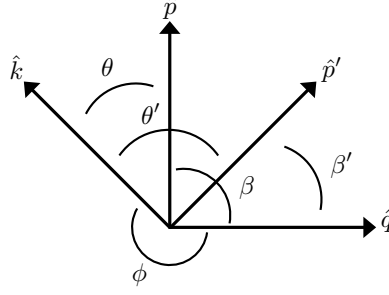


Figure D.6: Angles between unit vectors at fixed orientation in the calculation of M_0 . Only \hat{q} is not integrated over. We first fix \hat{k} , then perform the integrations over $d\hat{p} = d\theta$ and $d\hat{p}' = d\theta'$. This yields a function $J_{d_H}(k; \phi)$ that is then integrated over ϕ .

find

$$M_0 = \frac{\pi\nu L^2 p_F^{2-4d_H}}{2\sigma^2 \omega^2 i d_c} \int_0^{\Lambda/p_F} \frac{k dk}{4\pi^2} \int_0^{2\pi} d\phi J_{d_H}^2(k; \phi), \quad (\text{D.50})$$

where we have defined

$$J_{d_H}(k; \phi) = \int d\theta \frac{\cos(\theta - \phi) \sin^4 \theta}{(k^2 + 1 - 2k \cos \theta)^{2d_H}}. \quad (\text{D.51})$$

$J_{d_H}(k; \phi)$ is computed via substitution $z = e^{i\theta}$ followed by contour integration. Performing the remaining integrations yields M_0 , which is then trivially related to δ_c . The results for both $J_{d_H}(k; \phi)$ and δ_c are shown in Tab. D.4 for $d_H = 0, 1, 2$.

In terms of the dimensionless wavenumber, frequency, and disorder amplitude, we find the final results

$$D_c = D_0 \times \begin{cases} 1 & d_H = 0 \\ \left(1 + \frac{11\alpha^2 p_F^4 \tau}{24\omega}\right)^{-1} & d_H = 1 \\ \left(1 + \frac{3\alpha^2 \tau}{8\omega}\right)^{-1} & d_H = 2 \end{cases} \quad (\text{D.52})$$

Table D.4: Angular integration function $J_{d_H}(k; \phi)$ and δ_c for each of $d_H = 0, 1, 2$.

We use dimensionless frequency, wavenumber, and disorder amplitude.

d_H	δ_c	$J_{d_H}(k; \phi)$
0	0	0
1	$\frac{11\alpha^2 p_F^4 \tau}{24\omega}$	$\frac{\pi \min(k,1)(2 \max(k,1)^2 - \min(k,1)^2) \cos \phi}{8 \max(k,1)^5}$
2	$\frac{3\alpha^2 \tau}{8\omega}$	$\frac{\pi \min(k,1) \cos \phi}{2 \max(k,1)^5}$

D.3 Ward identity

In this section the vector nature of positions and wavenumbers are understood, and we omit bold-face lettering. Additionally, we deviate from the notation of the main text, and use \hat{G}^\pm to refer to the *unaveraged* Green's function. The WI is most easily derived using a functional integral representation for the Green's function [102]. We define the moment generating function

$$Z[j^+, j^-] = \int \mathcal{D}f^+ \mathcal{D}f^- e^{-\int A[f^+, f^-] - j^+ f^+ - j^- f^- d^2x}, \quad (\text{D.53})$$

where we have defined the total action as the sum of retarded/advanced actions

$$A[f^+(x), f^-(x)] = A^+[f^+(x)] + A^-[f^-(x)] \quad (\text{D.54})$$

that, in turn, are decomposed into the sum of a Gaussian action

$$A_0^\pm = \frac{\kappa}{2} (\nabla^2 f^\pm)^2 + \frac{\sigma \omega_\pm^2}{2} (f^\pm)^2, \quad (\text{D.55})$$

and a disorder interaction

$$A_{\text{int}}^\pm = \frac{Y}{d_c} (\hat{\mathcal{L}} f^\pm) \nabla^{-4} (\hat{\mathcal{L}} f^\pm). \quad (\text{D.56})$$

A_0^\pm and A_{int}^\pm are the real space representations of the DMV action in Eq. 6.13 and Eq. 6.14. The operator $\hat{\mathcal{L}}$ was defined in Eq. 6.20; for our purposes, it is most important to note that it is hermitian, *i.e.* for any two functions g and h , we have the identity

$$\int g \hat{\mathcal{L}} h d^2 x = \int h \hat{\mathcal{L}} g d^2 x. \quad (\text{D.57})$$

For a fixed realization of disorder, we may obtain the *unaveraged* Green's function in the usual way, via functional derivatives:

$$G^+(x, x') = \frac{\delta^2}{\delta j^+(x) \delta j^+(x')} \ln Z[j^+, j^-] \Big|_{j^\pm=0}. \quad (\text{D.58})$$

In this section, we will use different notation than the main text, with respect to averaging. The functional integral method first computes the Green's function as the two-point function of f^+ with regards to the ensemble dictated by the action. This is done at fixed disorder, and the resulting Green's function must subsequently be averaged over the disorder. We use angular brackets $\langle \dots \rangle$ to denote averaging over the f^+ ensemble, and an overline $\overline{\dots}$ to denote disorder averaging. In this notation, the Green's function is written as

$$\overline{G^+(x, x')} = \overline{\langle f^+(x) f^+(x') \rangle}. \quad (\text{D.59})$$

The four-point function can similarly be written

$$\phi(x, x'; y, y') = \overline{\langle f^+(x) f^+(x') \rangle \langle f^-(y) f^-(y') \rangle}. \quad (\text{D.60})$$

At zero external frequency Ω , the total action A possesses an $O(2)$ symmetry between retarded/advanced fields, and is invariant under the transformation

$$\begin{pmatrix} f^+ \\ f^- \end{pmatrix} \rightarrow \begin{pmatrix} \cos \theta & \sin \theta \\ -\sin \theta & \cos \theta \end{pmatrix} \begin{pmatrix} f^+ \\ f^- \end{pmatrix}. \quad (\text{D.61})$$

For nonzero Ω , we perform the change of variables

$$f^+ \rightarrow f^+ + \epsilon f^- \quad (\text{D.62a})$$

$$f^- \rightarrow f^- - \epsilon f^+, \quad (\text{D.62b})$$

for ϵ an infinitesimal parameter. Since ϵ is small, we Taylor expand the exponential and use invariance of the functional integral change of variables to find the equation

$$\langle -2\sigma\omega\Omega f^+ f^- + j^+ f^- - j^- f^+ \rangle = 0. \quad (\text{D.63})$$

In obtaining this equation, since the realization of disorder is identical for both f^+ and f^- fields, the variation δS_{int} vanishes. Taking two function derivatives $\frac{\delta^2}{\delta j^+ \delta j^-}$, setting $j^+ = j^- = 0$, then performing the disorder average we find

$$2\omega\Omega\phi(x, x'; y, y') = [G^+(x, x') - G^-(y, y')] \delta(x - y)\delta(x' - y') \quad (\text{D.64})$$

Using the position space definition of the Green's function

$$G^\pm(x, x') = \kappa\nabla^4 - \sigma\omega_\pm^2 - \hat{\Sigma}^\pm, \quad (\text{D.65})$$

we can formally divide by $\hat{G}^+\hat{G}^-$ and use the BS equation to find the solution

$$\Delta\hat{\Sigma}^\pm = \hat{U}\hat{\Delta}G^\pm. \quad (\text{D.66})$$

In the wavenumber basis, this takes the simpler form

$$\Delta\Sigma_p(q) = \sum_{p'} U_{pp'}(q)\Delta G_{p'}(q). \quad (\text{D.67})$$

The WI is identical to the well-known result for electrons in disordered media [154]. As a check, the WI can easily be seen to hold for the choice of irreducible vertex $U_{pp'}^0(q)$ (Fig. D.5 and Eq. D.48) and self-energy (Eq. D.17) used in this chapter.

D.4 Derivation of Diffuson and Cooperon

We begin with deriving the diffuson, which we denote as $\hat{\Gamma}$. In the position basis, the diffuson is a function of four points $\Gamma(x_1, x_2, x_3, x_4)$, and in the Fourier basis a function of three wavenumbers $\Gamma_{pp'}(q)$ due to translational invariance. The diffuson is an IR divergent four-point vertex, that diverges in the limit $q, \Omega \rightarrow 0$. This divergence ensures that even after disorder averaging, the diffuson is long-range object, and hence represents a two-particle propagator associated with the diffusive dynamics of the intensity field.

The Green's functions $G^\pm(\mathbf{x}, \mathbf{x}'; \omega)$ represent plane waves of frequency ω propagating forward/backward (+,-) in time from position $\mathbf{x}' \rightarrow \mathbf{x}$, and can be interpreted as particles (see section 6.5). The four-point function is the disorder averaged quantity describing propagation of two paired particles in space. From this representation, we can define the diffuson as the contribution to this amplitude from all paths whereby the paired particles undergo identical scattering paths. In Fourier space, these correspond to the ladder type diagrams of Fig. D.7.

Summation over ladder diagrams is formally given as a Bethe-Salpeter equation

$$\hat{\Gamma} = \hat{U} + \hat{U} : \hat{G}^+ \otimes \hat{G}^- : \hat{\Gamma}. \quad (\text{D.68})$$

The colons indicate that \hat{U} and $\hat{\Gamma}$ are contracted with the tensor product of $\hat{G}^+ \otimes \hat{G}^-$. We keep the same notation as in the text that all Green's functions represent their disorder average. $\hat{\Gamma}$ decomposes into the two-particle irreducible vertex U (which is currently unspecified), plus the set of ladder diagrams connecting additional vertices by a retarded and advanced propagator. In Fourier space, we find the less abstract

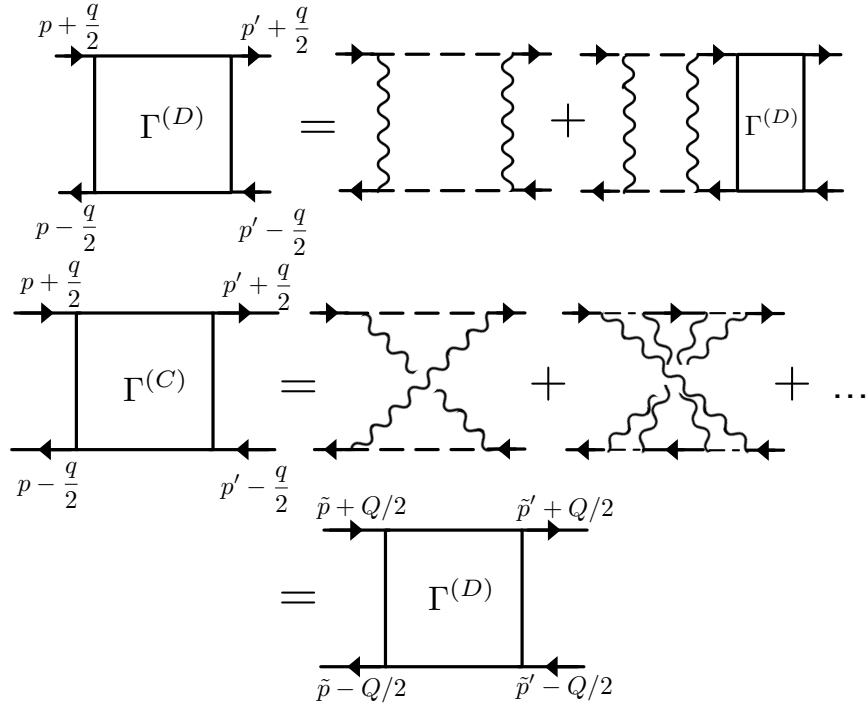


Figure D.7: Dominant contributions to the four-point vertex in the diffusive limit. Upper/lower lines carry retarded/advanced propagators, each with frequency $\omega + (-)\Omega/2$. The frequency is a passive index and is not integrated over since the disorder field is quenched. Top: diagrammatic representation of the Bethe-Salpeter equation defining the diffuson contribution to the four point vertex $\hat{\Gamma}$. Bottom: diagrammatic derivation of the cooperon. The new wavenumbers are $\tilde{p} = \frac{1}{2}(p - p' + q)$, $\tilde{p}' = \frac{1}{2}(p' - p + q)$, and $Q = p + p'$, in agreement with Fig. 6.2.

form

$$\Gamma_{pp'}(q) = U_{pp'} + \sum_k U_{pk} G_{k+q/2}^+ G_{k-q/2}^- \Gamma_{kp'}(q). \quad (\text{D.69})$$

Since we are interested in contributions to $\Gamma_{pp'}(q)$ that diverge in the limit $\Omega, q \rightarrow 0$, we have replaced the first $U_{pp'}(q)$ on the right with its $q = 0$ value $U_{pp'}$.

When all of the external legs of the reducible vertex $\hat{\Gamma}$ are put on shell, we obtain the four-point function of Eq. 6.25. Explicitly,

$$\phi_{pp'}(q) = G_{p+q/2}^+ G_{p-q/2}^- \Gamma_{pp'}(q) G_{p+q/2}^+ G_{p'-q/2}^-. \quad (\text{D.70})$$

This relation allows us to directly use our results from section 6.4 to solve for $\Gamma_{pp'}(q)$. Looking at the small q, Ω limit, we set $q = 0$ in the Green's functions and use the identity $G_p^+ G_p^- = \Delta G_p / 2i \text{Im} \Sigma_p$. Comparing to the solution for $\phi_{pp'}(q)$ in Eq. 6.55, we immediately find

$$\Gamma_{pp'}^{(\text{D})}(q) = \frac{2}{\pi \nu L^2} \frac{\text{Im} \Sigma_p \text{Im} \Sigma_{p'}}{-i\Omega + D_c(\omega) q^2}. \quad (\text{D.71})$$

The superscript (D) emphasizes this is not the full reducible vertex, but instead its long time/length limit, the *diffuson*. The appearance of D_c in the denominator is a consequence of the choice $U = U_0$ for the irreducible vertex, where U_0 is the bare irreducible vertex defined in Fig. D.5. This choice generates the sum of all non-crossing box diagrams.

The cooperon is derived by first crossing all bare vertices \hat{U}^0 , then individually crossing the wavy lines within each \hat{U}^0 as shown in the lower half of Fig. D.7. This is equivalent to a summation over all maximally crossed box diagrams. By left-right reflection of the lower lines (*i.e.* reversing all of the arrows), we can un-cross the box diagrams, thereby obtaining an identical set of ladder diagrams as used for the diffuson. The new wavenumbers are reversed and of opposite sign. We thus find the

cooperon

$$\Gamma_{pp'}^{(C)}(q) = \Gamma_{\frac{1}{2}(p-p'+q), \frac{1}{2}(p'-p+q)}^{(D)}(p+p'). \quad (\text{D.72})$$

Finally, we note that by including cooperon insertions into the ladder diagrams defining the diffuson [154], we find corrections to the diffusion coefficient D_c that recover the weak localization calculation of section 6.5.

D.5 Full analytic expressions

D.5.1 $d_H = 0$

$$D_c = D_0 = \frac{2}{\pi} \frac{(2/3)^{1/3}}{\alpha^{4/3} \omega \Lambda^{2/3}} \quad (\text{D.73})$$

$$\ell = \frac{(96)^{1/6} \Lambda^{1/3}}{\pi \alpha^{5/6} \omega^{3/2}} \quad (\text{D.74})$$

$$\delta D = \frac{1}{\pi} \left(\frac{3}{2}\right)^{4/3} \alpha^{1/3} \Lambda^{2/3} \ln\left(\frac{L}{\ell}\right) \quad (\text{D.75})$$

$$\xi = \sqrt{\exp\left(\frac{4(2/3)^{5/3}}{\alpha^{5/3} \Lambda^{4/3} \omega}\right) - 1} \quad (\text{D.76})$$

$$\nu = \frac{(2/3)^{4/3}}{2\pi \alpha^{1/3} \Lambda^{2/3}} \quad (\text{D.77})$$

D.5.2 $d_H = 1$

For convenience we define the quantity

$$H = \sqrt{3\alpha + 12\alpha \ln\left(\frac{\Lambda}{p_F}\right) + 1}. \quad (\text{D.78})$$

$$p_F = \frac{2^{1/4}\sqrt{\omega}}{\left(\sqrt{12\alpha \ln\left(\frac{\Lambda}{\sqrt{\omega}}\right) + 3\alpha + 1 + 1}\right)^{1/4}} \quad (\text{D.79})$$

$$D_c = \frac{48p_F^2 \left(3\alpha + 24\alpha \ln\left(\frac{\Lambda}{p_F}\right) + 2H + 2\right)}{\alpha^2\omega \left(33\alpha \left(8 \ln\left(\frac{\Lambda}{p_F}\right) + 1\right) + 304\pi H + 22H + 22\right)} \quad (\text{D.80})$$

$$\ell = \frac{3 \left(3\alpha + 24\alpha \ln\left(\frac{\Lambda}{p_F}\right) + 2H + 2\right)}{19\pi\alpha^2 p_F H} \quad (\text{D.81})$$

$$\delta D = \frac{152p_F^2 \left(3\alpha + 24\alpha \ln\left(\frac{\Lambda}{p_F}\right) + 2H + 2\right)}{\omega \left(33\alpha \left(8 \ln\left(\frac{\Lambda}{p_F}\right) + 1\right) + 304\pi H + 22H + 22\right)} \ln\left(\frac{L}{\ell}\right) \quad (\text{D.82})$$

$$\nu = \frac{\omega H}{\pi p_F^2 \left(3\alpha + 24\alpha \ln\left(\frac{\Lambda}{p_F}\right) + 2H + 2\right)} \quad (\text{D.83})$$

$$\xi = \sqrt{e^{\frac{12}{19\alpha^2}} - 1} \quad (\text{D.84})$$

D.5.3 $d_H = 2$

$$p_F(\alpha \ll \omega) = \sqrt{\frac{1}{2} \left(\sqrt{9\alpha^2 + 4\omega^2} - 3\alpha\right)} \quad (\text{D.85})$$

$$p_F(\alpha \gg \omega) = \frac{\sqrt{2\omega}}{(6 \ln(\frac{\alpha}{\omega}) + 7)^{1/4}} \quad (\text{D.86})$$

$$D_c(\alpha \ll \omega) = \frac{2\sqrt{9\alpha^2 + 4\omega^2} (\sqrt{9\alpha^2 + 4\omega^2} - 3\alpha)^3}{3\alpha^2\omega (\sqrt{9\alpha^2 + 4\omega^2} + 4\pi (\sqrt{9\alpha^2 + 4\omega^2} - 3\alpha))}, \quad (\text{D.87})$$

$$\begin{aligned} D_c(\alpha \gg \omega) &= \frac{32\omega^2 \left(3 \ln \left(\frac{\alpha \sqrt{6 \ln(\frac{\alpha}{\omega}) + 7}}{2\omega} \right) + 2 \right) \left(6 \ln \left(\frac{\alpha \sqrt{6 \ln(\frac{\alpha}{\omega}) + 7}}{2\omega} \right) + 5 \right)^2}{3\alpha^2 (6 \ln(\frac{\alpha}{\omega}) + 7)^{3/2} \left(3 \ln \left(\frac{\alpha \sqrt{6 \ln(\frac{\alpha}{\omega}) + 7}}{2\omega} \right) + 8\pi + 2 \right)} \\ &\sim \frac{\omega^2}{\alpha^2}, \end{aligned} \quad (\text{D.88})$$

$$\ell(\alpha \ll \omega) = \frac{\sqrt{18\alpha^2 + 8\omega^2} \sqrt{\sqrt{9\alpha^2 + 4\omega^2} - 3\alpha}}{3\pi\alpha^2} \sim \frac{\omega^{3/2}}{\alpha^2} \quad (\text{D.89})$$

$$\begin{aligned} \ell(\alpha \gg \omega) &= \frac{2\sqrt{2}\omega^{3/2} \left(3 \ln \left(\frac{\alpha \sqrt{6 \ln(\frac{\alpha}{\omega}) + 7}}{2\omega} \right) + 2 \right) \left(6 \ln \left(\frac{\alpha \sqrt{6 \ln(\frac{\alpha}{\omega}) + 7}}{2\omega} \right) + 5 \right)}{3\pi\alpha^2 (6 \ln(\frac{\alpha}{\omega}) + 7)^{3/4}} \\ &\sim \frac{\omega^{3/2}}{\alpha^2} \end{aligned} \quad (\text{D.90})$$

$$\delta D(\alpha \ll \omega) = \frac{16\omega\sqrt{9\alpha^2 + 4\omega^2}}{3\alpha (\sqrt{9\alpha^2 + 4\omega^2} + 3\alpha) + 4(1 + 4\pi)\omega^2} \ln \left(\frac{L}{\ell} \right) \quad (\text{D.91})$$

$$\delta D(\alpha \gg \omega) = \frac{16 \left(3 \ln \left(\frac{\alpha \sqrt{6 \ln(\frac{\alpha}{\omega}) + 7}}{2\omega} \right) + 2 \right)}{\sqrt{6 \ln(\frac{\alpha}{\omega}) + 7} \left(3 \ln \left(\frac{\alpha \sqrt{6 \ln(\frac{\alpha}{\omega}) + 7}}{2\omega} \right) + 8\pi + 2 \right)} \ln \left(\frac{L}{\ell} \right) \quad (\text{D.92})$$

$$\xi(\alpha \ll \omega) = \ell \sqrt{\exp\left(\frac{(\sqrt{9\alpha^2 + 4\omega^2} - 3\alpha)^2}{3\alpha^2}\right) - 1} \quad (\text{D.93})$$

$$\xi(\alpha \gg \omega) = \ell \sqrt{\exp\left(\frac{4\omega^2 \left(6 \ln\left(\frac{\alpha \sqrt{6 \ln(\frac{\alpha}{\omega}) + 7}}{2\omega}\right) + 5\right)^2}{3\alpha^2 (6 \ln(\frac{\alpha}{\omega}) + 7)}\right) - 1} \quad (\text{D.94})$$

$$\nu(\alpha \ll \omega) = \frac{\omega}{2\pi \sqrt{9\alpha^2 + 4\omega^2}} \quad (\text{D.95})$$

$$\nu(\alpha \gg \omega) = \frac{\sqrt{6 \ln(\frac{\alpha}{\omega}) + 7}}{4\pi \left(3 \ln\left(\frac{\alpha \sqrt{6 \ln(\frac{\alpha}{\omega}) + 7}}{2\omega}\right) + 2\right)} \quad (\text{D.96})$$

BIBLIOGRAPHY

- [1] Karim M. Addas, Christoph F. Schmidt, and Jay X. Tang. Microrheology of solutions of semiflexible biopolymer filaments using laser tweezers interferometry. *Phys. Rev. E*, 70:021503, Aug 2004.
- [2] E Akkermans and R Maynard. Weak localization of waves. *Journal de Physique Lettres*, 46(22):1045–1053, 1985.
- [3] Eric Akkermans and Gilles Montambaux. *Mesoscopic physics of electrons and photons*. Cambridge university press, 2007.
- [4] Alexander Altland and Ben D Simons. *Condensed matter field theory*. Cambridge university press, 2010.
- [5] Philip W Anderson. Absence of diffusion in certain random lattices. *Phys. Rev.*, 109(5):1492, 1958.
- [6] Andrew J Archer and Robert Evans. Dynamical density functional theory and its application to spinodal decomposition. *The Journal of chemical physics*, 121(9):4246–4254, 2004.
- [7] Anthony E Armenàkas, Denos C Gazis, and George Herrmann. *Free Vibrations of Circular Cylindrical Shells*. Pergamon, 1969.
- [8] Yu N Barabanenkov and VD Ozrin. Asymptotic solution of the bethe-salpeter equation and the green-kubo formula for the diffusion constant for wave propagation in random media. *Physics Letters A*, 154(1-2):38–42, 1991.
- [9] Arthur W Barnard, Mian Zhang, Gustavo S Wiederhecker, Michal Lipson, and Paul L McEuen. Real-time vibrations of a carbon nanotube. *Nature*, 566(7742):89–93, 2019.
- [10] Mark Bathe, Claus Heussinger, Mireille MAE Claessens, Andreas R Bausch, and Erwin Frey. Cytoskeletal bundle mechanics. *Biophysical journal*, 94(8):2955–2964, 2008.
- [11] AR Bausch and K Kroy. A bottom-up approach to cell mechanics. *Nature physics*, 2(4):231–238, 2006.
- [12] G Bayer and T Niederdränk. Weak localization of acoustic waves in strongly scattering media. *Phys. Rev. letters*, 70(25):3884, 1993.

- [13] Nakul Prabhakar Bende, Arthur A Evans, Sarah Innes-Gold, Luis A Marin, Itai Cohen, Ryan C Hayward, and Christian D Santangelo. Geometrically controlled snapping transitions in shells with curved creases. *Proc. Natl. Acad. Sci. U.A.A.*, 112(36):11175–11180, 2015.
- [14] C Bower, R Rosen, L Jin, J Han, and O Zhou. Deformation of carbon nanotubes in nanotube–polymer composites. *Appl. Phys. Lett.*, 74(22):3317–3319, 1999.
- [15] C. P. Broedersz and F. C. MacKintosh. Modeling semiflexible polymer networks. *Rev. Mod. Phys.*, 86:995–1036, Jul 2014.
- [16] Chase P Broedersz, Martin Depken, Norman Y Yao, Martin R Pollak, David A Weitz, and Frederick C MacKintosh. Cross-link-governed dynamics of biopolymer networks. *Phys. Rev. Lett.*, 105(23):238101, 2010.
- [17] Vivien Brunel, Klaus Oerding, and Frédéric van Wijland. Fermionic field theory for directed percolation in $(1+1)$ -dimensions. *Journal of Physics A: Mathematical and General*, 33(6):1085, 2000.
- [18] Jakob Tómas Bullerjahn, Sebastian Sturm, Lars Wolff, and Klaus Kroy. Monomer dynamics of a wormlike chain. *EPL (Europhysics Letters)*, 96(4):48005, 2011.
- [19] Michel Campillo and Anne Paul. Long-range correlations in the diffuse seismic coda. *Science*, 299(5606):547–549, 2003.
- [20] Sudip Chakravarty and Albert Schmid. Weak localization: The quasiclassical theory of electrons in a random potential. *Physics Reports*, 140(4):193–236, 1986.
- [21] Daniel TN Chen, Qi Wen, Paul A Janmey, John C Crocker, and Arjun G Yodh. Rheology of soft materials. *Annu. Rev. Condens. Matter Phys.*, 1(1):301–322, 2010.
- [22] Bernard D Coleman, Ellis H Dill, and David Swigon. On the dynamics of flexure and stretch in the theory of elastic rods. *Arch. Ration. Mech. Anal.*, 129(2):147–174, 1995.
- [23] Moumita Das, F. C. MacKintosh, and Alex J Levine. Effective medium theory of semiflexible filamentous networks. *Phys. Rev. Lett.*, 99(3):038101, 2007.

- [24] David S Dean. Langevin equation for the density of a system of interacting langevin processes. *Journal of Physics A: Mathematical and General*, 29(24):L613, 1996.
- [25] Julien Dervaux and Martine Ben Amar. Morphogenesis of growing soft tissues. *Phys. Rev. letters*, 101(6):068101, 2008.
- [26] Ellis Harold Dill. Kirchhoff’s theory of rods. *Arch. Hist. Exact Sci.*, 44(1):1–23, 1992.
- [27] Masao Doi. Second quantization representation for classical many-particle system. *Journal of Physics A: Mathematical and General*, 9(9):1465, 1976.
- [28] H Dong and GT Evans. The freezing transition of a hard sphere fluid subject to the percus-yevick approximation. *The Journal of chemical physics*, 125(20):204506, 2006.
- [29] Elliot L Elson. Cellular mechanics as an indicator of cytoskeletal structure and function. *Annual review of biophysics and biophysical chemistry*, 17(1):397–430, 1988.
- [30] Arthur A Evans, Basanta Bhaduri, Gabriel Popescu, and Alex J Levine. Geometric localization of thermal fluctuations in red blood cells. *Proceedings of the National Academy of Sciences*, 114(11):2865–2870, 2017.
- [31] Arthur A Evans and Alex J Levine. Reflection and refraction of flexural waves at geometric boundaries. *Phys. Rev. letters*, 111(3):038101, 2013.
- [32] Ralf Everaers, Ralf Bundschuh, and Kurt Kremer. Fluctuations and stiffness of double-stranded polymers: railway-track model. *EPL (Europhysics Letters)*, 29(3):263, 1995.
- [33] Emmanuel Farge and Anthony C Maggs. Dynamic scattering from semiflexible polymers. *Macromolecules*, 26(19):5041–5044, 1993.
- [34] Shechao Feng, M. F. Thorpe, and E. Garboczi. Effective-medium theory of percolation on central-force elastic networks. *Phys. Rev. B*, 31:276–280, Jan 1985.
- [35] Pablo Fernández, Steffen Grosser, and Klaus Kroy. A unit-cell approach to the nonlinear rheology of biopolymer solutions. *Soft Matter*, 5:2047–2056, 2009.

- [36] Richard P. Feynman. Statistical mechanics: A set of lectures (the advanced book program), 1998.
- [37] Theodore Frankel. *The geometry of physics: an introduction*. Cambridge university press, 2011.
- [38] Margaret L Gardel, Fumihiko Nakamura, John H Hartwig, John C Crocker, Thomas P Stossel, and David A Weitz. Prestressed f-actin networks cross-linked by hinged filamins replicate mechanical properties of cells. *Proceedings of the National Academy of Sciences*, 103(6):1762–1767, 2006.
- [39] Doron Gazit. Structure of physical crystalline membranes within the self-consistent screening approximation. *Phys. Rev. E*, 80:041117, Oct 2009.
- [40] F. Gittes and F. C. MacKintosh. Dynamic shear modulus of a semiflexible polymer network. *Phys. Rev. E*, 58:R1241–R1244, Aug 1998.
- [41] F. Gittes, B. Schnurr, P. D. Olmsted, F. C. MacKintosh, and C. F. Schmidt. Microscopic viscoelasticity: Shear moduli of soft materials determined from thermal fluctuations. *Phys. Rev. Lett.*, 79:3286–3289, Oct 1997.
- [42] Roy J Glauber. Time-dependent statistics of the ising model. *Journal of mathematical physics*, 4(2):294–307, 1963.
- [43] C. Gordon, D. Webb, and S. Wolpert. Isospectral plane domains and surfaces via riemannian orbifolds. *Inventiones Mathematicae*, 110(1):1–22, 1992.
- [44] Kurt Gottfried and Tung-Mow Yan. *Quantum Mechanics: Fundamentals*. Springer Science & Business Media, 2013.
- [45] R Granek. From semi-flexible polymers to membranes: anomalous diffusion and reptation. *Journal de Physique II*, 7(12):1761–1788, 1997.
- [46] Oskar Hallatschek, Erwin Frey, and Klaus Kroy. Propagation and relaxation of tension in stiff polymers. *Phys. Rev. Lett.*, 94(7):077804, 2005.
- [47] Oskar Hallatschek, Erwin Frey, and Klaus Kroy. Tension dynamics in semiflexible polymers. i. coarse-grained equations of motion. *Phys. Rev. E*, 75(3):031905, 2007.
- [48] Oskar Hallatschek, Erwin Frey, and Klaus Kroy. Tension dynamics in semiflexible polymers. i. coarse-grained equations of motion. *Phys. Rev. E*, 75(3):031905, 2007.

- [49] Oskar Hallatschek, Erwin Frey, and Klaus Kroy. Tension dynamics in semiflexible polymers. ii. scaling solutions and applications. *Phys. Rev. E*, 75(3):031906, 2007.
- [50] Oskar Hallatschek, Erwin Frey, and Klaus Kroy. Tension dynamics in semiflexible polymers. ii. scaling solutions and applications. *Phys. Rev. E*, 75(3):031906, 2007.
- [51] Jean-Pierre Hansen and Ian R McDonald. *Theory of simple liquids*. Elsevier, 1990.
- [52] David A Head, Alex J Levine, and F. C. MacKintosh. Deformation of cross-linked semiflexible polymer networks. *Phys. Rev. Lett.*, 91(10):108102, 2003.
- [53] Douglas Henderson. *Fundamentals of inhomogeneous fluids*. CRC Press, 1992.
- [54] Claus Heussinger. Cooperative crosslink (un) binding in slowly driven bundles of semiflexible filaments. *Phys. Rev. E*, 83(5):050902, 2011.
- [55] Claus Heussinger, Mark Bathe, and Erwin Frey. Statistical mechanics of semiflexible bundles of wormlike polymer chains. *Phys. Rev. Lett.*, 99(4):048101, 2007.
- [56] Claus Heussinger, Mark Bathe, and Erwin Frey. Statistical mechanics of semiflexible bundles of wormlike polymer chains. *Phys. Rev. Lett.*, 99(4):048101, 2007.
- [57] Claus Heussinger, Felix Schüller, and Erwin Frey. Statics and dynamics of the wormlike bundle model. *Phys. Rev. E*, 81(2):021904, 2010.
- [58] Tetsuya Hiraiwa and Takao Ohta. Viscoelastic behavior of a single semiflexible polymer chain. *Journal of the Physical Society of Japan*, 77(2):023001, 2008.
- [59] P. C. Hohenberg and B. I. Halperin. Theory of dynamic critical phenomena. *Rev. Mod. Phys.*, 49:435–479, Jul 1977.
- [60] Akira Ishimaru. *Electromagnetic wave propagation, radiation, and scattering: from fundamentals to applications*. John Wiley & Sons, 2017.
- [61] IL Ivanovska, PJ De Pablo, B Ibarra, G Sgalari, FC MacKintosh, JL Carras-cosa, CF Schmidt, and GJL Wuite. Bacteriophage capsids: tough nanoshells with complex elastic properties. *Proc. Natl. Acad. Sci. U.A.A.*, 101(20):7600–7605, 2004.

- [62] Paul A Janmey, Margaret E McCormick, Sebastian Rammensee, Jennifer L Leight, Penelope C Georges, and Fred C MacKintosh. Negative normal stress in semiflexible biopolymer gels. *Nature materials*, 6(1):48, 2007.
- [63] Sajeev John, Haim Sompolinsky, and Michael J Stephen. Localization in a disordered elastic medium near two dimensions. *Phys. Rev. B*, 27(9):5592, 1983.
- [64] Mark Kac. Can one hear the shape of a drum? *The American Mathematical Monthly*, 73(4P2):1–23, 1966.
- [65] Devin Kachan, Robijn Bruinsma, and Alex J Levine. Casimir interactions in semiflexible polymers. *Phys. Rev. E*, 87(3):032719, 2013.
- [66] Devin Kachan, Kei W Müller, Wolfgang A Wall, and Alex J Levine. Discontinuous bundling transition in semiflexible polymer networks induced by casimir interactions. *Phys. Rev. E*, 94(3):032505, 2016.
- [67] Hyeran Kang, Qi Wen, Paul A Janmey, Jay X Tang, Enrico Conti, and Fred C MacKintosh. Nonlinear elasticity of stiff filament networks: strain stiffening, negative normal stress, and filament alignment in fibrin gels. *The Journal of Physical Chemistry B*, 113(12):3799–3805, 2009.
- [68] Mehran Kardar. *Statistical physics of fields*. Cambridge University Press, 2007.
- [69] Karen E Kasza, Amy C Rowat, Jiayu Liu, Thomas E Angelini, Clifford P Brangwynne, Gijsje H Koenderink, and David A Weitz. The cell as a material. *Current opinion in cell biology*, 19(1):101–107, 2007.
- [70] Philip Kearey, Keith A Klepeis, and Frederick J Vine. *Global Tectonics*. John Wiley & Sons, Singapore, 3rd edition, 2009.
- [71] Jonathan Kernes and Alex J Levine. Equilibrium fluctuations of a semiflexible filament cross linked into a network. *Phys. Rev. E*, 101(1):012408, 2020.
- [72] TR Kirkpatrick. Localization of acoustic waves. *Phys. Rev. B*, 31(9):5746, 1985.
- [73] William S Klug, Robijn F Bruinsma, Jean-Philippe Michel, Charles M Knobler, Irena L Ivanovska, Christoph F Schmidt, and Gijs JL Wuite. Failure of viral shells. *Phys. Rev. Letters*, 97(22):228101, 2006.

- [74] Gijssje H Koenderink, Zvonimir Dogic, Fumihiko Nakamura, Poul M Bendix, Frederick C MacKintosh, John H Hartwig, Thomas P Stossel, and David A Weitz. An active biopolymer network controlled by molecular motors. *Proceedings of the National Academy of Sciences*, 106(36):15192–15197, 2009.
- [75] Andrej Košmrlj and David R. Nelson. Response of thermalized ribbons to pulling and bending. *Phys. Rev. B*, 93:125431, Mar 2016.
- [76] Michael Korn. Seismic waves in random media. *Journal of applied geophysics*, 29(3-4):247–269, 1993.
- [77] Andrej Košmrlj and David R Nelson. Mechanical properties of warped membranes. *Phys. Rev. E*, 88(1):012136, 2013.
- [78] Andrej Košmrlj and David R Nelson. Thermal excitations of warped membranes. *Phys. Rev. E*, 89(2):022126, 2014.
- [79] Erwin Kreyszig. *Introduction to differential geometry and Riemannian geometry*. University of Toronto Press, 1968.
- [80] Johann Kroha, CM Soukoulis, and P Wölfle. Localization of classical waves in a random medium: A self-consistent theory. *Phys. Rev. B*, 47(17):11093, 1993.
- [81] Tatiana Kuriabova and Alex J Levine. Nanorheology of viscoelastic shells: Applications to viral capsids. *Phys. Rev. E*, 77(3):031921, 2008.
- [82] Stéphane Lafortune, Alain Goriely, and Michael Tabor. The dynamics of stretchable rods in the inertial case. *Nonlinear Dynamics*, 43(1-2):173–195, 2006.
- [83] L.D. Landau and E.M. Lifshitz. Pergamon, Oxford, 3rd edition, 1986.
- [84] F. C. Larche, J. Appell, G. Porte, P. Bassereau, and J. Marignan. Extreme swelling of a lyotropic lamellar liquid crystal. *Phys. Rev. Lett.*, 56:1700–1703, Apr 1986.
- [85] Olga Latinovic, Lawrence A Hough, and H Daniel Ou-Yang. Structural and micromechanical characterization of type i collagen gels. *Journal of Biomechanics*, 43(3):500–505, 2010.
- [86] Eric Lauga and Thomas R Powers. The hydrodynamics of swimming microorganisms. *Reports on Progress in Physics*, 72(9):096601, 2009.

- [87] Arnaud Lazarus, HCB Florijn, and Pedro M Reis. Geometry-induced rigidity in nonspherical pressurized elastic shells. *Phys. Rev. Lett.*, 109(14):144301, 2012.
- [88] Pierre Le Doussal and Leo Radzihovsky. Self-consistent theory of polymerized membranes. *Phys. Rev. Lett.*, 69:1209–1212, Aug 1992.
- [89] Pierre Le Doussal and Leo Radzihovsky. Flat glassy phases and wrinkling of polymerized membranes with long-range disorder. *Phys. Rev. B*, 48(5):3548, 1993.
- [90] Alex J Levine and FC MacKintosh. The mechanics and fluctuation spectrum of active gels. *The Journal of Physical Chemistry B*, 113(12):3820–3830, 2009.
- [91] Jack Lidmar, Leonid Mirny, and David R Nelson. Virus shapes and buckling transitions in spherical shells. *Phys. Rev. E*, 68(5):051910, 2003.
- [92] O. Lieleg, M. M. A. E. Claessens, C. Heussinger, E. Frey, and A. R. Bausch. Mechanics of bundled semiflexible polymer networks. *Phys. Rev. Lett.*, 99:088102, Aug 2007.
- [93] Oliver Lieleg, Mireille MAE Claessens, and Andreas R Bausch. Structure and dynamics of cross-linked actin networks. *Soft Matter*, 6(2):218–225, 2010.
- [94] Oliver Lieleg, Kurt M Schmoller, Christian J Cyron, Yuxia Luan, Wolfgang A Wall, and Andreas R Bausch. Structural polymorphism in heterogeneous cytoskeletal networks. *Soft Matter*, 5(9):1796–1803, 2009.
- [95] James Lighthill. Flagellar hydrodynamics. *SIAM review*, 18(2):161–230, 1976.
- [96] Yi-Chia Lin, Gijsje H Koenderink, Frederick C MacKintosh, and David A Weitz. Viscoelastic properties of microtubule networks. *Macromolecules*, 40(21):7714–7720, 2007.
- [97] Emanuel N Lissek, Tobias F Bartsch, and Ernst-Ludwig Florin. Resolving filament level mechanics in collagen networks using activity microscopy. *bioRxiv*, page 382903, 2018.
- [98] F. C. MacKintosh, Josef Käs, and P. A. Janmey. Elasticity of semiflexible biopolymer networks. *Phys. Rev. Lett.*, 75(24):4425, 1995.
- [99] Fred C MacKintosh and Alex J Levine. Nonequilibrium mechanics and dynamics of motor-activated gels. *Phys. Rev. Lett.*, 100(1):018104, 2008.

- [100] Umberto Marini Bettolo Marconi and Pedro Tarazona. Dynamic density functional theory of fluids. *The Journal of chemical physics*, 110(16):8032–8044, 1999.
- [101] Umberto Marini Bettolo Marconi and Pedro Tarazona. Dynamic density functional theory of fluids. *Journal of Physics: Condensed Matter*, 12(8A):A413, 2000.
- [102] AJ McKane and Michael Stone. Localization as an alternative to goldstone’s theorem. *Annals of Physics*, 131(1):36–55, 1981.
- [103] JP Michel, IL Ivanovska, MM Gibbons, WS Klug, CM Knobler, GJL Wuite, and CF Schmidt. Nanoindentation studies of full and empty viral capsids and the effects of capsid protein mutations on elasticity and strength. *Proc. Natl. Acad. Sci. U.A.A.*, 103(16):6184–6189, 2006.
- [104] Daisuke Mizuno, DA Head, FC MacKintosh, and CF Schmidt. Active and passive microrheology in equilibrium and nonequilibrium systems. *Macromolecules*, 41(19):7194–7202, 2008.
- [105] Daisuke Mizuno, Catherine Tardin, Christoph F Schmidt, and Frederik C MacKintosh. Nonequilibrium mechanics of active cytoskeletal networks. *Science*, 315(5810):370–373, 2007.
- [106] David C Morse. Viscoelasticity of concentrated isotropic solutions of semiflexible polymers. 1. model and stress tensor. *Macromolecules*, 31(20):7030–7043, 1998.
- [107] David C Morse. Viscoelasticity of concentrated isotropic solutions of semiflexible polymers. 2. linear response. *Macromolecules*, 31(20):7044–7067, 1998.
- [108] David C Morse. Viscoelasticity of tightly entangled solutions of semiflexible polymers. *Phys. Rev. E*, 58(2):R1237, 1998.
- [109] David C Morse. Viscoelasticity of concentrated isotropic solutions of semiflexible polymers. 3. nonlinear rheology. *Macromolecules*, 32(18):5934–5943, 1999.
- [110] David C Morse and Tom C Lubensky. Curvature disorder in tethered membranes: A new flat phase at $t = 0$. *Phys. Rev. A*, 46(4):1751, 1992.

- [111] Kei W Müller, Robijn F Bruinsma, Oliver Lieleg, Andreas R Bausch, Wolfgang A Wall, and Alex J Levine. Rheology of semiflexible bundle networks with transient linkers. *Phys. Rev. Lett.*, 112(23):238102, 2014.
- [112] David R Nelson, Tsvi Piran, and Steven Weinberg. *Statistical Mechanics of Membranes and Surfaces*. World Scientific, Singapore, 2nd edition, 2004.
- [113] DR Nelson and L Peliti. Fluctuations in membranes with crystalline and hexatic order. *Journal de physique*, 48(7):1085–1092, 1987.
- [114] Philip Nelson. *Biological physics*. WH Freeman New York, 2004.
- [115] F.I. Niordson. *Shell Theory*. North-Holland, Amsterdam, 2012.
- [116] Benedikt Obermayer and Erwin Frey. Tension dynamics and viscoelasticity of extensible wormlike chains. *Phys. Rev. E*, 80:040801, Oct 2009.
- [117] Benedikt Obermayer and Oskar Hallatschek. Coupling of transverse and longitudinal response in stiff polymers. *Phys. Rev. Lett.*, 99(9):098302, 2007.
- [118] Su-Chan Park, Doochul Kim, and Jeong-Man Park. Path-integral formulation of stochastic processes for exclusive particle systems. *Phys. Rev. E*, 62(6):7642, 2000.
- [119] Su-Chan Park and Jeong-Man Park. Generating function, path integral representation, and equivalence for stochastic exclusive particle systems. *Phys. Rev. E*, 71(2):026113, 2005.
- [120] YongKeun Park, Catherine A Best, Kamran Badizadegan, Ramachandra R Dasari, Michael S Feld, Tatiana Kuriabova, Mark L Henle, Alex J Levine, and Gabriel Popescu. Measurement of red blood cell mechanics during morphological changes. *Proc. Natl. Acad. Sci. U.A.A.*, 107(15):6731–6736, 2010.
- [121] YongKeun Park, Catherine A Best, Tatiana Kuriabova, Mark L Henle, Michael S Feld, Alex J Levine, and Gabriel Popescu. Measurement of the nonlinear elasticity of red blood cell membranes. *Phys. Rev. E*, 83(5):051925, 2011.
- [122] L Peliti. Path integral approach to birth-death processes on a lattice. *Journal de Physique*, 46(9):1469–1483, 1985.

- [123] Olivier Pelletier, Elena Pokidysheva, Linda S Hirst, Nate Bouxsein, Youli Li, and Cyrus R Safinya. Structure of actin cross-linked with α -actinin: a network of bundles. *Phys. Rev. Lett.*, 91(14):148102, 2003.
- [124] JK Percus. One-dimensional classical fluid with nearest-neighbor interaction in arbitrary external field. *Journal of Statistical Physics*, 28(1):67–81, 1982.
- [125] Robyn H Pritchard, Yan Yan Shery Huang, and Eugene M Terentjev. Mechanics of biological networks: from the cell cytoskeleton to connective tissue. *Soft matter*, 10(12):1864–1884, 2014.
- [126] Leo Radzihovsky and Pierre Le Doussal. Crumpled glass phase of randomly polymerized membranes in the large d limit. *Journal de Physique I*, 2(5):599–613, 1992.
- [127] Leo Radzihovsky and David R Nelson. Statistical mechanics of randomly polymerized membranes. *Phys. Rev. A*, 44(6):3525, 1991.
- [128] TV Ramakrishnan and M Yussouff. Theory of the liquid-solid transition. *Solid State Communications*, 21(4):389–392, 1977.
- [129] TV Ramakrishnan and M. Yussouff. First-principles order-parameter theory of freezing. *Phys. Rev. B*, 19(5):2775, 1979.
- [130] Jorgen Rammer. *Quantum transport theory*. CRC Press, 2018.
- [131] C. R. Safinya, D. Roux, G. S. Smith, S. K. Sinha, P. Dimon, N. A. Clark, and A. M. Bellocq. Steric interactions in a model multimembrane system: A synchrotron x-ray study. *Phys. Rev. Lett.*, 57:2718–2721, Nov 1986.
- [132] Jun John Sakurai and Eugene D Commins. *Modern quantum mechanics, revised edition*. American Association of Physics Teachers, 1995.
- [133] J Lyell Sanders Jr. Nonlinear theories for thin shells. *Quarterly of Applied Mathematics*, 21(1):21–36, 1963.
- [134] Andrés Santos. A concise course on the theory of classical liquids. *Lecture Notes in Physics*, 923, 2016.
- [135] KM Schmoller, O Lieleg, and AR Bausch. Structural and viscoelastic properties of actin/filamin networks: cross-linked versus bundled networks. *Biophysical journal*, 97(1):83–89, 2009.

- [136] B Schnurr, F Gittes, F. C. MacKintosh, and CF Schmidt. Determining microscopic viscoelasticity in flexible and semiflexible polymer networks from thermal fluctuations. *Macromolecules*, 30(25):7781–7792, 1997.
- [137] Matthew D Schwartz. *Quantum field theory and the standard model*. Cambridge University Press, 2014.
- [138] Udo Seifert, Wolfgang Wintz, and Philip Nelson. Straightening of thermal fluctuations in semiflexible polymers by applied tension. *Phys. Rev. Lett.*, 77(27):5389, 1996.
- [139] M Sheinman, C. P. Broedersz, and F. C. MacKintosh. Nonlinear effective-medium theory of disordered spring networks. *Phys. Rev. E*, 85(2):021801, 2012.
- [140] Ping Sheng. *Introduction to wave scattering, localization and mesoscopic phenomena*, volume 88. Springer Science & Business Media, 2006.
- [141] Jack Sherman and Winifred J Morrison. Adjustment of an inverse matrix corresponding to a change in one element of a given matrix. *The Annals of Mathematical Statistics*, 21(1):124–127, 1950.
- [142] Amit R Singh, Andrej Košmrlj, and Robijn Bruinsma. Finite temperature phase behavior of viral capsids as oriented particle shells. *Phys. Rev. Lett.*, 124(15):158101, 2020.
- [143] Michael D Spivak. *A Comprehensive Introduction to Differential Geometry*. Publish or Perish, Houston, 3rd edition, 1999.
- [144] L Starrs and P Bartlett. One-and two-point micro-rheology of viscoelastic media. *Journal of Physics: Condensed Matter*, 15(1):S251, 2002.
- [145] Cornelis Storm, Jennifer J Pastore, Fred C MacKintosh, Tom C Lubensky, and Paul A Janmey. Nonlinear elasticity in biological gels. *Nature*, 435(7039):191, 2005.
- [146] Uwe C Täuber. *Critical dynamics: a field theory approach to equilibrium and non-equilibrium scaling behavior*. Cambridge University Press, 2014.
- [147] David J Thouless. Electrons in disordered systems and the theory of localization. *Physics Reports*, 13(3):93–142, 1974.

- [148] Lloyd N Trefethen. *Spectral Methods in MATLAB*, volume 10. Siam, 2000.
- [149] Meint P Van Albada and Ad Lagendijk. Observation of weak localization of light in a random medium. *Phys. Rev. letters*, 55(24):2692, 1985.
- [150] Meint P van Albada, Bart A van Tiggelen, Ad Lagendijk, and Adriaan Tip. Speed of propagation of classical waves in strongly scattering media. *Phys. Rev. letters*, 66(24):3132, 1991.
- [151] MCW van van Rossum and Th M Nieuwenhuizen. Multiple scattering of classical waves: microscopy, mesoscopy, and diffusion. *Reviews of Modern Physics*, 71(1):313, 1999.
- [152] Bart A van Tiggelen, Ad Lagendijk, Meint P van Albada, and Adriaan Tip. Speed of light in random media. *Phys. Rev. B*, 45(21):12233, 1992.
- [153] Ashkan Vaziri and L Mahadevan. Localized and extended deformations of elastic shells. *Proc. Natl. Acad. Sci. U.A.A.*, 105(23):7913–7918, 2008.
- [154] Dieter Vollhardt and Peter Wölfle. Self-consistent theory of anderson localization. In *Modern Problems in Condensed Matter Sciences*, volume 32, pages 1–78. Elsevier, 1992.
- [155] Lifeng Wang and Haiyan Hu. Flexural wave propagation in single-walled carbon nanotubes. *Phys. Rev. B*, 71(19):195412, 2005.
- [156] R Waugh and EA Evans. Thermoelasticity of red blood cell membrane. *Biophysical Journal*, 26(1):115–131, 1979.
- [157] Qi Wen and Paul A Janmey. Polymer physics of the cytoskeleton. *Current Opinion in Solid State and Materials Science*, 15(5):177–182, 2011.
- [158] Chris H Wiggins, D Riveline, Albrecht Ott, and Raymond E Goldstein. Trapping and wiggling: elastohydrodynamics of driven microfilaments. *Biophysical Journal*, 74(2):1043–1060, 1998.
- [159] Jan Wilhelm and Erwin Frey. Elasticity of stiff polymer networks. *Phys. Rev. Lett.*, 91(10):108103, 2003.
- [160] Pierre-Etienne Wolf and Georg Maret. Weak localization and coherent backscattering of photons in disordered media. *Phys. Rev. letters*, 55(24):2696, 1985.

- [161] Yali Yang, Jun Lin, Bugra Kaytanli, Omar A Saleh, and Megan T Valentine. Direct correlation between creep compliance and deformation in entangled and sparsely crosslinked microtubule networks. *Soft Matter*, 8(6):1776–1784, 2012.
- [162] K. V. Zakharchenko, R. Roldán, A. Fasolino, and M. I. Katsnelson. Self-consistent screening approximation for flexible membranes: Application to graphene. *Phys. Rev. B*, 82:125435, Sep 2010.
- [163] John M Ziman. *Models of disorder: the theoretical physics of homogeneously disordered systems*. CUP Archive, 1979.
- [164] Jean Zinn-Justin. *Quantum field theory and critical phenomena*. Clarendon Press, 1996.